Universidade de Évora

Departamento de Física

SPATRAM

- SPectrometer for Atmospheric TRAcers Measurements -

a Prototype Equipment for the monitoring of minor compounds of the atmosphere

Daniele Bortoli

Supervisor: Professor Doctor Ana Maria Guedes de Almeida e Silva
Co – Supervisor: Doctor Giorgio Giovanelli

A dissertation submitted to the University of Évora to obtain the Degree of Doctor of Philosophy in Physics

Évora

2005

Acknowledgment

Contents

Figure Index

Table Index

Resumo

O presente trabalho desenvolveu-se para atingir dois objectivos; um de vertente tecnológica e o segundo de vertente científica: o primeiro, que visou o desenvolvimento de um novo espectrómetro que opera nas regiões espectrais do ultravioleta (UV) e visível (Vis), com as tecnologias mais avançadas disponíveis, assim como a realização do equipamento e a sua instalação no Centro de Geofísica de Évora (CGE); o segundo objectivo, visou o estudo dos algoritmos da Espectroscopia de Absorção Óptica Diferencial (DOAS) e da sua aplicação às medidas espectrais das secções eficazes de absorção de gases traçadores atmosféricos (principalmente dióxido de azoto – NO_2 e ozono – O_3 presentes na estratosfera) a partir dos quais se pode obter as quantidades colunares desses gases. Finalmente, e ainda inserido nos objectivos científicos, foi possível comparar valores colunares de gases atmosféricos, quimicamente relevantes obtidos a partir de observação à superfície (SPATRAM), com valores correspondentes obtidos a partir de observações de satélite. Foi ainda investigada a relação entre episódios de aerossóis (aerossóis do deserto do Sahara) e os conteúdos colunares de gases traçadores atmosféricos.

O primeiro objectivo da tese de Doutoramento foi completamente alcançado. Os estudos de física da atmosfera e dos diferentes tipos de equipamento usado para efectuar as medições e para a caracterização da radiação solar, permitiram o desenvolvimento de um protótipo, o espectrómetro denominado SPectrometer for Atmospheric TRAcers Measurements (SPATRAM). O SPATRAM opera no UV e Vis (250-950nm) com uma resolução típica de 0.5 nm e está equipado com três possíveis entradas da radiação, uma delas correspondente à observação no zénite . O SPATRAM encontra-se instalado no observatório do CGE desde Abril 2004 e é presentemente utilizado para fazer medições da radiação difusa no zénite. Os estudos da metodologia DOAS permitiram a implementação de uma ferramenta para a determinação da concentração ao longo do percurso óptico da medição de alguns dos componentes atmosféricos com características de absorção muito marcadas (principalmente NO_2 e O_3) na região espectral coberta pelo SPATRAM. Este objectivo foi também atingido e esta ferramenta foi aplicada tanto a medidas espectrais obtidas com o SPATRAM como com um equipamento semelhante (GASCOD - Gas Analyzer Spectrometer Correlating Optical Differences) instalado na Estação Italiana na Antárctica, desde 1995. Foi ainda possível com o desenvolvimento da metodologia DOAS investigar a influência das diferentes temperaturas da secção eficaz do mesmo composto.

Abstract

The goals of this research can be divided in two main subjects: the technological one, regarding the development of a new UV-Visible spectrometer with the most advanced available technologies, the realization of the equipment and its installation at the Geophysics Centre of Évora (CGE). The scientific topic concerning both the deep studies of the Differential Optical Absorption Spectroscopy (DOAS) algorithms and their application to the measured spectral data as well as the measurements and the monitoring of some atmospheric gases (mainly stratospheric NO_2 and O_3) and the comparison of the obtained results with satellite data. In addition, a relation between episodes of aerosol contamination and the content of atmospheric trace gases is expected to be found.

The first goal of the doctorial project was completely reached. The studies on the atmospheric physics and on the different types of equipment used for the measurements and for the characterization of the solar radiation, allowed for the development of a spectrometer prototype called SPectrometer for Atmospheric TRAcers Measurements (SPATRAM).The SPATRAM is a multi purpose UV-Vis. Spectrometer (250-950 nm), with a typical spectral resolution of 0.5nm; it is equipped with three radiation input, one pointing the zenith direction. The SPATRAM is installed at the CGE Observatory since April 2004 and it is presently utilized to carry-out measurements of the zenith scattered radiation.

The studies of the DOAS methodology are aimed to the implementation of a tool for the determination of the Slant Column Density (SCD) of some atmospheric compounds with marked absorption spectral features (mainly nitrogen dioxide - NO_2 and ozone - O_3) in the spectral range covered by SPATRAM. Also this goal was reached, and the tool was applied to the spectral measurements obtained as with the SPATRAM as well as with similar equipment (the GASCOD - Gas Analyzer Spectrometer Correlating Optical Differences) installed at the Antarctic Italian Station since 1995. Also the influence of the different temperatures of the same absorber's cross section utilized in the retrieval was investigated.

Riassunto

Gli obiettivi di questo progetto di ricerca possono essere suddivisi in due diversi tipologie: quella tecnologica che prevede la progettazione, sviluppo e realizzazione di un nuova spettrometro operante nelle regioni spettrali del visibile e dell'ultravioletto, munito delle più avanzate soluzioni tecnologiche disponibili e la sua installazione al centro di geofisica dell'Università di Evora. L'aspetto scientifico di questa ricerca prevede sia lo studio approfondito degli algoritmi della Spettroscopia ad Assorbimento Ottico Differenziale (DOAS), a la loro applicazione alle serie spettrali misurate con lo spettrometro, sia la misura ed il monitoraggio di alcuni composti minori dell'atmosphera (principalmente biossido di azoto – NO_2, e ozono – O_3, in questa prima fase della ricerca) e il confronto dei risultati ottenuti con la strumentazione al suolo con quelli ottenuti da strumenti installati su satelliti. Inoltre, ci si aspetta di ottenere una relazione tra il contenuto di gas atmosferici ed episodi di contaminazione da particolato (aerosoli).

Il primo obiettivo del progetto di dottorato è stato completamente raggiunto. Gli studi condotti sui processi fisici in atmosfera e sui diversi tipi di strumenti utilizzati per la misura e la caratterizzazione della radiazione solare, hanno permesso di progettare e realizzare un prototipo di spettrometro che è stato chiamato SPATRAM (SPectrometer for Atmospheric TRAcers Measurements). Al fine di ottenere uno strumento multi funzione lo SPATRAM è dotato di tre diversi ingressi (uno punta direttamente lo zenith con un campo di vista di $1.1 \cdot 10^{-5}$ sr, e due ingressi via fibra ottica), che consistono in una serie di specchi piani e sferici che focalizzano la radiazione in ingresso sulla fenditura d'ingresso al monocromatore. SPATRAM è uno spettrometro UV-Vis. che opera nella regione spettrale da 250 a 950nm, con una risoluzione ottica tipica di 0.5nm. L'intero intervallo spettrale è indagato in finestre successive di 60nm ognuna, grazie all'uso di un motore passo-passo che variando la posizione del reticolo, modifica l'intervallo spettrale che raggiunge il sensore. Quest'ultimo è un CCD (Charged Coupled Device – dispositivo ad accoppiamento di carica) che permette di ottenere prestazioni molto migliori di quelle ottenibili con i rivelatori CMOS (Complementary Metal Oxide Semiconductor). Il maggior vantaggio nell'uso dei CCD risiede nell'alto rapporto segnale rumore che può essere ottenuto.

Lo SPATRAM è installato all'osservatorio del CGE dall'Aprile del 2004 ed è attualmente utilizzato per la misura di radiazione solare diffusa lungo la verticale.

Gli studi sulla metodologia DOAS erano finalizzati all'implementazione di uno strumento software per la determinazione della concentrazione lungo il percorso ottico di misura di alcuni composti minori dell'atmosfera con pronunciate caratteristiche di assorbimento (principalmente biossido di azoto - NO_2, ed ozono – O_3 in questa prima fase della ricerca)nella regione spettrale coperta da SPATRAM. Anche questo obiettivo è stato raggiunto, e nella prima parte di questo lavoro di dottorato (a causa della non

disponibilità di dati ottenuti con SPATRAM che era ancora in fase di realizzazione) il software sviluppato è stato applicato a serie di dati spettrali ottenuti con strumentazione simile allo SPATRAM, il GASCOD (Gas Analyzer Spectrometer Correlating Optical Differences) che è installato nella base italiana in Antartide. La fase di test degli algoritmi ha permesso di ottimizzare il software ed il chiarimento degli effetti causati dallo spettro scelto come riferimento, sul valore calcolato della concentrazione lungo l percorso ottico di misura della specie gassosa analizzata. Inoltre è stato studiato l'effetto sui risultati ottenuti dovuto ai coefficienti di assorbimento degli assorbitori a diverse temperature

I risultati ottenuti ad alte latitudini per le concentrazioni colonnari integrate lungo la verticale per biossido di azoto ed ozono stratosferici sono stati rispettivamente confrontati con i risultati dello spettrometro GOME (Global Ozone Monitoring Experiment) e con quelli del TOMS (Total Ozone Mapping Spectrometer), esibendo un ottimo accordo in termini sia di variazioni stagionale che giornaliera

In seguito gli algoritmi della DOAS sono stati applicati ai dati spettrali ottenuti con lo SPATRAM installato al Centro di Geofisica di Evora. Si sono ottenute sia le variazioni stagionali che giornaliere per NO_2 ed O_3; la forte attività fotochimica dei composti attivi dell'azoto conduce a valori di concentrazione colonnare di NO2 all'alba (valori AM) sistematicamente inferiori a quelli ottenuti al tramonto (valori PM); al contrario, per l'ozono i valori AM e quelli PM sono sostanzialmente gli stessi. Per quanto riguarda la variazione stagionale, si è osservato il comportamento atteso, mostrando il massimo valore durante la stagione estiva ed il minimo è ottenuto per i mesi invernali. Anche per questi risultati si è proceduto ad un confronto dei valori ottenuti con quelli satellitari del GOME e del TOMS, ottenendo un ottimo accordo. I risultati della comparazione attestano che sia lo strumento SPATRAM (in configurazione zenitale), sia il Software implementato per l'applicazione degli algoritmi della DOAS, sono strumenti appropriati per il monitoraggio dei costituenti minori dell'atmosfera. Per quanto concerne l'influenze del particolato atmosferico sul calcolo dei contenuti verticali dei gas, è stato analizzato un caso avvenuto il 20-21 Maggio 2004. Lo strano comportamento osservato per il contenuto verticale di ozono osservato durante il 20 Maggio, suggeriva un aumento del contenuto dell' ozono stesso. Considerati sia la stagione, sia la localizzazione di Evora (lontano da zone in cui si ha inquinamento da ozono), si sono dovuti considerare altri possibili fattori. L'analisi dell'"Indice degli aerosoli" (Aerosol Index), che è un prodotto operazionale del TOMS, si è potuto apprezzare un evento di contaminazione di particolato desertico nel sud del Portogallo il 20 Maggio. Quindi gli alti valori di contenuto colonnare di ozono ottenuti per il 20 Maggio non sono da considerarsi relazionati ad un vero e proprio aumento di ozono, bensì ad una diminuzione della radiazione misurata provocata dall'assorbimento da parte degli aerosoli desertici. Queste considerazioni aprono un altro campi di possibili applicazioni delle misure DOAS: la possibilità di ottenere informazioni su episodi di contaminazione da particolato desertico.

List of Acronyms

ACS – Absorption Cross Section

AD Converter – Analogical Digital Converter

AERONET - AErosol RObotic NETwork

AMEFCO – Atmospheric Model for Enhancement Factor COmputation

AMF – Air Mass Factor

CCD – Charged Coupled Device

CFC - Chlorofluorocarbons

CGE – Centro de Geofísica de Évora

CMOS - Complementary Metal Oxide Semiconductor

DAS - Data Acquisition Software

DCL – DTA Camera Library

DCS – Differential Cross Section

DOAS – Differential Optical Absorption Spectroscopy

DSCD – Differential Slant Column Density

DU – Dobson Unit

Dx – Opto-switch number x

ECU - Electronic and Control Unit

ENEA - Ente per le Nuove Tecnologie, l'Energia el'Ambiente

ENVISAT - ENVIronmental SATellite

EOS - Earth Observing System

EPA - Environmental Protection Agency

ERS - European Remote-Sensing satellite

FT-IR – Fourier Transform-Infrared Spectroscopy

FWC – Full Well Capacity

GASCOD – Gas Analyzer Spectrometer Correlating Optical Differences

GOME - Global Ozone Monitoring Experiment

GOMOS - Global Ozone Monitoring by Occultation of Stars

ISAC – Istituto di Scienze dell'Atmosfera e Clima

LBAA – Lambert-Beer law in Absence of Absorbers

LIDAR – Light Detection And Ranging

LIS – Laser Induced Spectroscopy

MGUI – Morello Graphic User Interface

MIGE - Multiple Input Geometry Equipment

MSL – Minimum Scattering Layer

NASA - National Aeronautics and Space Administration (of the USA)

NDSC – Network for the Detections of the Stratospheric Changes

NH – Northern Hemisphere

NIR – Near Infrared

NOAA - National Oceanic and Atmospheric Administration (of the USA) (and its polar satellite series)

OMI – Ozone Monitoring Instrument

OMU - Optical and Mechanical Unit

PBL – Planetary Boundary Layer

PSC – Polar Stratospheric Clouds

QE – Quantum Efficiency

RADAR - RAdio Detection And Ranging

ROI – Relais Opto Interface

RTM – Radiative Transfer Model

SCD – Slant Column Density

SCIAMACHY - SCanning Imaging Absorption spectroMeter for Atmospheric ChartographY

SDP – Similar DOAS Procedure

SH – Southern Hemisphere

SMx – Stepper Motor number x

SNR – Signal to Noise Ratio

SODAR - SOnic Detection and Ranging

SOS – Sum of Square

SPATRAM – Spectrometer for Atmospheric Tracers Measurements

STP – Standard Pressure and Temperature

SVD – Singular Value Decomposition

SZA – Solar Zenith Angle

TAD – Temperature Adapter Device

TDLAS – Tunable Diode Spectroscopy Laser

TOA – Top Of the Atmosphere

TOMS - Total Ozone Mapping Spectrometer

UV – Ultraviolet

UVSPEC -

VCD – Vertical Column Density

VOC – Volatile Organic Compounds

WMO - World Meteorological Organization

List of Symbols

E$_\lambda$ – Monochromatic radiance $\qquad\qquad\qquad\qquad$ $(W.m^{-2}.sr^{-1}.\mu m^{-1})$

G – Gravitational acceleration $\qquad\qquad\qquad\qquad$ $(9.8\, m \cdot s^{-2})$

I$_\lambda$ – Monochromatic radiance $\qquad\qquad\qquad\qquad$ $(W.m^{-2}.sr^{-1}.\mu m^{-1})$

I$_{0\lambda}$ – TOA incident solar monochromatic radiance $\qquad\qquad$ $(W.m^{-2}.sr^{-1}.\mu m^{-1})$

J$_\lambda$ – Monochromatic source function $\qquad\qquad\qquad$ $(W.m^{-2}.sr^{-1}.\mu m^{-1})$

M$_a$ – Mean molecolar weight of the atmospheric gas $\qquad$ $(\approx 29 \times 10^{-3}\, kg / K \cdot mol)$

n – Refractive index $\qquad\qquad\qquad\qquad\qquad\qquad\qquad$ -

n$_0$ – Refractive index to the ground $\qquad\qquad\qquad\qquad$ -

T – Absolute temperature $\qquad\qquad\qquad\qquad\qquad\qquad$ (K)

V – Velocity of a source $\qquad\qquad\qquad\qquad\qquad\qquad$ $(m \cdot s^{-1})$

z – Altitude of the first radiation deflection $\qquad\qquad\qquad$ (m)

λ - Wavelength $\qquad\qquad\qquad\qquad\qquad\qquad\qquad\qquad$ (μm)

k - Boltzmann constant $\qquad\qquad\qquad\qquad\qquad$ $(1.3806 \times 10^{-23}\, J.K^{-1})$

ν - Frequency $\qquad\qquad\qquad\qquad\qquad\qquad\qquad\qquad$ (s^{-1})

χ - Mass extinction cross section $\qquad\qquad\qquad\qquad$ $(m^2 \cdot kg^{-1})$

α_λ - Monochromatic absorptivity of the atmosphere $\qquad\qquad$ -

ε_λ - Monochromatic emissivity of the atmosphere $\qquad\qquad$ -

h - Planck constant $\qquad\qquad\qquad\qquad\qquad\qquad$ $(6.6262 \times 10^{-34}\, J.s)$

θ - Solar Zenith angle $\qquad\qquad\qquad\qquad\qquad\qquad\qquad$ $(^{\circ})$

$\beta_{\lambda_{abs}}$ - Spectral absorption coefficient $\qquad\qquad\qquad$ (m^{-1})

$\beta_{\lambda_{ext}}$ - Spectral extinction coefficient $\qquad\qquad\qquad$ (m^{-1})

$\beta_{\lambda_{scat}}$ - Spectral scattering coefficient $\qquad\qquad\qquad$ (m^{-1})

c - Velocity of light in vacuum $\qquad\qquad\qquad\qquad$ $(2.9979 \times 10^8\, m.s^{-1})$

σ - Stefan-Boltzmann constant $\qquad\qquad\qquad$ $(5.67 \times 10^{-8}\, W \cdot m \cdot K^{-4})$

σ_R - Rayleigh scattering coefficient $\qquad\qquad\qquad$ (m^2)

σ_λ - Absorption Cross Section $\hspace{2cm}$ (m^2)

$\Delta\sigma_\lambda$ - Differential Absorption Cross Section $\hspace{2cm}$ (m^2)

$\sigma_{\lambda,Smoothed}$ = Smoothed Absorption Cross section $\hspace{2cm}$ (m^2)

C_{AIR} - Air Molecules typical Concentration (STP) $\hspace{1cm}$ $(2.4 \times 10^{19} cm^{-3})$

ε_R - Rayleigh extinction coefficient $\hspace{2cm}$ (m^{-1})

θ_r - Refracted Solar Zenith angle $\hspace{2cm}$ $(^o)$

θ_{nr} - Not Refracted Solar Zenith angle $\hspace{2cm}$ $(^o)$

ε_M - Mie extinction coefficient $\hspace{2cm}$ (m^{-1})

β – Solar Angle of incidence at the top of the atmosphere $\hspace{1cm}$ $(^\circ)$

$I_{\lambda\ell}$ - Down-welling radiance in the ℓ layer $\hspace{1cm}$ $(W.m^{-2}.sr^{-1}.\mu m^{-1})$

ℓ - number of atmospheric layer $\hspace{2cm}$ -

p_ℓ - scattering probability $\hspace{2cm}$ -

ξ_λ = Differential spectrum $\hspace{2cm}$ -

$Ln_{Smoothed}\left(I_{\lambda,0}/I_\lambda\right)$ = Smoothed series of the log-ratio of the Reference spectrum with the measured one $\hspace{2cm}$ -

1. Introduction

1.1. Overview

The mid-latitudes atmosphere is a complex region of our planet, where air masses coming from lower and higher latitudes meet, essentially, to balance the temperature gradient. The study of the relationship between the Polar Regions and the mid-latitudes is well developed nowadays, due to the polar ozone decrease. On the other hand the interaction between tropics subtropics and mid-latitude regions still remains insufficiently understood.

In the last thirty years, the stratospheric ozone in the Northern Hemisphere (NH) mid-latitudes has suffered a meaningful decrease. The analysis of results obtained from TOMS (Total Ozone Mapping Spectrometer), installed on the Nimbus 7 satellite, underlines the significant reduction of the ozone total column even before the Pinatubo eruption. During the eighties, studies on ozone profile temporal series in the NH show that the annual average ozone concentration increases in the troposphere and decreases in the low stratosphere [1]. Other authors confirm these results [2], [3] underlining that in Southern Europe, the stratospheric ozone trend per decade is higher than the one found in the United States, although the considered areas are at the same latitudes and with equal values of superficial nitrogen oxides.

Comparisons of the results obtained for both hemispheres lead to the conclusion that ozone loss is smaller at northern high latitudes than the Antarctic depletion phenomena. At mid-latitudes this difference is balanced with equivalent values between 5% and 8% per decade [4], but it would seem greater in the NH. Nevertheless, the physical processes that can justify these decreases in the ozone budget of the north mid-latitude, is not completely explained. For some years the nitrogen compounds were thought to be the greatest responsible for the ozone catalytic destruction. The understanding of the dynamical processes, chemical and photochemical reactions involving nitrogen compounds in the stratosphere has improved [5], [6]. Stratospheric ozone is continuously subordinated to chemical processes of creation and destruction by chemically active compounds as chlorofluorocarbons, and also from other gases like nitrogen, bromine, chlorine and iodine oxides. Measurements of atmospheric trace gas in European border regions (as Portugal) can supply useful information on the atmospheric background content of these species, to be compared with the values obtained from satellite observations. The nitrogen oxides NO_X are created in the atmosphere from natural and artificial sources. The NO_X compounds manifest a strong diurnal variability due to the photochemical nature of the dissociation

reactions. Recent observations of iodine monoxide (IO) concentrations seem to confirm the hypothesis that it plays a non negligible role in the ozone depletion processes. Therefore, studies of total column of atmospheric trace gases, for example as the ones obtained with DOAS methodology, in nadir view or in zenith sky or off-axis configuration, are of extreme importance either from the satellite observations [7] - [15] or from the aircraft instruments [16], [17] as well as from the ground based station [19] - [24] .

The recent launch of the ENVISAT [25] - [27] and EOS-Aura satellites [29] - [31], have enlarged the number of existing sensors (SCIAMACHY, GOMOS, OMI) for the retrieval of atmospheric gases total column variations. The utilized methodology is now efficient; nevertheless, the research can focus on the improvement of the algorithms and on the validation of satellite data with results obtained by means of precise and high spectral resolution ground-based spectrometers [32] - [35].

1.2. Objectives

The general goals of this research can be divided in two main subjects

- i) the technological one, regarding the development of a new spectrometer operating in the UV-Visible spectral region with the most advanced available technologies, the realization and the installation of the equipment at the Geophysics Centre of Evora
- ii) the scientific ones concerning:
  - a) the deep studies of the DOAS algorithms and their application to the measured spectral data
  - b) the measurements and the monitoring of some atmospheric trace gases (mainly stratospheric NO_2 and O_3 in this first step of the research) and the attempt to relate the obtained results with episodes of aerosol contamination.

1.3. Structure of the thesis

This thesis is divided into 8 major chapters.

The first chapter introduces the thesis, presenting a review of the related work, emphasizing the central role that satellite remote sensing and ground based measurements play on the studies regarding the atmospheric trace gases. Chapter 2 introduces the propagation of electromagnetic radiation in the atmosphere and its interaction with the Earth's surface and atmospheric constituents, which are responsible for the absorption, emission and scattering of radiation in the atmosphere. Chapter 3 deals with the minor gaseous atmospheric

compounds, presenting the chemical cycles and the role in the atmospheric processes of some tracers responsible for great part of the alterations in the atmosphere, although present in very low concentrations. Due to the primary importance of the ozone among the minor species influencing the radiative budget, the chapter is focused on this last compound. Other species (such as Nitrogen, Chlorine and Sulphur compounds) are presented evidencing the narrow tie with ozone, since they owe their importance mainly due to the consequences that they provoke on the ozone equilibrium. Since in chapter 7 some results and discussion regarding results of Nitrogen Dioxide and Ozone obtained at high latitude are presented, a brief parenthesis on the topic of the so-called "Ozone Hole" is introduced at the end of chapter 3.

Chapter 4 presents some hints on the main remote sensing equipments and the Differential Optical Absorption Spectroscopy (DOAS) technique is introduced.

The birth of the DOAS and its evolution are presented, together with the positive and negative aspects that the methodology offers. The DOAS-Master-Equation is obtained and explained as well as the formulation of a ray tracing Radiative Transfer Model for the interpretation of the outputs of the DOAS algorithms

In chapter 5 the SPATRAM instrument is presented and its functionality is completely described. The various modules constituting the equipment are singularly analyzed; the Optical and Mechanical Unit (OMU) is sectioned and fully explained; the electronic elements forming the Electronic and Control Unit (ECU) are listed and illustrated. The principles of operation of such kind of optical instrument are discussed. The software for the Data Acquisition (DAS), implemented in the frame of this doctorial work for the management of the developed equipment, is introduced (a more detailed presentation, even if not fully exhaustive, of the DAS is contained in the Annex 3).The testing phase, dealing with the identification of the Fraunhofer's lines in the solar spectrum, is also presented in this chapter.

Chapter 6 presents the developed DOAS algorithms. A qualitative approach allowing for the evaluation of the goodness of the retrieval is presented. The utilized method for the estimation of the 'Background' content in the spectral series used as reference spectrum in the DOAS processing is explained and the temperature dependence of the absorber's cross sections in the retrieval of the Nitrogen Dioxide (NO_2) vertical column is discussed.

Chapter 7 shows the results (in terms of diurnal and seasonal variations) obtained at high latitude with the forefather of SPATRAM (The GASCOD – Gas Analyzer Spectrometer Correlating Optical Differences) installed at the Italian Antarctic Station. The seasonal variation of NO_2 and Ozone over Évora are obtained applying the DOAS methodology to the SPATRAM measurements. A case study

regarding the detection of a dust event intrusion with the DOAS measurements is also presented and discussed. In addition, comparisons of the ground-based results with data obtained with similar satellite borne equipment are shown.

In chapter 8 the conclusions arising from this work are summarized, and a discussion on the possible work to be developed in future investigations is presented.

Finally 3 annexes are contained in this work:

Due to the importance of the SPATRAM and of the optical parts of the spectrometer, particularly the diffraction grating, the first Annex deals with the grating laws and mountings in order to give a clear view of the complexity of the field.

Annex 2 contains the basics of the CCD technology and a glossary with the aim of clarifying the importance of the type of detector utilized in the SPATRAM.

Annex 3 shows the most important features of the Data Acquisition System (DAS) developed in the frame of this doctorial work for the management of the SPATRAM.

2. Radiative Transfer in the atmosphere

2.1. Solar Radiation

The atmosphere can be considered a gas mixture exposed to the flow of the incoming solar radiation. The atmosphere absorbs some of the incident radiation and, after the interaction with the land surface, it is emitted both by the land surface and by the atmosphere back to space; in such way the Earth-atmosphere system is in a quasi radiative equilibrium with the incoming solar radiation absorbed by this system.

The radiative transfer constitutes therefore the main mechanism of energy exchange between the various layers of the atmosphere and between these and the Earth's surface, playing a prominent role in its chemical and dynamical processes [36]. Moreover the solar radiation produces thermal effects: it is absorbed by ozone in the upper stratosphere and by oxygen in the upper levels of the atmosphere (mesosphere), and it is quickly converted in thermal energy by means of chemical reactions like photo dissociation of O_3 and O_2. The heating, caused by the absorption of ultraviolet radiation is balanced with the radiative heat loss due to the emission of infrared radiation by carbon dioxide, water vapour and ozone. The atmospheric temperature depends therefore on the equilibrium of these processes and other phenomena like the emission of latent heat in the troposphere.

2.1.1. Emission spectrum of the Sun

Each body irradiates and absorbs electromagnetic waves; in order to have a precise description of the mechanisms through which this happens, it is useful to analyze the behaviour of an ideal emitter and absorber, called "black body". Therefore some of the most important laws of the black body [36] are presented here:

2.1.1.1. Planck Radiation Law

The intensity of radiation emitted by a blackbody per surface area unit into a fixed direction (radiance) depends on its temperature T and on the wavelength λ of the monochromatic energy and is given by:

$$E_\lambda = \frac{C_1}{\lambda^5 (e^{C_2/\lambda T} - 1)}$$

(2.1)

In $W \cdot m^{-2} \cdot \mu m^{-1} \cdot sr^{-1}$, where:

E_λ = monochromatic radiance emitted by the black body;

T = absolute temperature;

$$C_1 = 2\pi hc^2 = 3.74 \times 10^{-16} \, Wm^2$$

$$C_2 = \frac{hc}{k} = 1.44 \times 10^{-2} \, mK$$

This is the basic equation for the deduction of the fundamental laws in photometry studies, in particular the following:

2.1.1.2. Stefan – Boltzmann Law

The Stefan-Boltzmann law that relates the irradiance with temperature, is obtained integrating the Planck function (Eq. *(2.1)*) on the entire spectrum and for all directions, assuming that blackbody radiation is isotropic:

$$E = \sigma T^4$$

(2.2)

In $W \cdot m^{-2}$ Where σ is the Stefan-Boltzmann constant, which has a value of $5.67 \times 10^{-8} \, W \cdot m^{-2} \cdot K^{-4}$. The strong dependency of the emitted irradiance with the fourth power of the temperature explains the great difference in the spectral distribution intensity between the Sun and the Earth emission spectra (Figure 2.1). That is mainly due to the fact that the Sun irradiates to space like a black body with an effective temperature of approximately 5780 K, while the Earth with a temperature of 255 K.

2.1.1.3. Wien's Displacement Law

This law describes the relation between the wavelength of the peak of maximum emission λ_m and the absolute temperature T

$$\lambda_m T = 2897$$

(2.3)

In $\mu m \cdot K$, since λ_m is expressed in μm and T in Kelvin degrees.

An important consequence is that the solar radiation (effective temperature of the Sun is 5780 K) is concentrated in the visible and the near-infrared spectral regions, while the radiation emitted from the Earth and other planets and from their atmospheres is confined to the infrared spectral region (Figure 2.1).

2.1.1.4. Kirchoff Law

The radiation emitted by a real body differs from the one emitted by a black body at the same temperature. Therefore the monochromatic emissivity (ε_λ), is defined

in order to have the measure of how much the emission of a real source approximates that of a black body at a given wavelength:

$$\varepsilon_\lambda = E_{source\lambda}/E_{blackbody\lambda}$$

Analogously, the *monochromatic absorptivity* (a_λ) can be defined:

$$a_\lambda = E_{absorb\lambda}/E_{blackbody\lambda}$$

that describes the amount of radiation absorbed by the body with respect to the blackbody, under thermodynamic equilibrium.
According to Kirchoff law, the monochromatic emissivity of a real body is equal to the monochromatic absorptivity, at the same wavelength

$$\varepsilon_\lambda = a_\lambda$$

(2.4)

In qualitative terms, the materials behaving as strong absorbers at a fixed wavelength, are also optimal emitters at the same wavelength; vice versa weak absorbers behave themselves as weak emitters, at the same wavelength. For a blackbody $\varepsilon_\lambda = \alpha_\lambda = 1$ for all wavelengths and for a grey body $\varepsilon_\lambda = \alpha_\lambda < 1$ for all wavelengths. The Kirchoff law can be applicable to the atmosphere if local thermodynamic equilibrium is assumed, which is a reasonable assumption for a localized volume below approximately 40 km.
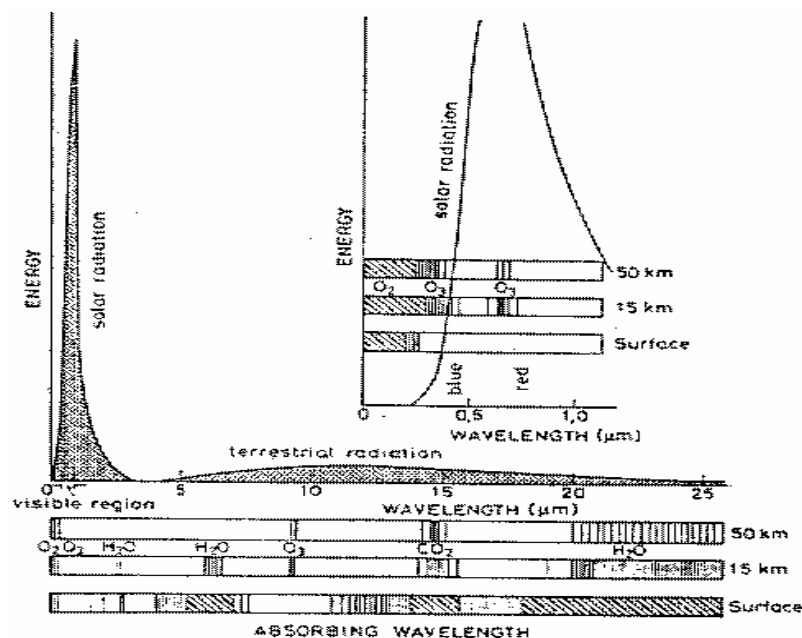
Figure 2.1 - Spectral distribution of the solar and terrestrial radiation and atmospheric absorption as a function of the wavelength and of the altitude [37]

2.2. Mechanisms of attenuation in the atmosphere

2.2.1. Interaction between solar radiation and atmosphere

When the electromagnetic radiation of the Sun enters the atmosphere, it can suffer physical and photochemical interactions determining a partial or total extinction. As for the physical interactions, the main processes are scattering and absorption of radiation by particles and gas molecules. The photochemical interactions strongly depend on the wavelength of the incident radiation (Figure 2.2) and on the nature of the interacting compounds; it is possible as a first approach, to subdivide the curve in Figure 2.2 in four broad 'steps' on the wavelength basis (Table 2.1) affecting different atmospheric layers.
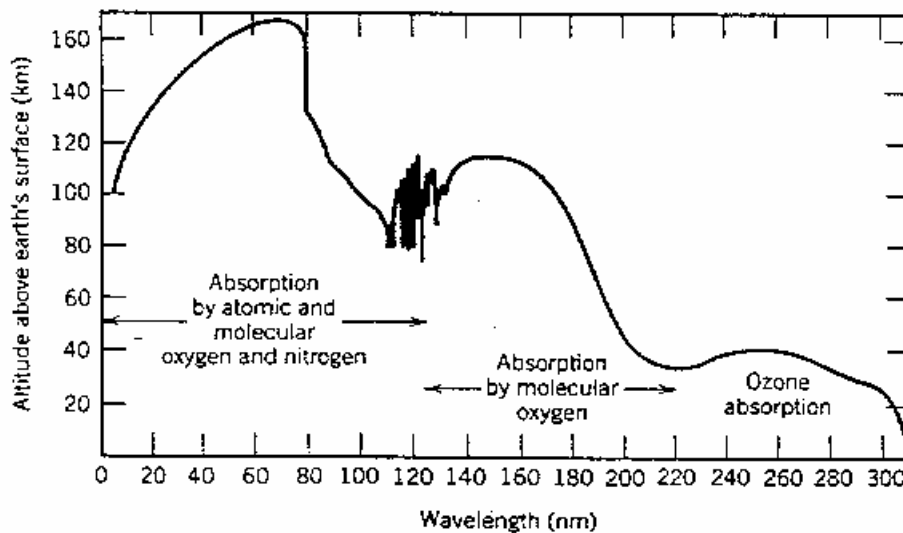
Figure 2.2 - Atmospheric regions of maximum absorption of the incident solar radiation perpendicular to the top of the atmosphere, as a function of the altitude and of the wavelength [38].

Table 2.1 – Absorption of solar radiation in the Earth's atmosphere

Wavelength band λ (μm)	Layer where radiation absorbed in earth's atmosphere (Km)	Primary absorption mechanism
$\lambda < 0.1$	90-200	Photo ionization
$0.1 < \lambda < 0.2$	50-110	Photo dissociation of O_2
$0.2 < \lambda < 0.31$	30-60	Photo dissociation of O_3
$\lambda > 0.31$	0-10	Absorption by water vapor

In each of these layers several photochemical processes occur involving different spectral ranges of the incident radiation [36]:

1- solar radiation with $\lambda < 0.1\ \mu m$ has sufficient energy for the ionization of the atomic and molecular oxygen and nitrogen (O, O_2, N and N_2), strongly contributing to the formation of the ionosphere; the radiation is mostly absorbed above 90 Km.

2-The radiation with $0.1 < \lambda < 0.2\ \mu m$ is almost completely absorbed in the reaction of photo dissociation of O_2,

$$O_2 + h\nu = O + O \tag{2.5}$$

strongly influencing the successive ozone formation through the reaction

$$O_2 + O + M = O_3 + M \tag{2.6}$$

This process interests mainly the mesosphere, between 50 and 90 Km.

3-The radiation with $\lambda > 0.2\ \mu m$ can penetrate deeper in the atmosphere, reaching the stratosphere where the ozone is concentrated in a region comprised between 23 and 19 Km. The radiation is absorbed here mainly due to the ozone photo dissociation

$$O_3 + h\nu = O_2 + O \quad (\lambda < 1100\ \mu m) \tag{2.7}$$
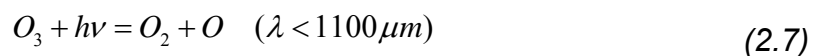
This originates a series of processes that involve reactions *(2.6)* and *(2.7)*; these in turn present as only effect, the absorption of radiation without other chemical processes. Consequently, thanks to the great ozone absorbing power for wavelengths lowers than 0.31 μm and to the rapidity with which these reactions happen, the ozone in the stratosphere is able to absorb almost whole solar radiation with $0.2 < \lambda < 0.31\ \mu$m.

4-The absorption mechanisms described above refer to the higher layers of the atmosphere and involve less than 2% of all the incident solar radiation. The remaining 98% correspond to $\lambda > 0.31\ \mu$m, which reach the troposphere nearly unchanged (Figure 2.4).

Figure 2.3 shows the incident solar radiation at the top of the atmosphere (higher curve) and the solar radiation reaching the sea level for a solar zenith angle of 0° (lower curve); the area between the two curves represents the attenuation suffered by radiation when crossing the atmosphere. Such area is constituted by the non-highlighted part that corresponds to the backscattering and absorption effects of clouds and aerosols and to the backscattering due to the air molecules, and by the highlighted part corresponding to gas absorption.
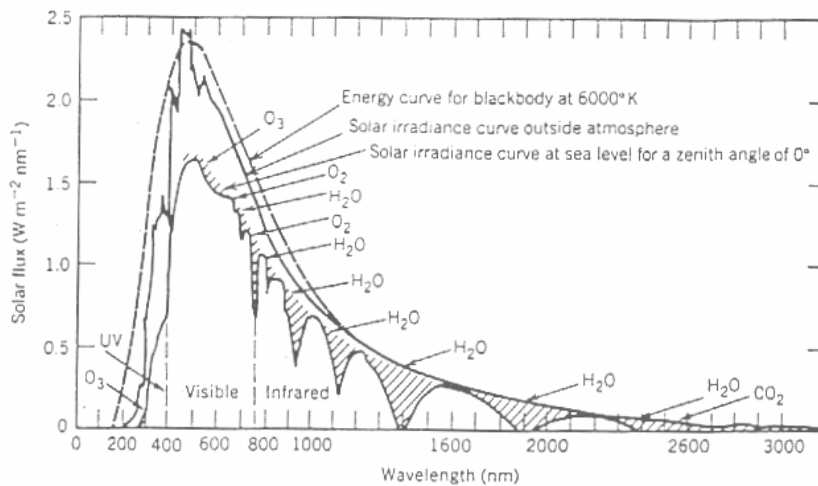
Figure 2.3 – Solar irradiance outside the atmosphere and at sea level and emission spectrum of a black body at 6000 K. The highlighted region corresponds to the absorption of the radiation as a function of wavelength, due to the main gaseous atmospheric constituents [38].

Figure 2.4 shows the spectrum of absorption in the spectral interval of the solar and Earth radiation: comparing fig. 2.4c with fig. 2.4b, it turns out obvious that the radiation with λ < 0.35 μm remains practically unchanged. Moreover, in the visible region there is a great 'spectral window' through which more than 50% of the radiation reaches the ground.
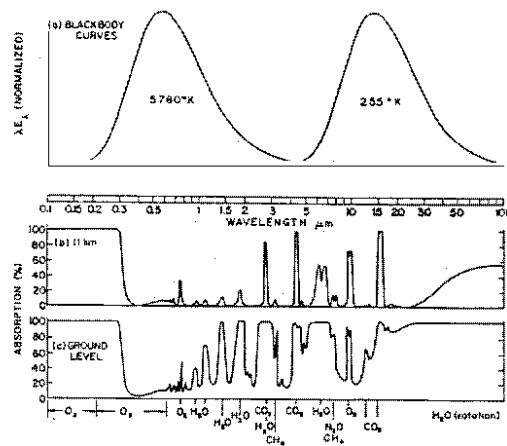
Figure 2.4 - (a) Normalized blackbody curve for temperatures of 5780 K (representative of the Sun) and 255 K (representative of the Earth), plotted on a logarithmic wavelength scale. The ordinate is multiplied by wavelength so that the area under the curves is proportional to irradiance. (c) Atmospheric absorption in limpid air, of solar radiation with zenith angle of 50° and of diffuse terrestrial radiation. (b) Same conditions of (c), but considering only the atmosphere above 11 Km, in correspondence of the tropopause at mid-latitudes [36].

2.2.2. Atmospheric Attenuation

The propagation of the solar radiation through the atmosphere is influenced by two processes: the absorption and the scattering by gas molecules and aerosols (particles).

In the absorption process, a fraction of the energy that spreads through an air layer is absorbed by atmospheric constituents and it can be re-emitted at a different wavelength. In this process, the selective absorption by the permanent atmospheric gaseous constituents such as N_2, CO_2, O_2 and water vapour and from the minority polluting agents (O_3, NO_2, CH_4, SO_2…) predominates.

In addition to absorption, a fraction of the energy passing through the atmosphere is scattered. The way it happens strongly depend on the dimensions of the scattering object with respect to the wavelength of the incident radiation, usually air molecules are involved (Rayleigh scattering) or aerosol particles (Mie scattering).

Due to the extinction process (absorption plus single scattering), the incident solar radiation suffers an attenuation that follows an exponential law, the well known *Lambert –Beer law*

$$I_\lambda = I_{0\lambda} e^{-\beta_{\lambda_{ext}} \ell}$$

(2.8)

where

$I_{0\lambda} =$ intensity of the incident monochromatic radiation at the top of the atmosphere;

$I_\lambda =$ intensity of radiation transmitted to the surface;

$\beta_{\lambda_{ext}} =$ spectral extinction coefficient. It represents the combined effect of the absorption and single scattering processes of gas and particles and corresponds therefore to the sum of two terms

$$\beta_{\lambda_{ext}} = \beta_{\lambda_{abs}} + \beta_{\lambda_{scat}}$$

(2.9)

where $\beta_{\lambda_{abs}}$ is the absorption coefficient and $\beta_{\lambda_{scat}}$ the scattering coefficient.

ℓ = path length of the radiation beam in the Equation *(2.8)* is obtained considering a parallel beam of monochromatic radiation of intensity I_0 that crosses an infinitesimal layer of a homogenous material where no inner radiation sources are present in the layer. The incident radiation beam will suffer an attenuation dI that, experimentally, is proportional to the intensity of the incident radiation, to the thickness of the crossed layer $d\ell$ and to the density of the material ρ :

$$dI_\lambda = -I_\lambda \chi_\lambda \rho d\ell$$

(2.10)

where χ_λ it is a coefficient of proportionality.

In case the absorber thickness is low (when the material can be considered homogeneous), this expression is integrated obtaining equation *(2.8)*. In this case the extinction coefficient is $\beta_{ext} = \chi\rho$.

The term $\rho d\ell$ it indicates the amount of matter crossed by the radiation (that is, the mass in a cylinder of unitary section and length $d\ell$), and it is expressed in kg/m^2; consequently the coefficient χ will have the inverse dimensions, m^2/kg and it is called mass extinction cross section.

Alternatively, the density of the substance can be considered as number of molecules per volume N (m^{-3}) and the previous relation becomes:

$$dI_\lambda = -I_\lambda \sigma_\lambda N d\ell \qquad (2.11)$$

where the coefficient σ_λ has the dimensions of an area (m^2). The coefficient σ_λ is called extinction cross-section.

a) ABSORPTION PROCESSES

According to Grotthus – Draper Law, only the radiation absorbed by a molecule can induce chemical changes. Therefore, in order to be able to estimate the evolution of a photochemical system like the atmosphere, it is essential to know the absorption spectrum of all species contained in it. In the absorption process, part of the energy in the incident beam is transformed in energy of secondary emission (at a different wavelength) or in inner energy of the particle, provoking mainly excitation, ionization and dissociation.

Depending on the type of spectrum of a substance, the absorption is called continuous (characteristic of solid bodies and incandescent liquids), or selective (in lines or bands, characteristic of the gaseous substances).

1.The continuous absorption occurs through phenomena of photodissociation and photoionization; it starts regularly with a threshold value of frequency, characteristic of the atom or of the molecule involved, corresponding to the chemical bond energy. Radiation mainly involved in such processes clearly turns out the most energetic (with smaller wavelength).

2. The selective absorption, different from the previous one, takes place in isolated lines relatively distanced (if the gaseous substance is at its atomic state) or as numerous lines bring back together in groups that compose bands (if the gaseous substance is at its molecular state).

In order to describe the attenuation that a beam of monochromatic radiation undergoes when crossing a gas layer, due only to the single absorption, equation *(2.11)* leads to:

$$I_\lambda = I_{0\lambda} e^{-\sigma_\lambda C \ell}$$

(2.12)

in case the scattering is negligible, with:

I_0= intensity of the incident monochromatic radiation;

I= intensity of the monochromatic transmitted light through the gas layer;

C = concentration of the gas absorber (m^{-3});

ℓ = path length of the radiation beam(m);

σ_λ = spectral absorption cross section expressed in m^2. It defines the probability of absorption, characteristic of a gas and closely related to its chemical nature. This quantity has great importance in spectrometry since it determines the type of absorber under examination.

Equation *(2.12)* refers to absorption due to single gaseous species; in the atmosphere assortment of diverse absorbers exist, each of them with an absorption coefficient and a certain concentration. Consequently the Lambert - Beer law indicated to such a system becomes:

$$I_\lambda = I_{0\lambda} e^{-\sum_{i=1}^{n} \sigma_{\lambda i} C_i \ell}$$

(2.13)

where n corresponds to the number of absorbers.

b) SCATTERING PROCESSES

Beyond absorption, the solar radiation endures processes of diffusion due to the presence of great concentrations of air molecules and aerosol particles.

This phenomenon, called scattering, is a physical process in which one particle that interacts with a electromagnetic wave takes a fraction of energy from the incident wave and reradiates it in all directions.

The atmospheric particles responsible for the scattering cover a dimension interval that varies between $\approx 10^{-8}$ cm (gas molecules) to 1 cm (rain drops and hail). Since, as already mentioned, the type of scattering process strongly depends on the relationship between the wavelength of the radiation beam and the dimensions of the scattering object, it is possible to distinguish the different types of scattering according to such relationship [36]:

➢ When the dimensions of particles are much smaller than the wavelength, the Rayleigh Scattering process dominates; the molecules of small dimensions, non-absorbing, with low density are included in this case. Given the dependency of the scattering coefficient with the wavelength[1] , the ultraviolet radiation is the most scattered by air molecules. According to this model, therefore, the predominance of such smaller wavelengths in the diffuse radiation is responsible for the blue colour of the sky ($\lambda_{blue} \approx 0.47$ μm). Analogously, the predominance of longer wavelengths in the transmitted solar radiation without being diffused, confers a red colour to objects seen at the direct sunlight, especially at dawn or sunset, when the atmospheric path of the radiation is longer.

➢ As the particle dimension approximates the wavelength of incident radiation, the Mie scattering process becomes predominant; this type of scattering process involves fog particles, smoke and smog.

➢ When the dimension of particles continues to grow with respect to the wavelength of the incident radiation, the regime of geometric scattering applies, which is described by the laws of the classical optics. In this case particles of great dimensions, as cloud droplets, rain drops and ice particles, produce various optical phenomena such as the rainbows and the halos.

In general however, the atmosphere is constituted by molecules and particles of variable dimensions. Therefore the visible light is not scattered by any prevailing scattering process over another, and the atmosphere appears neutral and without colour.

Since in the present work the absorbing spectrometry principles are applied to study and monitor the minor atmospheric gaseous compounds, the most important physical absorbing mechanisms of electromagnetic radiation by atmospheric molecules are described here.

---

[1] *The volume-scattering coefficient derived from the classical electromagnetic theory (Rayleigh scattering) is defined by the following equation:*

$$\sigma_R = \frac{\pi(n^2-1)^2}{2N\lambda^4}(1+\cos^2\theta) \quad (in\ m^2)$$

where θ represents the angle between the incident and scattered radiation beams, λ is the wavelength of the scattered radiation, N is the number of molecules per cm^2 and n is the refractive index of the scattering molecule.

2.3. Absorption and emission molecular spectra

Each molecule have a certain amount of energy under the form of kinetic and electrostatic potential energy, while the remaining part involves the vibration of single atoms around their position of equilibrium, the position of electrons around the nuclei and the spin of molecules around their mass centre; the energies involved are electronic vibrational and rotational.

Quantum mechanics foresees that only some configurations of electronic orbits are allowed for an atom, and that only certain frequencies, vibrational amplitudes and certain spins are allowed for a molecule.

The combination of electronic, vibrational and rotational orbits comes identified from a particular energetic level representing the sum of the three types of energy.

Every molecule can endure a transition to a superior energetic level absorbing electromagnetic radiation and analogously it can decay to an inferior emitting radiation.

Since the energy transmitted from the electromagnetic radiation is composed by discrete units called photons, only discrete variations between the molecular energetic levels are possible, in such a way that the amount of energy associated is given by:

$$\Delta E = h\nu$$

where ν is the frequency of the radiation and h it is the Planck constant. $\Delta E = E_k - E_j$, where k corresponds to the highest state of energy and j to the state with lower energy.

Since the radiation propagates at the speed of light, the frequency and the wavelength are related as follows

$$\nu = c/\lambda$$

in such way that the amount of energy contained in one photon of radiation is inversely proportional to the wavelength λ.

Since an isolated molecule can absorb and emit radiation in discrete amounts corresponding to the transitions allowed between the different energetic levels, it can only interact with radiation having certain wavelengths. Therefore its absorbing and emitting properties can be described in terms of spectral lines constituted by a finite number of absorption or emission lines situated in close proximity, separated by "forbidden intervals".

According to the type of transition, diverse energies are involved, and therefore various spectral intervals.

As an example, the energy associated with the molecular electronic configuration describes the distribution of electrons in atomic or molecular orbital. Since the

energetic 'jump' between several electronic states is rather high (of the order of the electron volt), the photons able to induce transitions of this type belong, in general, to the ultraviolet and visible spectral regions.

The molecules also possess vibrational and rotational energy, but the differences of energies associated to these types of transitions are much lower, therefore the photons absorbed or emitted in these processes correspond to the infrared and far infrared spectra (Figure 2.5).
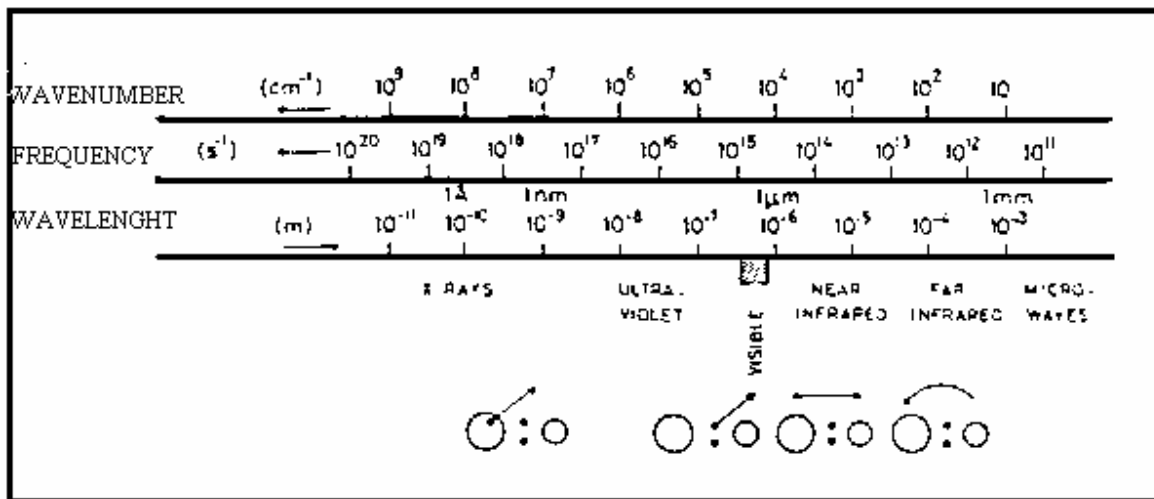
Figure 2.5 - Spectral regions of the radiation and their effects on molecules; from left to right: ionization, dissociation, vibration and rotation [37].

The vibrational transitions play an important role in the thermal radiation budget of the atmosphere, since they constitute the fundamental process in great part responsible for the cooling that happens in the infrared.

The transitions between electronic states due to the absorption of photons of relatively elevated energy introduce two important consequences in the atmosphere: on one hand they are the greatest source of heat and on the other they start photochemical processes, like the photolysis or the photo ionization, which play a prominent role in the distribution of the atmospheric minor compounds. Each atom or molecule can be ionized by radiation with high energy; this process, called photo ionization, demands photons with sufficient energy to remove one or more electrons from their external orbits. Unlike the processes that involve vibration, rotation and electronic transitions, the photo ionization can involve radiation with a continuous interval of wavelengths, provided that it is greater than a certain threshold value, characteristic of every molecule. In general, the spectral region relative to the ionization processes correspond to wavelengths lower than 0.1 μm.

Sometimes the energy of the radiation absorbed by a molecule is able to 'destroy' it in atomic constituents; vice versa unstable atoms can be arranged in order to form a much more stable molecule emitting the excess of energy under the form of radiation.

In these photochemical reactions the absorption and emission of electromagnetic radiation play a crucial role in supplying or removing energy (equation *(2.5)* is an example).

In the atmosphere the greater part of the photochemical reactions involve ultraviolet and visible radiation. The energy in excess is converted in kinetic energy of atoms and contributes to increase the gas temperature influencing the atmospheric thermal budget. This is why the stratosphere play an important role in the climate system.

2.4. Increase of the spectral lines

As a consequence of the Heisenberg uncertainty principle, which expresses the impossibility to determine simultaneously with precision the position and the speed of one particle, the single spectral lines of absorption or emission of an isolated molecule have always a finite width.

However, the amplitude of the observed spectral lines greatly exceeds the theoretical one that would be expected; in absence of strong external magnetic fields, this phenomenon can be explained by the following causes:

1."broadening of the spectral lines by collision"; this is due to the reduction of the emission duration of excited atoms, following to their electrostatic interaction with other atoms. This can be discriminated in "self-broadening" if the collision happens between molecules of the same species, and "foreign-broadening" in the case of hits between the molecules under examination and the non-absorbing gas. The broadening α due to collisions prevails in the lower layers of the atmosphere, under 30 km, and can be expressed by the relation:

$$\alpha = \alpha_0 \frac{P}{P_0} \sqrt{\frac{T_0}{T}} \qquad (2.14)$$

where
α = width of the spectral line at half height;
α_0 = the same, but in standard conditions (T_0= 298 K, P_0= 1 atm).
P = gas pressure;
T = gas temperature;
2."broadening of the spectral lines due to the Doppler effect (Doppler broadening)";
it is associated to accidental motions of atoms and molecules. The atoms due to

the thermal agitation, move with different speed and direction therefore, as a result of the Doppler effect, a broadening of the spectral lines appears and it is larger for more intense thermal agitation, that is, the higher the gas temperature is. The broadening due to the Doppler effect is not negligible for light elements and for low concentrations, which are found in the higher levels of the atmosphere, and is described by the following relation:

$$\alpha = \frac{v}{c}\sqrt{\frac{2RT\ln 2}{M}}$$

(2.15)

where

v = the velocity of the source (v is assumed positive when the source is approaching)

c = speed of the light in the vacuum;

R = Universal constant of gases;

M = weight of a gram atom (gram molecule).

2.5. Composition and Structure of the atmosphere

After the presentation and discussion of the main laws that rule the radiative transfer in the atmosphere, a short description of the atmosphere, the greatest protagonist of these phenomena, is given here mainly from a radiative point of view.

The main atmospheric constituents (nitrogen, oxygen, argon and water vapour, being the amount of the latter variable), although represent alone more than 99.9% of the total in volume, possess insufficient importance in the radiative budget: all the gases present in the atmosphere are in fact equally responsible for the scattering, while only some of them present a meaningful absorption of radiation.

The strong influence of absorption on the atmospheric energy budget has to do with the fact that some gases absorb solar radiation in the ultraviolet and visible spectral regions , causing a selective reduction of the incoming radiant energy to the "Earth-atmosphere" system , while others absorb in the infrared spectral region causing attenuation of the outgoing radiation.

The energy absorbed by the atmosphere constitutes approximately 16% of the total radiation reaching the Earth and is used in part for its heating (therefore to supply energy to the local and general circulation) and in part for photochemical processes. Because of the strong connection between the atmospheric composition, temperature and chemical dynamics, the study of the processes involved turn out to be extremely complex.

2.5.1. Pressure, density, temperature

The density of the air at the sea level, is approximately 1 kg/m^3 and the standard pressure is P_0= 1013.25 mb (101325 N/m^2 (Pascal)).

The decrease of density and pressure with increasing height in the atmosphere follow an exponential relationship, until about 100 km.

This exponential profile is explained by:

1. the equation of state of the gases that relate these two quantities (density and pressure) with the temperature (eq. *(2.16)*);

2. the hydrostatic equation, which states that the change in pressure with the change in height equals the gravitational force per unit volume. The negative sign is due to the fact that pressure decreases with height (eq. *(2.17)*).

The equation of state of perfect gases can be written:

$$\rho = \frac{M_a \cdot P}{R \cdot T} \qquad (2.16)$$

where:

M_a= mean molecular weight of the atmospheric gas ($\approx 29 \times 10^{-3} \, Kg / K \cdot mol$),

P = pressure,

R = Gas constant,

T = Absolute temperature;

The hydrostatic equation is

$$\frac{dP}{dz} = -\rho \cdot g \qquad (2.17)$$

with:

g = acceleration due to gravity $\cong$ 9.8 m/s^2.

Combining equations *(2.16)* and *(2.17)*, the pressure is:

$$P = P_0 \cdot \exp\left[-\frac{1}{R} \cdot \int_{z_0}^{z} \frac{M_a \cdot g}{T} d\zeta \right] \qquad (2.18)$$

and replacing equation *(2.18)* in equation *(2.17)*, the density is:

$$\rho = \frac{M_a P_0}{RT} \cdot \exp\left[-\frac{1}{R} \cdot \int_{z_0}^{z} \frac{M_a \cdot g}{T} d\zeta \right] \qquad (2.19)$$

It can be noted that the functions would be exact exponentials if g, M_a, and T were independent from height, and equations would become:

$$P = P_0 \cdot \exp\left[-\frac{z}{H}\right] \quad \text{and} \quad \rho = \rho_0 \cdot \exp\left[-\frac{z}{H}\right]$$

where H (scale height) = $\dfrac{R \cdot T}{M_a \cdot g}$

A better approximation is obtained using a vertical profile of temperature; in such case equations *(2.18)* and *(2.19)* can be integrated for layers in which the value of T is the mean temperature of the layer.

2.5.2. Vertical Structure

It is usual to subdivide the atmosphere in layers based on the vertical profile of temperature; in fact, such layers present very different chemical-dynamical characteristics and composition between them.

For a better understanding of what is described in the next paragraphs, it is necessary to shortly describe the vertical structure of the atmosphere [36], represented schematically in Figure 2.6.
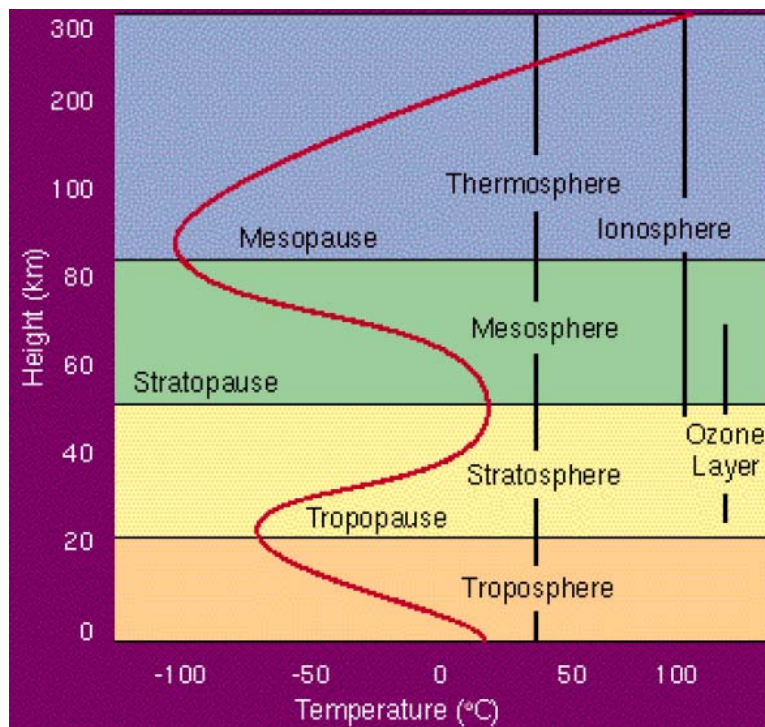
Figure 2.6 - Vertical profile of the temperature

➢ The **troposphere** is confined in the first 10-12 km, starting from the Earth's surface; it is characterized by a decrease of the temperature with increasing height, of approximately 6.5 °C / km, due to the radiative balance and the convective transport of energy from the surface to the atmosphere. The troposphere contains approximately 80% of the total mass of the atmosphere and virtually all the water vapour, clouds and rain. It introduces a strong vertical mixing that, together with the aerosol wet scavenging, determines the residence time of particles, which is rather short (usually of the order of days, at the most of weeks). From 10 up to 15-20 km the atmosphere is characterized by an isothermal layer. Then the temperature changes abruptly, with a marked inversion, up to the stratosphere.

➢ In the **stratosphere**, the atmospheric region above the troposphere, the temperature starts to increase progressively reaching a maximum of 270 K at approximately 50 km of height: this increase has to do with the absorption of solar radiation by molecular oxygen and ozone. During these processes ozone is cyclically produced and destroyed, generating a situation of dynamical equilibrium in which its concentration remains almost constant (Chapman theory [39]):

$$O + O_2 + M \rightarrow O_3 + M$$
$$O_2 + h\nu \rightarrow O + O \quad (\lambda < 242.6nm)$$
$$O_3 + O \rightarrow O_2 + O_2$$
$$O_3 + h\nu \rightarrow O_2 + O \quad (\lambda < 1150nm)$$
$$O + O + M \rightarrow O_2 + M$$

(2.20)
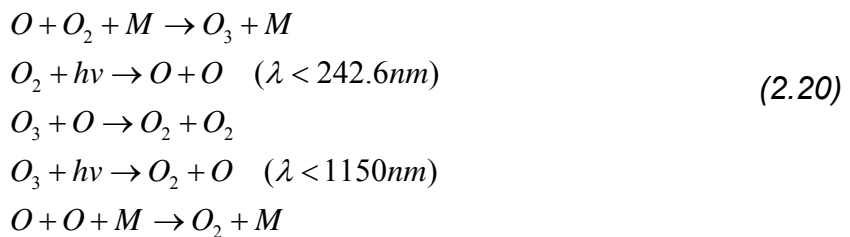
Such equilibrium is fundamental for life on Earth since ozone absorbs nearly completely the solar radiation with wavelength lower than 290 nm (therefore of elevated energy), that turns out to be harmful in a generalized manner for man and in general for all living species. In fact, if the stratospheric ozone amount would progressively diminish, for example because of the chlorofluorocarbons and nitrogen oxides emissions (as it seems is happening), the increase of harmful radiation that would reach the ground could provoke serious damages to human health and to the ecosystem. This problem will be deeply discussed in the end of the chapter because of the great importance that it covers within atmospheric physics, as well as because of its tight connection with the work done and presented along this dissertation: one of the main applications of the spectrophotometer developed in the framework of the present thesis consists on the study of the stratospheric ozone depletion and of the photochemical processes involved. Beyond the massive ozone presence and due to the fact that the stratosphere is a very stable atmospheric layer, the stratosphere contains detritus of nuclear outbreaks and powders of volcanic eruptions that happened many years before. The very low vertical mixing in this region, in fact, allows for the long

residence time of a substantial number of aerosol particle and gas molecules. The stratosphere can therefore be considered like an enormous particle tank: the stratosphere together with the troposphere, contain approximately 99% of the matter in the entire atmosphere.

➢ The **mesosphere** is located between 50 and 85 km approximately; this region is characterized by a temperature decrease from $\approx$ 270 K to the absolute minimum of $\approx$ 200 K in correspondence of the **mesopause**. Such temperature trend has to do with the progressive diminution of ozone with height, which reduces the amount of heat released in photochemical reactions *(2.20)*. The mesosphere contains 0.99% of the atmospheric mass and its main constituents are the molecular nitrogen and oxygen that constitute, respectively, approximately 80% and 20% of the total.

These first three atmospheric layers, in particular the mesosphere, are characterized by a general uniformity in the vertical composition, therefore are grouped in the same region called **homosphere**, that extends from the surface up to about 100 km.

At this height (100 km), a discontinuity zone is found, the **turbopause**, that represents the transition level from the "low" atmosphere, where the turbulent mixing prevails, to the "high" atmosphere, where the main distribution mechanism of the gaseous constituents is the molecular diffusion. The turbopause is therefore a transient boundary between turbulent and laminar flows of the atmospheric species.

The molecular diffusion tends to produce an atmosphere in which the mean molecular weight of the gas mixture gradually decreases with height, therefore a stratified distribution of the gaseous species is obtained: for this reason the region over 100 km takes the name of **heterosphere**.

➢ Over the mesopause a layer called **thermosphere** is found, that extends up in the atmosphere for many hundreds of kilometres. It is characterized by a strong temperature increase with height, reaching very high values (from 500 K to 2000 K, according to the solar activity). Such heating has to do with the greater absorption of solar radiation by molecular oxygen and nitrogen, for wavelengths lower than 200 nm,. The thermosphere composition is rather different from that of the layers below since it presents a progressive increase of atomic oxygen, that becomes the predominant constituent above 120 km, and a simultaneous gradual diminution of molecular oxygen and nitrogen caused by photodissociation.

➢ The **ionosphere** is the part of the upper atmosphere where free electrons occur in sufficient density to have an appreciable influence on the propagation of radio frequency electromagnetic waves. This ionization depends primarily on the Sun and its activity. The Ionosphere is divided into four broad regions (structures)

called D, E, F, and topside. These regions may be further divided into several regularly occurring layers, such as F1 or F2:

- D-Region - The region between about 75 and 95km above the Earth's surface in which the (relatively weak) ionization is mainly responsible for absorption of high-frequency radio waves.

- E-Region - The region between about 95 and 150km above the Earth that marks the height of the regular daytime E-layer. Other subdivisions, isolating separate layers of irregular occurrence within this region, are also labeled with an E prefix, such as the thick layer, E2, and a highly variable thin layer, Sporadic E. Ions in this region are mainly O2+.

- F-Region - The region above about 150km in which the important reflecting layer, F2, is found. Other layers in this region are also described using the prefix F, such as a temperate-latitude regular stratification, F1, and a low-latitude, semi-regular stratification, F1.5. Ions in the lower part of the F-layer are mainly NO+ and are predominantly O+ in the upper part. The F-layer is the region of primary interest to radio communications.

- Topside - This part of the Ionosphere starts at the height of the maximum density of the F2 layer of the Ionosphere and extends upward with decreasing density to a transition height where O+ ions become less numerous than H+ and He+. The transition height varies but seldom drops below 500km at night or 800km in the daytime, although it may lie as high as 1100km. Above the transition height, the weak ionization has little influence on radio signals.

The major part of the ionization is produced by solar X-ray and ultraviolet radiation and by corpuscular radiation from the Sun. The most noticeable effect is seen as the Earth rotates with respect to the Sun; ionization increases in the sunlit atmosphere and decreases on the shadowed side. Although the Sun is the largest contributor toward the ionization, cosmic rays give a small contribution.

3. Main Minor Atmospheric Compounds

The minor gaseous compounds present in the atmosphere, also called "tracers", constitute a class of gases of great importance in the study of the photochemistry and atmospheric dynamics. Although present in very low concentrations (inferior to a part per million), they are responsible for great part of the variations in the atmospheric composition.

Generally they are classified as "Primary" if directly emitted from natural or anthropic sources, and as "Secondary" if they represent the product of chemical reactions that happen in the atmosphere.

The main tracers, described in the following paragraphs, belong to the nitrogen, chlorine, bromine, carbon and hydroxyl radicals. Due to the primary importance of the ozone among the minor species that influence the radiative budget, the analysis will start from this last one. The other compounds will be introduced evidencing their tight connection with ozone, since they owe their importance to the consequences that provoke on its photochemical equilibrium.

3.1. OZONE

Ozone (O_3) is a relatively unstable molecule made up of three atoms of oxygen (O). Although it represents only a tiny fraction of the atmosphere, ozone is crucial for the life on Earth. Depending on where ozone resides, it can protect or harm life on Earth. Most ozone resides in the stratosphere, where it acts as a shield to protect Earth's surface from the sun's harmful ultraviolet radiation. In the troposphere ozone is a harmful pollutant that causes damage to lung tissue and plants. The amounts of "good" stratospheric ozone and "bad" tropospheric ozone in the atmosphere depend on a balance between processes that create ozone and those that destroy it. A perturbation in the ozone balance can have serious consequences for life on Earth, according to the findings of scientists the "bad" tropospheric ozone is increasing in the air we breathe, and the "good" stratospheric ozone is decreasing in our protective ozone layer.

In the stratosphere (Figure 3.1), ozone is created primarily by ultraviolet radiation. When high-energy ultraviolet rays strike ordinary oxygen molecules (O_2), they split the molecule into two single oxygen atoms, known as atomic oxygen. A free oxygen atom then combines with another oxygen molecule to form a molecule of ozone *(2.20)*, (Figure 3.2). There is so much oxygen in our atmosphere, that these high-energy ultraviolet rays are completely absorbed in the stratosphere.
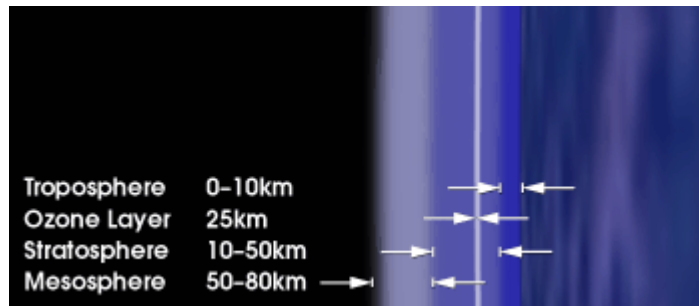
Figure 3.1 - The relative heights of atmospheric layers.
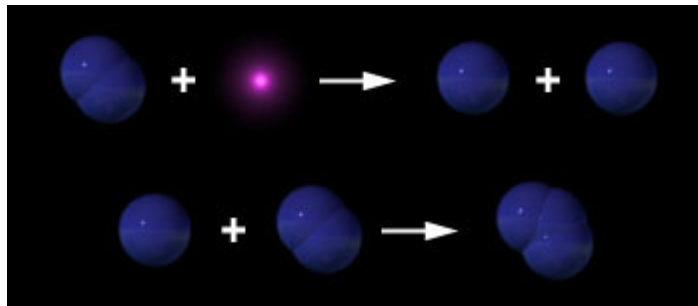
Figure 3.2 - The formation of ozone

Ozone is extremely valuable since it absorbs a wide range of ultraviolet energy. When an ozone molecule absorbs even low-energy ultraviolet radiation, it splits into an ordinary oxygen molecule and a free oxygen atom. Usually this free oxygen atom quickly re-joins with an oxygen molecule to form another ozone molecule. Because of this "ozone-oxygen cycle," harmful ultraviolet radiation is continuously converted into heat.

Natural reactions other than the "ozone-oxygen cycle" described above also affect the concentration of ozone in the stratosphere. Because ozone and free oxygen atoms are highly unstable, they react very easily with nitrogen, hydrogen, chlorine, and bromine compounds that are found naturally in the Earth's atmosphere (released from both land and ocean sources). For example, single chlorine atoms can convert ozone into oxygen molecules where this ozone loss balances the production of ozone by high-energy ultraviolet rays striking oxygen molecules.

In addition to the natural ozone balance, the ozone levels change periodically as part of regular natural cycles such as the changing seasons, winds, and long time scale sun variations. Moreover, volcanic eruptions may inject materials into the stratosphere that can lead to an increase of the ozone destruction.

Over the Earth's lifetime, natural processes have regulated the balance of ozone in the stratosphere. A simple way to understand the ozone balance is to think of a leaky bucket. As long as water is poured into the bucket at the same rate that water is leaking out, the amount or water level in the bucket will remain the same.

Likewise, as long as ozone is being created at the same rate that it is being destroyed, the total amount of ozone will remain the same.

However, starting in the early 1970's, evidences were found that human activities were disrupting the ozone balance. Human production of chlorine-containing chemicals such as chlorofluorocarbons (CFCs) has added an additional factor that destroys ozone. CFCs are compounds made up of chlorine, fluorine and carbon bound together. Because they are extremely stable molecules, CFCs do not react easily with other chemicals in the lower atmosphere. One of the few forces that can break up CFC molecules is ultraviolet radiation. In the lower atmosphere, CFCs are protected from ultraviolet radiation by the ozone layer itself. Thus CFC molecules are able to migrate intact up into the stratosphere. Although the CFC molecules are heavier than air, the air currents and mixing processes of the atmosphere carry them into the stratosphere primarily from the upper tropical troposphere. Atmospheric air motions then transport the gases upper in the air and toward the poles in both hemispheres.

Once in the stratosphere, the CFC molecules are no longer shielded from ultraviolet radiation by the ozone layer. Bombarded by the sun's ultraviolet energy, CFC molecules break up and release chlorine atoms. Free chlorine atoms then react with ozone molecules, taking one oxygen atom to form chlorine monoxide and leaving an ordinary oxygen molecule (Figure 3.3).

$$O_3 + hv \rightarrow O + O_2$$
$$O + ClO \rightarrow Cl + O_2$$
$$Cl + O_3 \rightarrow ClO + O_2$$
$$2O_3 + hv = 3O_2$$

(3.1)
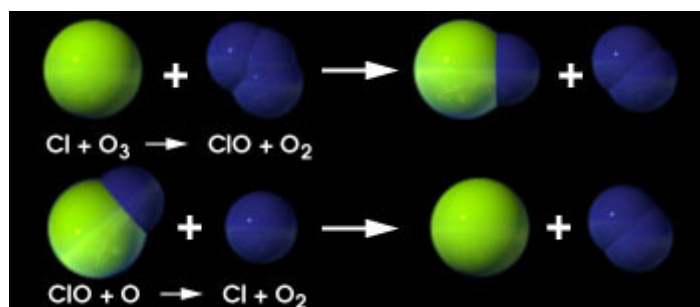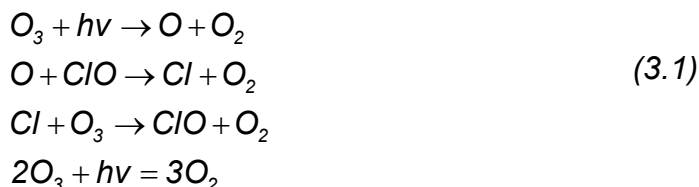
Figure 3.3 - The destruction of ozone

If each chlorine atom released from a CFC molecule destroyed only one ozone molecule, CFCs would pose very little threat to the ozone layer. However, when a chlorine monoxide molecule encounters a free atom of oxygen, the oxygen atom breaks up the chlorine monoxide, stealing the oxygen atom and releasing the

chlorine atom back into the stratosphere to destroys more ozone. This reaction occurs repeatedly, allowing a single atom of chlorine to act as a catalyst, destroying several ozone molecules. Fortunately, chlorine atoms do not remain in the stratosphere forever. When a free chlorine atom reacts with gases such as methane (CH_4), it is bounded up into a molecule of hydrogen chloride (HCl), which can be carried downward from the stratosphere into the troposphere, where it can be washed away by rain. Therefore, if man stop injecting CFCs and other ozone-destroying chemicals into the stratosphere, the ozone layer may eventually repair itself.

The term "ozone depletion" means more than just the natural destruction of ozone, it means that ozone loss is exceeding ozone creation. Think again of the "leaky bucket." Putting additional ozone-destroying compounds such as CFCs into the atmosphere is like increasing the size of the holes in our "bucket" of ozone. The larger holes cause ozone to leak out at a faster rate than ozone is being created. Consequently, the level of ozone protecting us from ultraviolet radiation decreases. During the last 15 years, an additional mechanism was found in the areas over the Antarctic and Arctic that rapidly destroys ozone. Over the Earth's poles during their respective winters, the stratosphere cools to very low temperatures and polar stratospheric clouds (PSCs) form. In the polar stratosphere, nearly all the chlorine is in the form of inactive or "reservoir" gases such as hydrogen chloride (HCl) and chlorine nitrate ($ClONO_2$) that do not react with ozone or one with the other. However, chemical reactions of these "reservoir" chlorine gases can occur on the polar stratospheric cloud particle surfaces, converting the chlorine gases into very reactive forms that rapidly destroy ozone. This "polar chemistry" on the stratospheric cloud particles has caused very large decreases in ozone concentrations over Antarctica and the Arctic (the so-called "Ozone Hole").
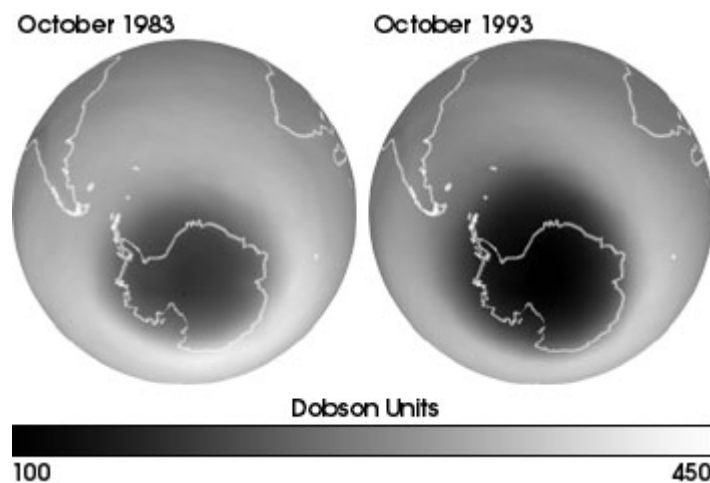
Figure 3.4 - Ozone levels measured by the Total Ozone Mapping Spectrometer (TOMS).

In addition, in the stratosphere also the active nitrogen contributes to the destruction of ozone via photochemistry through the so-called catalytic cycle (see § 3.2.1).

Since the 1920's, ozone has been measured by ground-based instruments. Scientists place instruments in locations around the globe to measure the amount of ultraviolet radiation getting through the atmosphere at each site. From these measurements, they calculate the concentration of ozone in the atmosphere above that location. These data, although useful in learning about ozone, does not provide an adequate picture of global ozone concentrations.

The amount and distribution of ozone molecules in the stratosphere varies greatly over the globe. Ozone molecules are transported around the stratosphere as much as water clouds are transported in the troposphere. Therefore, scientists observing ozone fluctuations over just one spot could not know whether a change in local ozone levels meant an alteration in global ozone levels, or simply a fluctuation in the concentration over that particular spot. Satellites have given scientists the ability to overcome this problem because they provide a picture of what is happening daily over the entire Earth. The United States satellite measurement program for ozone, run jointly by NASA and the National Oceanic and Atmospheric Administration (NOAA), has measured the ozone distribution by season, latitude, and longitude, and has observed long-term changes over more than 20 years using a variety of satellite instruments. The instruments in use today will be replaced over the next five to ten years by a new generation of improved and more sophisticated instruments.

Measurements and research are being used to improve models for predicting ozone levels. In fact, early model predictions have already aided policy makers in determining solutions to the ozone depletion problem. Faced with the strong possibility that CFCs could cause serious ozone depletion, policy makers from around the world signed the Montreal Protocol treaty in 1987, limiting CFC production and usage. By 1992, the growing scientific evidence of ozone loss prompted diplomats to strengthen the Montreal Protocol. The revised treaty called for a complete phase out of CFC production in developed countries by 1996. As a result, most CFC concentrations are slowly decreasing around the globe.

Much remains to be learned about the processes that affect ozone. To create accurate models, all of the factors affecting ozone creation and destruction have to be studied simultaneously. Moreover, these factors have to be monitored both from the space as from the ground continuously, over many years, and over the entire globe. NASA's Earth Observing System (EOS) will allow scientists to study ozone in this way. The EOS series of satellites will carry a sophisticated group of instruments that allow to measure the interactions within the atmosphere that

affect ozone. Based on many years of data gathered by previous NASA and NOAA missions, these measurements will increase considerably our knowledge of the chemistry and dynamics of the upper atmosphere and our understanding of how human activities are affecting Earth's protective ozone layer.

Also Europe is very active in this field of research; the "old" GOME (Global Ozone Monitoring Experiment) instrument installed on the ERS2 satellite (launched in April 1995 and still operating), and the new SCIAMACHY Spectrometer on board the ENVISAT satellite (launched in March 2002), are providing useful information about the variation of the global ozone layer. Regarding the ground based monitoring of the ozone as well as of the nitrogen dioxide, the Network for the Detection of the Stratospheric Changes (NDSC) supplies since the eighty's extremely interesting measurements of the atmospheric compounds.

3.2. NITROGEN

The nitrogen is the most abundant element in the atmosphere (70%). The molecule of N_2 is extremely stable but minor compounds as the nitrous oxide (N_2O), the nitric oxide (NO), the nitrogen dioxide (NO_2), the nitric acid (HNO_3) and ammonia (NH_3) are chemically active and play important roles in the actual environmental problems going from the formation of acid rains to the photochemical smog and pollution and to the destruction of stratospheric ozone.
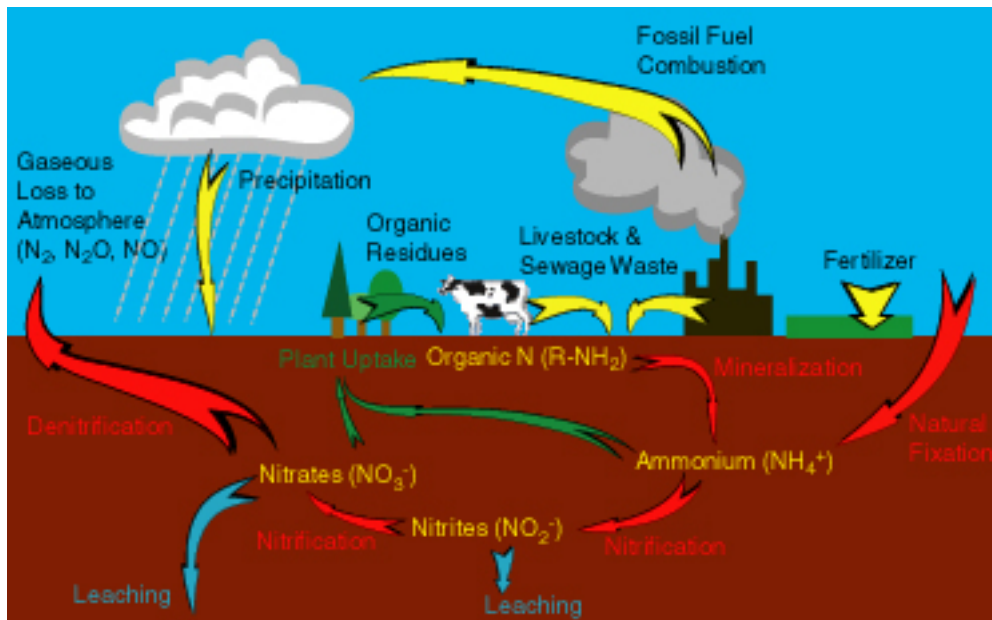
Figure 3.5 - The nitrogen cycle. Yellow arrows indicate human sources of nitrogen to the environment. Red arrows indicate microbial transformations of nitrogen. Blue arrows indicate physical forces acting on nitrogen. And green arrows indicate natural, non-microbial processes affecting the form and fate of nitrogen.

The active nitrogen compounds , usually identified with NO_X (mainly NO and NO_2), are formed in the atmosphere from natural and artificial sources. NO_Y is a larger class of nitrogen compounds (= NO_X + NO_3 + N_2O_5 + HNO_3 + HONO + HO_2NO_2). Between the natural processes, the most important are the synthesis of nitrogen and oxygen in the atmospheric electricity, the forests fires and the emissions from the ground.

The greater anthropogenic sources are instead: the combustion processes, the fertilizer use, the drainage products of supersonic airplanes and the nuclear outbreaks [40].

Chemistry of the NO_X directly and indirectly influences also the concentration of hydroxyl radical (OH) that together with ozone constitutes the main tropospheric oxidant converting many emitted primary atmospheric compounds in secondary products that are more easily removed through deposition (dry or wet). On the contrary, in the stratosphere, the active nitrogen contributes to the destruction of ozone via photochemistry through the so-called catalytic cycle.

In the following sections the chemistry of active nitrogen in stratosphere and troposphere will be briefly described. Figure 3.6 shows the schematic diagram of the nitrogen compounds cycle.

3.2.1. Active Nitrogen in the stratosphere

The members of the nitrogen oxides family take part in a number of homogeneous and heterogeneous chemical reactions, playing a very important role in the stratospheric processes.

The chemistry determining the contents of ozone and other trace gases in the stratosphere is extremely complex due to the presence of many reactive compounds (oxygen, nitrogen, hydrogen, halogens, sulfur and carbon) interacting thanks to the solar radiation. This last has a great variability depending on the season, the height and the wavelength. The N_2O is an example of the interaction between Earth and atmosphere. N_2O is emitted mainly by the Earth surface (Figure 3.5) and passing quite undamaged through all the troposphere it catches up the stratosphere where it is photolyzed by the UV radiation in order to produce NO with the following reaction:

$$N_2O + hv \rightarrow N_2 + O(^1D)$$
$$N_2O + O(^1D) \rightarrow NO + NO \qquad (58\%)$$
$$N_2O + O(^1D) \rightarrow N_2 + O_2 \qquad (42\%)$$

$$(3.2)$$
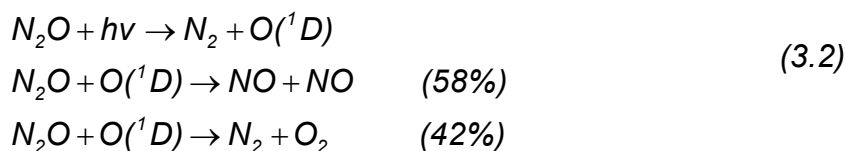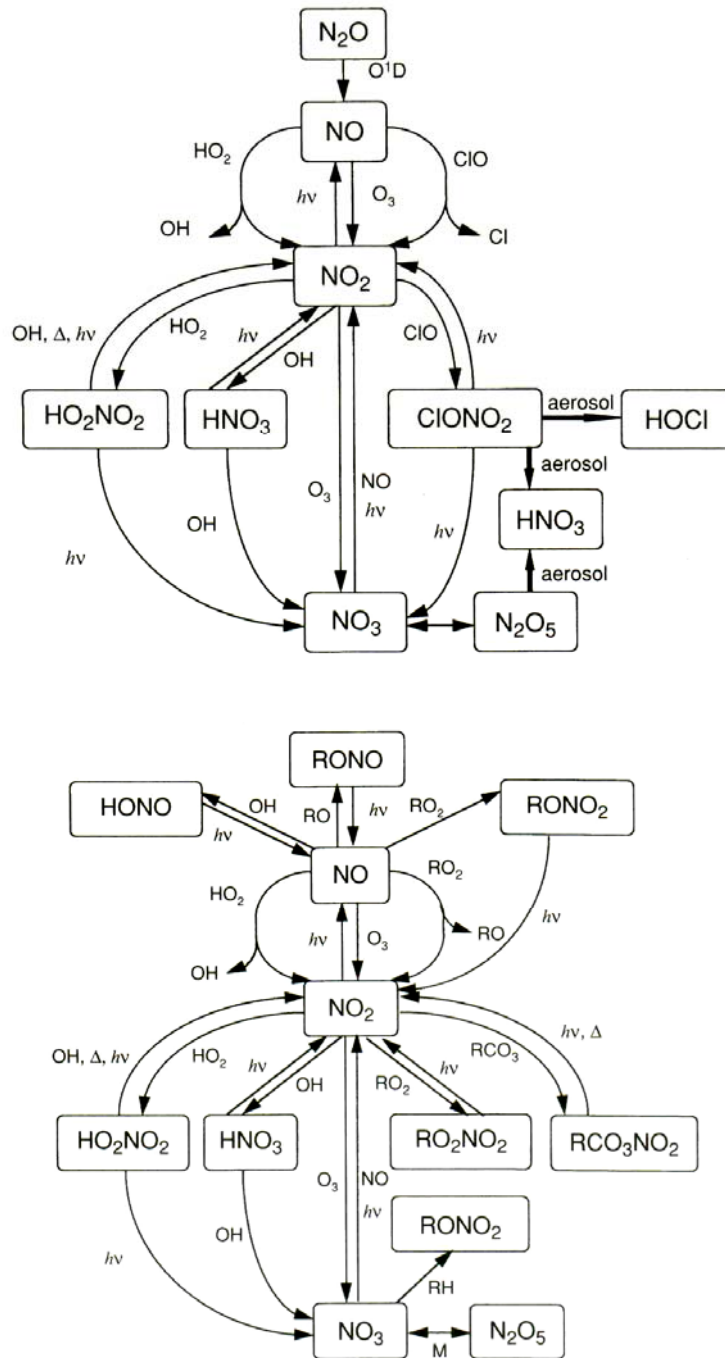
Figure 3.6 - Schematic diagram of the active nitrogen chemistry (NOx); in the stratosphere (upper) e troposphere (lower)[37].

The production of active nitrogen mainly occurs in the middle and high stratosphere. Therefore since NO_Y is produced to expenses of the N_2O such species shows a negative correlation in the stratosphere, while the correlation between NO_Y and O_3 is positive having both the same photochemical source at

approximately 30-40 km of height and common sinks, since both gases are transported in the troposphere. The division of the NO_Y between its several constituents is function of the latitude, of the season and of the hour of the day. In summer HNO_3 is the dominant active constituent in the low stratosphere, while the NO_X is the dominant species at higher altitudes, this because of the conversion rate increase of the HNO_3 in NO_X. Other compounds as N_2O_5 and $ClONO_2$ have mixing ratios much smaller though they are fundamental for the understanding of the chemical reactions taking place in the stratosphere.

The stratospheric NO is quickly oxidized in NO_2 thanks to the ozone. On the other hand, for wavelengths smaller than 420nm, the photolysis of the NO_2 recreates NO according to the following reactions:

$$
\begin{array}{ll}
NO + O_3 \rightarrow NO_2 + O_2 & \text{(a} \\
\underline{NO_2 + h\nu \rightarrow NO + O \qquad \lambda \leq 420\text{nm} \qquad \text{(b}} \\
\quad O_3 \rightarrow O + O_2
\end{array}
\qquad (3.3)
$$
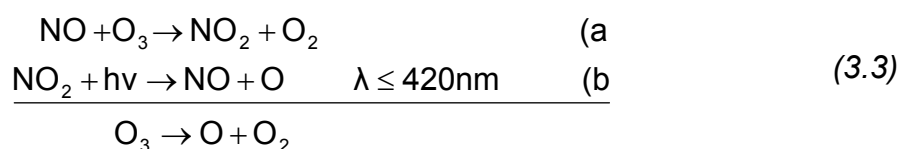
Such reactions constitute a null cycle for active oxygen ($Ox = O + O_3$) since the atom of created oxygen can be recombined with the O_2 in order to recreate ozone, and also for the NO_X as there is an exchange of NO and NO_2 but the total number is maintained. However in the high stratosphere, the concentration of the atomic oxygen produced from the photolysis of O_2 and O_3 becomes sufficient to establish reactions with other compounds creating therefore a destructive cycle of the following type:

$$
\begin{array}{ll}
NO + O_3 \rightarrow NO_2 + O_2 & \text{(a} \\
\underline{NO_2 + O \rightarrow NO + O_2 \qquad \text{(b}} \\
\quad O + O_3 \rightarrow O_2 + O_2
\end{array}
\qquad (3.4)
$$
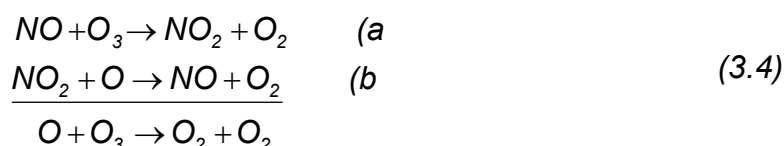
Reactions *(3.4)* produce the destruction of ozone while the NO_X is still conserved. Many of these cycles can be established before that active NO_X is transformed in less reagents compounds of the NOY group. Such cycle is an example of the classic cycle of ozone destruction in the stratosphere. In fact, if NO is replaced with HO, Cl, Br the catalytic processes involving HOx, ClOx and BrOx are obtained. These lasts reactions have become famous since they have been indicated to be the cause of the famous ozone hole measured during the polar spring. There are also other catalytic cycles destroying ozone in which active nitrogen compounds are involved. An example is constituted from the following cycle:

$$ClONO_2 + hv \rightarrow Cl + NO_3$$
$$NO_3 + hv \rightarrow NO + O_2 \qquad \lambda < 640nm$$
$$Cl + O_3 \rightarrow ClO + O_2$$
$$NO + O_3 \rightarrow NO_2 + O_2$$
$$\underline{ClO + NO_2 + M \rightarrow ClONO_2 + M}$$
$$2O_3 \rightarrow 3O_2$$

(3.5)
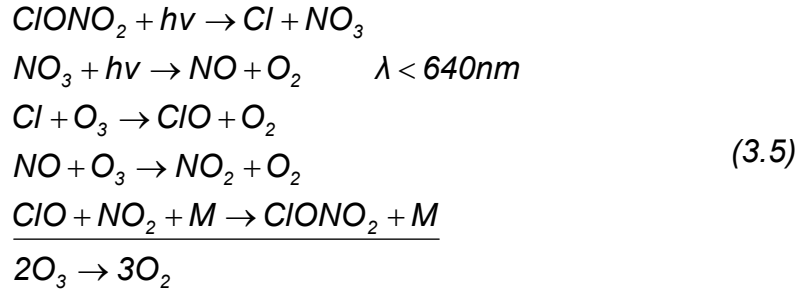
This cycle is less efficient than the *(3.4)*, since 90% of the photolysis of NO NO_X produces NO_2 + O and only the remaining 10% produces $NO+O_2$. Moreover, there are cycles in which NO_X, CO and CH NO_X are involved for the ozone production and those cycles are important in order to understand the ozone trend in the troposphere and in the lower stratosphere.

The catalytic cycles involving NO_X depend on the solar radiation, therefore it turns out clear that both the NO_2 and the NO show a significant diurnal variation; the NO disappears during the night while after the sunrise NO_2 begins to be photolyzed in order to recreate NO. During the day the inter-conversion between NO and NO_2 is rather fast in the stratosphere as well as in the troposphere and the approximation of stationary state gives, with good accuracy, the relationship between NO_2 and NO. In fact considering equations *(3.3)* and *(3.4)* and equaling the derivatives of the NO_2 and NO concentration to zero (hypothesis of stationary state), the following relation is obtained:

$$\frac{[NO_2]}{[NO]} = \frac{k_{3.3a}[O_3]}{(j_{3.3b} + k_{3.4b}[O])} \approx \frac{k_{3.3a}[O_3]}{j_{3.3b}}$$

(3.6)

where k and j are the constant of reaction and the relative coefficient of photolysis of the reactions respectively. The term with [O] just has been neglected because the hypothesis of lower-middle stratosphere and high troposphere is assumed.

The NO_2 is involved in catalytic ozone destruction and at the same time in the "buffering" of ozone destroying halogen oxides into more stable reservoir substances.

At night NO_2 can be oxidized by O_3 to form NO_3, a strong atmospheric oxidant and a precursor to the formation of dinitrogen pent-oxide, N_2O_5. Because NO_3 is rapidly photolyzed at visible wavelengths, both its daytime concentration and chemistry are of relatively minor importance in the lower and middle stratosphere.

In contrast, N_2O_5 can have morning concentrations in the lower stratosphere comparable to NO_X ($NO+NO_2$) even though its production requires the formation of NO_Y

$$NO_2 + O_3 \rightarrow NO_3 + O_2$$
$$NO_3 + hv \rightarrow NO + O_2$$
$$NO_3 + hv \rightarrow NO_2 + O \qquad (3.7)$$
$$NO_3 + NO_2 + M \Leftrightarrow N_2O_5 + M$$
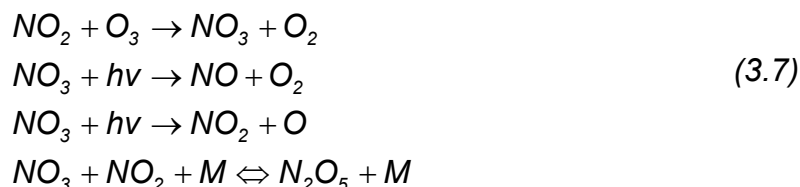
The explanation results primarily from the different photolysis rates of N_2O_5 and of NO_3. During the night N_2O_5 builds at the expense of NO, or more precisely at the expense of NO_2.
After sunrise, N_2O_5 can be photolyzed essentially in two NO_X molecules

$$N_2O_5 + hv \rightarrow NO_3 + NO_2 \qquad (3.8)$$

but the photolysis time constant is dependent on both the usual factors (zenith angle, altitude, albedo, etc.) and the temperature. (Figure 3.7 shows the diurnal variation of the main active nitrogen compounds) In summer typical photolysis times range from 7 to 24 h in the stratospheric layer between 20 Km up to 30 Km.
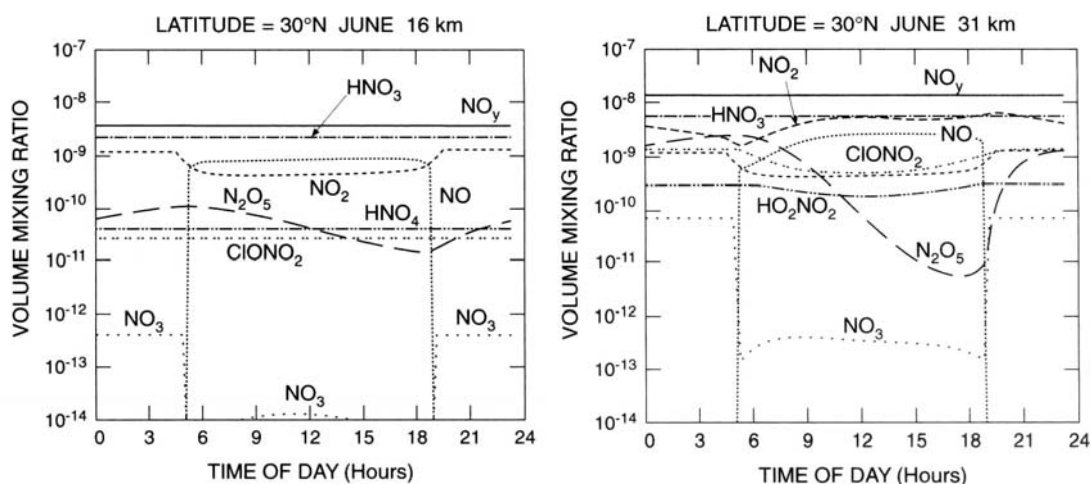
Figure 3.7 – Diurnal Variation of the nitrogen active compounds in the stratosphere at two different altitudes: 16 Km (left) and 31 Km (right) [37].

The formation of N_2O_5 is an example of formation of a long-lived odd-nitrogen reservoir that occurs at night or in Polar winter. Other important reservoir constituents are bromine nitrate ($BrONO_2$) and the chlorine analog ($ClONO_2$), nitric acid (HNO_3) and peroxynitric acid (HO_2NO_2). The homogeneous formation of the reservoir species requires the molecular chain termination reactions *(3.9)*, .

$$NO_3 + NO_2 + M \leftrightarrow N_2O_5 + M \qquad (a$$
$$NO_3 + OH + M \rightarrow HNO_3 + M \qquad (b$$
$$NO_2 + HO_2 + M \rightarrow HO_2NO_2 + M \quad (c$$
$$NO_2 + ClO + M \rightarrow ClONO_2 + M \quad (d$$

$$(3.9)$$
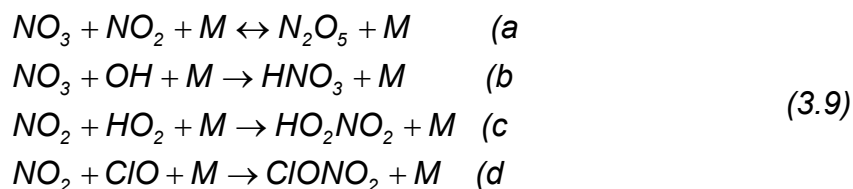
The occurrence of these reactions not only curtail O_3 destruction through temporary removal of active NO_X, but they also sequester HO_X. and ClO_X, radicals and thus decrease the contribution of their catalytic cycles to O_3 destruction. Alternatively, any other stratospheric process that diminishes NO_X, directly or indirectly will enhance the abundance of active HO_X and ClO_X by decreasing the rates of *(3.9)* and therefore increasing their ozone destruction efficiency.

3.2.2. Active Nitrogen in the troposphere

In the troposphere, nitrogen oxides are formed during high temperature combustion processes from the oxidation of nitrogen in the air or fuel. The principal source of nitrogen oxides - nitric oxide (NO) and nitrogen dioxide (NO_2), collectively known as NO_X - is road traffic, which is responsible for approximately half the emissions in Europe. NO and NO_2 concentrations are therefore higher in urban areas where traffic is heaviest. Other important sources are power stations, heating plants and industrial processes. Nitrogen oxides are released into the atmosphere mainly in the form of NO, which is then readily oxidized to NO_2 by reaction with ozone. High levels of NO_X occur in urban environments under stable meteorological conditions, when the airmass is unable to rise up and the gases cannot disperse. Nitrogen dioxide presents a variety of environmental and health impacts. It is a respiratory irritant, may exacerbate asthma and possibly increase susceptibility to infections. In the presence of sunlight, it reacts with hydrocarbons to produce photochemical pollutants such as ozone. In addition, nitrogen oxides have a lifetime of approximately 1 day with respect to conversion to nitric acid. This nitric acid is in turn removed from the atmosphere by direct deposition on the ground, or transfer to aqueous droplets (e.g. cloud or rainwater), thereby contributing to acid deposition.

But the role of NO_X cannot be limited to that of polluting agent. When interacting with active compounds of hydrogen, analogous to those already seen in the

stratosphere, the NO_X can strongly influence the concentration of hydroxyl radical (OH) that is the most important oxidant in the troposphere, transforming primary emissions in secondary ones.

Because of the insufficient presence of the photo-dissociated oxygen atom in the troposphere, reaction *(3.4)*b does not succeed to compete with *(3.3)*b therefore the catalytic destruction of the O_3 turns out negligible. The NO_X indeed favors the ozone creation that is often considered as a polluting agent, in the troposphere, forgetting its essential role in determining the OH concentration that is the essential agent for the removal of the primary emissions in the atmosphere. These ambivalence roles of different compounds contributes to create the difficulty in defining who "the good" compound is and who "the bad one" is.

In the whole troposphere there are two main ozone sources: transport from the stratosphere and photochemical local production. Till now there are no evidences for a clear trend of O_3 increase or decrease in the free troposphere, suggesting that such sources are equally balanced by the destruction at the Earth's surface and by local photochemical loss. Where the atmosphere is very dense, the oxygen atoms created from the reaction *(3.3)*b (the only possible channel in troposphere where the radiation under 290 nm does not arrive) are recombined immediately in order to recreate O_3 through:

$$O + O_2 + M \rightarrow O_3 + M \qquad\qquad (3.10)$$

The molecule of NO, created by the reaction *(3.3)*b, is immediately oxidized from the O_3 giving therefore a null cycle in which the only effect is the usual inter-conversion between NO and NO_2, evidencing that in the troposphere the approximation *(3.6)* is more trustful. Therefore, the cycles producing O_3 have to be searched elsewhere. There are essentially three and all of them are driven by the solar radiation; The three cycles begin with an oxidation due to the presence of the hydroxyl radical and the Volatile Organic Compounds (VOC), which are considered as the "fuel" of such reactions. The prevalence of a cycle over the others in the various zones of the atmosphere depend only on the abundance of such "fuels".

Also in the upper troposphere there is abundance of these liable to tarnish organic compounds, typically the carbon monoxide (CO) and methane (CH_4) that are responsible for two cycles of ozone creations:

$$OH + CO \rightarrow CO_2 + H \qquad (a$$
$$H + O_2 + M \rightarrow HO_2 + M \qquad (b$$
$$HO_2 + NO \rightarrow NO_2 + OH \qquad (c \qquad\qquad (3.11)$$
$$NO_2 + hv \rightarrow NO + O \qquad (d$$
$$\underline{O + O_2 + M \rightarrow O_3 + M \qquad (e}$$
$$CO + 2O_2 + hv \rightarrow CO_2 + O_3$$
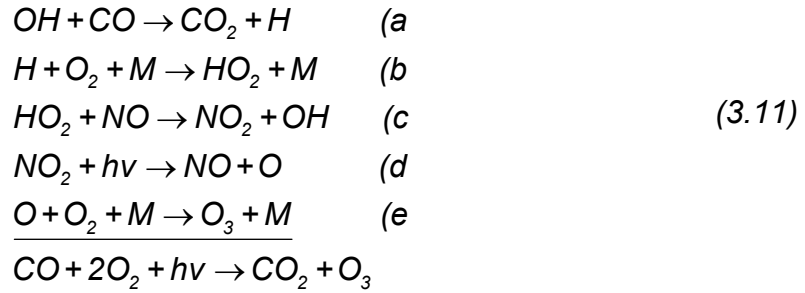
Where there is any loss of NO_X and HO_X (= OH + HO_2) and

$$OH + CH_4 \rightarrow CH_3 + H_2O \qquad (a$$
$$CH_3 + O_2 + M \rightarrow CH_3O_2 + M \qquad (b$$
$$CH_3O_2 + NO \rightarrow CH_3O + NO_2 \qquad (c \qquad\qquad (3.12)$$
$$CH_3O + O_2 \rightarrow HO_2 + H_2O \qquad (d$$
$$HO_2 + NO \rightarrow OH + NO_2 \qquad (e$$
$$2(NO_2 + hv \rightarrow NO + O) \qquad (f$$
$$\underline{2(O + O_2 + M \rightarrow O_3 + M) \qquad (g}$$
$$CH_4 + 4O_2 + 2hv \rightarrow CH_2O + H_2O + 2O_3$$
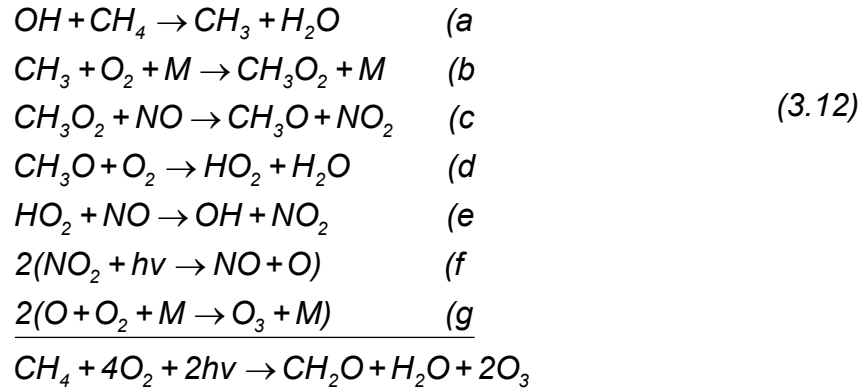
In opposition to the reaction *(3.3)*a here the peroxides radical HO_2 and CH_3O_2 can oxidize NO in NO_2 without spending O_3. Therefore the concentrations of NO_X must exist so that the reactions*(3.11)*c and *(3.12)*c are dominant regarding the re-combinations of the same peroxides radicals. Therefore the local production of O_3 ($P(O_3)$) can be written as:

$$P(O_3) = (k_{3.11c}[HO_2] + k_{3.12c}[CH_3O_2])[NO] \qquad\qquad (3.13)$$

The concentration of NO and peroxide radicals can depend one from the other, therefore these cycles are activated when there is a low content of NO_X, as it is in the greater part of the upper troposphere. Such dependency from the O concentration has lead to the definition of a critical concentration fixing the limit for the processes of creation and destruction of the tropospheric O_3; the threshold value is around 5-30 pptv at local noon and for the low troposphere.

In the planetary boundary layer (PBL), the role of the nitrogen active compounds is not so different from the one in the upper troposphere, although the oxidation

processes are much more complicate due to the availability of a great number of hydrocarbon to be used as 'fuel' for the reactions. In this zone also the secondary constituent, entering only in negligible processes in the upper troposphere, are considerably active, also the concentrations of peroxides radical (RO_2) and of the NO_X are much higher than elsewhere, generating a production of O_3 greater than in the free troposphere even if many of the processes of destruction of ozone, are much more efficient.

The O_3 formation cycle in this region can therefore be outlined with a generic cycle, similar to the one of the CO and of the CH_4 and in which the VOC are specified as RH and the carbonyl compounds (Aldehydes and Ketones) with R' CHO, where R' indicates residual organic having one carbon atom less than R

$$
\begin{aligned}
&OH + RH \rightarrow R + H_2O && (a\\
&R + O_2 + M \rightarrow RO_2 + M && (b\\
&RO_2 + NO \rightarrow RO + NO_2 && (c\\
&RO + O_2 \rightarrow HO_2 + R'CHO && (d\\
&HO_2 + NO \rightarrow OH + NO_2 && (e\\
&2(NO_2 + hv \rightarrow NO + O) && (f\\
&\underline{2(O + O_2 + M \rightarrow O_3 + M)} && (g\\
&RH + 4O_2 + 2hv \rightarrow R'CHO + H_2O + 2O_3
\end{aligned}
$$

$$(3.14)$$
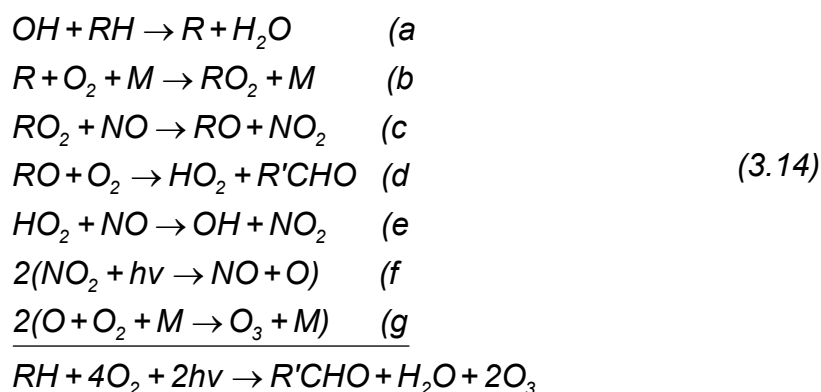
As in the previous chemical cycles the NO_X is not utilized directly. However there are also different ways for the permanent or temporary removal of the NO_X and such ways become very important in the low troposphere giving an extremely reduced lifetime of the NO_X compared with the remote troposphere one. The equation for the production of ozone presents a shape similar to *(3.12)* where the contributions of all the peroxides radicals are considered:

$$P(O_3) = (k_{3.10c}[HO_2] + \sum_i k_{3.11ci}[RO_2]_i)[NO] \qquad (3.15)$$

Moreover, we are in the conditions in which the concentration of NO_X is closely tied to that of the radicals. Therefore the production of O_3 is function of the ratio VOC/ NO_X. Obviously a determining factor establishing the catalytic power of the NO_X is their lifetime. If we consider the nitric acid formation (HNO_3) as the only process converting the NO_X in reserves species through the reaction

$$NO_2 + OH + M \rightarrow HNO_3 + M$$

$$(3.16)$$

the lifetime of NO_X can be written as

$$\tau_{NO_x} = \tau_{NO_2}(1 + \frac{[NO]}{[NO_2]})$$
(3.17)

where $\tau_{NO_2} = \frac{1}{k_{3.16}[OH][M]}$. Therefore in the upper troposphere, where the OH concentration is lower and the ratio NO/NO_2 is higher than in the low troposphere, a lifetime $\tau_{NO_x} \sim 4 - 7$ days is obtained, while in the low troposphere, where the trends are opposite, $\tau_{NO_x} \sim 1$ day.

3.3. CHLORINE

As already presented in the previous paragraphs, ozone can be destroyed by chemical cycles that react directly with it, or by those that react with the oxygen atom temporarily freed whenever an ozone molecule breaks apart. However, since in the stratosphere ozone concentrations are higher than those of most reactive chemicals, the only significant ozone destroyers are those that can participate in a "catalytic cycle", that is, where one trace catalytic chemical can be responsible for destroying tens or even hundreds of thousands of ozone molecules. Between the previous presented catalytic cycles, the most effective cycles involve chlorine (Cl) *(3.5)*. Also bromine (Br) has a similar cycle .

In the recent decades, various human activities have released ozone-destroying chemicals into the atmosphere. Halogen atoms are of particular importance -- chlorine and bromine. Chemicals released into the atmosphere by industrial practices include chlorocarbon compounds (such as CCl_4 and CH_3Cl_3), chlorofluorocarbon compounds, CFCs, (such as $CFCl_3$ and CF_2Cl_2), and halon compounds (such as CF_3Br and CF_2ClBr).

Once in the stratosphere, all of these chlorine- or bromine-containing halocarbon compounds are broken apart by solar ultraviolet radiation, releasing their chlorine or bromine atoms to initiate ozone destruction. Each chlorine atom can initiate a cycle that can destroy up to 100000 ozone molecules [41]. Bromine atoms are even more efficient destroyers.

In the early 1970s, the detection of significant concentrations of chlorocarbons and CFCs in the lower atmosphere was coupled with the consciousness that photochemical and rainout processes, which usually remove most pollutants from the lower atmosphere, were not working for these compounds. It became clear

that many halocarbons would remain in the atmosphere for a long time and might build up to atmospheric levels high enough to cause a real mischief. It is now known that many CFCs and halons are extremely stable and reach the stratosphere intact. They have atmospheric lifetimes between 50 and several hundred years, so that significant fractions of their peak concentrations will persist in the atmosphere long after the emissions of these chemicals have stopped.

3.4. HO$_X$ COMPOUNDS

The OH radical plays a decisive role in atmospheric chemistry. It is responsible for the removal of NO$_X$ and for the regeneration of chlorine radicals. The main ozone removal process involving HO$_X$ compounds is given by:

$$\begin{aligned}
OH + O_3 &\rightarrow HO_2 + O_2 \\
HO_2 + O &\rightarrow OH + O_2 \\
\hline
O + O_3 &\rightarrow 2O_2
\end{aligned}$$

(3.18)
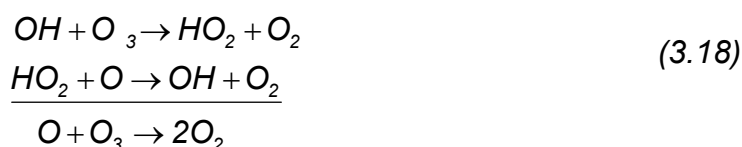
3.5. SULPHUR COMPOUNDS

Sulphur dioxide (SO$_2$) is a corrosive acid gas which combines with water vapour in the atmosphere to produce acid rain. Both wet and dry deposition have been implicated in the damage and destruction of vegetation and in the degradation of soils, building materials and watercourses.
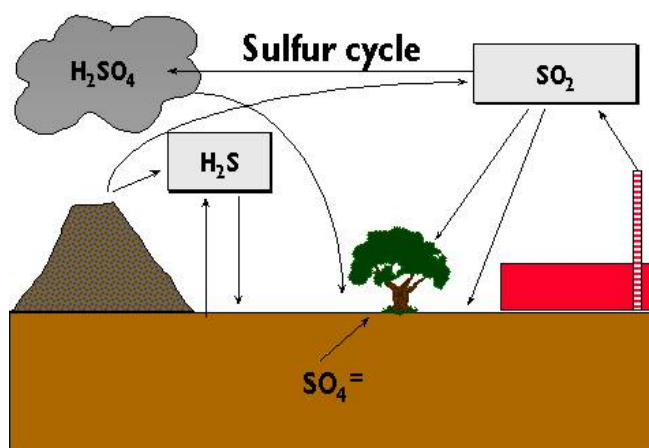
Figure 3.8 –Sulphur cycle

Sulphur enters the atmosphere through both natural and human sources. Natural sources can be for instance volcanic eruptions, bacterial processes, evaporation

from water, or decaying organisms. When sulphur enters the atmosphere through human activity, this is mainly a consequence of industrial processes (as power stations burning fossil fuels which contain sulphur), where sulphur dioxide (SO_2) and hydrogen sulphide (H_2S) gases are emitted on a wide scale.

Major SO_2 problems now tend only to occur in cities in which coal is still widely used for domestic heating, in industry and in power stations. As some power stations are now located away from urban areas, SO_2 emissions may affect air quality in both rural and urban areas.

When SO_2 enters the atmosphere it reacts with oxygen to produce sulphur trioxide gas (SO_3), or with other chemicals in the atmosphere, to produce sulphur salts. Sulphur dioxide may also react with water to produce sulphuric acid (H_2SO_4). Sulphuric acid may also be produced from demethyl sulphide, which is emitted to the atmosphere by plankton species.

All these particles will settle back onto Earth, or react with rain and fall back onto Earth as acid deposition. The particles may then be absorbed by plants again and released back into the atmosphere, so that the sulphur cycle starts over again.

3.6. CARBON COMPOUNDS

The carbon monoxides are produced naturally mainly during forests fires and biomass burning and by the oxidation of natural hydrocarbons in the atmosphere. Their main artificial sources are the combustion processes of fossil fuels (coal, oils). Part of the CO_2 cycle is still unknown, since it interacts in a complex way with the atmosphere, biosphere, hydrosphere and lithosphere. However, Figure 3.9 illustrates a picture of the carbon cycle between the atmosphere, oceans, biosphere, and geosphere.
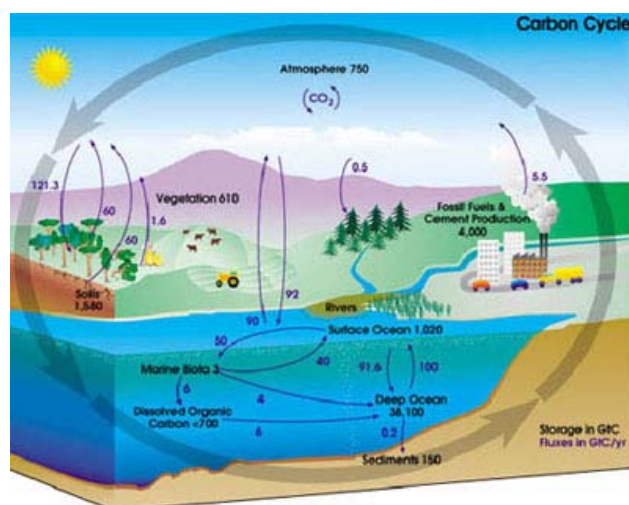
Figure 3.9 - The global carbon cycle. Pools (in black) are gigatons (1Gt = 1x10^9 Tons) of carbon, and fluxes (in purple) are Gt carbon per year.

This cycle consists of several storage pools of carbon (black text) and the processes by which the various pools exchange carbon (purple arrows and numbers). If more carbon enters a pool than leaves it, that pool is considered a *net carbon sink*. If more carbon leaves a pool than enters it, that pool is considered *net carbon source*.

The global carbon cycle, one of the major biogeochemical cycles, can be divided into geological and biological components. The geological carbon cycle operates on a time scale of millions of years, whereas the biological carbon cycle operates on a time scale of days to thousands of years.

3.6.1. The Geological carbon cycle

Since the formation of the Earth, geological forces have slowly acted on the global carbon cycle. Over long time-scales carbonic acid (a weak acid formed by reactions between atmospheric carbon dioxide, CO_2, and water) slowly combines with minerals at the Earth's surface. These reactions form carbonates (carbon-containing compounds) through a process called weathering. Then, through erosion, carbonates are washed into the ocean where they eventually settle to the bottom.

This cycle continues as seafloor spreading pushes the seafloor under continental margins in the process of subduction. As seafloor carbon is pushed deeper into the Earth by tectonic forces, it heats up, eventually melts, and can rise back up to the surface, where it is released as CO_2 and returned to the atmosphere. This return to the atmosphere can occur violently through volcanic eruptions, or more gradually in seeps, vents, and CO_2-rich hotsprings. Tectonic uplift can also expose previously buried limestone. One example of this occurs in the Himalayas where some of the world's highest peaks are formed by material that was once at the bottom of the ocean. Weathering, subduction, and volcanism control atmospheric carbon dioxide concentrations over time periods of hundreds of millions of years.

3.6.2. The Biological carbon cycle

Biology plays an important role in the movement of carbon between land, ocean, and atmosphere through the processes of photosynthesis and respiration. Virtually all multi cellular life on Earth depends on the production of sugars from sunlight and carbon dioxide (photosynthesis) and the metabolic breakdown (respiration) of those sugars to produce the energy needed for movement, growth, and reproduction. Plants take in carbon dioxide (CO_2) from the atmosphere during photosynthesis, and release CO_2 back into the atmosphere during respiration through the following chemical reactions:

$$C_6H_{12}O_6 + 6O_2 \rightarrow 6CO_2 + 6\,H_2O \quad \text{(a)}$$

$$(3.19)$$

$$6CO_2 + H_2O + hv \rightarrow C_6H_{12}O_6 + 6O_2 \quad \text{(b)}$$
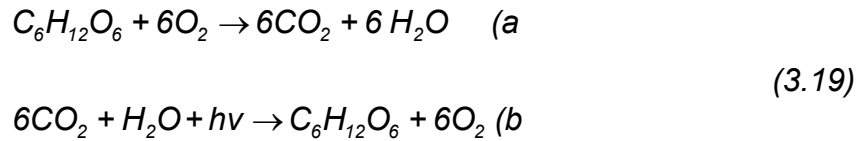
The *(3.19)*a is the reaction related to respiration, while the *(3.19)*b is for the photosynthesis. The effect of these two processes is reflected in the seasonal variation of the atmospheric CO_2 concentrations (Figure 3.10).

Recently, both short- and long-term measurements of atmospheric CO_2 levels have been studied. Charles Keeling, an oceanographer at the Scripps Institute of Oceanography, is responsible for creating the longest continuous record of atmospheric CO_2 concentrations, taken at the Mauna Loa observatory in Hawaii. This data (now widely known as the "Keeling curve," shown in Figure 3.10) revealed that human activities are significantly altering the natural carbon cycle.
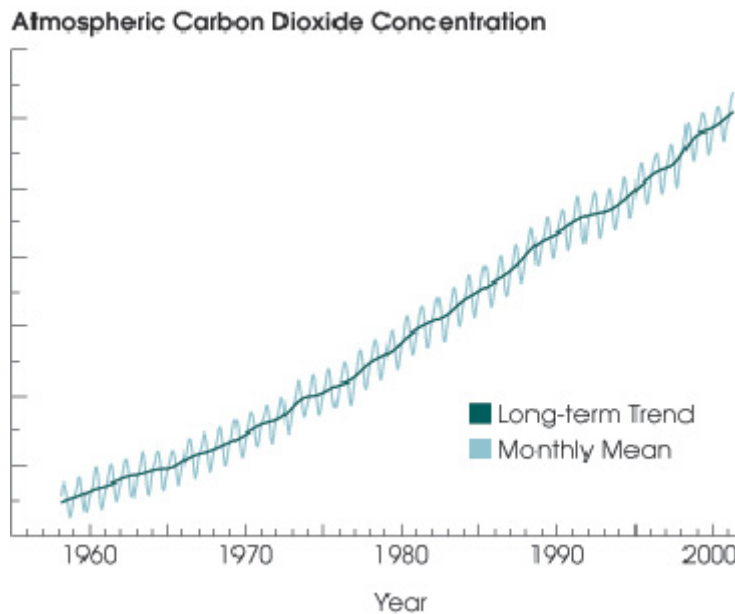
Figure 3.10. The "Keeling curve," a long-term record of atmospheric CO_2 concentration measured at the Mauna Loa Observatory (Keeling et al.). Although the annual oscillations represent natural, seasonal variations, the long-term increase means that concentrations are higher than they have been in 400,000 years. Graphic courtesy of NASA's Earth Observatory.

3.7. The special conditions of the Antarctic ozone hole

During the polar night, air temperatures fall as low as -80 ^{o}C. Under these conditions, the small amount of water and nitric acid present in the stratosphere freeze making nitric acid trihydrate and form polar stratospheric ice clouds. Five key conditions can now come together (Figure 3.11):
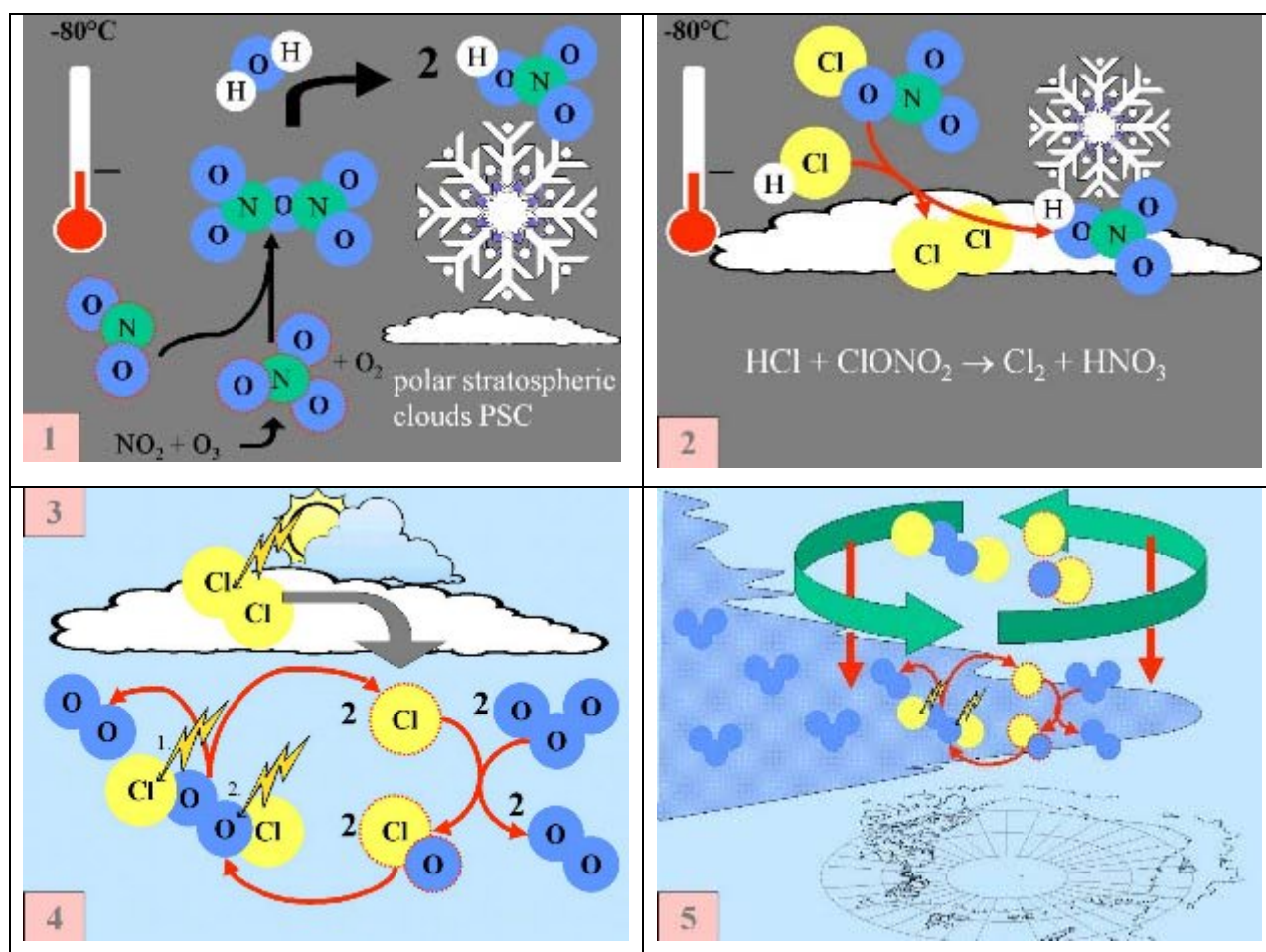
Figure 3.11 - Special conditions and chemistry in the ozone hole formation.[1])

Nitrogen oxide (NO) and nitrogen dioxide (NO$_2$), (which help to convert ClO into HCl, as shown above), are removed from the stratospheric gas phase through the reactions:

$$NO + O_3 \rightarrow NO_2 + O_2$$
$$NO_2 + NO_3 + M \rightarrow N_2O_5 + M$$
$$N_2O_5 + H_2O \rightarrow 2HNO_3$$

(3.20)
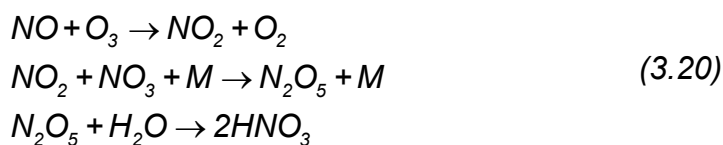
The end product is nitric acid HNO_3 which is incorporated into the polar stratospheric clouds (PSC).

2) HCl and $ClONO_2$ react with each other on the surface of the polar stratospheric clouds to produce Cl_2 and HNO_3. This nitric acid is immediately incorporated into the ice particles of the cloud.

3) When the sun rises at the end of the polar winter, Cl_2 is broken down by solar radiation to produce two chlorine (Cl) radicals.

4) If there are no nitrogen oxides present, the chlorine radicals start the catalytic chain of reactions *(3.5)*, leading to ozone destruction.

5) Normally chlorine species as Cl, ClO, and Cl_2O_2 are formed and concentrated in the upper stratosphere whereas ozone is found more in the lower stratosphere. Experts thought that ozone and ozone destroying chemicals would, therefore, only come together in border zones. As a result, ozone levels were not expected to decrease significantly although concentrations of chlorine containing compounds were rising in the stratosphere trough to the main global tropospheric circulation. However the polar vortex was not considered. This meteorologically stable vortex, (circumpolar wind) with the pole nearly at its centre, transports air rich in chlorine from the upper stratosphere to the lower stratosphere rich in ozone, allowing significant ozone destruction to occur.

All five conditions have to come together, to form the ozone hole. This is why the major ozone depletion occurs only over the poles (mainly Antarctica) and only in the spring as soon as the Sun rises after the polar winter.

Later in the year as the air temperatures increase, the polar clouds melt, nitrogen oxides become available again, the vortex breaks down preventing transport of reactive chlorine species to the lower stratosphere and the ozone layer recovers.

4. Differential Optical Absorption Spectroscopy

4.1. Introduction

In the last years, the problem of the analysis and monitoring of the air quality have assumed a remarkable importance. Some "Remote Sensing" techniques have been proposed allowing for the simultaneous measurements of different atmospheric compounds.

Among these the DOAS ("Differential Optical Absorption Spectroscopy")[42] undoubtedly occupies a chief place since it provide information simultaneously over different atmospheric compounds – mainly gases). It is also of simple use and contained costs. Such technique can be applied for the retrieval of the medium concentrations of the polluting agents in the troposphere. This is one of the most interesting and innovative methods for the monitoring of areas with high anthropic activity. Moreover, DOAS can be adopted for the measurements of the minor compounds in the stratosphere, with the aim for example to monitor and to study the so-called "ozone-hole".

In this chapter the birth of the DOAS and its evolution will be presented, together with the positive and negative aspects that the methodology offers.

4.2. Hints on the main spectrometric sense remotely

The monitoring of the atmospheric compounds through remote sensing (*rs*) techniques have always had great consensus, since they concur to obtain information generally more representative than those obtainable from the conventional nets of monitoring. In fact the rs techniques supplying a spatial distribution of the information beyond the temporal one, allow to strongly reduce the perturbations due to the small spatial scale of measurements obtained by the "in situ" sensor. Between the advantages of a remote sensing system, the main ones are:

- "the not-invasive" technique of monitoring, that is, it does not produce any chemical or physical alteration on the medium under examination;

- the utilization of both satellite and "ground based" measurements, though the second ones have best performance for studying the low atmosphere.

Usually, the remote sensing techniques are based on the interaction between a wave and the medium under examination; for example there are systems, like the SODAR, using the acoustic waves for the measurements of wind profiles and temperature; and systems that employ electromagnetic waves, as the RADAR, that exploits the radio-waves for the measurements of the particles distribution in

air, and the DOAS, that analyzing the visible and the ultraviolet radiation is able to get information about the absorption of some atmospheric trace gases.

Among the remote-sensing techniques, the spectro-photometric ones have always a number of applications in the field of the trace gas monitoring and in surveying the processes of transport and of atmospheric chemistry, mainly for the very low detection limits (until the 0.1 ppt) and high specificity in the direct determination of a component.

The rs techniques can be distinguished in two categories based on the type of the source employed:

the system is of 'passive' type if natural sources are used, as the radiation coming from the sun, the moon or the stars, or of the 'active' type if it uses artificial sources (lamps).

Moreover, the measure can be of the type ' line-integral' (in this case it supplies the value of the integral of the concentration along the measurement path and can be obtained both with "Active" and with "Passive" systems) or 'range-resolved' (supplying the spatial distribution of the concentration of gases in examination and can be obtained, only with active systems).

The total picture of the spectroscopic systems is very wide, so only some of them, the most innovative, will be illustrated; one of the currently more interesting spectroscopic techniques is the FT-IR("Fourier Transform Infrared Spectroscopy"); it allows for the simultaneous measurements of many gases, however its insufficient spectral resolution cannot avoid interference phenomena, particularly in spectral regions of great interest such as those where the absorption of CO_2 and H_2O is higher. The sensitivity of this system is not high, which limits the FT-IR to be suitable to measure in relatively polluted atmospheres. However, it has the ability to monitor complex molecules and to find the presence of species not foreseen [43]. Besides the FT-IR technique, there is another one of great interest operating in the infrared spectral region, the TDLAS ("Tunable Diode Spectroscopy Laser"); it has an extremely high spectral resolution and, consequently, a remarkable specificity. It is used mainly in the 'in situ' systems; in particular the compactness and instrumental mobility allow them to obtain measurements on ships and airplanes. However, it presents the disadvantage of monitoring only the concentrations of species of which the presence is already known and it is not capable to measure more than one gas at the same time.

Between the most sophisticated techniques, of great effectiveness but of elevated cost, there are those that employ the laser, like the LIS ("Laser Induced Spectroscopy"); it has a high sensibility and a good specificity, however it is not a universal method like the others since a different mechanism of excitation must be employed for each investigated species. Moreover, this method is very complex

(under an operative point of view) and demands the continuous presence of operators .

Another class of "rs" optical detectors to remote sensing with very high performances uses the LIDAR ("Light Detection And Ranging"). This technique allows for the monitoring of a 'ranges-resolved' extended zone giving a complete spatial distribution of the particle concentration in the atmosphere. Using two or more laser resonance wavelengths a DIAL ("Differential Absorption Lidar") system can be obtained. The DIAL combines the advantages of the radar in remote sensing to the chemical specificity of the spectroscopy and to the high spectral resolution of the laser constituting one of the most sophisticated techniques. However, the very high costs limit the use of this technique [44].

The use of conventional sources of light emitting especially in the visible and in the ultraviolet spectral regions is to the base of the DOAS ("Differential Optical Absorption Spectroscopy"); this technique does not have the same performances as the 'range resolved' ones like the LIDAR or the DIAL and it is not a universal method like the FT-IR. However a discreet number of gas molecules can be monitored at the same time with good specificity [43], [44]. Particularly the DOAS may be used either to measure the columnar content of atmospheric minor compounds or to monitor the pollution in cities and industrial areas. Moreover, the DOAS has a relative simplicity and flexibility. A sophisticated procedure of data analysis, which consists in the de-convolution of the atmospheric spectral data, allows to diminish the interference of other absorbers along the measurement path.

4.3. Origin of DOAS

Gordon Dobson pioneered during the '30, the basic idea in designing the famous Dobson Spectrophotometer for the monitoring of the total ozone in the atmosphere. The total atmospheric abundance of O_3 can be derived from a measure of the relative intensities of the solar light at 2 (or more) UV wavelengths.

The Differential Optical Absorption Spectroscopy (DOAS) is a relatively recent methodology since it has been introduced in the middle of the seventy's by J.F.Noxon for measurements in the stratosphere [5], [20]. In the first experiments, in the August of 1975 at the Fritz Peek Observatory (Colorado), Noxon carried out measurements of NO_2 making a comparison between solar spectra that suffered the atmospheric extinction with others spectra obtained in different conditions where the atmospheric extinction was negligible. Afterwards the DOAS analysis was extended to a large variety of tracers such as O_3 and $OClO$, NO_2, BrO, HNO_2. These last species are closely connected with the stratospheric photochemistry of O_3 [21], [22], [45].

The use of DOAS for the study of the tropospheric gases goes back to the end of the seventy's and was done by U.Platt and D.Perner. With their first observation of CH_2O, O_3 and NO_2 in marine and rural areas in the north of Europe they have opened an ulterior field of applications that have known a remarkable development in the following years [44], [46] - [50]. Their system was constituted by a source of light and a spectrometer placed at a variable distance ranging from 5 to 10 Km depending on the visibility; the light beam was focused with a spherical mirror on the entrance slit of the spectrometer and a mechanism for the grating displacement allowed for the analysis of the whole UV-Vis spectrum in consecutive windows of 13 nm each. In recent years the DOAS application to spectrometric systems equipped with the most advanced image sensors (CCDs), has remarkably increased the potentialities of the technique increasing the interest of many scientists.

Presently the DOAS methodology represents one of the most promising spectrometric technique for the tropospheric pollution control, as well as for the analysis of the minor compounds in the stratosphere. WMO ("World Meteorological Organization") and EPA ("Environmental Protection Agency") are considering the possibility of including DOAS among the reference techniques used for the environmental monitoring. Therefore the request for DOAS systems is increasing and in different research centers the theoretical and applied studies for the development of the technique and for improvements of the equipments are still on going.

4.4. DOAS: General Description

The DOAS technique is based on the absorption of the UV-Vis radiation from the minor compounds of the atmosphere, along an optical path that can extend from hundred meters to many kilometers.

As remembered in § 4.2, the remote sensing measurements can be obtained in two main configurations:

a) in the "passive mode" if natural sources are used, as the radiation coming from the sun or the moon

b) in the "active mode" if artificial sources (as lamps) are utilized as source of radiation.

Therefore if the DOAS algorithms are applied to spectral measurements obtained with remote-sensing systems (typically spectrometers) operating in the "active mode", it allows for the determination of average concentrations of compounds along the optical path linking the source and the light receptor. If DOAS is applied to measurements obtained in "passive mode" the results are values of columnar concentrations of tracers in the atmosphere.

The possibility to operate both in active and in passive configuration, requires different methodologies. Since the second part of this doctorial work is focused on the application of the DOAS to spectral measurements obtained in the "Passive mode", this last will be described in detail in the following paragraphs; however both methods have the same theoretical basis.

The main advantages of the DOAS technique are:

- the UV-Vis DOAS can be used for the monitoring of several gases of great interest for the atmospheric photochemistry as O_3, NO_2, OClO, SO_2, BrO, H_2O, CH_2O, OH and some aromatic hydrocarbons (CxHx); in particular it allows for the measurements of important gaseous species playing a key role in the troposphere (as HONO and NO_3) that cannot be monitored with sufficient sensibility using other techniques due to their low atmospheric concentrations [38];

- the UV-Vis DOAS, even applying the Lambert-Beer law, works on 'differential' absorption spectra; therefore it does not require the spectrum before being attenuated by the absorbers along the measurement path [46];

- opposite to the measurements obtained with the traditional 'is situ' analyzers, the remote-sensing systems, including DOAS systems, give average concentration values along the measurement path with a better description of the behaviour of the gases under examination and allowing for the decrease of the low scale fluctuations due to processes of local turbulence;

- the DOAS allows for the detection of species not easily identifiable, analyzing the absorption features of the DOAS algorithms residual;

- the relative conceptual simplicity and the limited costs compared to other remote-sensing systems, (LIDAR, FT-IR etc.) allows for its use not only in focalized research programs (as the study of the ozone depletion in the stratosphere), but also in the monitoring of the pollution in the troposphere;

- the UV-Vis DOAS, correlating one atmospheric spectrum with the series of the absorption coefficients (Cross Section - CS) of one gas, provides an 'absolute' measurement, therefore the complicate and sometimes inaccurate calibration procedures are not requested.

To the undoubtedly favorable characteristics above described, the UV-Vis DOAS opposes some limits that influence considerably the measurements, among which the main ones are:

- when measuring the diffused solar light, the scattering of the atmospheric particles, often provoked by fog and smog along the path, cause a remarkable attenuation of the source intensity;

- the overlapping of different species on the same spectral series;

- the precision with which the absorption coefficients are measured is the main factor in the determination of the accuracy of the DOAS methodology;

- the presence of radiation that does not belong to the spectral interval under analysis (the so-called 'stray light') limits the total resolution of the spectrometer, even if the 'stray light' can be reduced using band-pass filters;

- the aging of the lamp (in case of use in 'active mode') is responsible for the drift in time of the reference spectrum of the artificial source.

In conclusion the UV-Vis DOAS systems do not provide the information of IR interferometric systems. However they can furnish systematic and reliable measurements of different gas species at the same time with a simple method and relatively low costs.

4.5. The theoretical aspects

In chapter 2, (equation *(2.13)*) the Lambert-Beer law is presented:

Since DOAS is based on the previous law, in the following paragraphs some theoretical considerations allowing for the derivation of the so-called "DOAS-Master Equation" will be presented.

A collimated bundle of radiation passing trough a gas layer in the atmosphere is be in part absorbed by the interaction of the energy with the gaseous particles. Therefore the entering radiance I_λ in output is modified in $I_\lambda + dI_\lambda$ where the variation is proportional: i) to the density (ρ) of the gas layer (in particles number per volume units), ii) to the covered distance (ds), iii) to the extinction coefficient – extinction cross section σ_λ. (absorption and scattering) of that gas. Therefore:

$$dI_\lambda = -I_\lambda \chi_\lambda \rho d\ell$$

(4.1)

a positive contribution to the outgoing radiation can be given by the emission of the medium and by the multiple scattering that can bring back on the original way what has been previously spread.

Defining a source function J_λ it is therefore obtained:

$$\mathrm{d}I_\lambda = -\chi_\lambda \rho I_\lambda \mathrm{d}s + \chi_\lambda J_\lambda \rho \mathrm{d}s$$

(4.2)

that is the general equation of the radiative transfer.

It has to be noted that any contribution is wavelength dependent, therefore such relation is worth correctly for monochromatic radiation.

4.5.1. DOAS – Master Equation

The source term J_λ in *(4.2)* is negligible, due to the fact that the emission of the atmosphere and the multiple scattering are minor phenomena; in particular the multiple scattering is of two orders of magnitude less important than absorption. In this assumption equation *(4.1)* is a good approximation and it can be integrated along the path $0 - S_1$:

$$I_{\lambda,S_1} = I_{\lambda,0} \exp\left(-\int_0^{S_1} \sigma_\lambda \rho \mathrm{dl}\right) \qquad (4.3)$$

Therefore, defining the monochromatic optical thickness τ_λ as:

$$\tau_\lambda = \int_0^{S_1} \sigma_\lambda \rho \mathrm{ds} \qquad (4.4)$$

With
σ_λ = absorption cross section of the gas
The Lambert-Beer law is obtained,

$$I_{\lambda,S_1} = I_{\lambda,0} \exp\left(-\tau_\lambda\right) \qquad (4.5)$$

Where, as in the *(2.13)*:
$I_{\lambda,0}$ = intensity of the incident monochromatic radiation;

I_{λ,S_1} = intensity of the light transmitted through the gas layer;

From an experimental point of view: I_{λ,S_1} is the radiance that reaches the instrument (typically a spectrometer), after passing through the atmosphere. The electromagnetic radiation measured by the equipment, has a different trail in the atmosphere. Trying to model this aspect, a single path, representing the entire bundle, is considered[2]. Such path is a function of the density profile of each absorber, of the wavelength and of the Solar Zenith Angle and it is indicated with $S_\rho(\theta,\lambda)$. Then, fixing λ, ρ and θ, *both σ_λ as well as* $S_\rho(\theta,\lambda)$ are determined.

---

[2] *The criteria for the choice of the path will be explained (cfr § 4.6.4) with the Intensity Weighted Optical Path (IWOP) theory.*

Assuming σ_λ independent from the path (that is a reasonable assumption considering that the atmosphere is homogeneous), from relations *(4.4)* and *(4.5)* :

$$Ln\left(I_{\lambda,0}/I_\lambda\right) = \sigma_\lambda \int_{S_\rho(\theta,\lambda)} \rho \, ds \qquad (4.6)$$

The integral term in the right side of the equation *(4.6)* is defined as Slant Column Density (SCD(θ,λ)) that is the content of the investigated specie(s) along the measurement path:

$$SCD(\theta,\lambda) = \int_{S_\rho(\theta,\lambda)} \rho \, ds \qquad (4.7)$$

The term on the right side of the equation can be replaced considering the additive effect of each gas that contributes to the radiance attenuation:

$$Ln\left(I_{\lambda,0}/I_\lambda\right) = \sum_g \sigma_\lambda SCD(\theta,\lambda) \qquad (4.8)$$

Applying strictly this relation in order to retrieve the SCD, the main problem is the knowledge of the reference spectrum ($I_{\lambda,0}$), since the reference spectrum should be measured at the top of the atmosphere with the ground based equipment utilized for the I_λ measurements. Due to the difficulty to obtain such measurement, the spectrum measured at the local noon when the optical thickness is the smallest one[3], can be considered a reference spectrum

The different gases are identified thanks to their absorption cross sections, characteristic for each atmospheric compound. The low frequency (the linear or polynomial tendencies) of the various absorption spectra can be removed from the relation *(4.8)* with a high pass filter operator, providing the following relation:

$$Ln\left(I_{\lambda,0}/I_\lambda\right) - \overline{Ln\left(I_{\lambda,0}/I_\lambda\right)} = \sum_g \sigma_{\lambda g} SCD_g\left(\theta,\lambda\right) - \overline{\sum_g \sigma_{\lambda g} SCD_g\left(\theta,\lambda\right)} \qquad (4.9)$$

where the superscript represents the high pass filter operator removing the low frequency features of the spectral series. This 'filtering' operation is made in the

---

[3] *See § 6.2.2 for the description of the rules of the reference spectrum on the SCD retrieval*

wavelength domain, and the SCD is calculated as the averaged value ($SCD_{g,avg}$) over the spectral range under examination, therefore:

$$Ln\left(I_{\lambda,0}/I_\lambda\right) - \overline{Ln\left(I_{\lambda,0}/I_\lambda\right)} = \sum_g \Delta\sigma_{\lambda g} SCD_g(\theta) \qquad (4.10)$$

Where the filter operator is applied directly to the cross section of the absorbers ($\Delta\sigma_{\lambda g} = \sigma_{\lambda g} - \overline{\sigma_{\lambda g}}$), that is also called the 'differential' term. The *(4.10)* is called "DOAS Master Equation".

The main advantage of this approach is that, since the DOAS algorithm works on the 'differences', the measured spectral series do not have to be calibrated in intensity, but only in frequency (a misalignment of some Angstrom - 1Å = 10^{-1} nm - can introduce large errors in the retrieved values).

4.6. A model for the simulation of the radiative transfer in atmosphere

The solutions of the DOAS-Master-Equation are the Slant Column Density - SCD (molecule/cm^2) of the absorbers showing marked absorption features in the investigated spectral range. In order to obtain the actual Vertical Column Density (Total Column or VCD) of the analyzed species, more aspects have to be considered. Such measurements (the Slant Column Density), even being actual data of the absorber's concentration, require the use of a radiative Transfer Model (RTM) for their interpretation. In fact, the total columns are used for comparison and validation of the results. In order to convert the SCDs to VCDs it is necessary to estimate, using a RTM, the Air Mass Factor (AMF), that is the increase of the radiation along the optical path of measurements (oblique) compared with the vertical one. Such type of model for the interpretation of the ground based UV/Vis measurements has been used since the '80 [45] and subsequently improved with the addition of other atmospheric physical effects like the aerosol effects and the scattering [51]. The model used in this work, AMEFCO (Atmospheric Model for Enhancement Factor COmputation), has been developed at ISAC Institute and it is based on the IWOP (Intensity weighted Optical Path) approach [52]. An accurate description of the model is found in [21] and [53].The AMEFCO model is classifiable in the category of ray tracing models, that is, the path of the radiation is followed in every atmospheric shell, of variable thickness, and the extinction of the radiation along the path is calculated in order to obtain, as a function of the altitude,

a weighted function for the computation of the most probable path over which the AMF is estimated.

4.6.1. Definition of AMF and Geometric aspects of the model

As stated in *(4.7),* the Slant Column Density of a gas is:

$$SCD_g\left(\theta,\lambda\right) = \int_{S_g(\theta,\lambda)} \rho_g\left(z\right)\mathrm{d}s \qquad (4.11)$$

where the integral is extended to the geometric path $S_g\left(\theta,\lambda\right)$ of the radiation, and where the subscript g indicates the dependency of the gas under investigation from the vertical profile (see formulas *(4.21)* and *(4.24)*), while the Vertical Column is

$$VCD_g\left(\theta,\lambda\right) = \int_0^{Zt} \rho_g\left(z\right)\mathrm{d}z \qquad (4.12)$$

where Z_t is the top of the atmosphere.

The Air Mass Factor is defined as: $AMF = SCD_g/VCD_g$. Obviously the AMF is not constant, but it varies according mainly to three conditions:

i)   the profile of the gas in examination;

ii)   the Solar Zenith Angle (SZA or θ), since C_{sg} depends on the light path and therefore on the solar angle;

iii)   the spectral region where the measurements are obtained, since wavelength influences the light path.

Adding these conditions the AMF definition becomes:

$$AMF_g\left(\theta,\lambda\right) = SCD_g\left(\theta,\lambda\right)/VCD_g \qquad (4.13)$$

This parameter has to be calculated in order to obtain the total column of the analyzed compound; due to its complexity and variability it cannot be calculated analytically.

It is therefore necessary to have access to a model that describes the physics of the atmosphere from an optical point of view, both for the measurements of the light path at the variation of the SZA, as well as for the evaluation of the scattering processes depending on the wavelength. The model has also to take into account the vertical distribution of the absorbers in order to calculate the extinction of the radiation due to the gas absorption.

Such models already exist [54], [55]. Due to their complexity, they are subject to modifications and improvements.

Figure 4.1 illustrates the geometric model of the atmosphere considering it structured as spherical shells of 1 Km thickness.
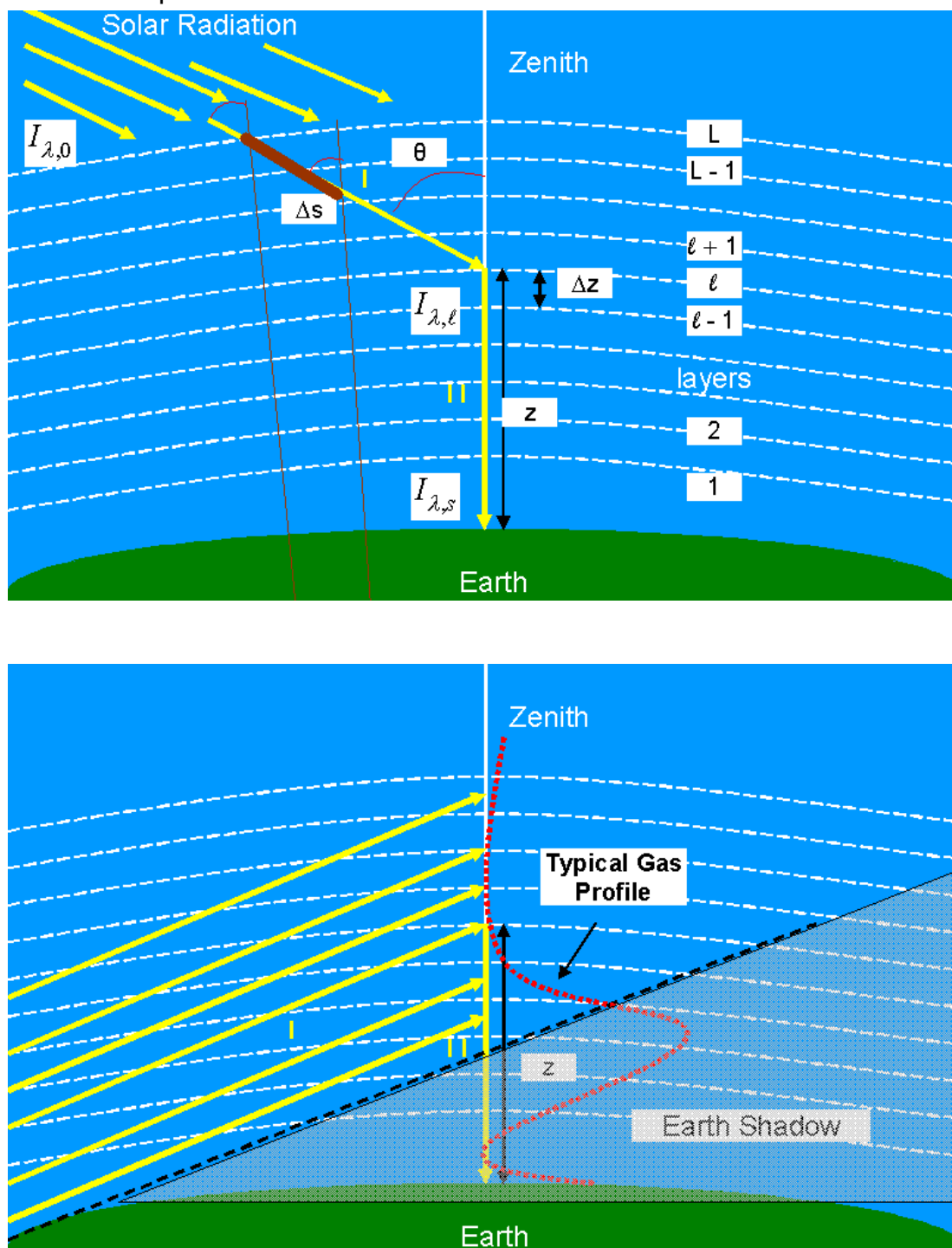
Figure 4.1 – Path of the radiation along the vertical direction for SZA<90° (upper panel) and for SZA>90° (lower panel)

From the geometric point of view, the first step is to find the relation between ds and the dz, that is, maintaining the symbolism previously used, the two parameters of integration on the slant path and the vertical one. The integrals are reduced to sums where the step is the thickness of the shells (1km). Δz is 1km and Δs is obtained through a simple recursive geometric relation by using the theorem of Carnot. For SZA greater than 90°, it has to be noted that the presence of a cone of shadow prevents the bundle to reach directly the lower layers. The minimal layer where the light is scattered is called MSL (Minimum Scattering Level) and is given by:

$$MSL = R_t \left(1/\cos(\theta - 90°) - 1 \right)$$

(4.14)

with R_t = radius of the Earth.

For θ = 93°, MSL is approximately 9 km that is almost all the troposphere is in shadow over the vertical direction. Therefore any gas below that altitude will scatter the radiation towards the instrument and along the path II (Figure 4.1) the absorption will be limited due to the short path and also to the low NO_2 and O_3 concentration in this trail.

4.6.2. The Extinction's processes

In order to simulate the absorption, the spectral series of the absorption cross section of the atmospheric constituents have to be known and relation *(4.8)* have to be applied to evaluate the produced attenuation. The scattering, instead, is a more complex phenomenon that has different behaviors depending on the ratio between the wavelength (λ) and the dimension (d) of the scattering particle.

In the condition $\lambda \ll d$, Rayleigh scattering is obtained. Therefore, given a medium with a refractive index n, density N (in molecules/cm^3), and incident radiation at wavelength λ,[56]:

$$\sigma_R(\lambda, \varphi) = \frac{\pi^2 (n^2 - 1)^2 (1 + \cos^2 \varphi)}{2N\lambda^4}$$

(4.15)

where σ_R has the dimensions of an area (m^2)

Obviously in the calculation of the extinction the radiation is considered moving in the same direction, therefore $\varphi = 180°$ and only the dependency from λ is kept. The extinction coefficient is:

$$\varepsilon_R(\lambda) = \sigma_R(\lambda) C_{AIR}$$

where C_{AIR} is the concentration of air molecules ($2.4 \times 10^{19} cm^{-3}$ in STP).

When $\lambda \gg d$ the Mie scattering is achieved; in the atmosphere this is mainly due to aerosols and clouds.

However, other models have demonstrated that the variation is limited to a 3% and the tendency is the increasing of the AMF since an extinction phenomenon is added. Solomon and Perliski [51] evidenced meaningful differences ($\sim 20\%$) only for tropospheric gases (O_4, H_2O etc.).

For the Mie scattering, the extinction coefficient can be considered of the order of [57]:

$$\varepsilon_M\left(\lambda\right) \approx \lambda^{-1}$$

Therefore the equation *(4.8)* can be rewritten as:

$$Ln\left(I_{\lambda,0}/I_\lambda\right) = \sum_g \sigma_{\lambda g} SCD_{sg}\left(\theta,\lambda\right) - \varepsilon_R\left(\lambda\right) - \varepsilon_M\left(\lambda\right) \qquad (4.16)$$

Typical values of the extinction coefficients of Rayleigh and Mie at 300 nm are $1.3 \cdot 10^{-6}$ cm^{-1} and $1\text{-}10 \cdot 10^{-6}$ cm^{-1}.

4.6.3. The refraction and the multiple scattering

In the calculation of the AMF, two more processes have to be considered: the refraction (for the strong relation between AMF and Solar Zenith Angle) and the multiple scattering.

 Regarding the refraction, a simple application of the Snell's law to spherical geometry gives:

$$R_t n_0 \sin\theta = \left(R_t + z\right) n \sin\beta \qquad (4.17)$$

where R_t is the Earth's radius [56]; the angular deviation between the solar angle of incidence at the top of the atmosphere (β), and that one apparently observed at the ground (θ), where z is the altitude of the first deflection, n respective refractive index and n_0 refractive index to the ground

Therefore the angle θ is:

$$\theta = \arcsin\frac{\left(R_t + z\right) n \sin\beta}{R_t n_0} \qquad (4.18)$$

With the aim of evaluating the influence of the atmospheric refraction on the AMF calculation, the approximated formula for the refractive index can be used [58]:

$$n = 1 + 77.6\left(1 + 7.52 \cdot 10^{-3} \lambda^{-2}\right) P/T \cdot 10^{-6} \qquad (4.19)$$

Where P and T are the standard pressure and temperature profiles respectively for the mid-latitudes during summer from the UVSPEC model [59][60]

In the spectral range 200-500nm, the variation of the ratio $n/n_0 \approx 0.9997$. In order to evaluate the deviation of the refracted SZA (θ_r) observed at the ground, from the SZA not refracted (θ_{nr}), fixing z=70 km, $(R_t + z)/R_t \approx 1.010$ and $\theta_{nr} = 90°$, with some geometrical considerations $\beta \approx 82°$, and applying the *(4.18)* the result is $\theta_r = 89.1°$. This result is in agreement with other estimates [61]

A correction of the order of one degree (10^{-2} radians), over a path of approximately 1200 km would involve an increase of about 10 km in the same path. But the deflection is significant only when the bundle enters in troposphere, therefore for gases that presents a minimum concentration here, the optical thickness does not suffer considerable modification. Typical values for the NO_2 in the troposphere are 10^8 mol/cm^3, therefore the columnar content variations would be of approximately 10^{14} mol/cm^2 against the 10^{16} mol/cm^2 which is the total number of molecules in the column: This means a variation of 1% which is smaller than the error associated to the measurements.

For angles greater than 90° the relation *(4.18)* is not valid anymore. However, it can be estimated that, at 94°, the correction is of the order of some degrees (3°-4°) that is, an increase of the path length of 50 km due to refraction assuming similar considerations made for the previous case. Therefore, for the considered gaseous species, this phenomenon can be neglected. However there exist models which take into account the atmospheric refraction [51] and it turns out that the refraction becomes important for tropospheric gases as H_2O and O_4.

The reconsideration of the multiple scattering in the model for the AMF calculation would have the purpose to correct the approximation previously made in § 4.5.1. However, studies on other models [54], [55] have shown as the corrections for the multiple scattering are of the order of some percent only for angles greater than 90° and, once again, the effects are larger in the troposphere.

Since the main studies of this work are addressed to the stratosphere it has been decided not to consider the multiple scattering for the AMF calculation.

4.6.4. The mathematical model

Considering the layer ℓ (Figure 4.1), the down-welling radiation at that altitude ($I_{\lambda,\ell}$) is reduced due to the scattering of air molecules and due to the absorption of the atmospheric gases depending on their absorption cross sections. Therefore:

$$I_\lambda(\ell) = I_\lambda(0) \exp\left[-\sigma_R(\lambda) \sum_{i=\ell}^{L} N_a(i) \Delta s_i(\theta) - \sum_{g=1}^{n} \sum_{i=\ell}^{L} \sigma_g(\lambda) N_g(i) \Delta s_i(\theta) \right] \quad (4.20)$$

where:

$N_a(i)$: density of the air in the i shell (in molecules/cm^3);

$\Delta s_i(\theta)$: slant path depending on Solar Zenith Angle and Altitude;

$N_g(i)$: gas profiles;

$\sigma_g(\lambda)$: absorption cross section of the gas.

The relation *(4.20)* is the same as *(4.5)* where the contributions of the absorption and the scattering have been distinguished and where the integrals have been reduced to sums. The $I_\lambda(\ell)$ that can reach the instrument at the ground is only the part that, after having been scattered at the altitude $\ell\Delta z$, suffers a new attenuation along the vertical path (II in Figure 4.1). Therefore:

$$I_{\lambda,s}(\ell) = G(\lambda,\theta,\ell\Delta z) \exp\left[-\sigma_R(\lambda) \sum_{i=1}^{\ell-1} \rho_a(i) \Delta z - \sum_{g=1}^{n} \sum_{i=1}^{\ell-1} \sigma_g(\lambda) \rho_g(i) \Delta z \right] \quad (4.21)$$

With $G(\lambda,\theta,\ell\Delta z) = I_\lambda(\lambda)\sigma_R(\lambda) f(\theta) N_a(\lambda\Delta z)\Delta z$ that is the part of energy scattered along the vertical direction towards the instrument[4].

In the case $\theta > 90°$, the i index of equation *(4.20)* has to be extended to the slant path involving twice the layers symmetric to the tangent point of the bundle with the Earth surface. This operation has to be repeated for any value of ℓ, therefore the total energy reaching the sensor is:

---

[4] *For the Rayleigh scattering of unpolarized light, $f(\theta) = \frac{3}{4}(1+\cos^2(\theta))$ is the scattering phase function defining the fraction of the flux scattered towards the ground as function of the SZA*

$$I_{\lambda,s} = \sum_{\ell=1}^{L} I_{\lambda,s}(\ell) \qquad (4.22)$$

Now the problem for the calculation of the AMF is the choice of the path ($S_g(\theta,\lambda)$), among the different ones that the radiation can cover:

The scattering probability can be defined (that is the probability that the bundle scattered at a predefined altitude catches up the instrument) as:

$$p_\ell(\theta,\lambda) = I_{\lambda,s}(\ell)/I_{\lambda,s} \qquad (4.23)$$

This last satisfy the condition $\sum_\ell p_\ell = 1$. The relation *(4.23)* can be used in order to assign a weight to any path reaching the layer ℓ of the vertical line[5]

The AMF is obtained adding the gas profile in the sum (giving the slant column density) and dividing by the vertical column:

$$AMF_g(\theta,\lambda) = \left\{ \sum_{\ell=MSL}^{L} \left[\sum_{\gamma(\ell)} \Delta s_{\gamma(\ell)}(\theta) \rho_g(\gamma(\ell)) \right] p_\ell(\theta,\lambda) \right\} / \Delta z \sum_{\ell=1}^{L} \rho_g(\ell) \quad (4.24)$$

Where $\gamma(\ell)$ is the index along the path intersecting the vertical in the ℓ layer.

An important assumption has been made: the N_g and N_a are supposed to be the same along all the path (I and II in Figure 4.1); therefore during sunset or sunrise, in a path of approximately 1000km, the vertical distributions of air and gas molecules remain unchanged.

The classical formula for the AMF is the secant of the SZA which is valid for SZA<90° and assuming a plane parallel atmosphere. However, below 86° the disagreement with the model is lower than 10%; for SZA>86° the differences grow up to an exponential deviation

The Kasten's formula [62] takes into account the refraction and the Earth sphericity, but, as the previous one, the corresponding AMFs are different from the model because the dependency from the gas profile and wavelength are not considered

A full analysis of the effects on the AMF of the variations of the model parameters (θ,λ,l and ρ_g) can be found in [53].

---

[5] *This is the method of the Intensity Weighted Optical Path (IWOP)*

5. SPATRAM (Spectrometer for Atmospheric TRAcers Measurements)

5.1. Introduction

The development of the SPATRAM instrument (Figure 5.1) is the result of the collaboration between CGE-UE, ISAC-CNR and ENEA.
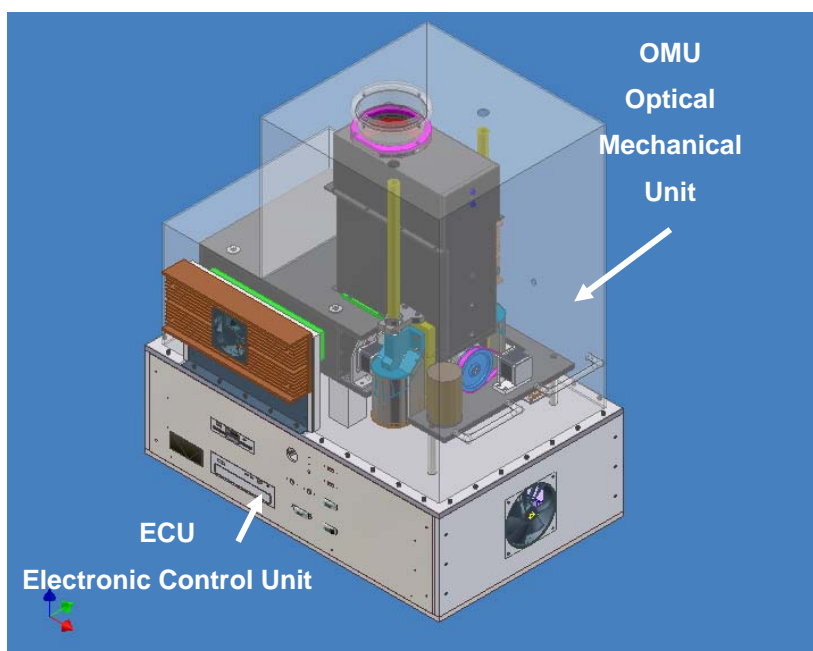
Figure 5.1 - SPATRAM instrument installed at CGE Observatory since April 2004

The "heart" of the SPATRAM – the monochromator, where the light is decomposed in its wavelengths – is based on the ones utilized in the GASCOD's type instrument [63] - [65]. GASCOD (Gas Analyzer Spectrometer Correlating Optical Differences) is a family of spectrometers developed at the ISAC institute in the last 15 years. Since the study of feasibility for the SPATRAM equipment started with the analysis of the GASCOD installed at Terra Nova Bay Station, a very brief description of the forefather of the developed instrument has to be done. The equipment consists of a 150 cm -f/5- Cassegrain telescope that focuses the incoming radiation onto the entrance slit of the spectrometer. This comprises a holographic spherical diffraction grating of 1200 grooves/mm and a multichannel detector featuring a 512 metal-oxide semiconductor diode array by Hamamatsu. The spectral dispersion is 2.4 nm/mm and the overall typical spectral resolution of about 0.5 nm. Figure 5.2 show the GASCOD3/3 installed at the Italian Antarctic Station since 1995 [66].
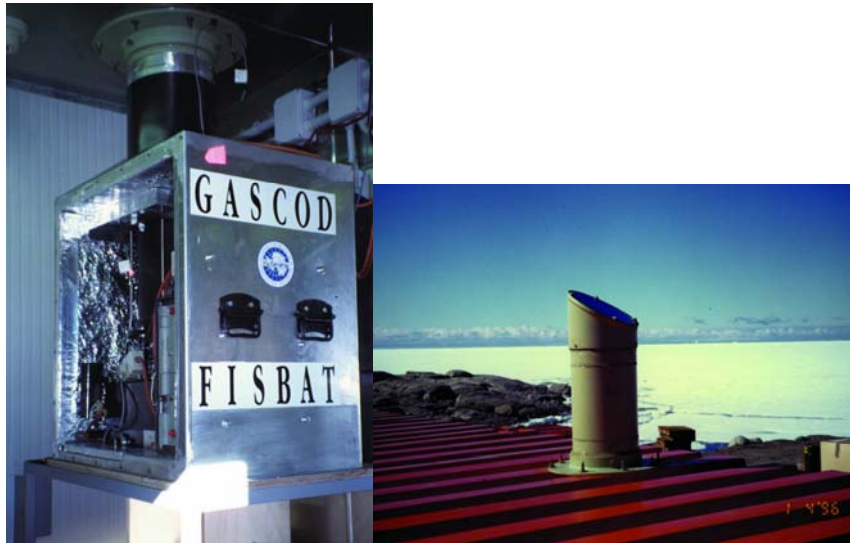
Figure 5.2 – GASCOD Spectrometer installed at the Italian Antarctic Station since 1995 (left), Optical chimney for the input of the radiation(right).

The optical design of the monochromator (entrance slit, grating and grating mount) is the only common feature of the two instruments. The main differences between the 2 instruments are found in the optical mount for the input radiation and in the use of a CCD Camera as detector instead of the CMOS utilized in the GASCOD. Furthermore, for the management of the SPATRAM, both the electronic unit as well as the software for the data acquisition were completely improved.

Since the physical principles of the grating are out of the scope of this doctorial work, but being the optic design and the grating mounts of the spectrometer monochromator of primary importance for a better understanding of the physics behind this optical instruments, Annex 1 includes the detailed explanation of the gratings laws.

5.2. OMU Optical Mechanical Unit

In the SPATRAM, the spectrometer is installed inside a thermostatic box able to keep the internal temperature within the working range of the instrument (typically 15°C for the Optical Mechanical Unit). The Electronic Control Unit (ECU), equipped with 1GHz CPU, drives the spectrometer both in automatic way and in an unattended mode according to predefined measurement cycles.

In the following paragraphs the structure and the components of the equipment will be presented and discussed in details.

In Figure 5.3 the Optical Mechanical Unit is shown and some of the components are highlighted:

the primary input for the radiation (also called Optic Tower)

the optic fiber inputs

the rotating mirror module for the selection of the desired input

the monochromator where the incoming radiation is dispersed

the ventilated box containing the CCD sensor

the modules for the thermoregulation of the OMU

Some other auxiliary devices as:

the interface between OMU and ECU

the switching power supply for the mercury calibration lamp
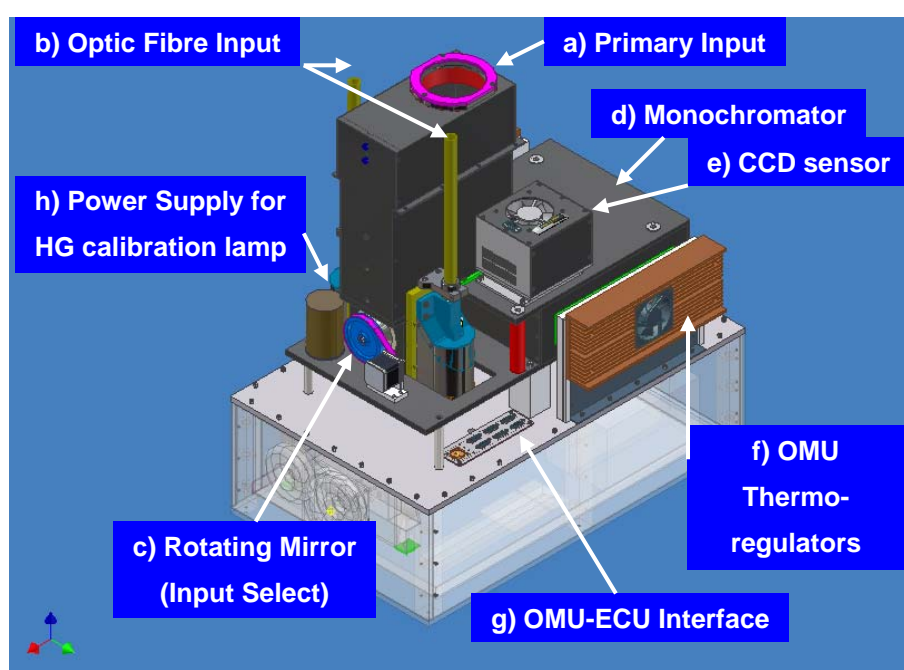
Figure 5.3 – Main modules in the Optical Mechanical Unit of the SPATRAM instrument

5.2.1. Primary Input

The Primary Input (Figure 5.4) is the default optic channel for the DOAS measurements carried out by the spectrometer. The light enter the instrument passing trough the quartz window (a).The light beam is reflected by the tilted flat mirror (b) over the spherical mirror (c) that focus the radiation on the input (d) of the rotating mirror module. The quartz window is placed in order to protect the optic parts contained in the optic tower. Moreover the features of transparency to the UV radiation of the fused silica allow the measurements of a wide spectral range (starting from 250 nm). If a normal glass has been utilized it should be impossible to have measurements above the 400 nm.

Instead of the classic Cassegrain telescope used in similar equipment, the "Optic Tower" described was preferred, mainly due to the low cost of realization, to the simple installation and also due to the relatively simplicity of the optical alignment.
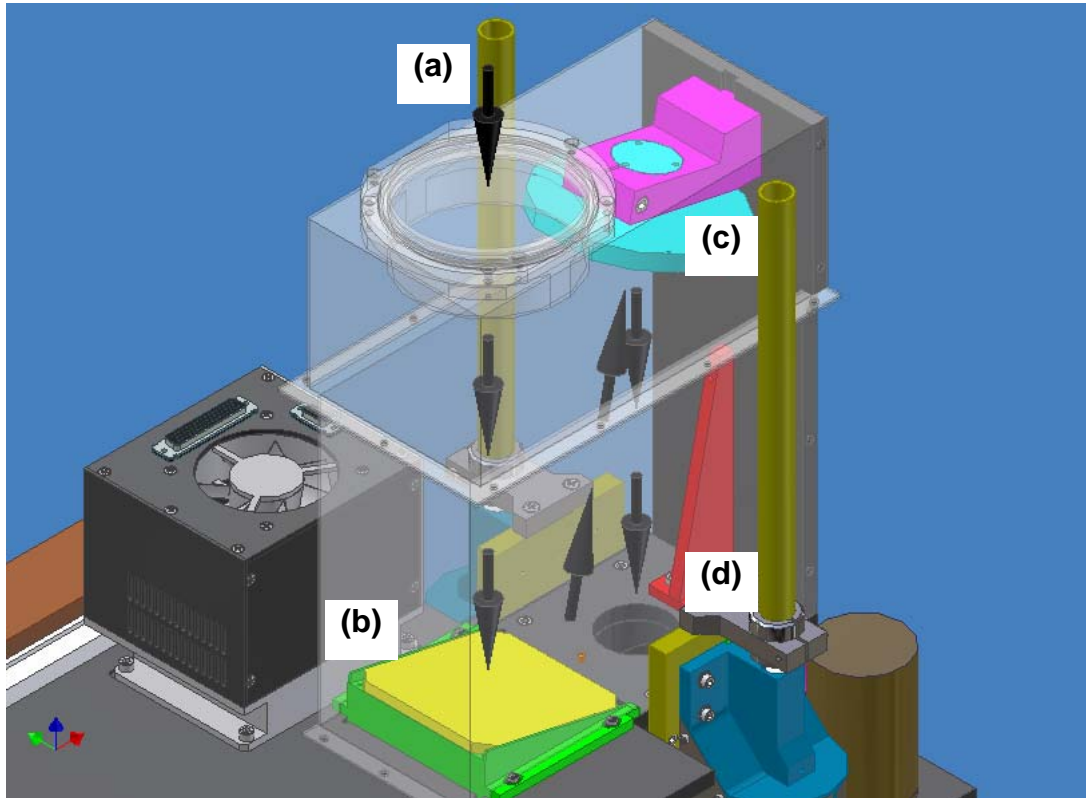
Figure 5.4 – SPATRAM Primary Input

The SPATRAM was not developed for routinely operations at the exterior, so an optical chimney, installed of the roof of the room\lab where the instrument works, could be provided to protect the whole equipment from the atmospheric conditions, namely rain, dew and frost.

5.2.2. Optic fibers input

The instrument is provided with two inputs via optic fibers (Figure 5.5) allowing for measurements in other geometric configurations depending on the type of the incoming device. These inputs are also useful when the primary input can not be used for direct measurements (i.e. when the optic chimney is not available)

Figure 5.6 – Optic Fibre Input adapted as incoming telescope.

Figure 5.5 – Optic Fibre Input

As for the primary input, the Optic fibre input is composed of 2 mirrors, but the first is a spherical mirror collecting the radiation coming from the optic fibre and focusing the light beam on the second flat mirror tilted at 45°, that send the radiation in the input of the rotating mirror module. Modifying the position of the spherical mirror, linking the optic characteristics of the spectrometer, the same optic system can be used as the telescope sending the radiation to the optic fibre input (Figure 5.6).

5.2.3. Rotating Mirror module

With a stepper motor that provide the desired position, the flat mirror tilted at 45° addresses the light beam, coming from one of the four available inputs, towards the entrance slit of the monochromator (Figure 5.7).

The four inputs are:

the vertical one (for measurements with the Primary Input)

the left and right ones (for measurements with the two Optic Fibers Inputs)

the lower one (for spectral or radiometric calibrations – see next paragraph)
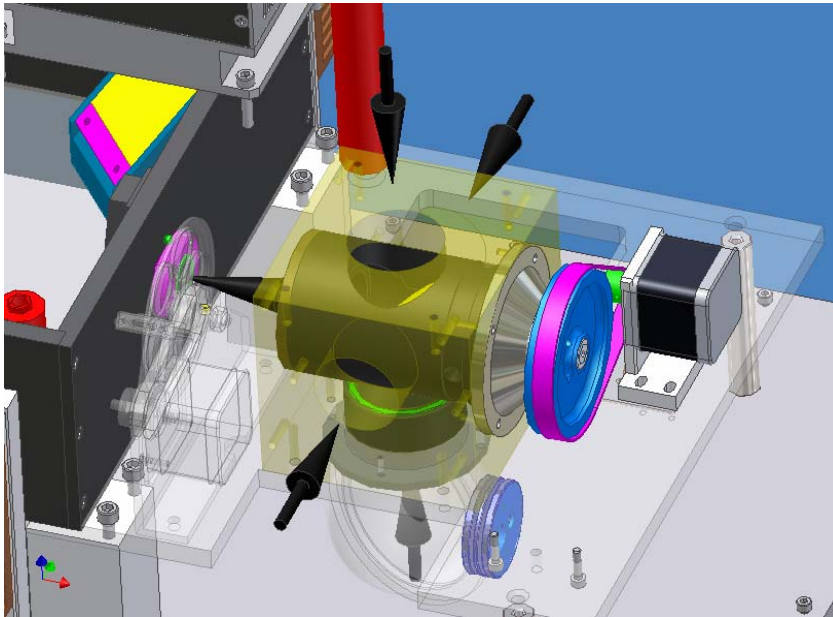
Figure 5.7 - Rotating Mirror Module

5.2.4. Calibration sphere and HG Calibration lamp's Power Supply

The calibration sphere (Figure 5.8) contains one low pressure mercury lamp that is a useful mean of calibrating the spectra in wavelength, and one halogen light source that produces an intense continuum spectrum from 400 nm to 2 microns used for radiometric calibration of the measured solar spectra.
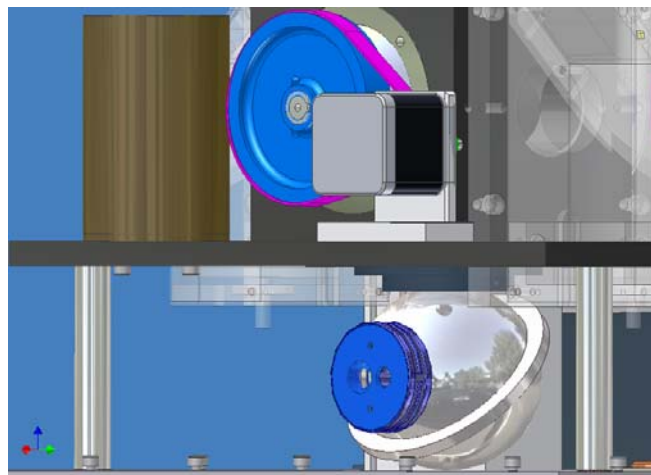
Figure 5.8 – Integration sphere and Power Supply for HG Calibration lamp

5.2.5. Filters wheel

The Filter Wheel (Figure 5.9) contains a set of band-pass filters (4) that have to be used in the different spectral intervals scanned by the SPATRAM, in order to select only the radiation belonging to the actual range of wavelengths. One Neutral density filter is also mounted in.

A band-pass filter has a transmission band surrounded by two blocking bands that allow only a portion of the spectrum to pass. These filters have broad spectral bandwidths in either the ultraviolet, visible, or infrared spectrums. The nearly black filters absorb visible radiation. They are perfect for ultraviolet or infrared detection applications.

Neutral Density (ND) filters appear gray in color and reduce the amount of light reaching the CCD camera. Since the transmission value only varies over a small percent in the visible, there is no effect on color balance. Instead of just stopping down the lens aperture due to high light levels, ND filters allow for wider apertures which can be used to decrease the depth of field. This allows the important information to be separated from the background. Compared to polarizing filters, ND filters are ideal for overall light reduction in cases of extreme light intensity. By stacking filters, it is possible to achieve other Optical Density (OD) values. All mounted filters can be threaded together with identical male and female threads on each mount. Optical Density exhibits an additive relationship; for example, stacking filters with OD values of 0.6 and 0.9 yields a resultant density of 1.5. The optical density is related to the transmission by the following equation: $T = 10^{-D} \times 100 =$ percent transmission.
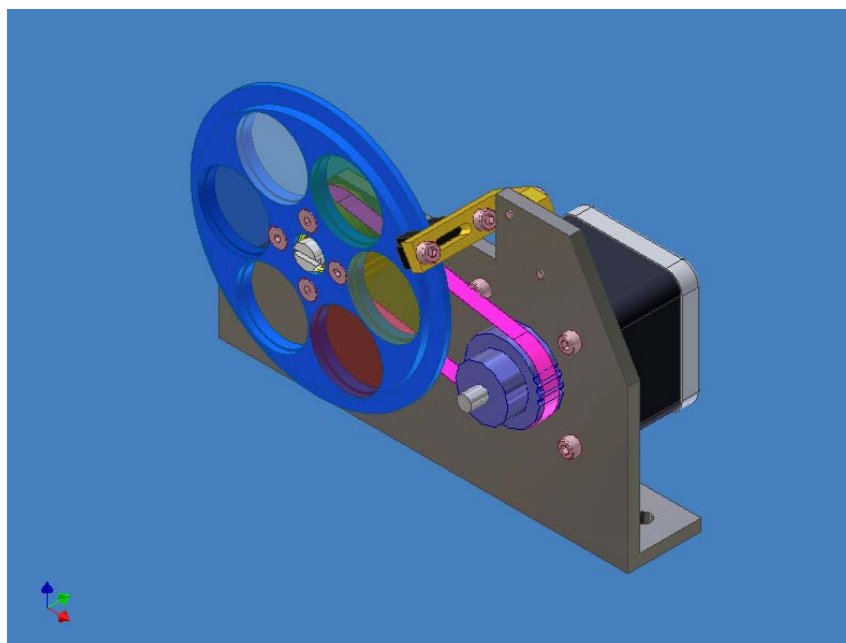
Figure 5.9 - Band-Pass Filter wheel

5.2.6. Thermoregulation modules

The 2 thermoregulation modules (each composed by 4 Peltier plates) (Figure 5.10) allow for the maintenance of a constant temperature inside the monochromator (typically 15°C), in order to prevent variations in the dispersion parameters of the grating due to mechanical deformations caused by the variation of the internal temperature.

Thanks to their unique operational characteristics, Peltier modules allow to reach the required cooling without huge technical problems. They are quite compact, convenient, reliable and efficient.
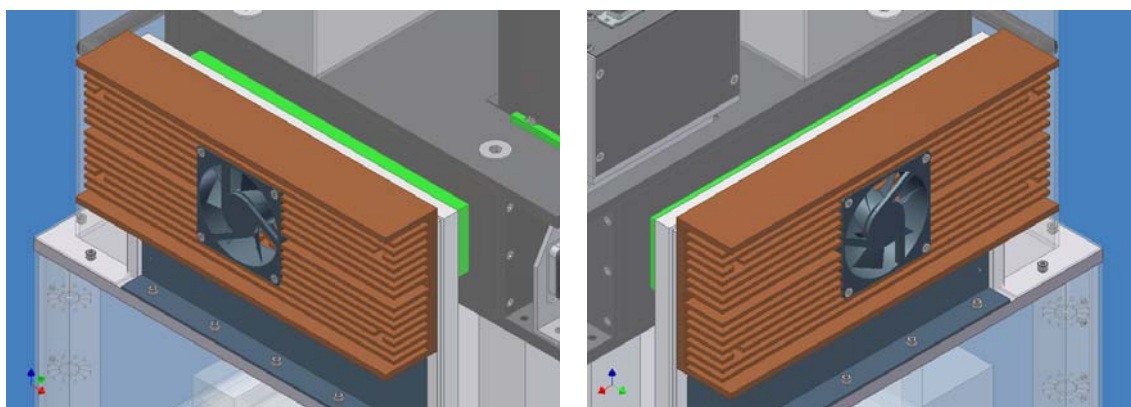
Figure 5.10 - Peltier Thermoregulation modules

Due to the peculiarity of the Peltier effect, some additional information about the physics causing this phenomenon will be provided

5.2.6.1. Peltier modules

They used a so called thermoelectric refrigerator based on Peltier effect. The given effect was called after a French watchmaker (1785-1845.), who discovered it in 1834.

If a drop of water is placed in the hollow on the joint of 2 semiconductors Cu and Bi, and the current switched on, the drop freezes (with the reverse direction of the current the drop would melt). This is how Peltier effect works.

Unlike the Joule heating effect, which is proportional to the square of the current intensity ($Q = RI^2t$), the Peltier is proportional to the current intensity and changes the sign (-/+) if the current changes the direction. The Peltier heat equals:

$$Q = P \cdot q$$

Where $q = I \cdot t$, P is a Peltier factor that depends on contacting materials and temperature.

Peltier heat is considered positive in case of dissipation, and negative in case of absorption.
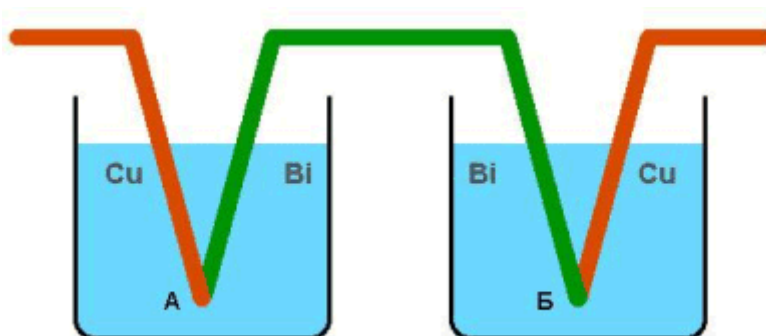
Figure 5.11 - The scheme of the experiment of Peltier heat measuring, Cu, Bi.

In this case the Joule heating in both calorimeters is the same (since R = R(Cu)+R(Bi)). But the Peltier heating differs in the sign. So, this experiment allows to calculate the Peltier factor.

In the table below several Peltier factors are indicated for different pairs of metals.

Table 5.1 - Peltier factors for different pairs of metals

Fe-constantan		Cu-Ni		Pb-constantan	
T, K	**P, mV**	**T, K**	**P, mV**	**T, K**	**P, mV**
273	13,0	292	8,0	293	8,7
299	15,0	328	9,0	383	11,8
403	19,0	478	10,3	508	16,0
513	26,0	563	8,6	578	18,7
593	34,0	613	8,0	633	20,6
833	52,0	718	10,0	713	23,4

Usually, a Peltier factor is calculated this way:
$$P = \alpha \cdot T$$

P - Peltier factor,

α - Tomson factor,

T - absolute temperature.

The Peltier effect is caused by the electrons speeding up or slowing down under the influence of contact potential difference. In the first case the kinetic energy of the electrons increases, and then, turns into heat. In the second case the kinetic energy decreases and the joint temperature falls down.

In case of usage of semiconductors of p- and n- types the effect becomes more vivid. Figure 5.12 shows how it works.

COLD

HEAT
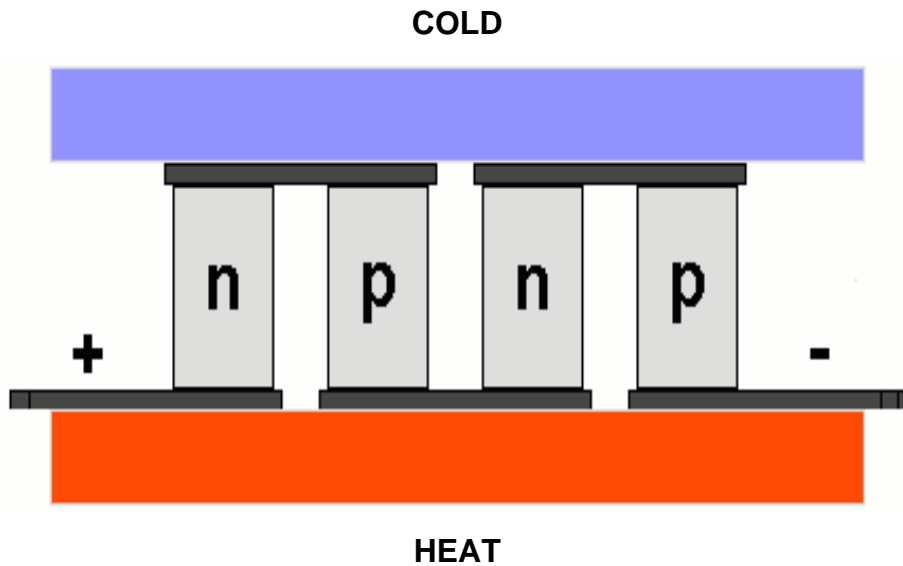
Figure 5.12 - Usage of semiconductors of p- and n-type in thermoelectric coolers.

Combination of many pairs of p- and n-semiconductors allows creating cooling units - Peltier modules of relatively high power (see the scheme below).
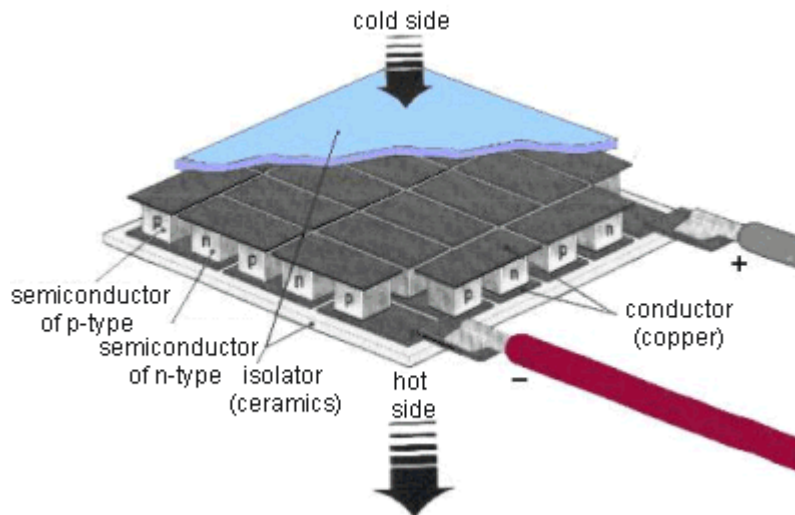
Figure 5.13 - Structure of a Peltier module

A Peltier module consists of semiconductors mounted successively, which form p-n- and n-p-junctions. Each junction has a thermal contact with radiators. When switching on the current of the definite polarity, a temperature difference is established between the radiators: one of them warms up and works as a heat sink, the other works as a refrigerator.
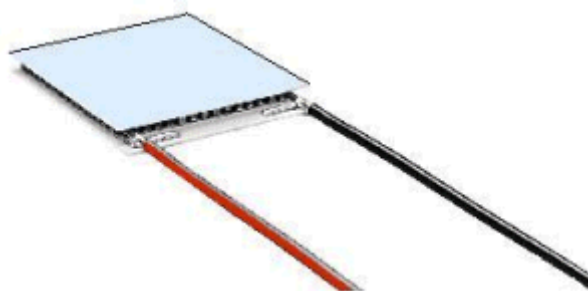
Figure 5.14 - Peltier module

A typical module provides a temperature difference of several tens degrees Celsius. With forced cooling of the hot radiator, the second one can reach the temperatures below 0 Celsius. For higher temperature differences the cascade connection is used.
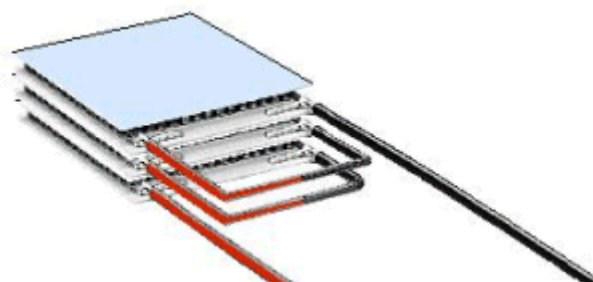
Figure 5.15 - An example of cascade connection of Peltier modules

The cooling devices based on Peltier modules are often called active Peltier refrigerators or Peltier coolers.

Peltier module's power depends on its size. The modules of low power may not be efficient enough. But the usage of the modules of too high power may cause moisture condensation, what is dangerous for electronic circuits.

5.2.7. Monochromator

The monochromator is the heart of the instrument (Figure 5.16). Here the light bundle, focused by the entrance slit (a), is decomposed in its wavelengths thanks to a holographic diffraction grating (b) of 1200 grooves/mm and 70mm of diameter. The grating is by Jobin-Yvon and has a dispersion of 2.4nm/mm at 300nm and spectral resolution of 0.5 nm at 430 nm.

The grating with its support is rotated by means of a stepper motors in order to investigate, in consecutive spectral windows of about 60nm each, the whole spectral range from 250 to 950 nm.

The decomposed light is addressed over a tilted mirror (c) reflecting the information to the CCD sensor (d).
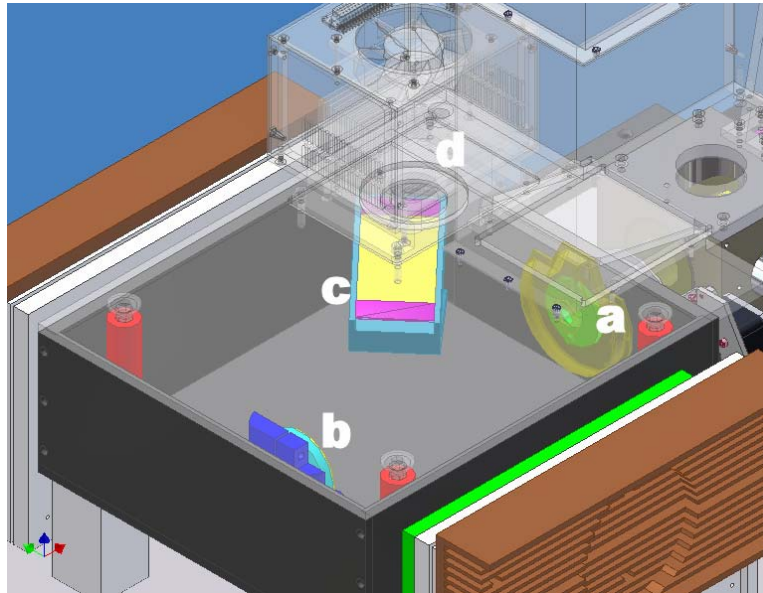
Figure 5.16 - Monochromator

5.2.7.1. Slit

The input slit of the spectrometer (obtained for photogravure on a covered quartz disc of 14 mm of diameter and 1 of thickness) is wide 150 micron and 8 mm of height, that it is equivalent to the vertical dimension of the CCD sensor.
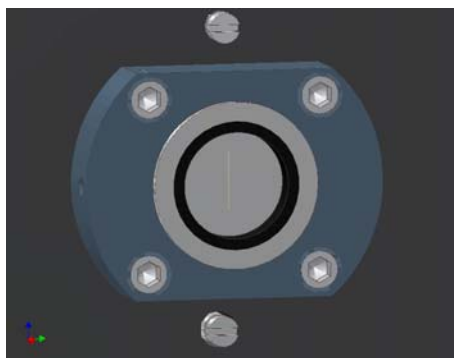
Figure 5.17 – Slit

5.2.7.2. Shutter

The shutter is a mechanical device that opens and closes to control the exposure time of the CCD camera. As in the photographic cameras the shutter should be

placed near the CCD, but in this equipment it is placed immediately after the entrance slit in order to maintain the monochromator clean, minimizing the probability of powder entrance.

The shutter is based on an electro-magnetic actuator. The shutter is actuated by applying an electronic pulse to the shutter, which varies its intensity during the shutter's exposure sequence, then removes the pulse to close the shutter.

The minimum exposure time is of the order of 10 ms.
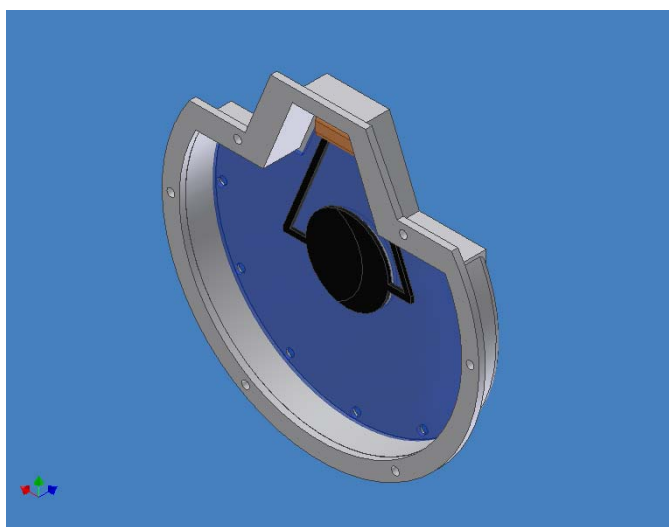
Figure 5.18 - Shutter

5.2.7.3.   The diffraction Grating

As remembered in the introduction of this chapter the optic module of the SPATRAM is similar to the GASCOD type instruments, so the SPATRAM is equipped with an holographic spherical diffraction grating (Figure 5.19) of 1200 grooves/mm in a particular constant deviation mount allowing for a spectral dispersion of 2.4 nm/mm and the overall typical spectral resolution of about 0.5 nm in the UV region; in the visible spectral region the spectral resolution is a little bit worse (0.7 nm), and in the NIR region is about 1.2 nm. The full spectral interval covered by the SPATRAM ranges from 250 to 950 nm.
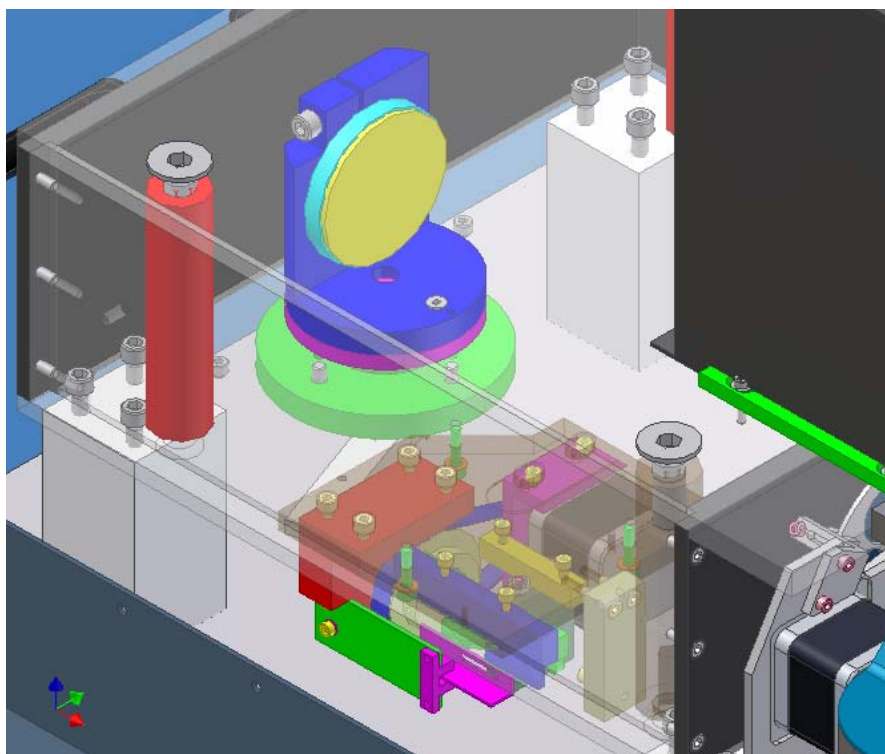
Figure 5.19 – The diffraction grating in the monochromator and the bottom view of the movements mechanism.

Due to the need to maintain the monocromator dimension small and due to the optical features of the CCD sensor, the full spectral range covered by the instrument can not be obtained with a single scan, but (as in § A1.1.17, applying a modified (A1.45)) with a rotation of the grating allowing for the analysis of the spectrum in successive windows of approximately 60 nm each. In order to reach this result, trying also to minimize the risk of degrading the spectra, a mechanism based on a micrometric screw allowing for positioning the grating was developed (Figure 5.20). This system has a precision in the movement of 0.05 nm, thanks to a mechanical reduction of ¼ , and a ratio of 1/256000 round/step in the stepper motor used to rotate the screw. An optoelectronic switch is used for the reference position and it can be adjusted in order to obtain the maximum performances of the grating. Two more electric switches are utilized to mark the limits of the useful mechanical path. All these devices are continuously monitored during the execution of the measurements minimizing the risk of wrong positioning of the grating.
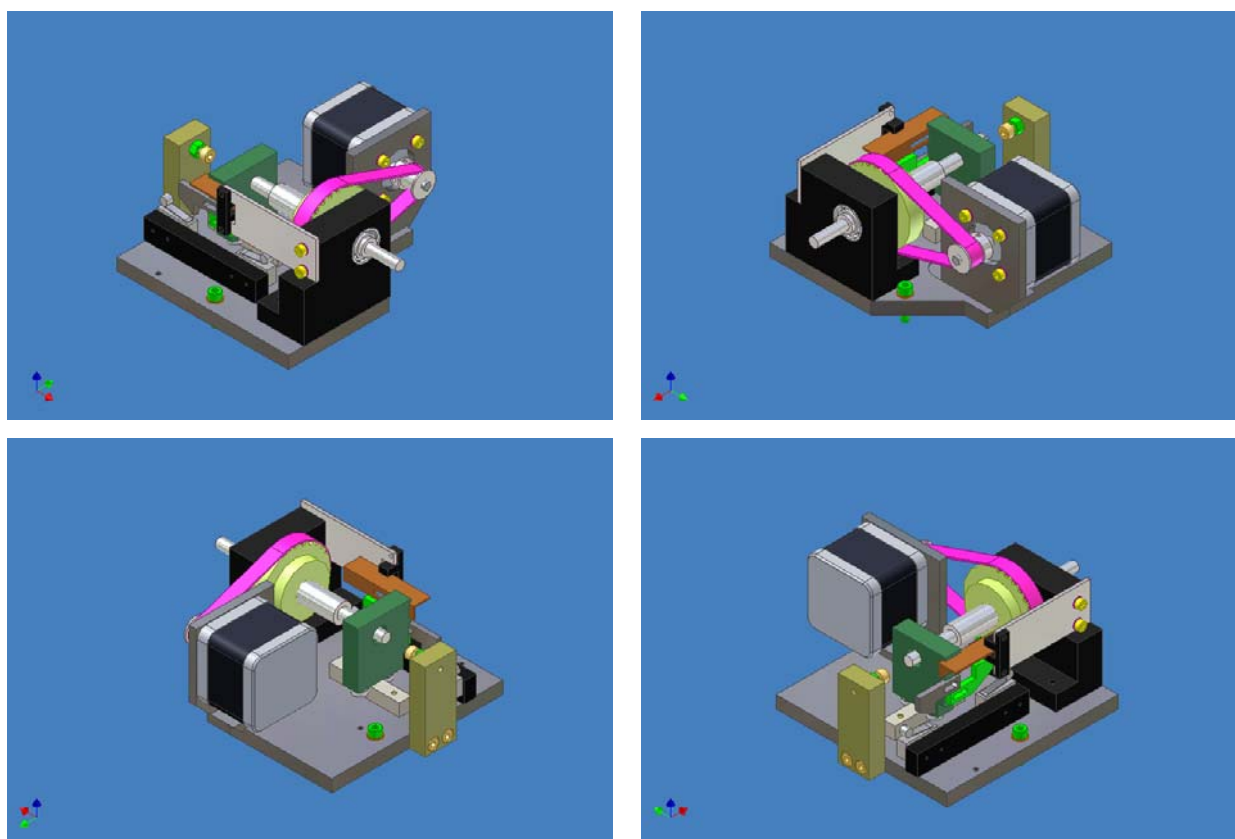
Figure 5.20 - The Movements for the diffraction grating

5.2.7.4. Mirror tilted 45⁰

The flat mirror tilted at 45° send the diffracted light beam to the CCD sensor. In order to take into account the astigmatism of the Rowland circle mounting (see § A1.1.15), the mirror is rotated towards the left of 0.6°. In fact, if the mirror is perpendicular to the tangential plane of the grating, the borders of the spectrum should be always defocused. In this manner more than 90% of the spectrum reaching the CCD sensor has the same focusing. In the previous instrument like the GASCOD, the quality of the mounting and of the focusing could be checked only in a qualitative way during the alignment of the grating, since both the detector and the software for the data acquisition, were not developed for this purpose. With SPATRAM it is possible to have the instantaneous visualization of the acquired spectrum of a calibration lamp and in addition, thanks to the array CCD detector utilized, the mirror can be exactly positioned for the best focusing.
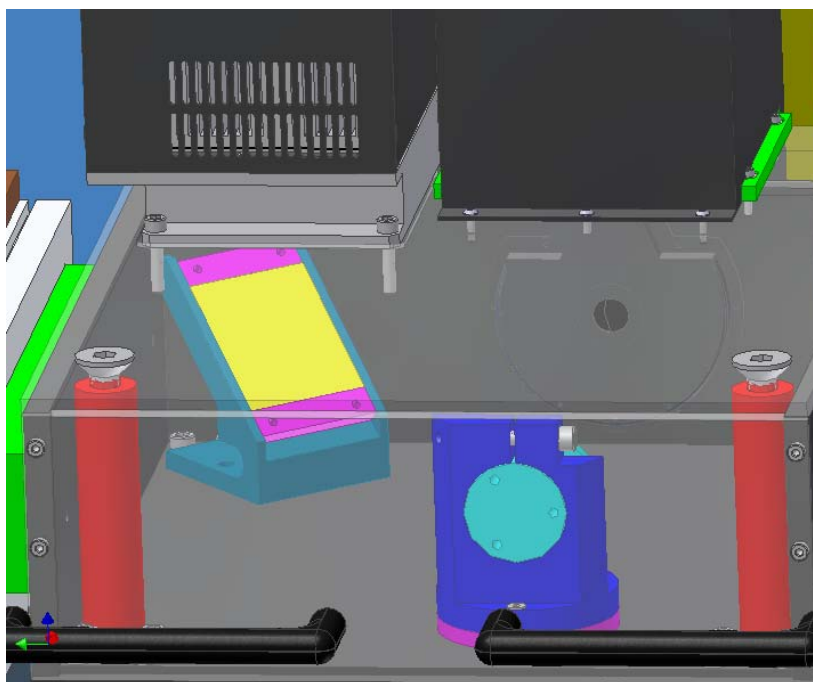
Figure 5.21 – Mirror Tilted 45°

5.2.8. CCD Camera

The CCD camera is composed of the exterior box containing the 16 bits AD Converter, the adapter for the transmission of the digitized signal to the PC, the Peltier device for the thermoregulation of the CCD sensor and the fan for the refrigeration of the whole device. The CCD sensor (mod. CCD30-11Bi, manufactured by Marconi) is contained in a small ultra vacuum chamber allowing for the maintenance of the temperature at -40°C.

Due to the importance assumed by the CCD device in this last years, in Annex 2 the main features of this kind of sensor are presented and the specific terms – the Glossary – of the CCD are explained.

In the following the main distinctive aspects of the detector adopted in the SPATRAM instrument are discussed.
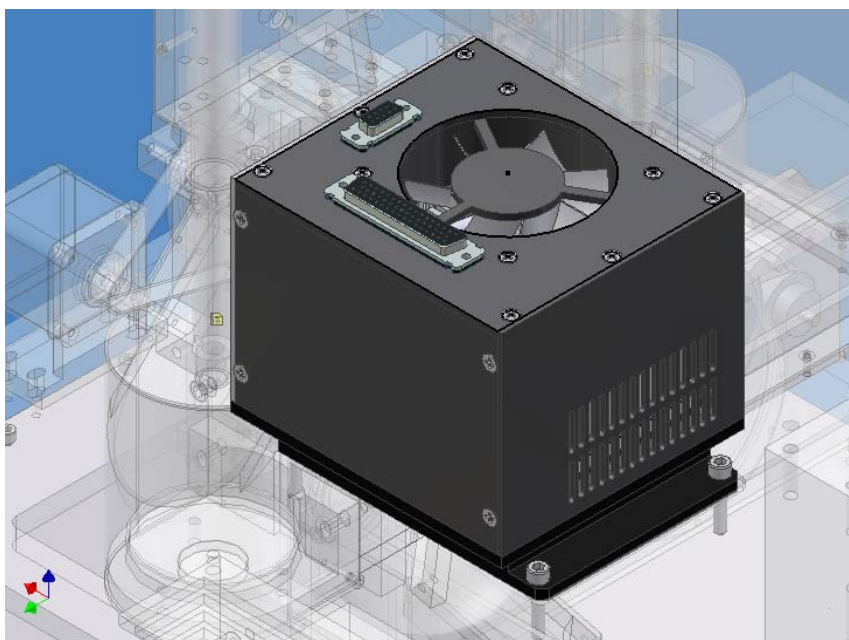
Figure 5.22 – CCD Sensor

The back illuminated CCD30-11 (Figure 5.23) is a high performance CCD sensor designed for use in the scientific spectroscopy instrument , where enhanced quantum efficiency is required. With an array of 1024x256, 26 mm square pixels it has an imaging area to suit most spectrometer outputs of 26.6 x 6.7 mm.

The back illuminated CCD30-11 has a Quantum Efficiency (see § A2.2.4) enhanced and an ultraviolet coating making it perfect for measurements in the UV-Visible spectral region (Figure 5.24) The signals degrade in the IR, but until 950nm the measurements are profitable.

The readout register is organized along the long (1024 pixel) edge of the sensor and contains an anti-blooming drain to allow high speed binning operations of low level signals which may be adjacent to much stronger signals. The output amplifier design has no light emission.
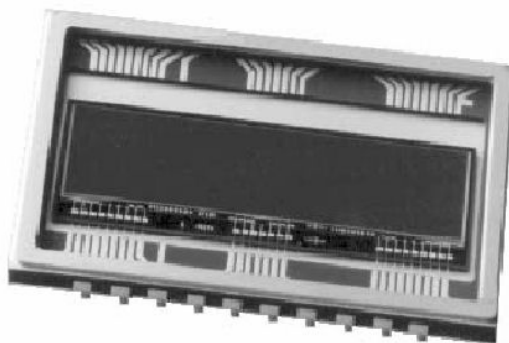
Figure 5.23 – CCD 30-11Back Illuminated High Performance CCD Sensor.
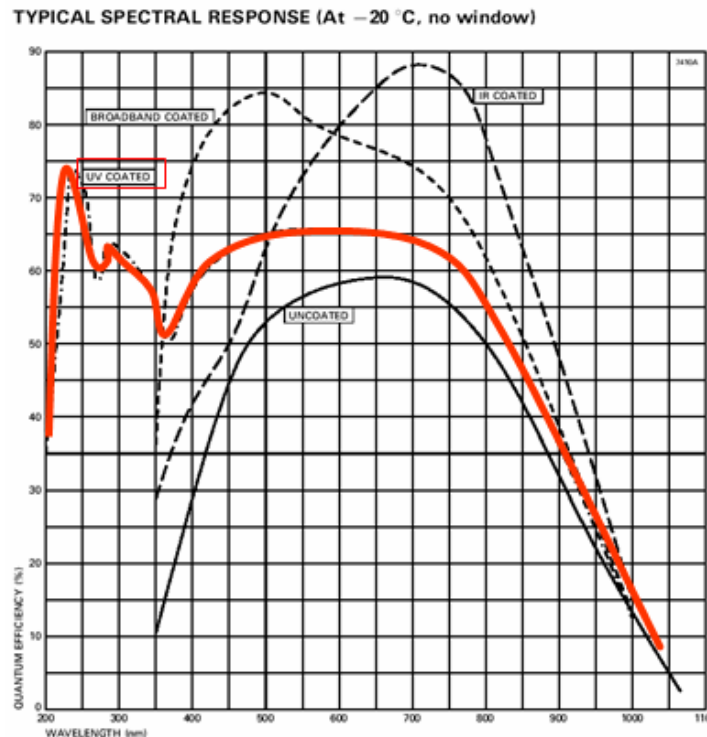
Figure 5.24 – Typical Spectral Response of the CCD 30-11Bi Sensor. The red line correspondes to the UV-Coated version installed on the SPATRAM equipment

The main advantage in using a back illuminated CCD has to be found in the higher Full Well Capacity (almost the double) of this type of sensor compared with the equivalent Front Illuminated ones; the CCD30-11Bi has a FWC of 500000 e-, against the 300000e- of the CCD30-11Fi. This difference is mainly due to the construction technology of the 2 types of sensors.

Figure 5.25 shows the two basic ways CCD chips are constructed. On the left, is a front-illuminated chip. Here, the incoming light strikes the gates. These are the tiny blocks on the SiO_2 insulation layer that are required for creating the charge that allows the device to convert photons into electrons. The problem is the photons must pass through these gates before they can be converted to electrons. The gates act as a mask, particularly in the blue regions where they are often opaque. On the right is a back-illuminated chip. While the light must pass through the substrate, the substrate is usually much thinner than for the front-illuminated chip. The main point, however, is that the photons do not have to pass through the gates. The back-illuminated chip is more sensitive than the front-illuminated chip. This is quite apparent in the figure where the back-illuminated chip has a much high quantum efficiency, i.e., more of the photons that hit the chip are converted to electrons.
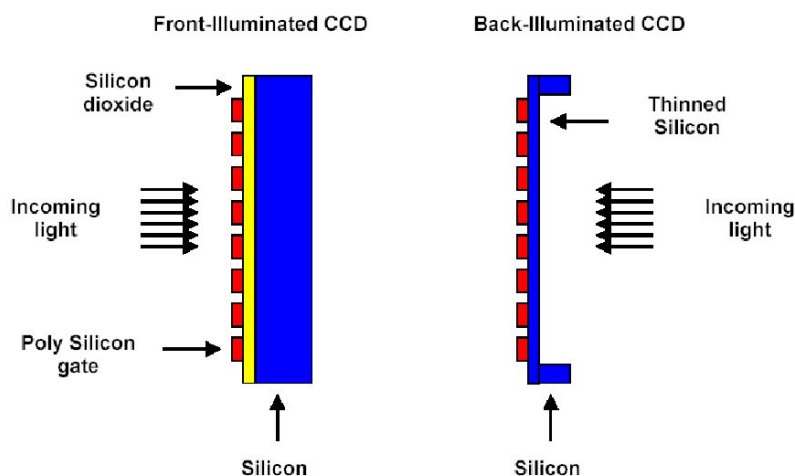
Figure 5.25 – technological differences between Front Illuminated (FI) and Back Illuminated (BI) CCD.

5.2.9. Other OMU Components

In this section some other mechanical and electrical components in the OMU will be listed (with the used acronyms) and briefly described:

SM1 - Stepper Motor for the movement of the input mirror. It has also a reference opto-switch (D1) correspondent to the "Vertical" position of the input mirror.

SM2 - Stepper motor for movement of the grating reticulum. It is equipped also of an opto-switch (D2) fixing the reference position at 4358A, and 2 electric switch fixing the mechanical limits

SM3 - Stepper motor for the filter wheel with the reference opto-switch (D3) corresponding to the "hole" position (no filters)

HGL - Mercury lamp for spectral calibrations (12 V DC, 6W)

QJL – Halogen lamp for radiometric calibration

probes of temperature (6)

5.3. ECU Electronic Control Unit

The Electronic Control Unit (ECU) is located under the OMU (Figure 5.26) to which it is connected with some D-Sub connectors placed in a panel called the OMU-ECU interface (Figure 5.27).
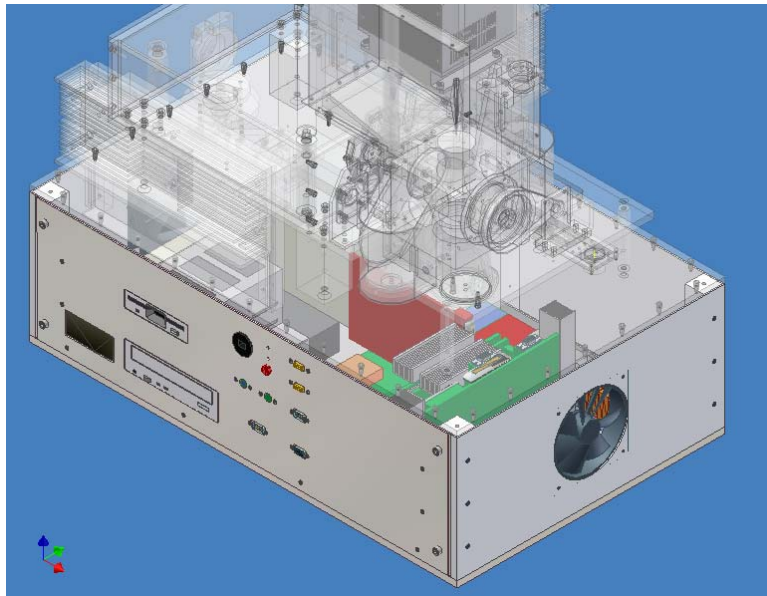
Figure 5.26 – ECU, Electronic Control Unit
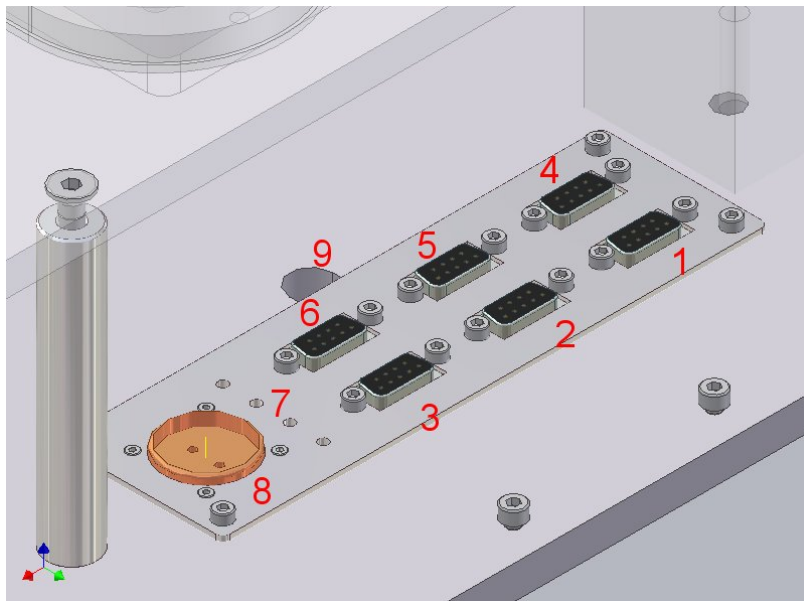
Figure 5.27 – OMU-ECU Interface; 1) SM1 – Input Mirror; 2) SM2 – Grating; 3) SM3 – Filter Wheel; 4) Temperature sondes; 5) Fan Peltier; 6) Shutter, Peltier CCD, Fan CCD; 7) Peltier Power; 8) Calibration lamps; 9) CCD SCSI Cable.

The ECU at the exterior seems like a normal personal computer; in fact in the front (Figure 5.28) can be recognized:

1. the power button,
2. the floppy drive,
3. the CD-ROM drive,

4. the net plug.
5. 2 status led and the reset button,
6. the PS2 keyboard and mouse ports
7. the parallel ports,
8. 2 USB ports,
9. the serial port
10. the VGA connector,
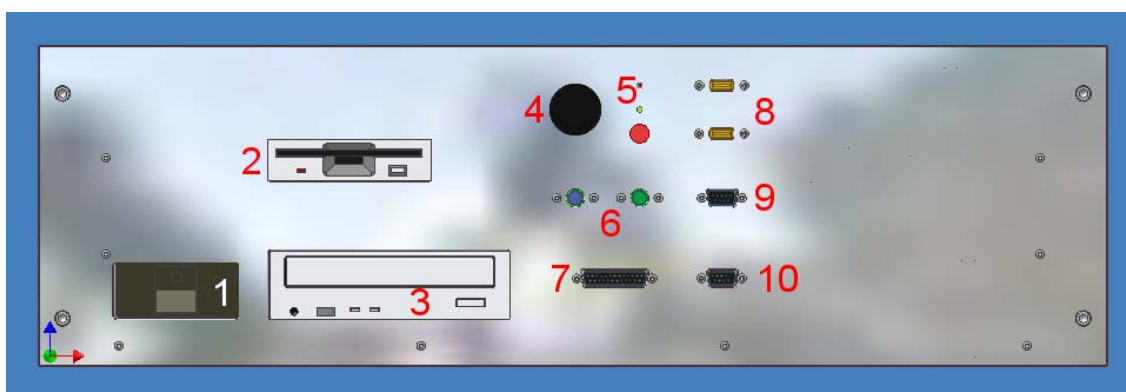
Figure 5.28 – ECU Front – 1) power button; 2) floppy drive; 3) CD-ROM drive; 4) network plug; 5) status led (2) and reset button; 6)PS2 keyboard and mouse ports; 7) parallel port; 8) 2 USB ports; 9) serial port; 10) VGA connector.

Inside the ECU (Figure 5.29) can be identified:
1. the 7892 NOVA Monoboard with 1 GHz CPU
2. the PCI interface adapter (FDL)
3. the HIRES device for the management of the CCD Camera (with the low noise power supply);
4. the 12 bit AD Converter. DIAMOND installed on the bus PC 104 of the NOVA monoboard, for the AD590 temperature sensors spread in the OMU and in the ECU;
5. the two stepper motors controllers (the AMS devices), connected to the NOVA trough the COM1 serial port. The AMSs drive the 3 stepper motors in the OMU. In addition one AMS provides the generation of a square wave for the thermoregulation of the entire OMU;

the TAD (Temperature Adapter Device) acting as a current/tension converter of the signals furnished by the AD590 Temperature sensors. The output of the TAD is the input of the DIAMOND Converter;

the ROI (Relais Opto Interface) for the control of the relais via the opto insulate decoupled ports of the AMS device.

the 12/24V Power Supply

the NOVA Power Supply

the 4 relais for: Peltier Heat/Cool, Fan Peltier, HG and QJ spectral Lamps On/Off

the fuses acting as a circuit protection
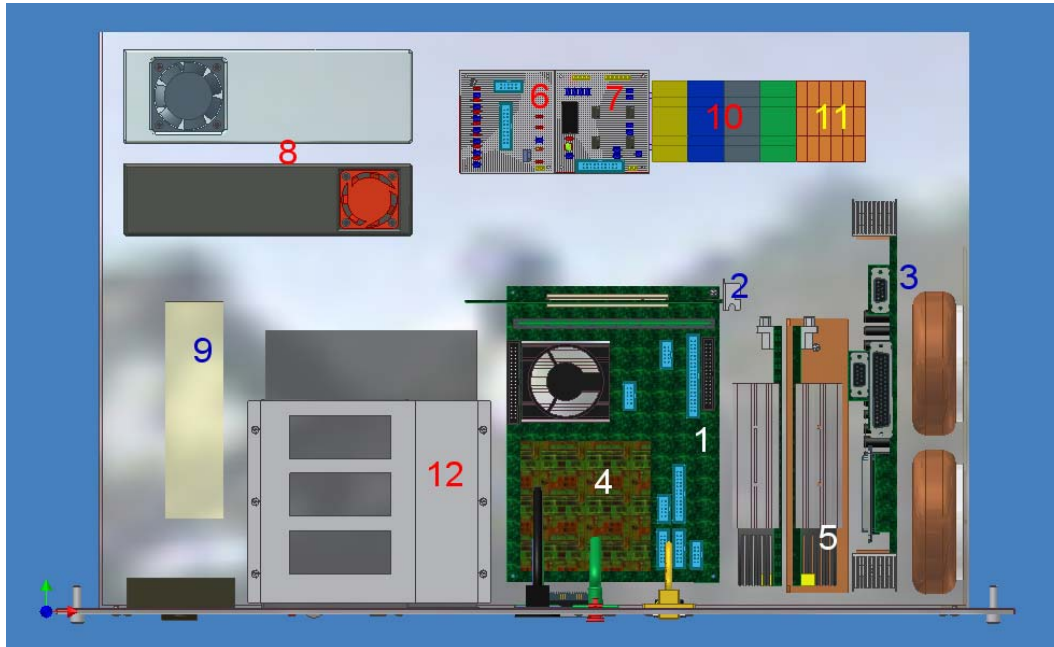
Figure 5.29 –ECU upper view – 1) NOVA 7892 (1 GHz-256MB RAM); 2)PCI interface adapter (FDL); 3) HIRES + power supply; 4) 12 bits AD Converter; 5) AMS; 6) TAD (Temperature Adapter Device); 7) ROI (Relais Opto Interface; 8) 12/24V Power Supply; 9) NOVA Power Supply; 10) Relais; 11) Fuses

SPATRAM is installed at the Observatory of the Geophysics Centre of Evora since April 2004 (Figure 5.30) and actually it is utilized to carry-out continuous measurements of the zenith scattered radiation, the so-called "Passive mode", in order to retrieve – applying the DOAS (Differential Optical Absorption Spectroscopy) methodology – the vertical content of some atmospheric tracers such as Ozone, Nitrogen Dioxide, Bromine Monoxide, Formaldehyde and others.
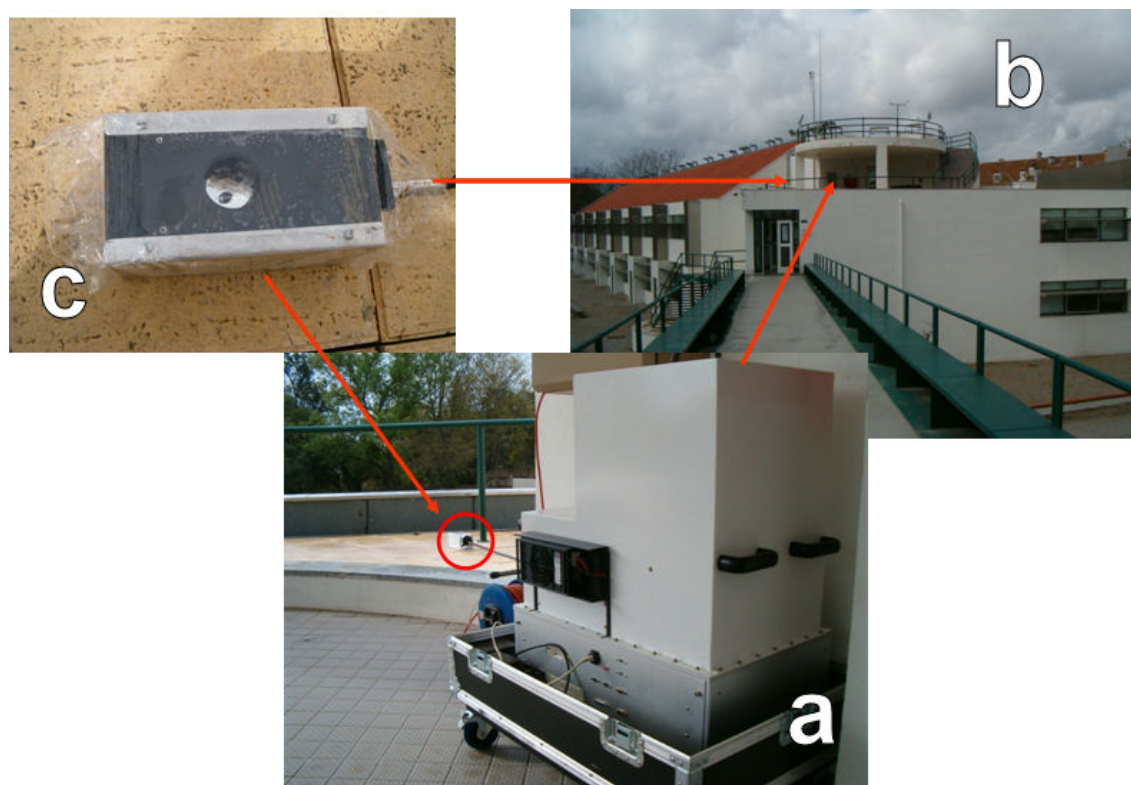
Figure 5.30 – SPATRAM (a) installed at the Observatory of the Geophysics Centre of Evora (CGE)(b) since the 1st of April 2004.The measurements are obtained with an optic fibre using one of the optic fibre input adapted as input telescope (c).

5.4. SPATRAM management

5.4.1. Introduction

The spectrometer is managed with a software tool completely developed in the frame of this doctorial work. This section will present only the programming philosophy and the main capabilities of Data Acquisition System (hereinafter DAS) program. A more exhaustive description of DAS can be found in Annex 3.

The DAS is implemented in ANSI C standard with the support of the multi-platform MGUI (Morello Graphic User Interface) library. The multiplatform features allows the program to run on computers equipped with Win9x, Win2000, WinXp and in the future also on Linux OS. Moreover the DCL (DTA Camera Library) allows for the control of the operations over the CCD sensor. Other libraries for the management of the serial port used by the drivers of the stepper motors (AMS), and for the realisation of some built-in algorithms. The code is compiled with the Microsoft Visual C++ 6.0.

5.4.2. Programming Philosophy

At the beginning of this project one of the main problems was the choice of the programming language to be used to manage all the devices in the instrument.

After some doubts the ANSI C Standard was chosen mainly because it is an 'open' language, that allows for the complete and clear control of the Operating System and of the devices (as parallel, serial port and PC104 bus).Moreover any kind of function or procedure can be developed and it can be linked with other modules (executables programs) written in other languages.

Another powerful tool of the C language is the use of 'pointers' that allows for the fastest execution of the instructions and the possibility to use 'structures' as collection of variables of different types and pointers to structures in the functions calls.

The Graphical User Interface (GUI) library that should be used was the other point of discussion: in fact the GUI of the Visual C/C++ (the windows API - Application Programming Interfaces) is developed only for the windows environment. Since some of the instruments managed by the DAS could be installed in remote sites (Arctic and/or Antarctica), and since Microsoft Windows doesn't ensure a complete stability of working for long periods, it is foreseen that DAS should be translate also for Linux OS. Mainly for this last reason, for the simplicity (even if only apparent) of usage and for the multiplatform feature, the choice fell on the Morello Graphic User Interface library.

The first BETA release of the DAS was a Control Panel displaying the activity of the CCD Camera and the movements of the stepper motors of the instrument. The implemented code was limited to the basic functions of management of the devices (positioning of the input mirror, of the grating, of the filter wheel and the capability of obtaining spectral measurements. The Visual C/C++ IDE (allowing for the identification of the resources of the project) was composed of 10 files (including sources, headers and library files).

Table 5.2 shows some numbers for the current release of DAS (2.8.7) and Figure 5.31 shows the Main panel of the DAS program.

Table 5.2 – Quantity of source files, implemented functions and lines of code for DAS Rel. 2.8.7

Source Files	34
Header and Definition Files	22
Library Files	11
Implemented Functions	~ 250
Lines of code (in *.c files)	~ 33000
Lines of code (in *.h files)	~ 4000

Figure 5.31 – DAS Main Panel

One of the main features of the DAS is the possibility to carry out measurements in unattended and automatic mode. By means of an ASCII file containing the key-words and the parameters for pre-defined measurements cycles (see § A3.6. Measurement chart)

5.5. SPATRAM Testing phase

As a first check of the capabilities of the SPATRAM, the Fraunhofer's spectral lines in the solar spectrum can be considered and identified.

In 1802, William Wollaston observed for the first time the spectral lines. Only in 1814 their systematic study begun, when the German optical Joseph von Fraunhofer observed and catalogued the spectral lines. Fraunhofer accurately recorded the position of the lines.

Figure 5.32 shows the well known spectrum of the visible light and some dark lines (listed also in Table 5.3) are clearly visible. The colored spectral lines produce the *emission spectrum,* meaning that one photon is emitted by an atom at a particular frequency. The dark spectral lines are instead the absorption lines creating the *absorption spectrum*, that means: photons with particular wavelengths are absorbed by the medium.
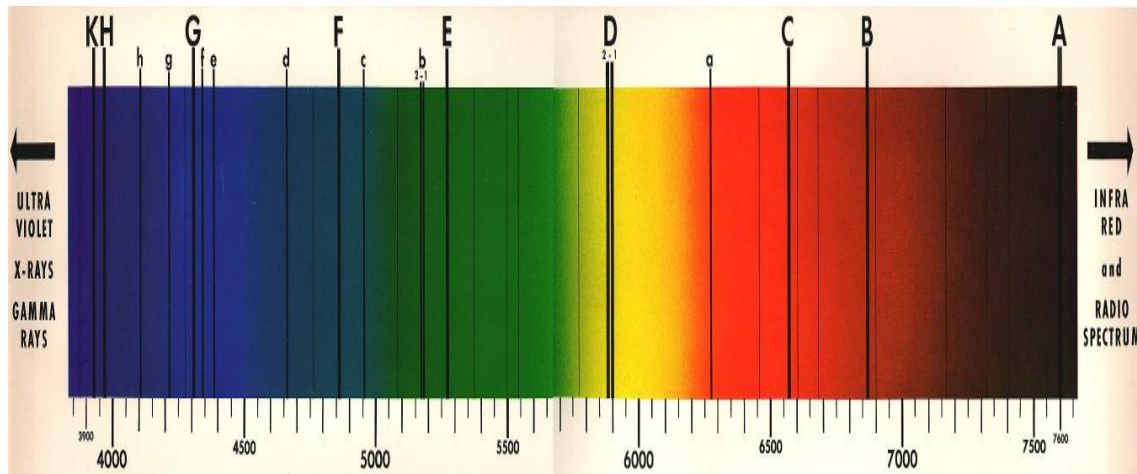
Figure 5.32 – Electromagnetic visible spectrum. The Fraunhofer lines are highlighted

Table 5.3 – Fraunhofer's lines with the corrispondent chemical elements and the wavelength.

Spectral Lines	Origin	Wavelength (nm)
A - (band)	O_2	759.4 – 762.1
B - (band)	O_2	686.7 – 688.4
C	H	656.3
a - (band)	O_2	627.6 – 628.7
D - 1, 2	Na	589.6 & 589.0
E	Fe	527.0
b - 1, 2	Mg	518.4 & 517.3
c	Fe	495.8
F	H	486.1
d	Fe	466.8
e	Fe	438.4
f	H	434.0
G	Fe & Ca	430.8
g	Ca	422.7
h	H	410.2
H	Ca	396.8
K	Ca	393.4

The SPATRAM operates from 250 nm to 950nm in successive windows of 60 nm each, and the main features of the solar spectrum can be identified.

Figure 5.33 shows the solar spectrum obtained with the SPATRAM in the 300.9-364.3 nm spectral range.
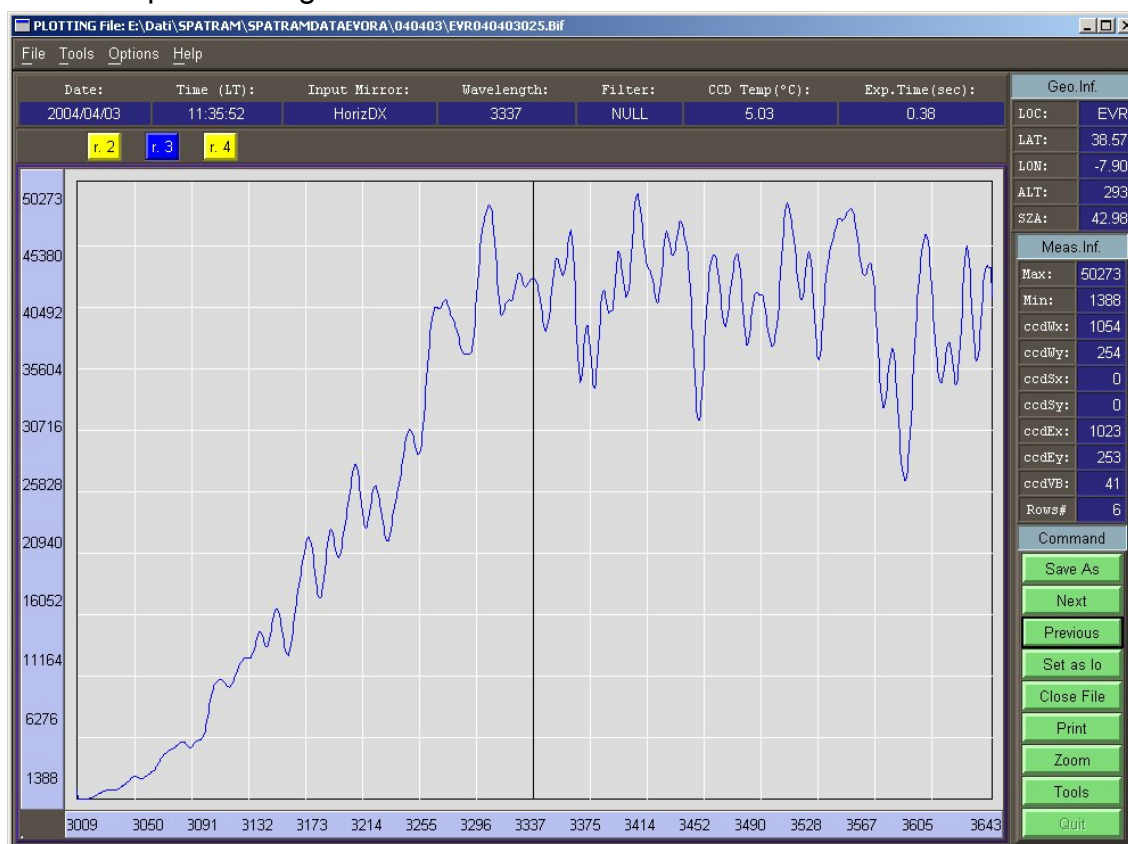
Figure 5.33 – SPATRAM – Scattered solar radiation in the 300.9 - 364.3 nm spectral range. The quite absolute absorption of radiation lower than 300 nm has to be noted.

This spectral region is still in the far UV, therefore there are no correspondences with the lines reported in table 5.7. It has to be notice that for wavelength lower than 300nm, the solar radiation is quite totally absorbed by the ozone layer in the stratosphere. This spectral region is particularly useful for the determination of the columnar content of ozone as already mentioned in chapter 3.

Figure 5.34 shows a measurement obtained in the 353.0 – 415.4 nm spectral range. The Fraunhofer's lines (Figure 5.32 and Table 5.3) codified as K (393.4 nm) and H (396.8 nm) and due to the absorption by the Calcium. Also this spectral window can be utilized for the retrieval of the ozone slant column even if its absorption for this frequency is lower than in the previous spectral range collected by SPATRAM. Moreover in this window others tracers (as SO2, BrO, HCHO) have absorption features that can be exploited for their slant column determination.
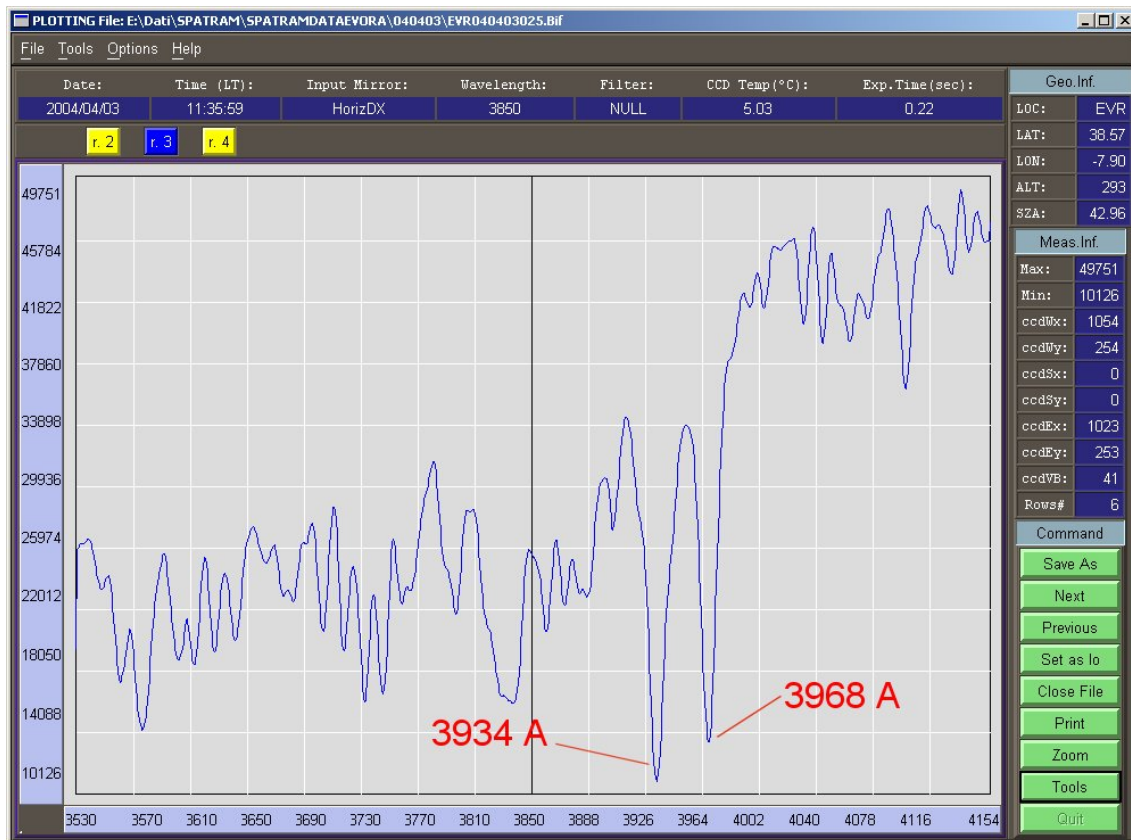
Figure 5.34 – SPATRAM – Scattered solar radiation in the 353.0 – 415.4 nm spectral range.

Figure 5.35 plots the 405.2 – 465.6 nm spectral range and the following spectral lines can be identified (Figure 5.32 and Table 5.3):

- o h - due to absorption of hydrogen at 410.2 nm
- o g - due to absorption of calcium at 422.7 nm
- o G - due to absorption of Iron and Calcium at 430.8 nm
- o e - due to absorption of Iron at 438.4 nm

This spectral window is the best for the retrieval of information about the atmospheric content of nitrogen dioxide, since it is in this region that the NO_2 shows the greater absorption
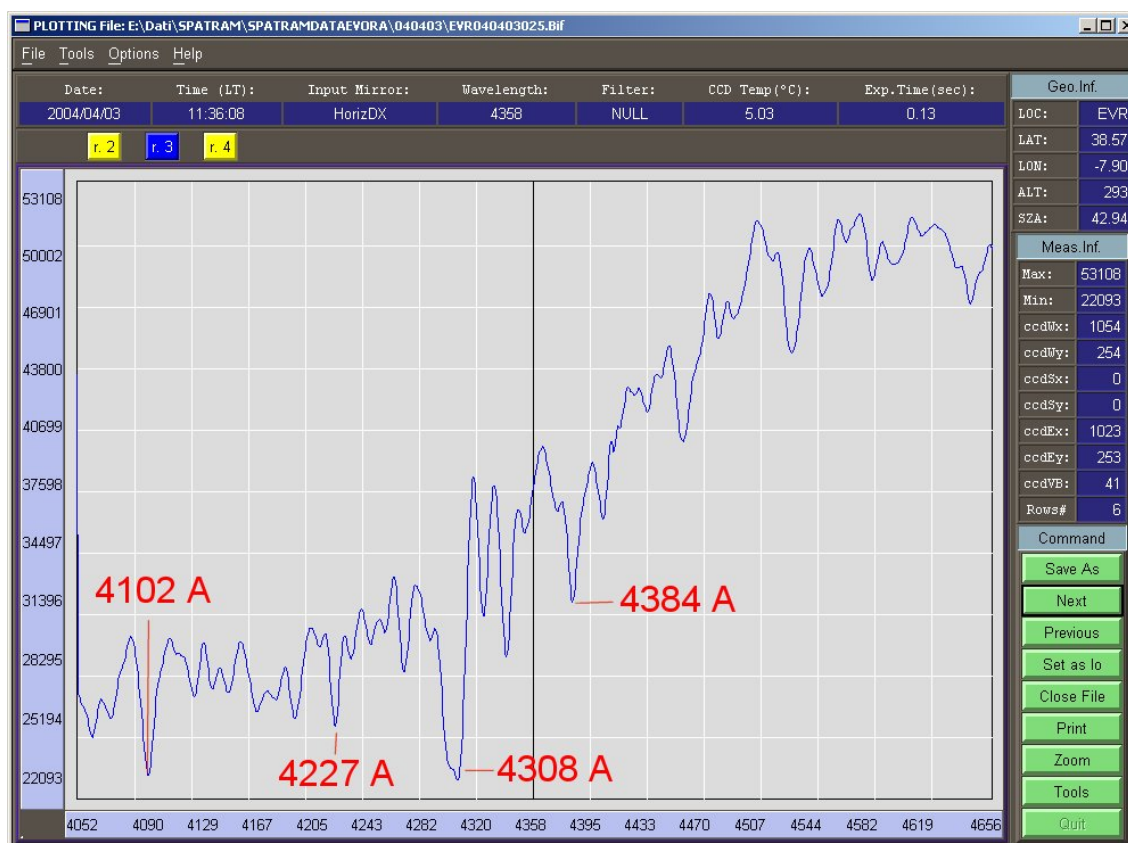
Figure 5.35 – SPATRAM – Scattered solar radiation in the 405.2 - 465.6 nm spectral range.

5.6. GASCOD vs SPATRAM

The main objective of this work was the development and realization of a new equipment (the SPATRAM), based on the optic module of the "old" GASCOD spectrometer, allowing for the retrieval of minor compounds in the atmosphere, with improved temporal resolution, flexible management and enhanced capability of measurements. Table 5.4 summarizes the most important improvements of the SPATRAM.

First of all, it has to be noted (record 1) that the SPATRAM is a stand alone instrument: it doesn't require any other device in order to perform and store reliable spectral measurements. On the contrary, GASCOD needs to be installed into a thermostatic box, where the temperature is controlled with an air conditioner installed outside the case, and in addition an external PC is also required for the data storage and the remote control of the instrument (in unidirectional mode – record 15). Furthermore SPATRAM is an all-in-one instrument meaning that the

optic and electronic unit, even if thermal separated, are collocated in the same box; instead GASCOD presents two different unit linked with a series of cables.

Record 2 of table 5.4 highlights that SPATRAM cover a wider spectral range than GASCOD, allowing for the detection of a great number of compounds (all that species with marked absorption features in the investigated spectral range).

Record 3 and 4 specify the increased number of inputs of the SPATRAM instrument (3 + 1, for the spectral and radiometric calibration) and the focusing optic system adopted. SPATRAM use a series of flat and spherical mirrors coupled with a rotating flat mirror that are more easy to align and also more economical than the cassegrain telescope used in the GASCOD spectrometer.

Records 5 to 11 summarize the improvements in the electronic modules adopted: first of all, the ECU components of the SPATRAM are of standard production and easily replaceable in case of failure. The GASCOD devices are the results of a deep study conducted during the eighties at the ISAC institute, in order to reduce the electric and electronic noises related to the adopted devices. Unfortunately these studies had not conducted to an industrial production of the electronic components so the life of the instruments is linked to the life of the electronic devices. The use of one microcontroller of the last generation with a frequency of 3 order of magnitude higher than the Z80, allows for obtaining performance incredibly superior than the GASCOD. The main difference in using a CCD detector instead of a CMOS sensor (record 7) are already discussed above.

The selection of one standard operating system as Win9x, Win2K/Xp or even Linux (as stated in record 8), is related to the project of a full compatible system. The DOS resident on the Read Only Memory (ROM) of the GASCOD spectrometer does not allow for multitasking operations as is possible to obtain with the currents operating systems based on the object programming and windows philosophy. In addition (record 9) the adoption of a standard programming language (as it is the C/C++) allows for the on line modification of the Data Acquisition Software (DAS) and the possibility to add new functions and modules in a short time. The GASCOD's DAS, is placed on one EEPROM (Electrically Erasable Read Only Memory), and in order to modify the DAS the EEPROM has to be removed from the device and placed on the EEPROM programmer for placing the new compiled code in it. The compiled code is obtained with a compiler in a different computer.

Record 10 highlights the improvement from 14 to 16 bits of the AD converter for the CCD sensor in GASCOD and SPATRAM respectively. This means that for GASCOD the maximum amplitude of the signal can be of 16384 counts instead for SPATRAM is 65536.

Record 11 shows the enhancement in the transfer rate of the measured data (from 4800 bps to 133MBps).

Records 12 and 13 demonstrate the improvement in terms of time resolution in the measurements of SPATRAM, since at the same wavelength the exposure time for SPATRAM is about 3 order of magnitude lower than for GASCOD.

Finally, record 14 emphasize the higher signal to noise ratio (SNR) of the measurements obtained with SPATRAM ($\sim 4 \times 10^4$) than the ones taken with GASCOD ($\sim 1 \times 10^3$). The value of the SNR is obtained applying the equation 5.1.

Table 5.4 – Summary of SPATRAM main improvements.

		GASCOD	**SPATRAM**
1.	*Additional devices required*	External PC for Data storage and remote control (via serial port)	Stand-alone
2.	*Spectral Range*	250-650 nm	250-950 nm
3.	*Number of inputs*	1 + 1 for calibration	3 + 1 for Calibration
4.	*Type of Inputs*	Cassegrain Telescope	Flat and spherical mirrors
5.	*ECU Components*	On demand	Standard industrial production
6.	*Microcontroller*	Z80 (8MHz)	Pentium 3 (1GHz)
7.	*Sensor*	Linear CMOS, 512 px	Array CCD, 1024x256 px
8.	*OS*	ROM DOS	Win9x, Win2K, WinXP, Linux
9.	*Acquisition Software*	ANSI C Text Mode (**EEPROM resident**) NO Multitasking	ANSI C Window Mode Multitasking utilized
10.	*Sensor AD Converter*	14 bit	16 bit
11.	*Data Tranfer rate*	4800 bps – COM Port	133 MBps – LPT Port
12.	*Typical Integration Time(λ_C = 435 nm) - 90° of SZA*	180 sec.	~1 sec
13.	*Typical Integration Time(λ_C = 435 nm) - 30° of SZA*	~ 20 sec.	~ 0.1 sec
14.	*Signal to Noise Ratio(SNR)*	$\sim 1 \times 10^3$	$\sim 4 \times 10^4$
15.	*Remote Control*	Unidirectional	Full (bidirectional)

$$SNR = \frac{B \cdot P \cdot Q_e \cdot t}{[\, B \cdot (P+S) \cdot Q_e \cdot t + D \cdot t + N_r^{\,2}\,]^{1/2}} \qquad (5.1)$$

where:

B = vertical binning,

S = the stray light inside the spectrometer (photons/pixel/second),

P = incident photon flux (photons/pixel/second),

Q_e = CCD quantum efficiency,

t = integration time (seconds),

D = dark current value (electrons/pixel/second),

N_r = read noise (electrons rms/pixel).

6. Developed DOAS Algorithms

In this chapter the DOAS algorithms implemented by the author in the last years for the processing of the spectral data will be presented and discussed. The writing of the program for the data analysis started before the begining of this doctorial work, but during the last years it was possible to obtain a software tool for almost operational product. The tool can be utilized not only for the SPATRAM data but also for similar equipment. Due to this capability some results obtained with the GASCOD instrument installed at Terra Nova Bay Station – Antarctica – will also be presented in this chapter as well as in the following one.

6.1. Common Procedure for DOAS methodology

Before the application of the DOAS algorithms, aiming to find a solution of the DOAS "master equation" *(4.10)*, some common procedures have to be applied to the spectral data obtained with a spectrometer, in order to achieve an homogeneous dataset as for the mathematical formulation, as for the physical assumptions of the DOAS. This is the so-called pre-processing of the data set.

The procedures that have to be applied to the spectral series I_λ e $I_{\lambda,0}$ (and also for the $\sigma_{\lambda g}$) are:

1. "linearization",
2. fair-spacing of the spectral data
3. smoothing,
4. differentiation

6.1.1.1. Linearization

An important step in the pre-processing of the spectral series is to replace the pixel numbers by wavelengths along the X axis. Usually, this operation is called spectral calibration (i.e. fix the wavelength zero point of the dispersion curve). In this work we prefer to call this operation as "linearization", since the spectral calibration is something more specific (see § 6.1.2); which follows the "linearization". With the expression, spectral calibration it is assumed that each pixel number is replaced with the corresponding real wavelength value, but this is not always true (due mainly to modification in the dispersion parameters as explained below) and can bring to wrong results. Instead, the linearization can always be done and only after some adjustments (spectral aligments), the calibrated spectrum is obtained.

In order to clarify the linearization procedure a brief mention to the classical equation for the spectral dispersion of a grating have to be done (In chapter 4 the argument will be treated deeply).

The function of spectral dispersion on the plan of the sensor for a short wavelength range, can be approximated with the linear relation:

$$\Delta\lambda = K_1 - K_2 \cdot \lambda$$

(6.1)

where the two parameters K_1 and K_2 have been calculated in the laboratory with the help of spectral lamps, (the values supplied from the manufacturer of the grating don't have the required precision and are used only as first guesses).

Assuming a proportionality between the parameters and the dimension of the pixels of the CCD camera, the following reactions can be written:

$$K_1(\Delta x) = K_1 \cdot \Delta x \quad and \quad K_2(\Delta x) = K_2 \cdot \Delta x$$

(6.2)

with Δx = width of the pixel (μm).

It has to be remembered that the values of K_1 and K_2 can vary not only with the wavelength, in agreement with relation *(6.1)*, but also due to thermomechanical causes. As an example one can point out the change of the temperature of the structure of the monocromator which affect the final values of K_1 and K_2 according to:

$$\Delta T < \frac{1}{R\alpha_t}$$

(6.3)

where:

ΔT = temperature variation;

$R = \dfrac{\Delta\lambda}{\lambda}$ = spectral resolution of the spectrometer;

α_t = coefficient of thermo-dilatation of the grating

Now two different methods developed for the linearization are explained.

The first one utilizes a spectral line emitted from a mercury calibration lamp. The algorithm foresees as fundamental the wavelength calibration. When the spectral interval 400 to 460 nm is analyzed, using the line of mercury at 435.8 nm, it is settled that such spectral line (Wl_C) falls, exactly, in the centre of the examined spectrum, that is between the central pixels of the CCD sensor. Applying simple geometric considerations, (Figure 6.1), the relation *(6.4)* is found.

$$Wl_{Px(C)} = Wl_C - \frac{K_1 - K_2 \cdot Wl_C}{2}$$

(6.4)

The relation *(6.4)* give the wavelength related to the central pixel ($Px(C)$) of the sensor of total pixels NPXS (so C = NPXS/2).
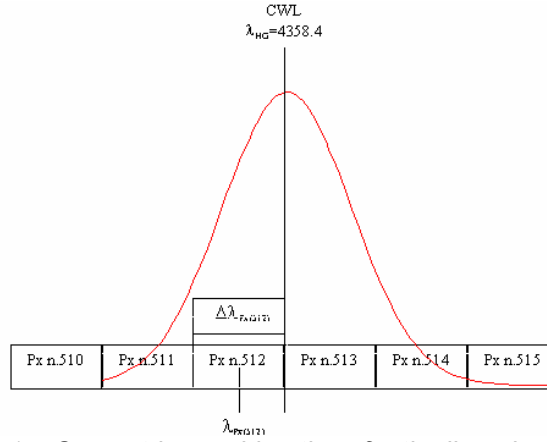
Figure 6.1 – Geometric considerations for the linearization procedure

Applying the relation *(6.1)* the spectral dispersion of the central pixel can be found

$$\Delta\lambda_{Px(C)} \cong K_1 - K_2 \cdot Wl_{Px(C)}$$

(6.5)

Combining *(6.4)* and *(6.5)*, the wavelength at the centre of the central pixel is obtained

$$Wl_{Px(C)} = \frac{2 \cdot Wl_C - K_1}{2 - K_2}$$

(6.6)

Now a recursive formula allowing for the linarization of the whole series can be written:

$$Wl_{Px(i)} = \frac{\left[(2 + K_2) \cdot Wl_{Px(i+1)} - 2 \cdot K_1\right]}{2 - K_2} \quad for\ i\ =\ C\ \text{-1},\ C\ \text{-2},\ \ldots,\ 2,\ 1$$

(6.7)

and

$$Wl_{Px(i)} = \frac{\left[(2 - K_2) \cdot Wl_{Px(i-1)} + 2 \cdot K_1\right]}{2 + K_2} \quad for\ i\ =\ C + 1,\ C + 2, \ldots,\ NPXS$$

(6.8)

Therefore the values of the wavelengths in the centre of each pixel are obtained, without any modification neither of the series intensity or of the spectral position.
In the previous chapters the SPATRAM was described and it is clear that a linear shift of the measured spectra has always to be taken into account in the

linearization algorithm. In order to consider this last possibility, an other factor has to be inserted in the relation *(6.4)*:

$$Wl_{Px(C)} = Wl_C - \frac{(K_1 - K_2 \cdot Wl_C) \times Shift}{2}$$

(6.9)

The *Shift* factor (also called DHG – Deviation from HG) is the term accounting for the possible linear shift of the measured spectrum.

Instead of the spectral line of the calibration lamp, the absorption features of the solar spectrum at high spectral resolution (usually called "Fraunhofer spectrum") can be used as reference for the linearization. In this case, the index "C" is not the central pixel, but the number of the pixel where the reference wavelength is found.

An ulterior advantage in using the Fraunhofer lines instead of the calibration lamp is that the measurements of the mercury lines are performed only periodically as a check of the grating position and not before each measurement. Therefore the time resolution of the spectral data increases, allowing for an elevated frequency of measurements during the most interesting periods that are the sunrise and the sunset due to the longest optical path of the measurement.
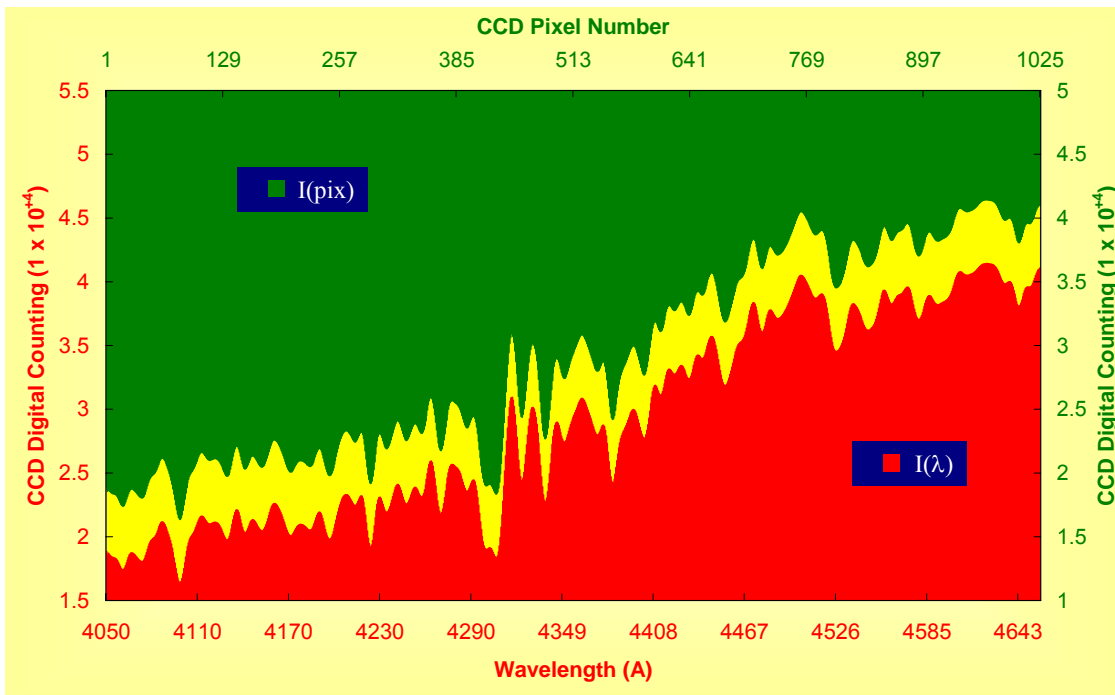
Figure 6.2 – Linearization procedure: the green series is a function of the CCD pixel Number (upper and right axes), the red one is the result of the procedure thus it is function of the wavelength. The bias of 0.5 is for the possibility to discriminate the 2 series, but the linearization doesn't introduce any modification of the intensity and in the spectral position.

6.1.1.2. Fair-spacing of the spectral data

This is the second one of the common procedures, that is applied to the measured spectrum I_s, to the reference spectrum I_0 and to the series of the absorber's cross section σ_g. The fair-spacing of the spectral data is obtained by means of polynomial interpolation procedure on 5 points of the original series. Moreover this procedure allows for choosing the value of the spectral step of the new series. A spectral step of 2Å is chosen in order to maintain the typical resolution of the instrument without degrading the resolution of the measured spectra , as discussed in Roscoe et al. [67].

6.1.1.3. Smoothing

The "Smoothing" is the filtering of the high frequency features in a spectral data series. It is applied to all the spectra involved in the data processing (the measured series and the cross section of the absorbers).

Three different methods of smoothing have been studied before the choice of the best one;

1 – The first one is the most simple and it demands minimal computation resources. The running average that is each value of the series is replaced with the average of *r* values after and before the considered point. The greater disadvantage of the running average is the loss of the data in the extremities of the series.

2 – The second method analyzed is the polynomial fitting of the high resolution spectral function. It can be obtained using polynomial functions of various orders, but it has to be noted that the presence of spikes in the original spectrum can give some problems.

3 - The last method involves a filtering procedure with a square function applied on the Fourier transformed series. The algorithm can be summarized as: i) looking for linear trend and removal; ii) Fast Fourier Transform (FFT) in the frequency domain; iii) Application of the selected filter; iv) inverse transform and reinsertion of the linear trend.

Although the FFT filtering is the most expensive one in terms of computation time and hardware resources, it is selected among the other two mainly due to portability and stability of the algorithm and for the less problems at the boundaries of the series. Figure 6.3 –shows an example of the FFT smoothing procedure applied to a spectral series at very high resolution.
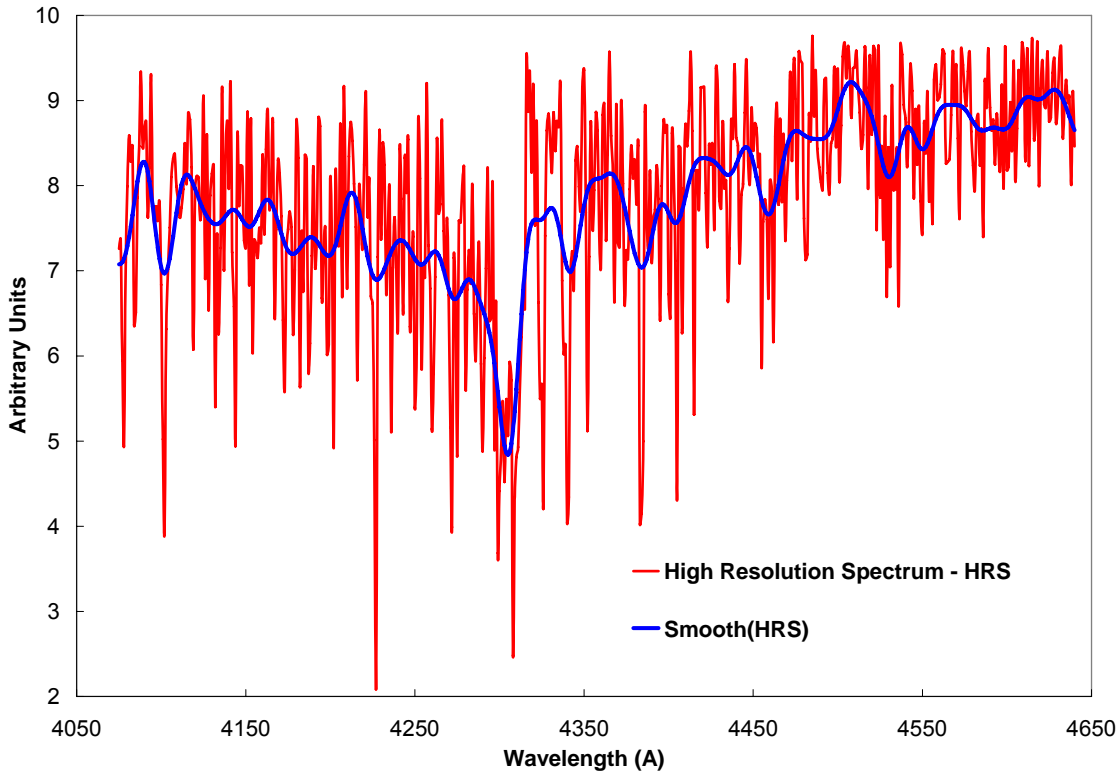
Figure 6.3 –FFT smoothing applied to a high resolution spectrum

The smoothing function plays a key role in the analysis of the spectral data obtained with a spectrometer; in fact, the choice of the filtering window is critical, and a wrong value can provoke loss of information, as the insertion in the differential spectrum of features not related with physical phenomena.

6.1.1.4. Differentiation

The "differential" spectrum (the term on the left of the DOAS-Master Equation *(4.10)*) is calculated as the difference point to point of the log ratio of the reference spectrum and the measured spectrum and its smoothing function. Following the general definition of "differential" spectrum the result of the difference is normalized with the ratio between the sum of the original series and the sum of the smoothed function, in order to obtain a differential series whose integral is zero, that is:

$$\xi_\lambda = \left[Ln\left(I_{\lambda,0}/I_\lambda \right) - Ln_{Smoothed}\left(I_{\lambda,0}/I_\lambda \right) \right] \cdot \frac{\sum_\lambda Ln\left(I_{\lambda,0}/I_\lambda \right)}{\sum_\lambda Ln_{Smoothed}\left(I_{\lambda,0}/I_\lambda \right)}$$

where:

$\xi_\lambda = $ Differential spectral series,

$I_{\lambda,0} = $ Reference Spectrum,

$I_\lambda = $ Measured Spectrum,

$Ln_{Smoothed}\left(I_{\lambda,0}/I_\lambda\right) = $ Smoothed series of the log-ratio of the Reference spectrum with the measured one.

An example of "Differential" spectrum (ξ_λ in the 320-360nm spectral range) is shown in Figure 6.4.
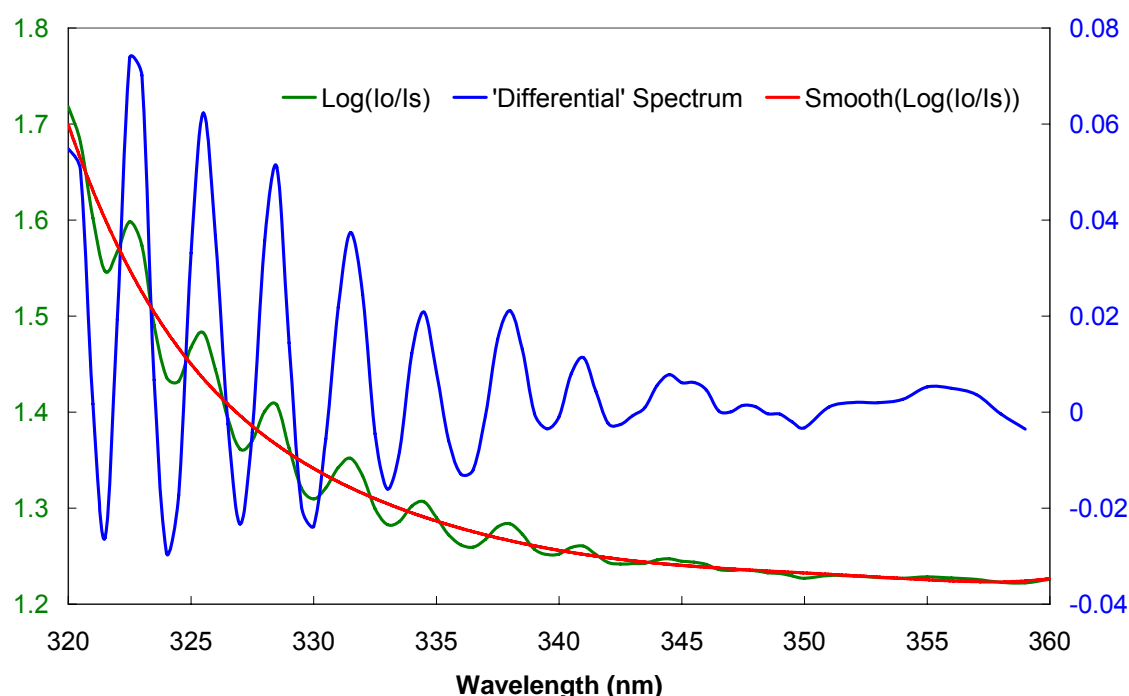
Figure 6.4 – Log ratio of the reference spectrum with a measured one (Log(Io/Is)), Smoothing Function (Smooth(Log(Io/Is))), and Differential Spectrum.

The differentiation procedure also is applied to the calculation of the Differential Cross Section (DCS) of the considered gas (Figure 6.5):

$$\Delta\sigma_\lambda = (\sigma_\lambda - \sigma_{\lambda,Smoothed}) \cdot \frac{\sum_\lambda \sigma_\lambda}{\sum_\lambda \sigma_{\lambda,Smoothed}} \quad (cm^2)$$

where

$\Delta\sigma_\lambda$ = Differential Absorption Cross Section

σ_λ = Absorption Cross section

$\sigma_{\lambda,Smoothed}$ = Smoothed Absorption Cross section
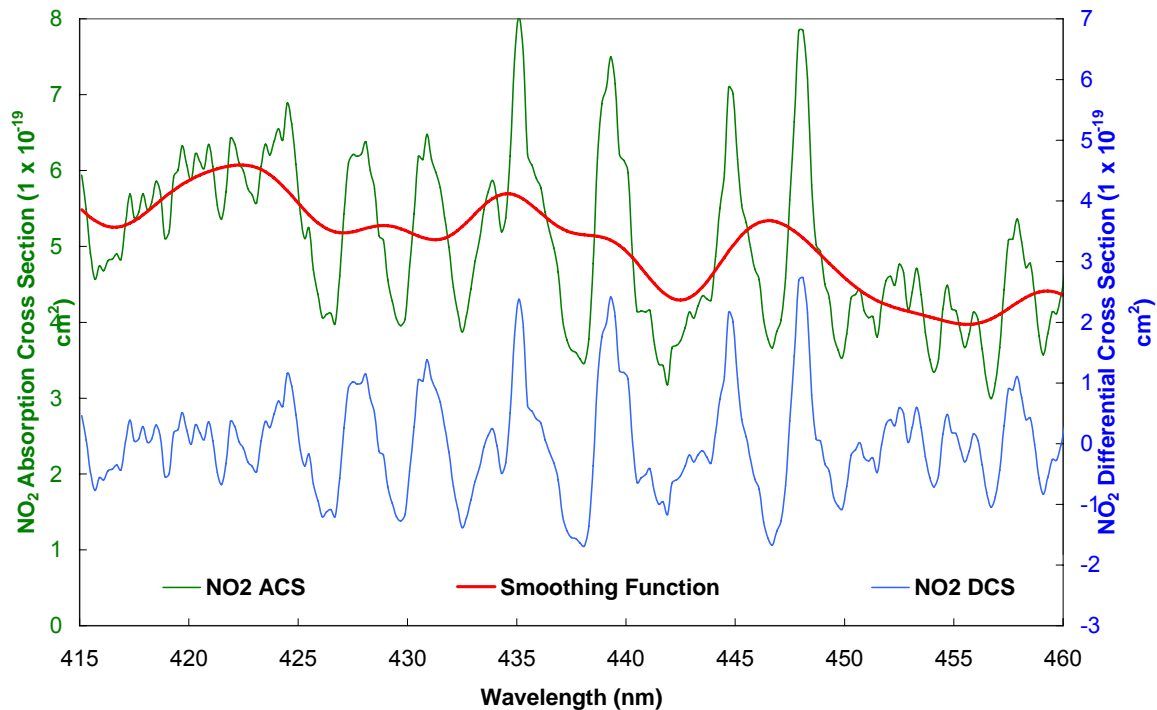
Figure 6.5 –NO$_2$ Absorption Cross Section (ACS), Smoothing Function, and NO$_2$ Differential Cross Section (DCS)

6.1.2. Reference Spectrum I$_\lambda$(0)

First of all, in order to apply the DOAS methodology correctly it is necessary to determine the reference spectrum that must be measured in optimal conditions: maximum height of the sun, clear sky, without clouds and with the minimal concentration of absorbers. Once the reference spectrum has been measured, the main remaining problem, before the use of the DOAS retrieval, is to know if the measurement of the reference spectrum is frequency calibrated.

Fish [68] has already discussed the problem of wavelength calibration. As an attempt to solve this problem for our observations, the data array, designed as I_0, is aligned with a spectrum of diffused solar radiation at high spectral resolution (the so-called "Fraunhofer" spectrum - I$_F$), using a similar DOAS procedure (SDP). The SDP results in a solution of the Lambert-Beer law in the Absence of Absorbers (LBAA).

In other words the identity $I_F = I_0$ is imposed.

In order to achieve a perfect spectral alignment, the so-called 'shift' and 'stretch' procedures are used. The first one is obtained with a shift given by the equation *(6.9)* of I_0 in the wavelength domain until an 'a priori' known spectral position is reached, the second by a variation of the dispersion parameters, that is, by modifying the slope and the intercept of the linear dispersion function *(6.5)* obtaining an accordion effect until the best spectral alignment is obtained. The solution of the LBAA is obtained by means of the Singular Value Decomposition (SVD). Marquardt's method [69] is used to minimize the Sum Of Square (SOS) of the residual spectrum, using the derivative of the SOS function and modifying the shift and stretch functional parameters. The output of the procedure is the wavelength calibrated I_0 spectrum (Figure 6.6). Obviously, for I_0 the dispersion parameters (K_1, K_2 and *Shift* in *(6.9)*) are different from the initial values (Table 6.1); the new values will be utilized as initial guess for the dispersion parameters in the application of the DOAS algorithm to the whole dataset of measurements.

Table 6.1 – Example of variation of the dispersion parameters for the I_0 calibration procedure

	$K_1(A)$	K_2	*Shift*
Init	6.375×10^{-1}	1.458×10^{-5}	1.000
Final	6.377×10^{-1}	1.445×10^{-5}	3.517
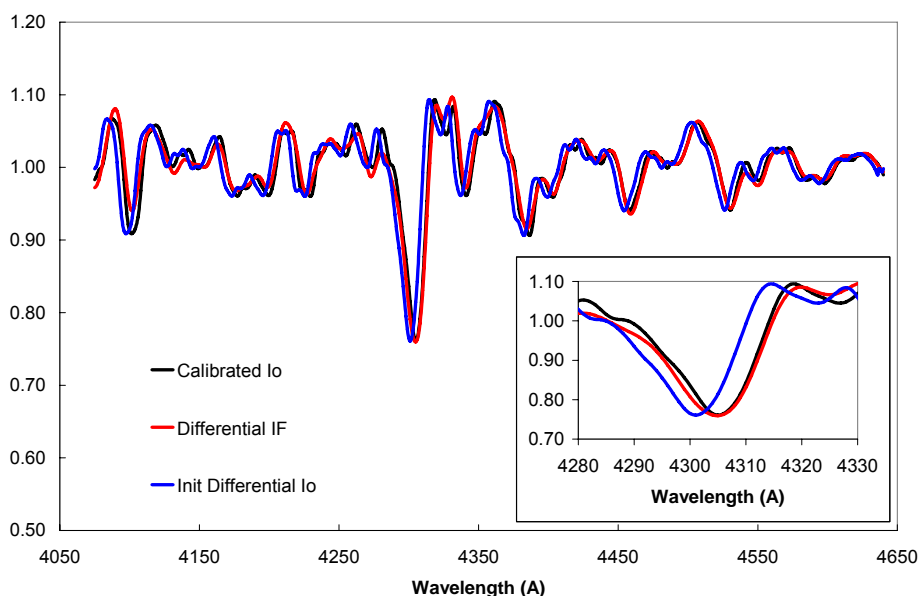
Figure 6.6 – Example of spectral alignment of $I_{\lambda 0}$ over I_F with SDP (Similar DOAS Procedure).

6.1.3. Cross-Section

The absorption coefficients of the investigated trace gases are fundamental in the analysis of the measured absorption spectra, so particular attention must be taken in the choice of the Absorption Cross Section (*ACS*) used in the DOAS processing. They must match the instrument resolution and the effects depending on temperature like their amplitude or shape variations have to be considered [70]. As shown by Sanders [71], a single representative temperature for the NO_2 absorption coefficients is the most reasonable choice although not exact from the viewpoint of atmospheric measurements,. Moreover it is the better approach to draw out the seasonal trend of the investigated compounds.

Furthermore if the spectral series of the absorption coefficients have not been obtained with the same spectrometer used for the acquisition of the solar spectra, a convolution function, typical of the instrument, has to be applied to the cross section (see next paragraph). Only after this step the Differential Cross Section (DCS) can be calculated.

6.1.4. Convolution and instrumental function

For the calculation of the convolution function of the spectrometer the best fit of the normal distribution function with the measurements of the spectral line obtained with the mercury calibration lamp can be used. Figure 6.7 shows an example of the simulations carried out in the laboratory with the aim to study the problem of the application of the convolution function to spectral series that will be used for the elaboration of the measured solar spectra.
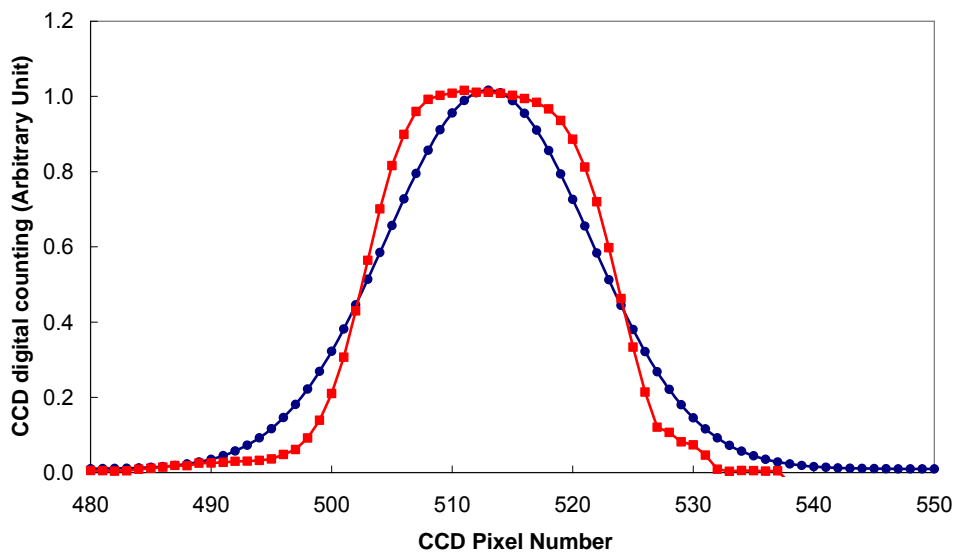
Figure 6.7 – Measurements of HG spectral lamp (red), Normal distribution fitting function (blue).

The analytic expression of the normal distribution in Figure 6.7 is:

$$G(\lambda) = a + b \cdot e^{-\frac{1}{2} \cdot \left(\frac{\lambda-c}{d}\right)^2}$$

(6.10)

With:

G(λ) = Convolution function

a=8.89·10^{-3},

b=1.0066,

c=5.25·10^{-2},

d=4.89.

Defining G(λ) as the convolution function and applying the definition of convolution to a spectral series:

$$S(\lambda) \otimes G(\lambda) = \sum_{i=\lambda_{iniz}}^{\lambda_{fin}} S(\lambda_i) \cdot G(\lambda - \lambda_i) \cdot \Delta\lambda_i$$

(6.11)

where:

S(λ) = spectral series not obtained with the utilized instrument (as the Fraunhofer spectral series or the absorption cross sections);

G(λ) = Convolution function*(6.10)*;

Δλ= spectral step (i.e. 2Å);

λ_{init} e λ_{fin} = Initial and Final wavelength of the considered spectral range.

By using the convolution theorem, which states that the Fourier Transform of the convolution of two functions is the product of the Fourier Transforms of these functions, the following equation can be written:

$$S(\lambda) \otimes G(\lambda) = F^{-1}\{\Sigma(K) \cdot \Gamma(K)\}$$

(6.12)

where Σ(k) and Γ(k) are the Fourier transforms F$\{S(\lambda)\}$ and F$\{G(\lambda)\}$ of S(λ) and of G(λ), respectively, and k the wave number. F^{-1} is the inverse Fourier transform.

Figure 6.8 shows the Fraunhofer spectrum after the application of the smoothing function (black line) and of the convolution *(6.11)* (red line).
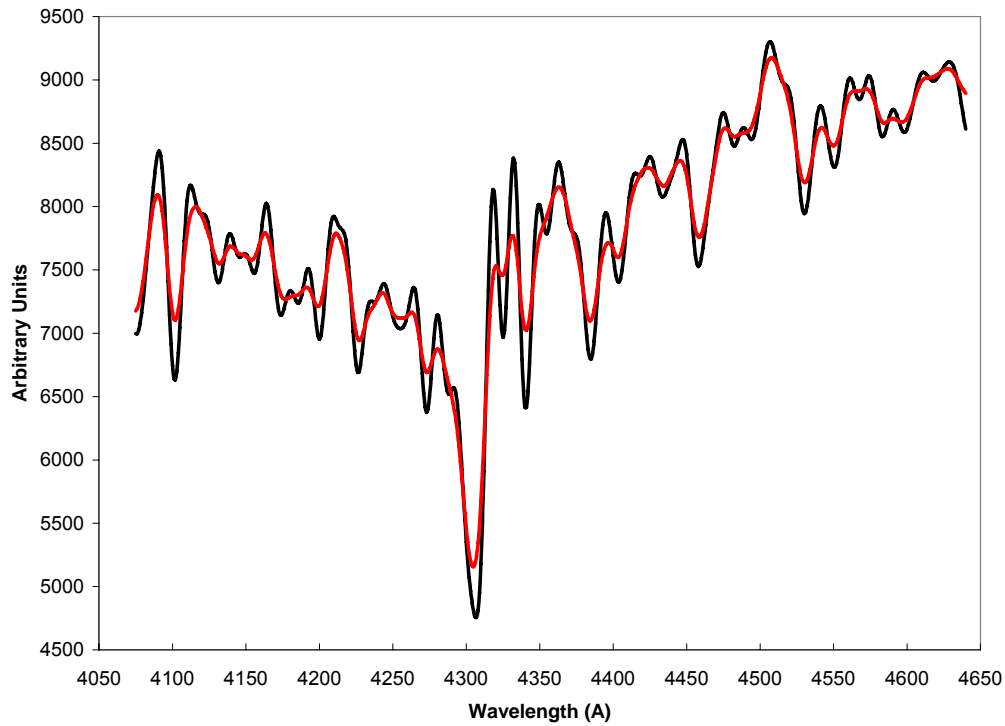
Figure 6.8 – Frahunofer spectrum (IF) with (red line) and without convolution (black line).
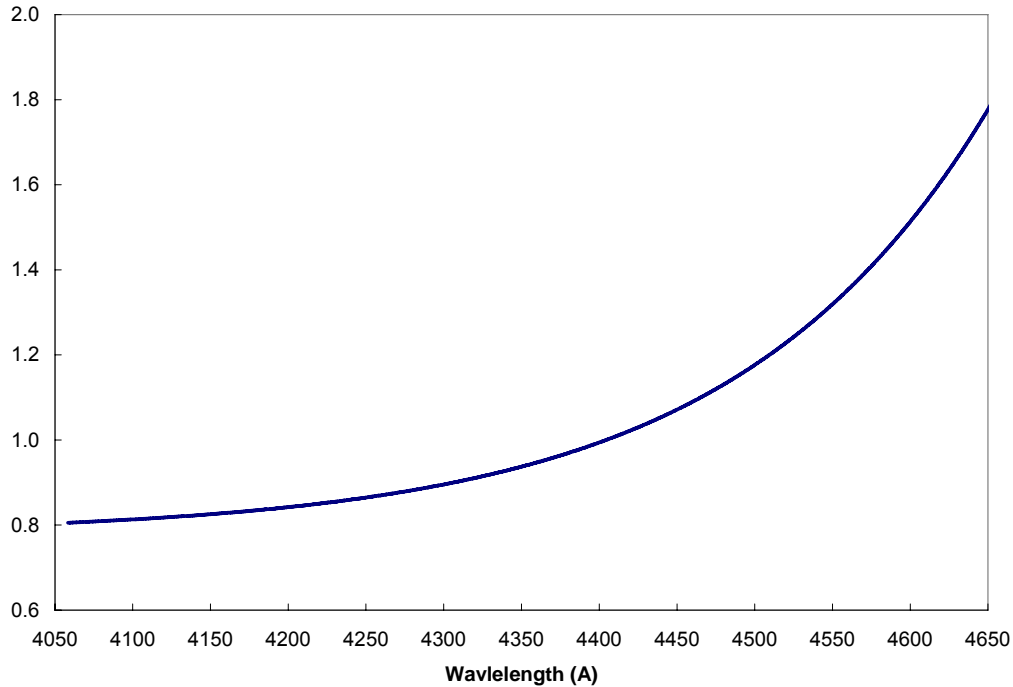
Figure 6.9 – Instrumental function of the spectrometer for 405nm < λ < 465nm.

The transfer function of the spectrometer can be calculated in the laboratory using spectral lamps with know spectra (Figure *6.9*).

Table 6.2 summarizes and clarifies which procedures have to be applied to each spectral series, both in the pre processing phase (the spectral calibration of $I_{\lambda,0}$ or in other words the $I_{\lambda,0}$ alignment with a wavelength calibrated spectrum) and in the application of the DOAS technique (involving also the absorption cross section of the compounds under examination - σ_λ).

Table 6.2 – Main procedures of the DOAS technique .

$I_{\lambda,0}$ Alignment	$I_{\lambda,0}$	I_F	$I_F/I_{\lambda,0}$
Convolution		X	
Linearization	X		
Fair Spacing	X	X	
Smoothing			X
Differentiation			X
I_λ DOAS Processing	I_λ	σ_λ	$Ln(I_\lambda/I_{\lambda,0})$
Convolution		X	
Linearization	X		
Fair Spacing		X	
Smoothing		X	X
Differentiation		X	X

6.2. DOAS Algorithms applications

6.2.1. Qualitative Approach

Figure 6.10 shows the comparison between the NO_2 Differential Cross Section (DCS) spectral series with the Differential Log Ratio spectrum of the reference and analyzed spectra. The two spectral series are properly scaled with the aim to allow for a direct evaluation of the spectral features. The strong correlation that can be noted demonstrates as in this spectral region the nitrogen dioxide is the main absorber. Figure 6.11 plots the same as in Figure 6.10, but in an other spectral window scanned by SPATRAM (320-360nm), and the absorbing features of the ozone can be easily identified, confirming that this spectral range can be utilized for the determination of the O_3 optical depth. The overlapping of the two curves is really amazing, even if further operations of 'Shift' and 'Stretch' of the measured spectrum are necessary in order to reach a perfect alignment of the two curves.
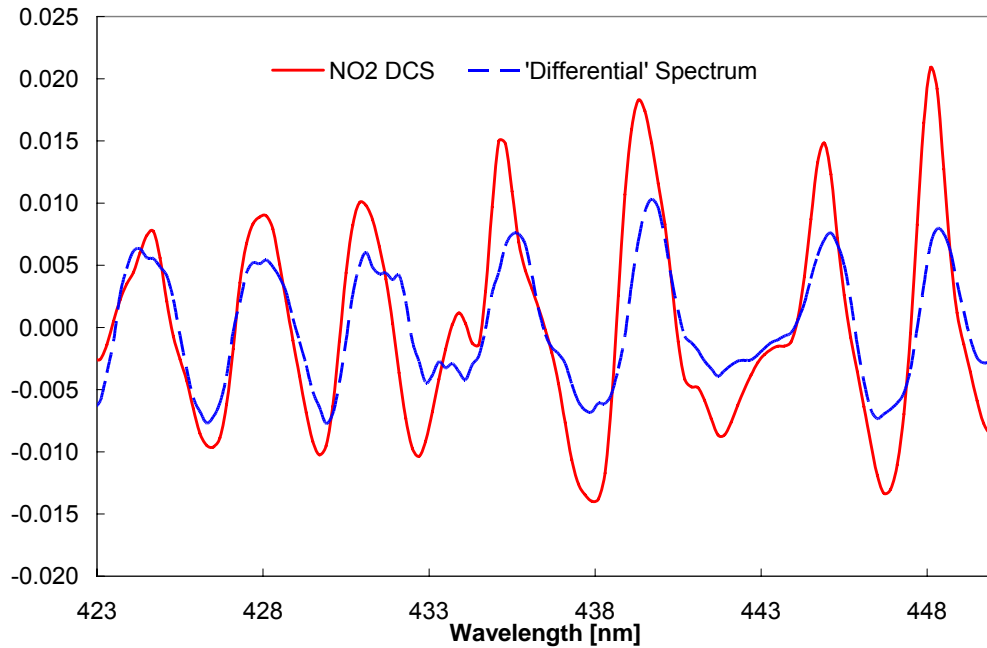
Figure 6.10 - The 'Differential' spectrum (the difference between Log-Ratio and Smooth (Log-Ratio)(blue line), where Smooth(x) is a low pass filter operator and the NO₂ Differential Cross Section(red line) – properly scaled - are plotted together. In the selected spectral range, the differential spectrum features show good agreement with the differential cross section of nitrogen dioxide, allowing for the determination of its atmospheric content.
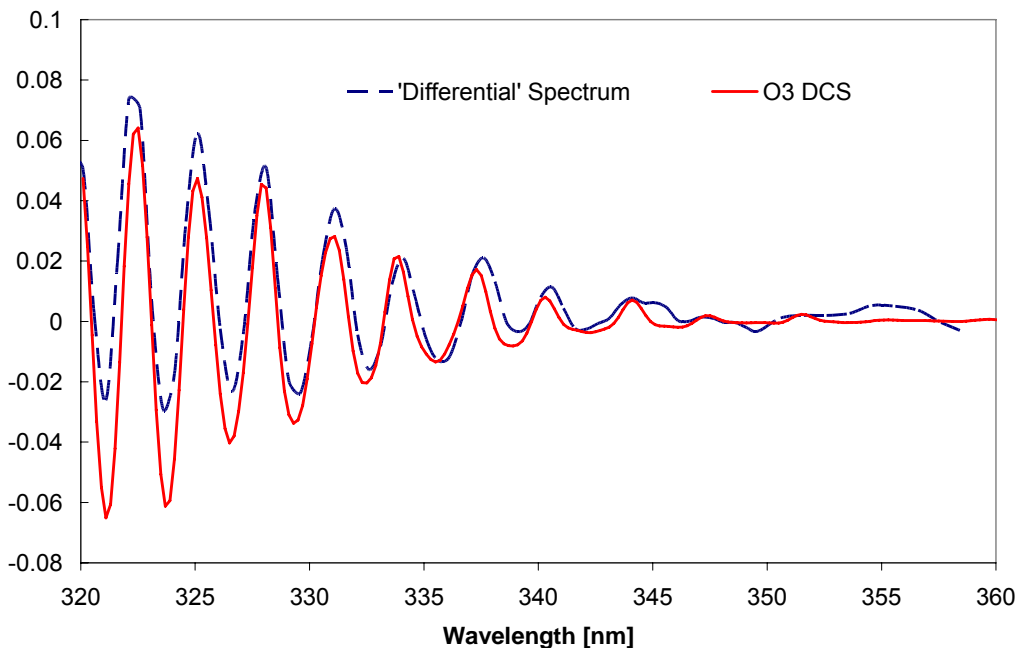
Figure 6.11 - The 'Differential' spectrum (the difference between Log-Ratio and Smooth (Log-Ratio), where Smooth(x) is a low pass filter operator) and the O₃ Differential Cross Section – properly scaled - are plotted. In the selected spectral range, the differential spectrum features show good agreement with the differential cross section of ozone, allowing for the determination of its atmospheric content.

6.2.2. Io effects on the Retrieval

As remembered in § 4.5 the outputs of the DOAS processing are usually called Slant Column Density (SCD – the number of molecules per square centimetre, along the optical path); it has to be taken into account that the reference spectrum is obtained at the local noon, when the absorption of the minor compounds is negligible but not zero, so the retrieved values are the Differential Slant Column Density (DSCD). These lasts are the difference between the gas content in the analyzed spectrum and the reference one. With that assumption ($I_{\lambda,0}$= reference spectrum obtained at local noon), here in after, in the DOAS Master-Equation, the SCDs have to be replaced by the DSCDs. The problem of the absorber content in $I_{\lambda,0}$ arise. For measurements obtained at high latitude (in polar regions) the problem is solved with some simple considerations [72]. At mid-latitudes usually the Langley plot of the AM and PM measurements versus the series of the Air Mass Factors, is utilized for the calculation of the minor compounds content in the reference spectrum. As described in § 4.6 the conversion of the Slant Column Density (SCD) to Vertical Column Density (VCD) quantities is obtained with the Air Mass Factor (AMF), that is the increase of the radiation along the optical path of measurements (oblique) compared with the vertical one.

In the following this problem will be discussed mainly for the NO$_2$ retrieval even if some examples regarding the O$_3$ will be presented

A spectrum, obtained with the SPATRAM instrument on 29 July 2004 at local noon on a cloudless day, is used. For calculation of the nitrogen dioxide amount in the background spectrum, the NO$_2$ DSCDs obtained for the 29 July are plotted versus the calculated AMF (Figure 6.12).

As expected for the NO$_2$ photochemical activity, the AM values are lower than the PM ones, that lead to 2 straight line converging to the value of NO$_2$ DSCD at local noon ($AMF \approx 1$). Due to the greater errors mainly caused by the shorter optical path of measurement, the separate best fits of the AM and PM values does not intercept themselves at the value of the minimum AMF of the day, but for a negative value of AMF (unrealistic). So the best fit line has to be calculated considering the AM and PM values together and not separately. Performing the above described computation the red line in Figure 6.12 is obtained and the DSCD for the minimum AMF of the chosen day is of 4.983×10^{+15}. This value is considered as the NO$_2$ background content (or reference amount) of the Reference Spectrum and has to be added to the retrieved DSCD in order to have the SCD (Figure 6.13 and Figure 6.14).

In order to check the processing procedure, the DOAS algorithm is applied to the spectrum chosen as $I_{0,\lambda}$, considering it also as the reference spectrum. The

retrieved value is equal to $1.2 \times 10^{+11} \, molecules \cdot cm^{-2}$, a very low amount compared with the typical range for AM and PM DSCD values ($1.0 \times 10^{+16} \sim 1.0 \times 10^{+17} \, molecules \cdot cm^{-2}$).
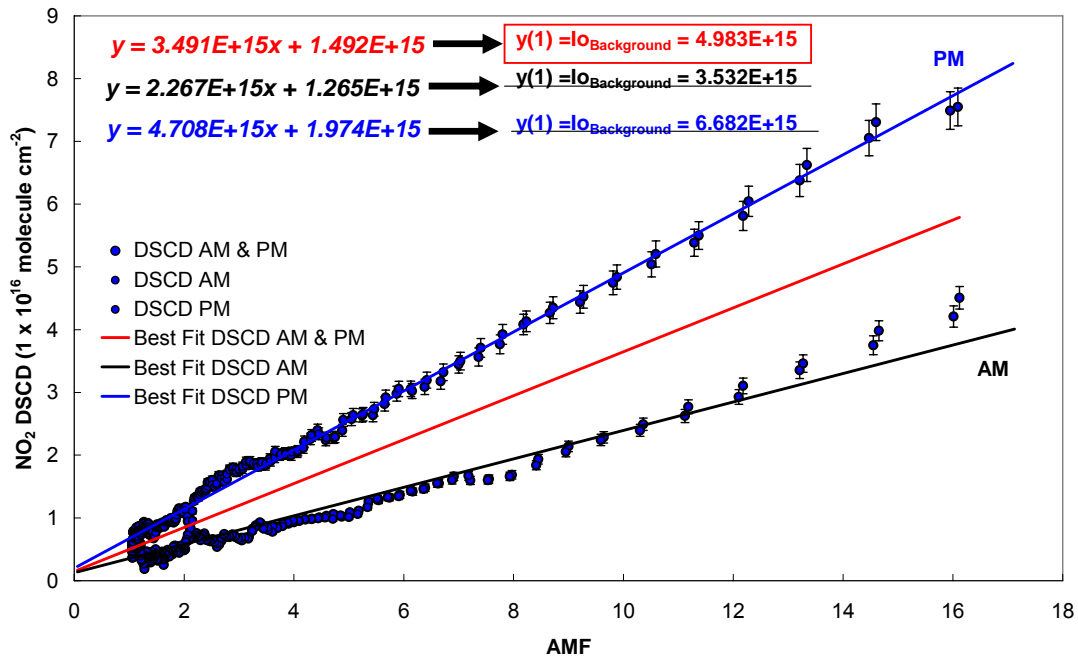
Figure 6.12 - NO_2 DSCD AM and PM values, obtained for the 29 July 2004, plotted versus the calculated AMF. The best fits for the AM values (Black line), PM values (Blue line) and for both (Red line) are shown.
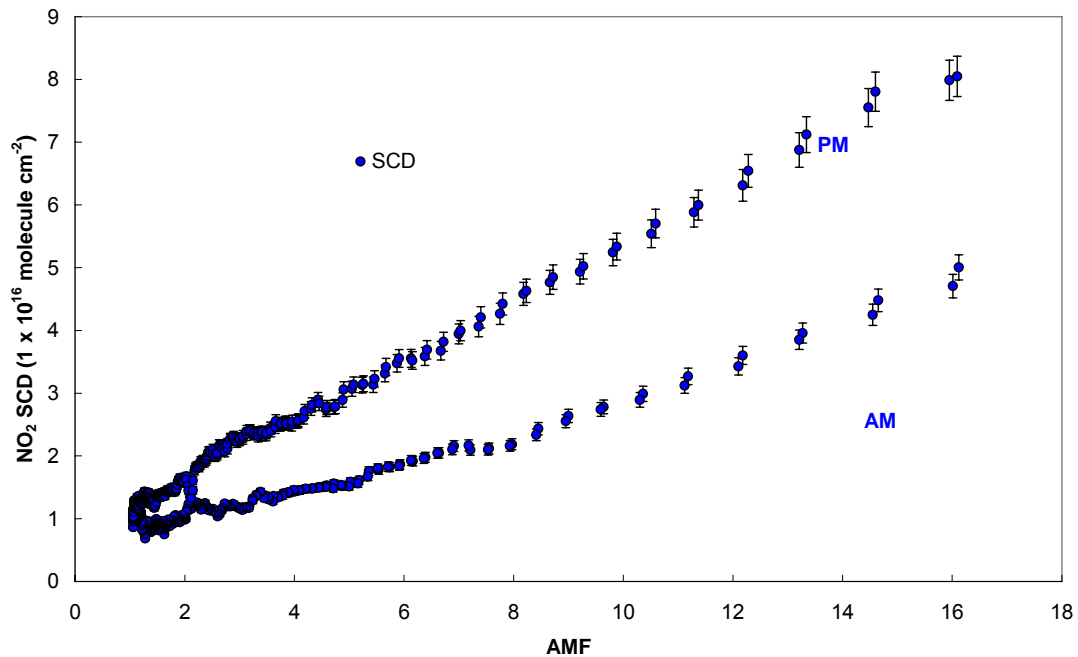
Figure 6.13 - NO_2 SCD AM and PM values, obtained for the 29 July 2004, plotted versus the calculated AMF
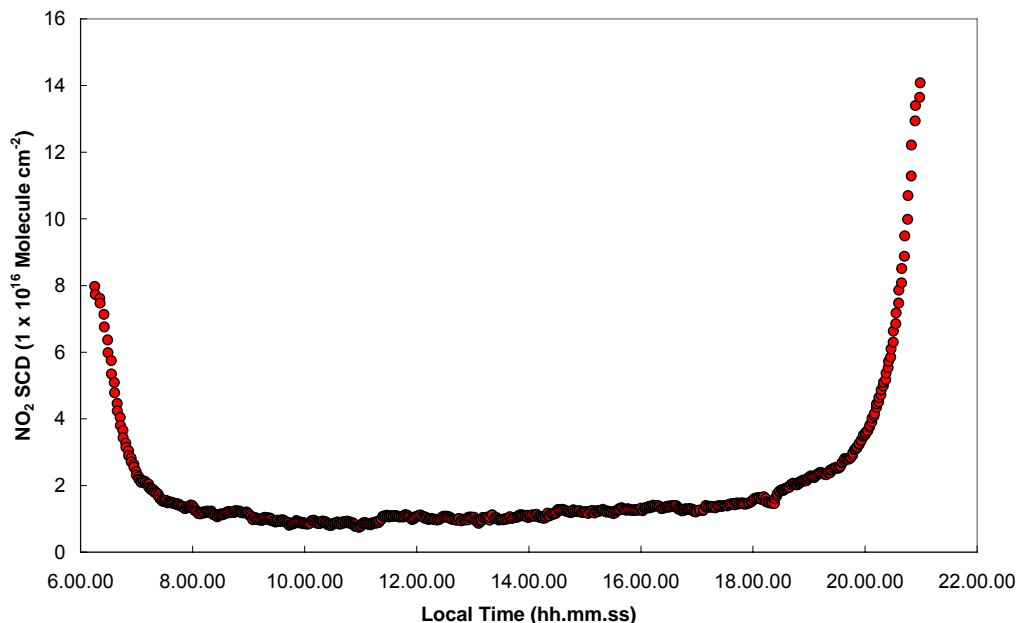
Figure 6.14 - Diurnal variation of NO$_2$ SCD, obtained for the 29 July 2004

Figure 6.15 shows AM and PM values for NO$_2$ SCD values, obtained for the 29 July 2004, and the AMF values calculated using the AMEFCO (Atmospheric Model for Enhancement Factor COmputation) model(see § 4.6), plotted versus the Solar Zenith Angle.
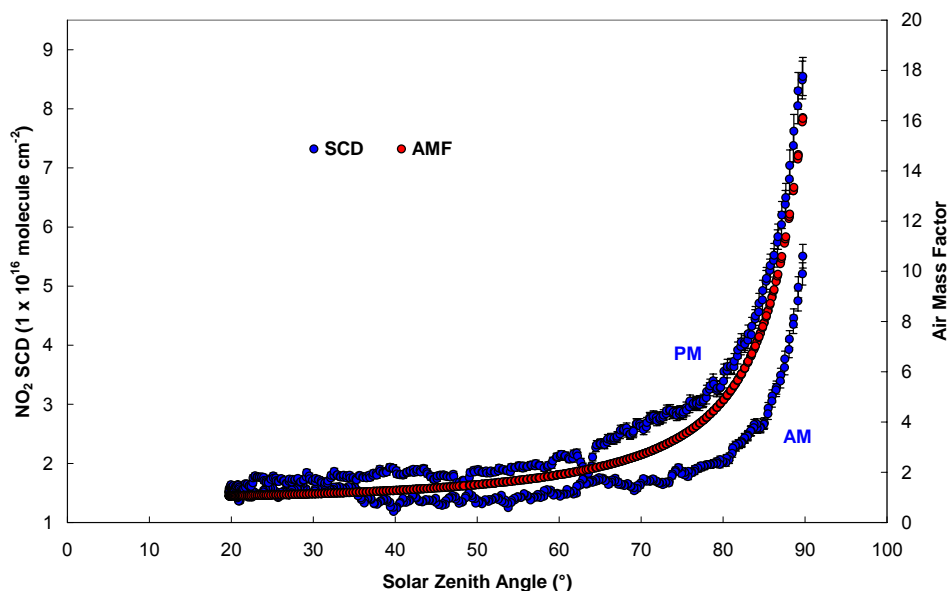
Figure 6.15 - NO$_2$ SCD AM and PM values, obtained for the 29 July 2004,and calculated AMF, plotted versus the Solar Zenith Angle. The mathematical model for the calculation of the AMF doesn't contain the photo-chemical module therefore the AMF function lies between the AM and PM values for NO$_2$ SCD

The mathematical model for the calculation of the AMF doesn't contain the photo-chemical module therefore the AMF function lies between the AM and PM NO_2 SCD values.

Figure 6.16 shows the diurnal variation of the NO_2 Vertical Column Density values (units are molec cm^{-2}). Figure 6.17 presents the NO_2 average concentration (in molec cm^{-3}) assuming the typical altitude for the NO_2 bulk is 30 Km, and considering the atmosphere of 50Km high by means of a simple division:

$$VCD(molec/cm^3) = VCD(molec/cm^2)/(5 \times 10^6 cm)$$
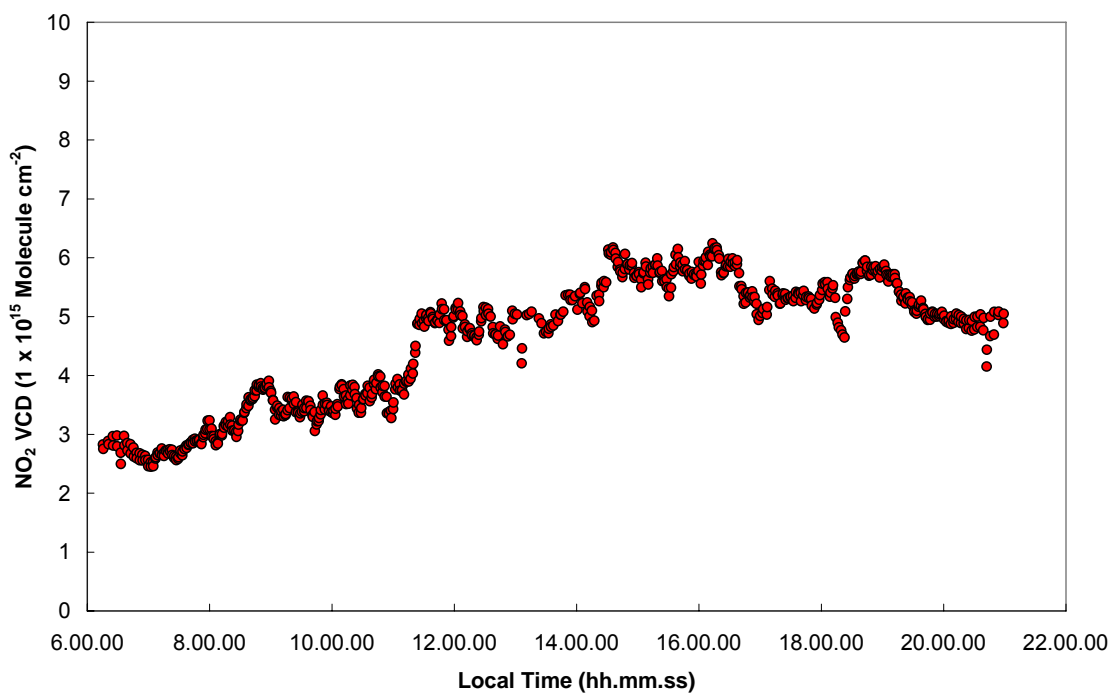
Figure 6.16 - Diurnal variation of NO_2 VCD, obtained for the 29 July 2004
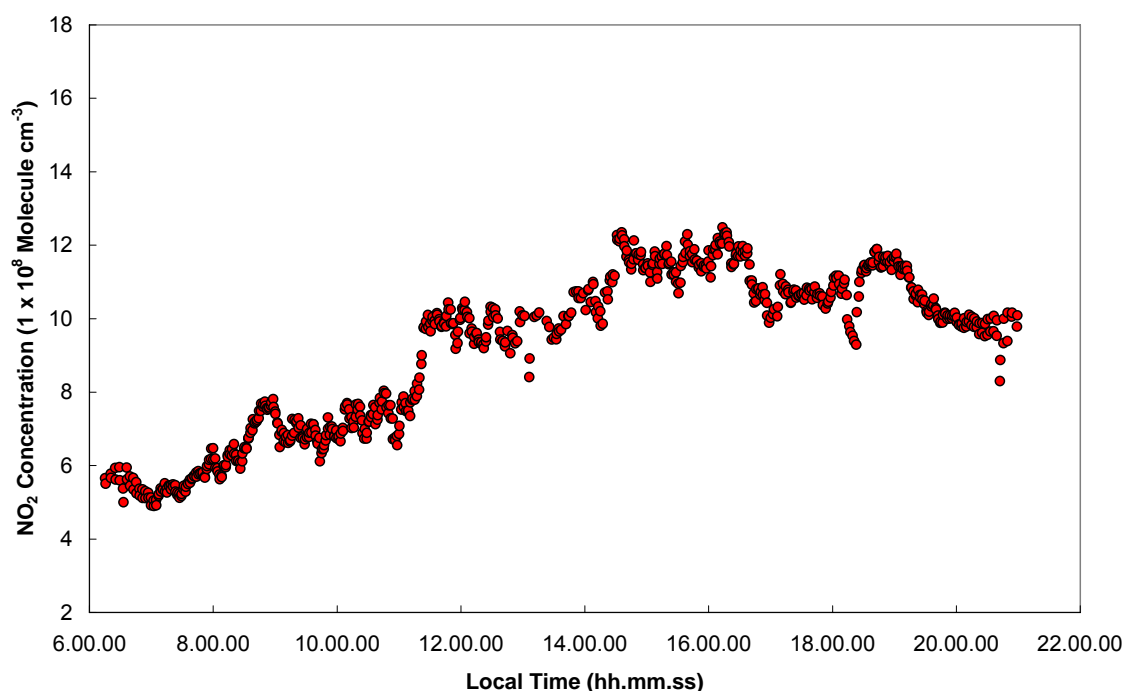
Figure 6.17 - Diurnal variation of NO$_2$ concentration, obtained for the 29 July 2004

In science applications it is convenient to calculate the volume mixing ratio, defined as the ratio of the number density of the gas (i.e. number of molecules per unit volume) to the total number density of the atmosphere.

Figure 6.18 shows the diurnal variation of the NO$_2$ Mixing Ratio (MR_{NO_2}) (in ppbv-parts per billion by volume) obtained applying the formula:

$$MR_{NO_2} = \frac{VCD_{NO_2}}{5} \cdot \frac{(R \cdot T)}{P \cdot NAv} \cdot 1 \times 10^9 \qquad (6.13)$$

where:

MR_{NO_2} = NO$_2$ Mixing Ratio

VCD_{NO_2} = Vertical Column Density (molec cm^{-2})

R: 8.314 J/K mol

T = Temperature (K)

P = 1.01325 x10^5 Pascal

NAv = Avogadro Number = 6.023 x10^{23} molec/mol

The relation (6.13) is obtained from the well known equation of state of the Ideal gas [36].
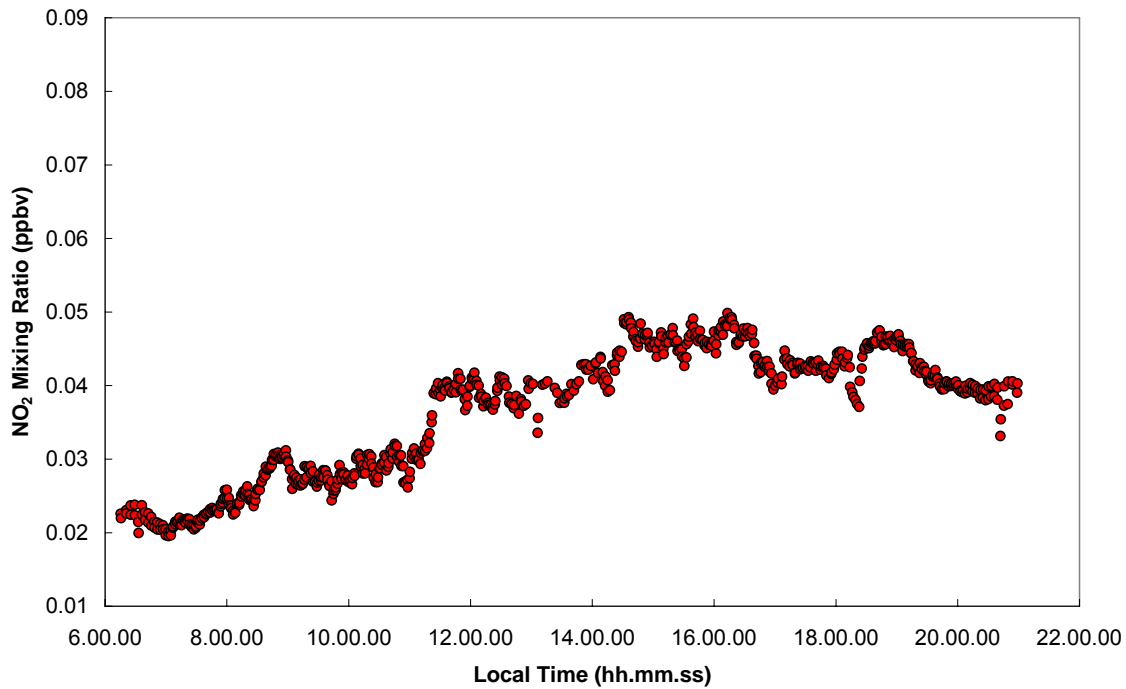
Figure 6.18 - Diurnal variation of NO₂ Mixing Ratio, obtained for the 29 July 2004

In the field of air pollution, the concentration units (mg/m^3) are often used, for example when threshold values are defined. Sometimes it is common to apply simple factors to convert one unit into the other (e.g. 1 ppb – part per billion - O_3 corresponds to about 2 μg/m^3). Or the exact conversion factor at a single temperature (e.g. 20°C) and standard pressure is used.

The NO_2 concentration, plotted in Figure 6.19, can be calculated applying:

$$\rho_{NO_2} = \frac{VCD_{NO_2}}{5} \cdot \frac{M_{NO_2}}{NAv} \cdot 1 \times 10^6 \quad \text{in} \quad \mu\text{g/m}^3 \qquad (6.14)$$

where:

VCD_{NO_2} = NO₂ Vertical Column Density (molec cm^{-2})

M_{NO_2} = Molar weight of NO₂

NAv = Avogadro's Number = 6.023 x10^{23} mol^{-1}
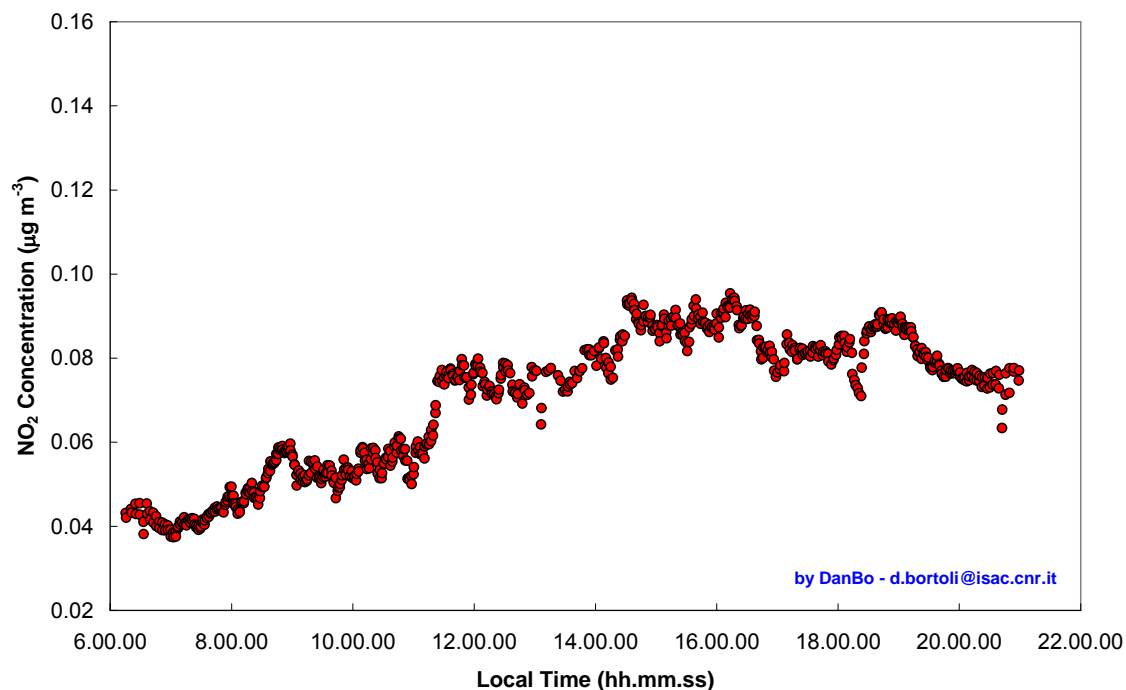
Figure 6.19 - Diurnal variation of NO$_2$ concentration, obtained for the 29 July 2004

Also for the O$_3$, the same argumentation used for the NO$_2$ can be employed.

As done for the NO$_2$ the calculation of the amount of ozone in the reference spectrum was done considering a spectral series obtained on 3 April 2004 at local noon on a cloudless day. Figure 6.20 plots, the O$_3$ DSCD values obtained for the 3 of April versus the calculated AMF.

The photochemical activity of Ozone is not so important as for NO$_2$, therefore the AM and the PM values for ozone are almost overlapped and the linear fitting function of both series can be used in order to evaluate the ozone content in the reference spectrum. For AMF = 1 the value of $2.493 \times 10^{+17}$ is obtained; applying the inverse definition of Dobson Unit, the results is 9.2 DU This value is considered as the O$_3$ background content of the Reference Spectrum and has to be added to the retrieved DSCD values in order to have the SCD values (Figure 6.21).
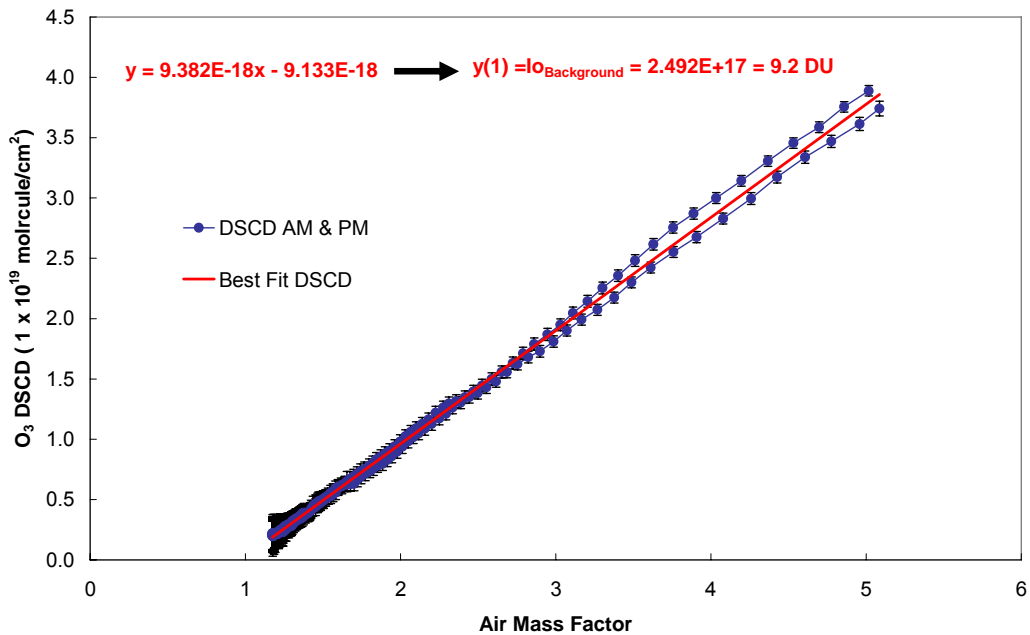
Figure 6.20 - O₃ DSCD AM and PM values, obtained for 3 April 2004, plotted versus the calculated AMF. The best fits for the AM and PM values is shown.

Fore the estimation of the goodness of the O_3 SCD values retrieved, and in order to evaluate the calculated AMF, both are plotted in Figure 6.22 versus the SZA. Since O_3 is not so photo-chemical active as the NO_2, the AMF function overlaps the AM and PM O_3 SCD values.
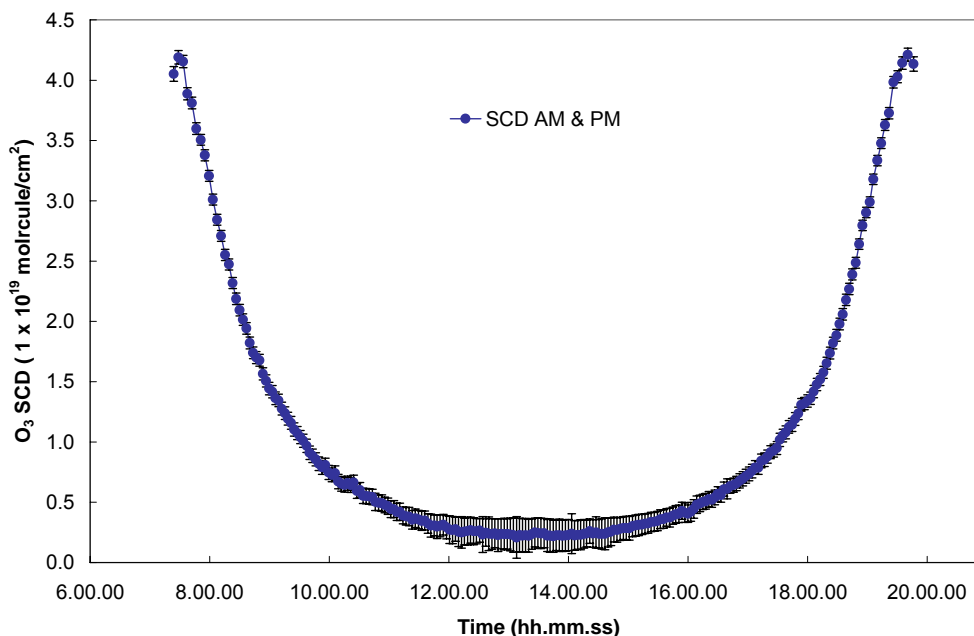
Figure 6.21 - Diurnal variation of O₃ SCD, obtained for 3 April 2004

Comparing the shapes of the AMF and of the SCD values in the plots 6.14 and 6.21, it is clear the importance of the spectral range of measurement in the

calculation of the AMF. First of all the intensities are very different (the maximum for the 423-450nm spectral range is about 17, whereas for 320-360nm the maximum is about 5); in addition also the locations in the domain of the SZA are very different: in the Visible region (423-450nm) the maximum value is reached at a SZA of 90°; whereas in the UV (320-360nm) the maximum is reached at a SZA of 86°. The AMF is applied for the calculation of the Vertical column content of O_3 and by means of the definition of Dobson Unit (DU) the plot in Figure 6.23 is obtained. As expected the behavior of the diurnal variation of the two species (NO_2 and Ozone) is very different (Figure 6.16 and Figure 6.23). Figure 6.16 shows how the vertical columns of NO_2 grow during the day, mainly due to the photochemical activity of this compound that, trough the reaction *(3.8)*, increases towards the sunset time. In addition the VCD values at the sunrise are lower than the sunset ones (Only one day is plotted here, but in the following chapter the NO_2 and O_3 VCDs seasonal variation along the first year of measurements with SPATRAM will be presented where it is clear the systematic differences between the sunrise and sunset VCD values of both species).
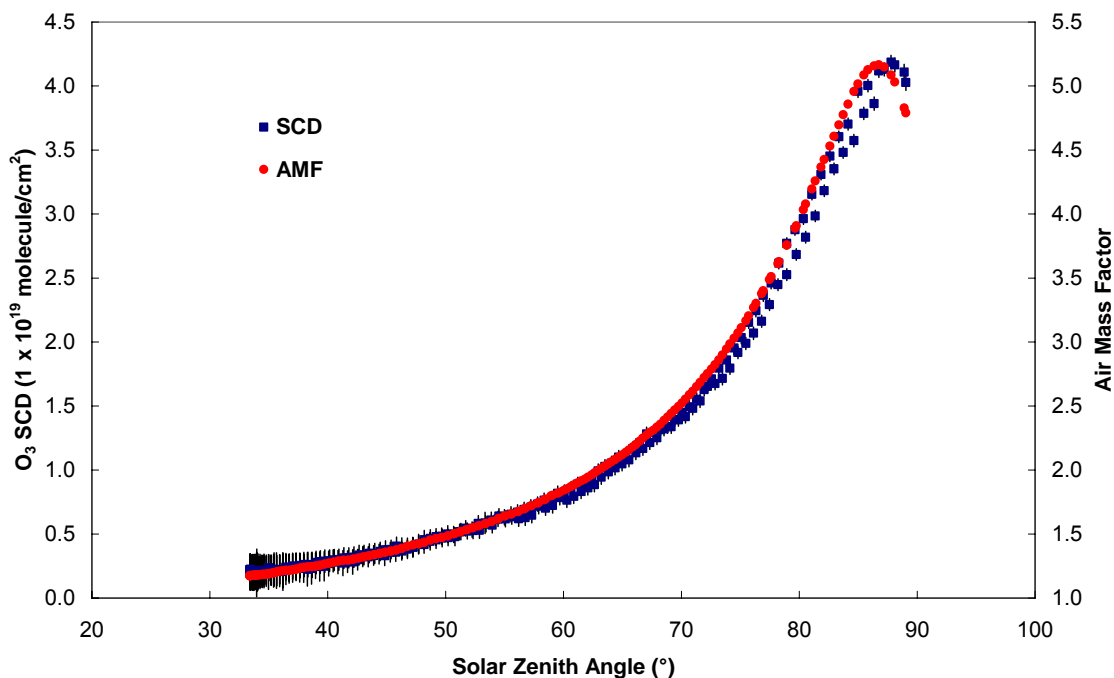
Figure 6.22 - O_3 SCD AM and PM values, obtained for 3 April 2004, and calculated AMF, plotted versus the Solar Zenith Angle.
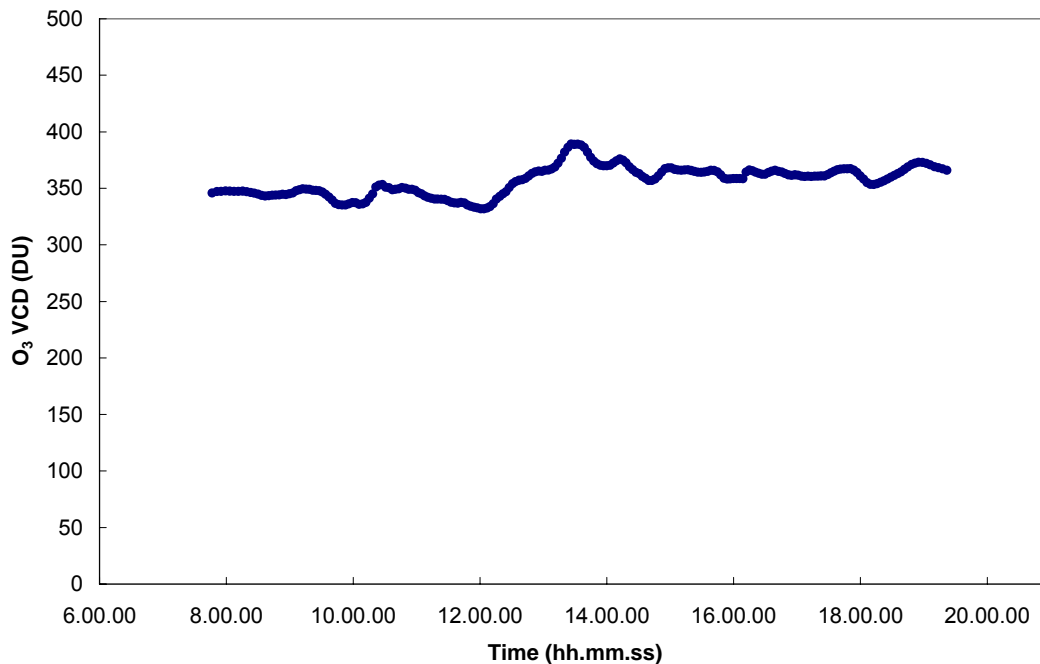
Figure 6.23 - Diurnal variation of O₃ concentration, obtained for 3 April 2004

For the Ozone values (Figure 6.23) it has to be observed that along the day their deviations from the daily mean value (357 DU) is very small during the sunset and sunrise periods, and increase for the central hours of the day (for values of SZA lower than 50°). This last feature is mainly due to the errors related to the measurements, that increase as the Solar Zenith Angle decreases or, in other words, when the optic path of measurement becomes too "short" (see § 4.6.1 and Figure 4.1).

6.2.3. DCS effects on the Retrieval

A sensitive study was performed in order to determine the effect of different acs at different temperatures 221, 241, 273 and 293 K [73] upon AM and PM NO_2 Slant Column Density values for a solar zenith angle of 90°. The results are shown in Figure 6.24.

Analysing Figure 6.24, it is immediately possible to note that the AM values are lower than the PM, mainly due to the photochemical activity of the nitrogen dioxide. It is important to underline the higher slant columns values obtained for higher absorption cross section temperatures.
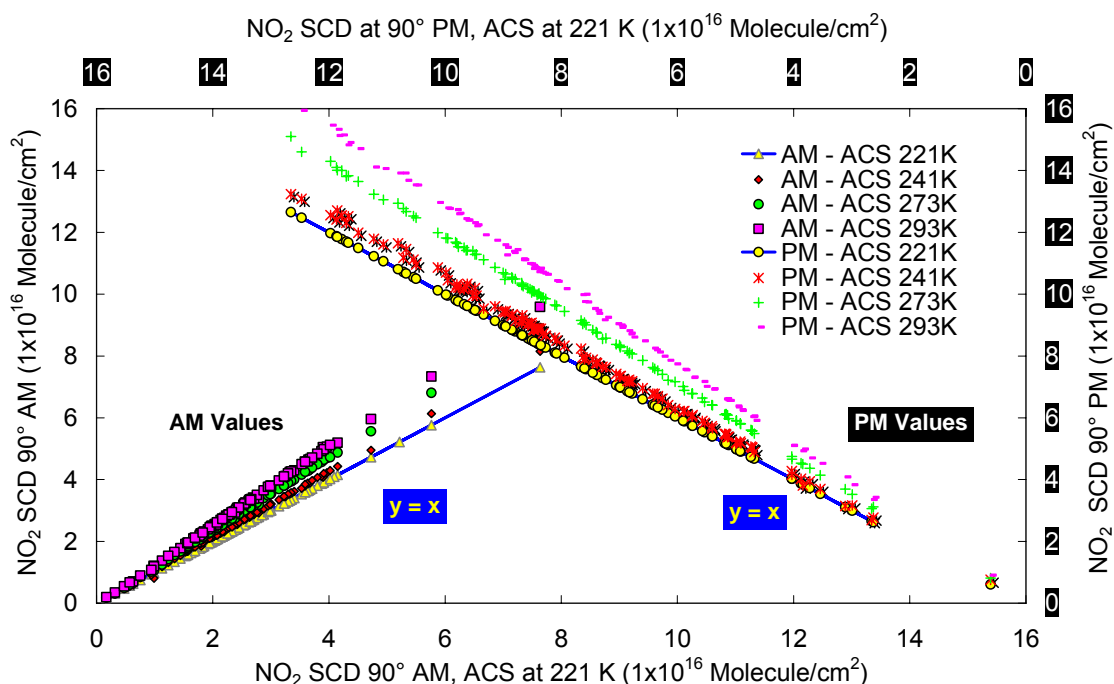
Figure 6.24 - Evora Station - Retrieved values of NO$_2$ AM sc and PM sc at 90° SZA obtained with Absorption Cross-Sections (ACS) at various temperatures.

This confirms the importance of choosing the right absorption spectra used in the DOAS data processing. In fact, if the cross section at 293K is adopted for the retrieval of *AM DSCD* values, the slant column values are overestimated by about 26%. For the *PM* slant column values, the overestimation can reach 28%; the difference between AM and PM errors are imputable to polarisation phenomena not accounted in the polarisation cross sections adopted in the DOAS processing. The slope of the linear fitting functions, summarized in Table 6.3 confirms this fact too. With the aim to verify the obtained results for different absorption cross sections temperatures, the Terra Nova Bay station data have also been processed. Figure 6.25 shows these results and Table 6.4 summarizes the slope of the linear fitting functions for this site.

Table 6.3 - Slopes of the linear fitting function of the results presented in Figure 6.24

NO$_2$ ACS Temp (°K)	AM Fitting slope	NO$_2$ ACS Temp (°K)	PM Fitting Slope
221	1	221	1
241	1.06	241	1.07
273	1.17	273	1.18
293	1.26	293	1.28
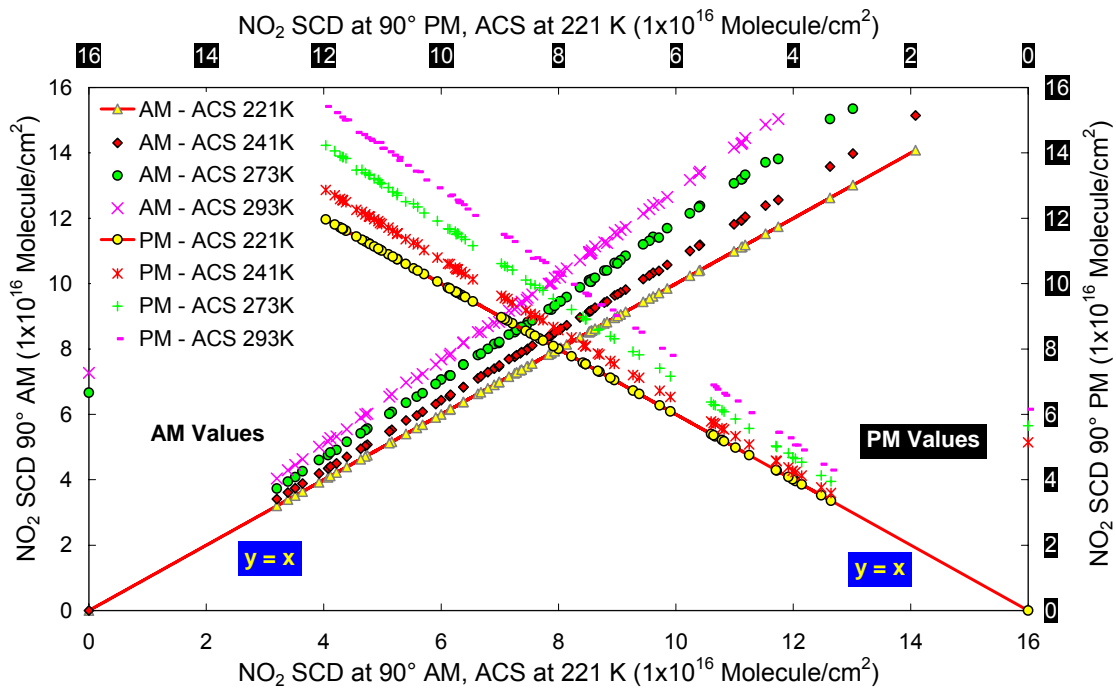
Figure 6.25 - Terra Nova Bay station - Retrieved values of NO₂ AM sc and PM sc at 90° SZA obtained with Absorption Cross-Sections (ACS) at various temperatures.

Table 6.4 - Slopes of the linear fitting function of the results presented in Figure 6.25.

NO₂ ACS Temp (°K)	AM Fitting slope	NO₂ ACS Temp (°K)	PM Fitting Slope
221	1	221	1
241	1.07	241	1.07
273	1.18	273	1.18
293	1.28	293	1.28

For the Antarctic scenario it is possible to highlight the constancy of the errors related to the different *ACS* temperatures associated with *AM sc* and *PM sc* values. A possible cause of this behaviour may be due to the fact that the atmosphere of the south Polar Regions is generally more 'clean', and also in the greater light-time variation that occurs at high latitude.

Figure 6.24 and Figure 6.25 present a clear linear dependency between slant column errors and *ACS* temperature. The equation that describes the relation is of the form:

$$Y = K \cdot \Delta T \qquad (6.15)$$

where: ΔT is the temperature variation of the absorption cross section and *K* the parameter depending on the geographical position and time of the measurement. Table 6.5 summarizes the obtained values for *K* and R^2:

Table 6.5 - K and R^2 values obtained for equation 1

	K	R^2
High latitudes	0.383	0.994
AM Mid-Latitudes	0.356	0.989
PM Mid-Latitudes	0.386	0.996

The application of equation *(6.15)* to the retrieved NO_2 SCD values allows for their correction if a temperature for the NO_2 absorption cross section different from the real one is utilized in the DOAS processing, without the application of the methodology to the full dataset.

7. Results and discussion

7.1. Introduction

In this chapter some results of NO_2 and O_3 VCD values obtained at high and mid latitudes respectively with the GASCOD and the SPATRAM instruments are presented and discussed. Comparisons of the obtained results with satellite retrievals of O_3 and NO_2 VCD values are also shown and examined.

7.2. Satellite Data Source - GOME and TOMS

ERS-2 was launched in April 1995 into a near-polar sun-synchronous orbit at a mean altitude of 795 km. The descending node crosses the equator every 2800 km at 10:30 local time. GOME (Global Ozone Monitoring Experiment), on board ERS-2 satellite, is a nadir-scanning double monochromator covering the 237 nm to 794 nm wavelength range with a spectral resolution of 0.17 - 0.33nm (depending on the spectral region). The spectrum is split into four spectral channels, each recorded quasi-simultaneously by a 1024-pixel photodiode array. The global spatial coverage is obtained within 3 days at the equator by a 960 km across-track swath (4.5 s forward scan, 1.5 s back scan). The ground pixel size of the measurements is 320 X 40 km^2. The solar irradiance is measured daily. Details of the overall scientific objectives of GOME, instrument concept, and scientific results are reported elsewhere [8], [9] [74] - [79]

The Nimbus7 spacecraft was in a south-to-north, sun-synchronous polar orbit so that it was always close to local noon/midnight below the spacecraft. Thus, ozone measurements from TOMS (Total Ozone Mapping Spectrometer) on board Nimbus7 satellite) were taken for the entire world every 24 hours. TOMS directly measures the ultraviolet sunlight scattered by the Earth's atmosphere. Total column ozone is inferred from the differential absorption of scattered sunlight in the ultraviolet range. Ozone is calculated by taking the ratio of two wavelengths (312 nm and 331 nm), one wavelength where ozone absorbs and another where absorption is very weak. The instrument has a 50 km^2 field of view at the sub-satellite point. TOMS collects 35 measurements every 8 seconds as it scans right to left producing approximately 200,000 ozone measurements daily.

7.3. Ground-Based results and Satellite Comparison

The above mentioned sensors on board ERS-2 and Nimbus 7 satellites and the ground-based spectrometers capture major stratospheric features similarly.

Although it is difficult to evaluate precisely the accuracy of the NO_2 total column due to various problems such as the diurnal variation of NO_2 and the profile shape effect on the Air Mass Factor (AMF), the overall accuracy in areas of low tropospheric NO_2 is estimated to fall within the 5% to 20%.

7.3.1. High Latitudes

As remembered at the beginning of Chapter 5, GASCOD is the forefather of the SPATRAM equipment and the DOAS algorithms were developed and improved with their application to the data obtained during 9 years in the Antarctic Station of Terra Nova Bay. Also the first results for NO_2, and O_3 VCD were retrieved with the application of the DOAS algorithms to the Antarctic data. In addition the comparison with the satellite retrievals obtained with the GOME spectrometer was performed. Mainly for the above mentioned reasons some results obtained with the GASCOD at high latitudes will be presented and discussed below.

7.3.1.1. Seasonal variations

A clear seasonal trend emerges from the results obtained for the whole period of activity of the GASCOD spectrometer at Terra Nova Bay station (Figure 7.1).
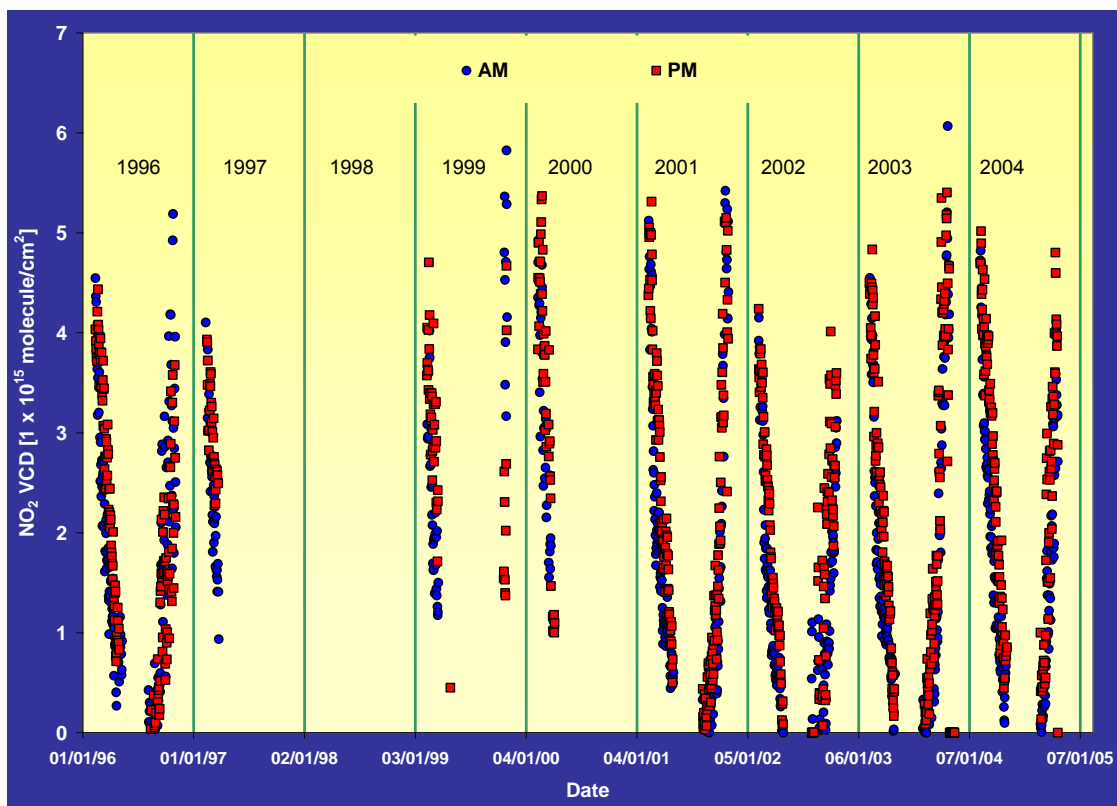
Figure 7.1 - NO₂ vertical column Amounts measured by GASCOD at Terra Nova Bay station (1996-2004), during morning and evening twilight.

During the first year of activity (1996) the equipment worked well. In the following years (1997, 1999 and 2000), some hardware and software bugs caused the loss of data during the austral spring season. In 1998 problems occurred to the power supply of the station and prevented data acquisition. From 2001 to 2004 the GASCOD provided data for the whole period.

In the austral autumn (when the sun starts to descend below the horizon – 10/11 February) the NO$_2$ VCD values decrease from a value of about $5.0 \times 10^{15}\ molecule/cm^2$ to less than $1.0 \times 10^{15}\ molecule/cm^2$, at the beginning of the winter season (when the sun remains always below the horizon – 7/8 May). At the end of the polar night (8/9 August) the nitrogen dioxide total columns increase with a different slope starting from more or less $1.0 \times 10^{14}\ molecule/cm^2$. Both features are due to the know processes of the lower stratospheric denoxification (conversion of NO and NO$_2$ into HNO$_3$) in the winter season. In other words: the length of the daylight strongly affects the NO$_2$ total columns that are also influenced by the stratospheric temperature. The small pre- and post-winter column amounts are the result of gas phase reactions converting NO$_2$ in N$_2$O$_5$, heterogeneous reactions converting N$_2$O$_5$ and ClONO$_2$ into HNO$_3$, and possible denitrification (that is sedimentation of HNO$_3$ particles leading to reduced NO$_y$) as described in § 3.2. In the summer months the lifetime of HNO$_3$ is reduced by photolysis and reactions with OH, both releasing NO$_2$.The continuous sunlight in summer inhibits the formation of N$_2$O$_5$, thus reducing the diurnal variation. In winter there is no daylight to photolyze N$_2$O$_5$, which similarly reduces the diurnal variation.

7.3.1.2. Daily variations

In order to clarify the daily variation of NO$_2$ at high latitudes the NO$_2$ DSCD values are plotted in Figure 7.2 as a function of the SZA for two different days of 2001.

On 13 February, the NO$_2$ AM and PM DSCD (Figure 7.2, green circles and violet squares respectively) are of the same magnitude: this means that no substantial photochemical processes contributed to the NO$_2$ diurnal variation. In fact, the horizon covers the sun for a few minutes only, therefore the Earth's shadow cannot reach the altitude of the nitrogen dioxide bulk (about 30 Km). For this reason, the reactions driving the NO$_2$ to N$_2$O$_5$ conversion during night-time cannot take place. However the DSCD behaviour is different for 15 March, when the AM DSCD (Figure 7.2, blue circles) values are systematically lower than the NO$_2$ PM DSCD (Figure 7.2, red squares), due to the deactivation of photochemical reactions caused mainly by the decrease of the daylight period.
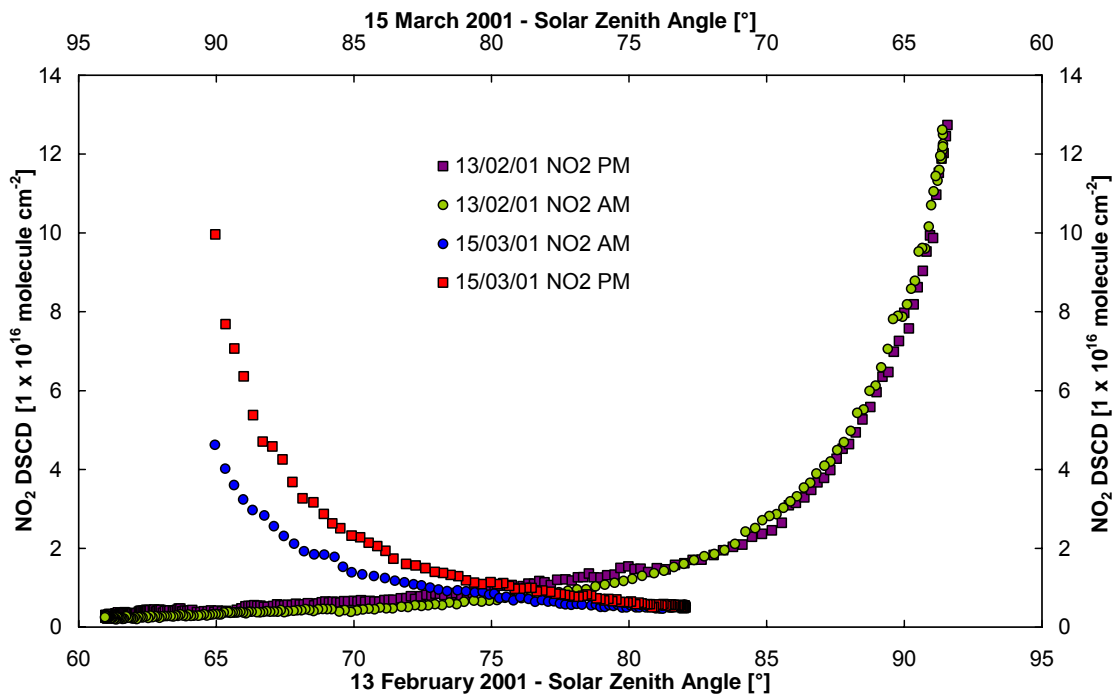
Figure 7.2 - Terra Nova Bay Station – Antarctica. NO_2 slant column (DSCD) variations during 13 February 2001 (left and lower axes) and 15 March 2001 (right and upper axes). On 13 February no substantial chemical processes contribute to NO_2 diurnal variation AM DSCD ~ PM DSCD. On 15 March, the decrease in the daylight period causes the deactivation of photochemical reactions. The formation of N_2O_5 during the night and its subsequent photolysis during the day lead to greater NO_2 DSCDs in the evening twilight than in the morning.

In fact the formation of N_2O_5 during the night and its subsequent photolysis during the day, lead to greater NO_2 DSCD values in the evening than in the morning [5]. The continuous sunlight in summer inhibits the formation of N_2O_5, thus reducing the diurnal variation. In winter there is no daylight to photolyze N_2O_5, which similarly reduces the diurnal variation. At the beginning of the winter, the reduction of NO_2 takes place when, firstly all NO_x is converted to N_2O_5 in the absence of light and, later on, to HNO_3 and then gravitationally eliminated. This can also be observed in Figure 7.1, but the long GASCOD activity period at Terra Nova Bay, prevents a clear view which is possible only by zooming in to certain regions of the plot. The author has chosen to zoom in during the year 2004 (Figure 7.3).
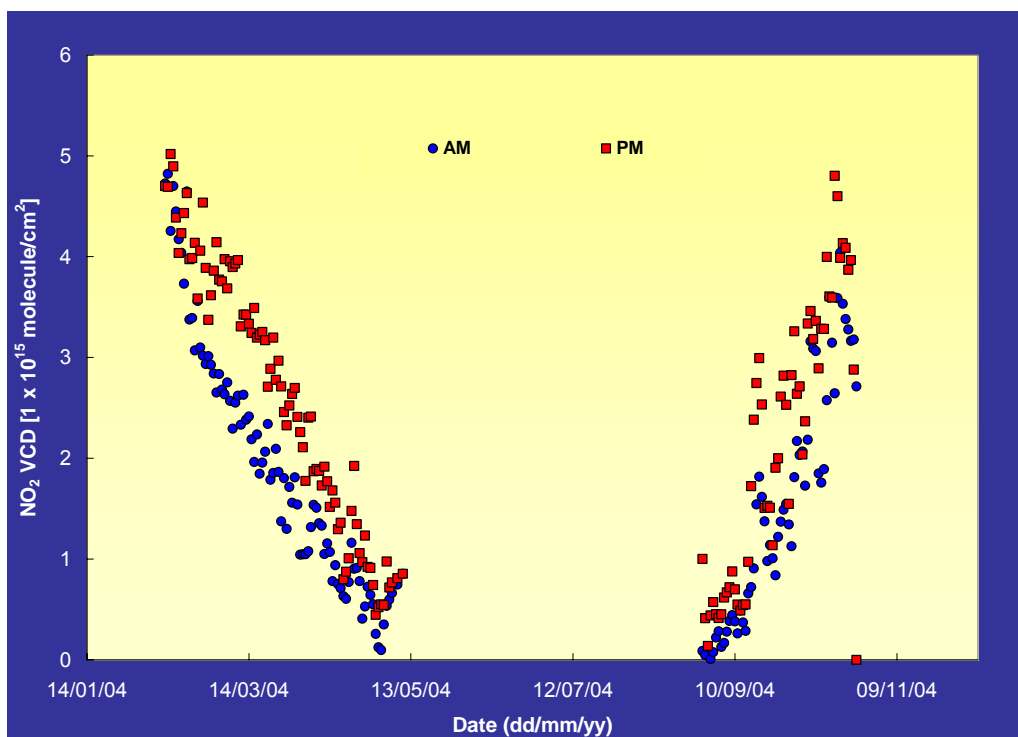
Figure 7.3 - NO$_2$ vertical column amounts measured by GASCOD at Terra Nova Bay station for 2004, during morning and evening twilight. The evening measurements are largest in spring and autumn, when morning and evening twilight are well separated.

During the end of the summer season and for the period of the austral autumn (February - May) the shape of the AM and PM NO$_2$ VCD values is quite regular in all the presented years of measurements, with the AM values systematically lower than the PM ones. For the austral spring (September – November) it is also possible to note some inversions in AM and PM values and more scattered results, mainly due to the Terra Nova Bay geographical location which cause the station to be inside the vortex in some periods and outside in others. In this situation, the dynamical effects hide the usual photochemistry described above. Moreover, during the spring season, the ozone is depleted through a number of catalytic reactions in the presence of halogens and light, already pointed out in chapter 3. The NO$_2$ does not react directly with ozone but, as discussed in Kondo et al. [80], via the chemical reaction ClO + NO$_2$ +M --> ClONO$_2$ +M and, via heterogeneous reactions on the Polar Stratospheric Clouds (PSCs), the NO$_2$ reduces the amount of ClO$_x$ which directly affects O$_3$ depletion (Figure 7.4).

Figure 7.4 shows the Ozone vertical column density for 2001 over Terra Nova Bay Station, as obtained with the TOMS, GOME and GASCOD instruments. During the last months of the summer season (February-early March) ozone VCD values within the range of 270-340 DU (1 DU = 2.89 x 10^{16} molecules/cm^2) are observed; a significant decrease occurred in ozone VCDs below 200 DU in late March.

Springtime observations (Late August – October) are typical for ozone hole conditions. At the end of August ozone starts to decrease and reach its minimum value of about 100 DU at the end of September. The end of the ozone hole period occurs at the end of October, with background values of around 280 DU.

As shown by Bortoli [72], the observation of stratospheric NO_2 and O_3 carried out in the Antarctic regions with the GASCOD instrument allowed for the identification of the Sudden Stratospheric Warming occurred in 2002, that caused the early disappearance of the polar vortex and of the ozone hole process.
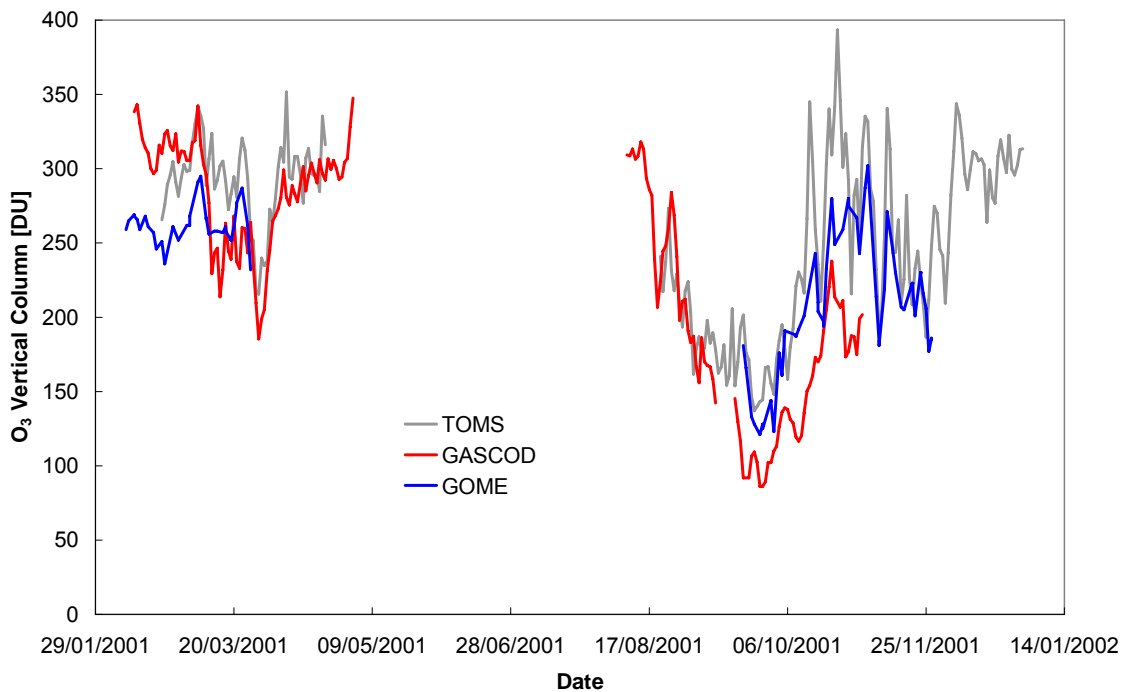
Figure 7.4 - Time series of TOMS, GASCOD and GOME O₃ VCD values for 2001 at Terra Nova Bay station

Ground-based measurements collocated in time and space with the satellite ones are of great importance in estimating the real accuracy of satellite and ground based NO_2 data. Comparison of GOME NO_2 total content measurements in 2001 with the simultaneous ground-based observations at Terra Nova Bay station was accomplished as it can be observed in Figure 7.5.

The results in ground-based measurements are in good agreement with the GOME total nitrogen dioxide especially during the autumn mainly due to the low number of cloudy days [32]. Figure 7.6 shows the good correlation of the two data set. A positive correlation of r = 0.97 has been found between GOME NO_2 vc and GASCOD NO_2 vc. It is meaningful that the two series of data are in good agreement also for rather low values of concentration (of about $1.0 \times 10^{15} \, molecule / cm^2$)
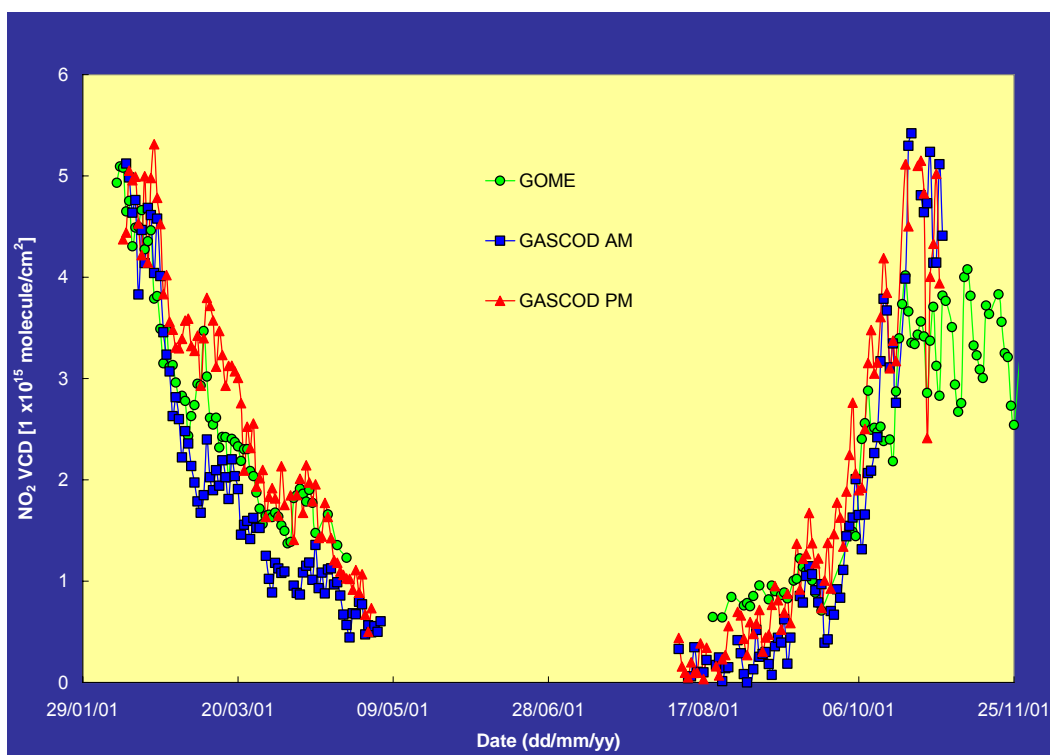
Figure 7.5 - Time series of GASCOD and GOME NO$_2$ vc values for 2001 at Terra Nova Bay station
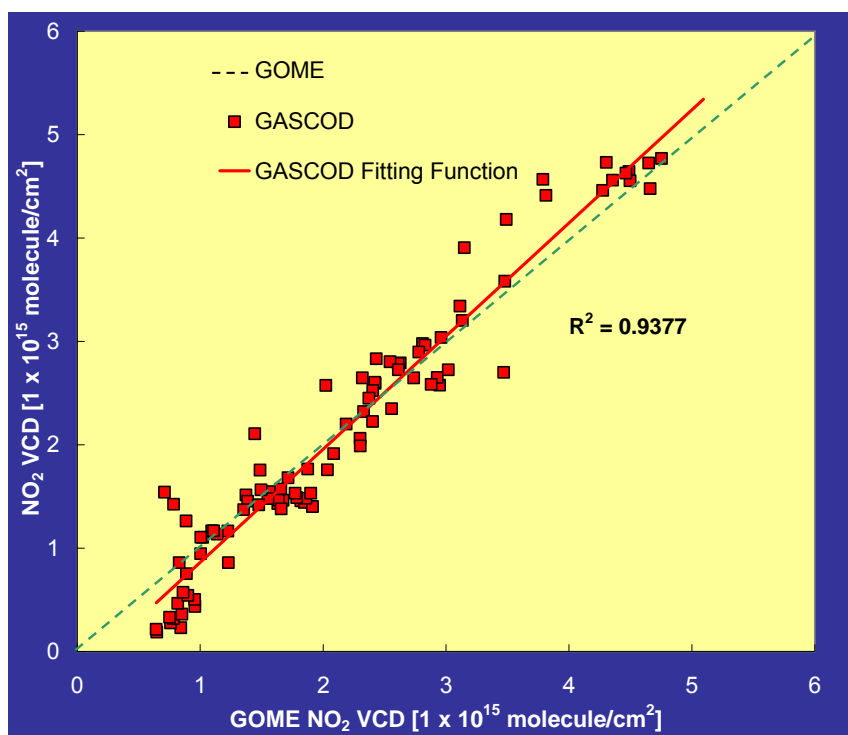
Figure 7.6 - Scatter plot of GASCOD and GOME NO$_2$ vc values

7.3.1.3. AM/PM behaviour

At high latitudes, the fact that the sun remains above the horizon for a long period (at Terra Nova Bay about 90 days) involves characteristic AM/PM seasonal variations that are presented in Figure 7.7.
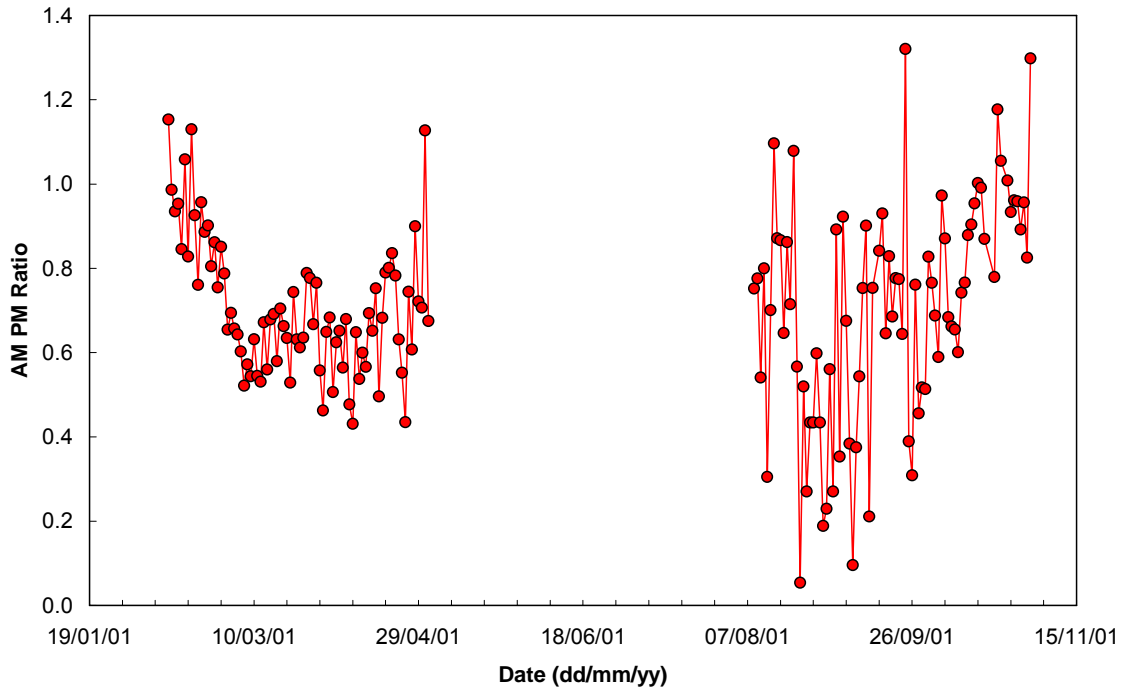
Figure 7.7 - NO$_2$ AM/PM ratio values obtained for Terra Nova Bay station for 2001

It is possible to verify that for polar regions the AM/PM ratio converges to 1 in the summer. In February it begins to decrease until about the end of March and then the ratio increases again until the end of April. After this period for some days before the beginning of the polar night, the AM/PM ratio decreases again. The reason for this observed behaviour could be caused by the very low values of NO$_2$ VCD measured, which are near the detection limit of the instrument. At the beginning of the spring season the AM/PM ratio increases with opposite slope, but occasionally it assumes values greater than 1, revealing an inversion in the normal behaviour of the NO$_2$ amount at sunset and sunrise. Inside the polar vortex, in this period, the largest phenomena of ozone depletion occur, because of chlorine activation events which also cause low concentrations of nitrogen dioxide. As pointed out above, Terra Nova Bay is within the polar vortex only during certain periods, so when it is out of the vortex, the inversion in the AM/PM ratio could be due to the vortex drift to the vertical of Terra Nova Bay, causing advection of ozone-depleted (and denitrified) air masses from the highest latitudes.

Short-term fluctuations of about two weeks in the AM and PM slant column can also be noted and may be linked to planetary wave transport. Waves are unable to transport trace species deep into the polar vortex, but can erode material from the edge of the vortex [81], so the fluctuations correspond to air masses with high and mid-latitude characteristics, which correspond to alternately viewing air with different AM/PM ratios.

7.3.2. Mid Latitudes

This section will be mainly devoted to the presentation of the results of the stratospheric NO_2 and O_3 seasonal variation obtained with the SPATRAM instrument, installed at the Observatory of the Geophysics Centre of Evora since April 2004 (Figure 5.30). Some aspects of the daily variations in NO_2, and O_3 will also be discussed.

7.3.2.1. Daily variations

As stated in § 7.3.1.2, at high latitudes the daily variation of NO_2 fluctuates during the year for the particular condition of the polar regions (the 24 hours of light or of dark respectively during the polar summer and the polar winter). At mid latitudes the typical behaviour of the NO_2 DSCD daily variation is shown in Figure 7.8, with the AM values always lower than the PM ones.
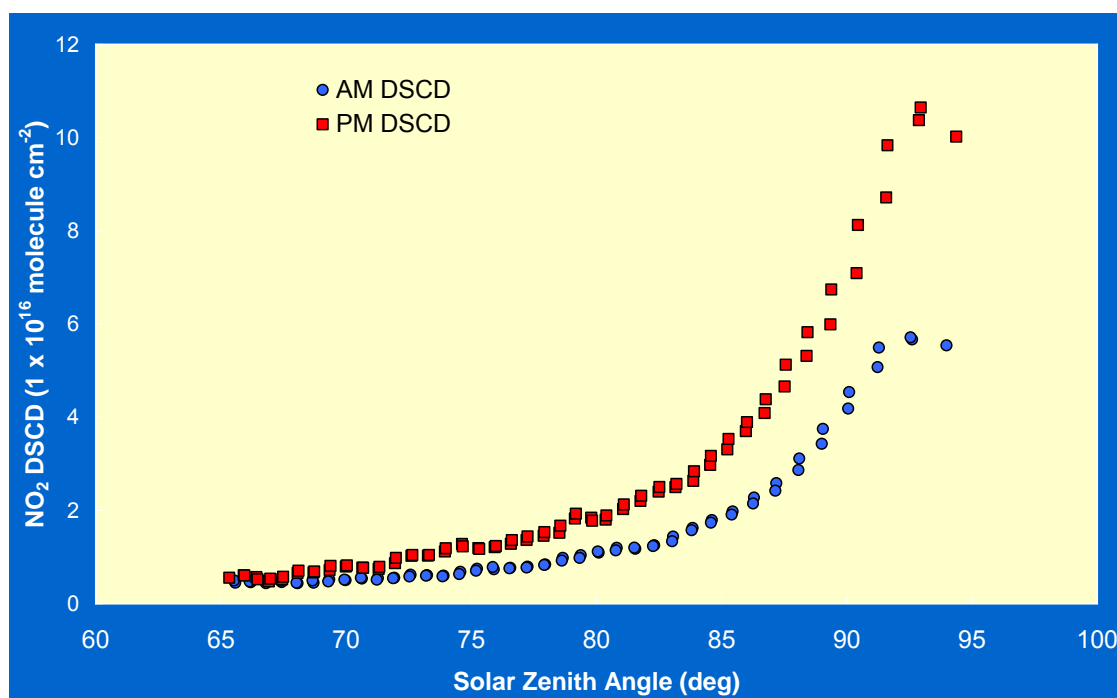
Figure 7.8 - NO$_2$ slant column density versus Solar Zenith Angles for the 13th of May 2004.

From the point of view of the performances of the SPATRAM equipment, Figure 7.8 underlines that the measurements can be obtained also for SZA greater than 90° (till about 95°), while the "Old" GASCOD can obtain trustful measurements only for SZA lower than 90° ~ 91°. This 'technological' aspect (mainly due to the use of a CCD sensor instead of a CMOS detector as in the GASCOD spectrometer) opens also new perspectives as the possibility to utilize the obtained results in inversion methods for the determination of the NO_2 vertical profile [84]

7.3.2.2. Seasonal Variation

Figure 7.9 shows the comparison of the results of NO_2 obtained with the SPATRAM spectrometer and the GOME instrument for this first 40 days of activity of the ground-based equipment. The GOME data are closer to the SPATRAM AM results due to the fact that the overpass of the ERS-2 satellite over Evora is around 11:30 in the morning, when the photochemical process of NO_2 creation has just started. It is also possible to appreciate the positive seasonal trend of NO_2 VCD.
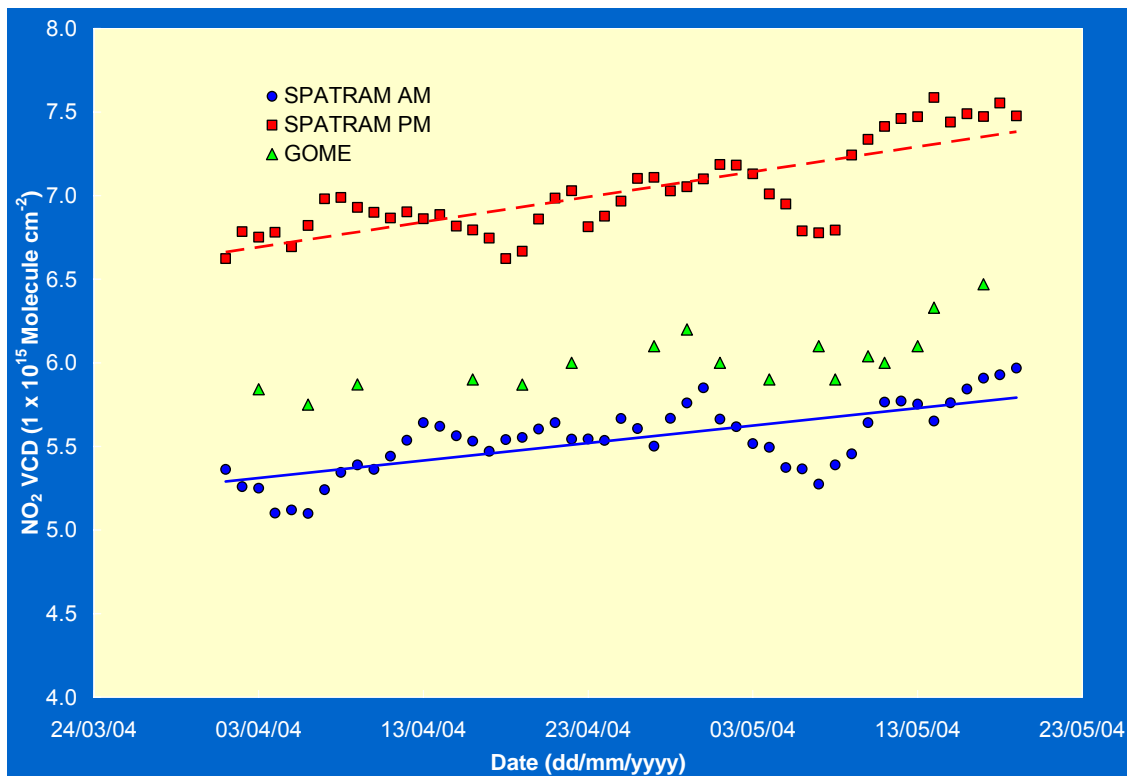
Figure 7.9 - NO_2 VCD at 90° of SZA (AM - sunrise and PM - sunset) obtained with SPATRAM and GOME results for the first period of activity of the ground based equipment.

The comparison of the O_3 results obtained with the SPATRAM instrument with the ones retrieved from TOMS and GOME spectrometers on board the two satellites are showed in Figure 7.10. In this plot the SPATRAM results for Ozone VCD are the daily averages of all the data obtained in the first 40 days of activity of the instrument during the day (for SZA in the range 65°-95°, in order to maximize the signal to noise ratio of the measurements).

Both TOMS and GOME results are in good agreement with the SPATRAM data. The episodic events of under or over estimation of the ozone VCD of the ground based equipment are mainly due to the different meteorological conditions of the zenith sky measurements and to the point of view of the instruments (from the space and from the ground). For this short period of measurements the seasonal variation of the stratospheric ozone can not be appreciated as it was for the case of NO_2.
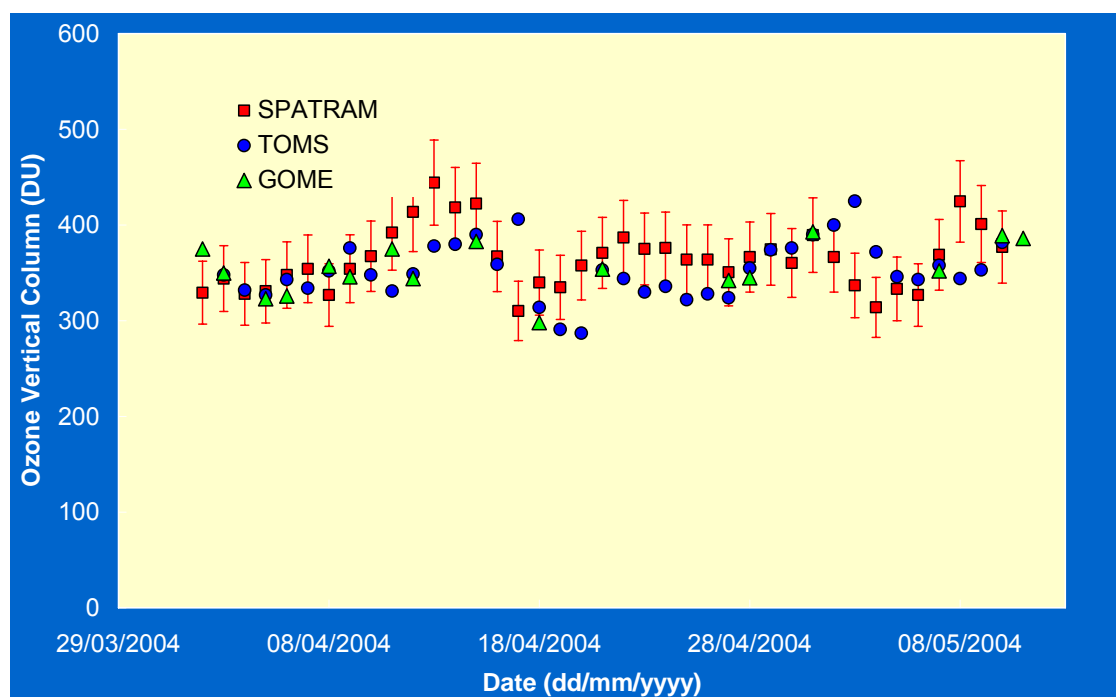
Figure 7.10 - SPATRAM, GOME and TOMS results for O_3 VCD during the period of activity of the ground based spectrometer.

Figure 7.11 plots the time series of the NO_2 AM and PM VCD values at the solar zenith angle of 90° (during sunrise and sunset) for more than 1 year of activity of the SPATRAM equipment. The expected seasonal trend, foreseen also from Figure 7.9, emerges, presenting the maximum in summer and the minimum in winter. The results obtained for the summer 2004 are more spread than in the winter season, but the AM and PM values remain well separated; a decrease

(increase) of the AM values is followed by lower (higher) values also for the PM ones. The reason of that appears to be due mainly to the atmospheric instability as for example intrusions in the Iberian peninsula of oceanic or Saharan dust contaminated air masses, quite usual in the summer season in Evora. It should be pointed out here that the first 3-4 months of measurements were also used as testing phase of the instrument and of the Data Acquisition Software, which implies a deeper analysis of the results shown in Figure 7.11. The NO_2 VCD values obtained for the period September 2004 - May 2005 are really interesting. The last period of measurements presents more scattered data as in the beginning of the SPATRAM activity. The AM and PM values stay well split.
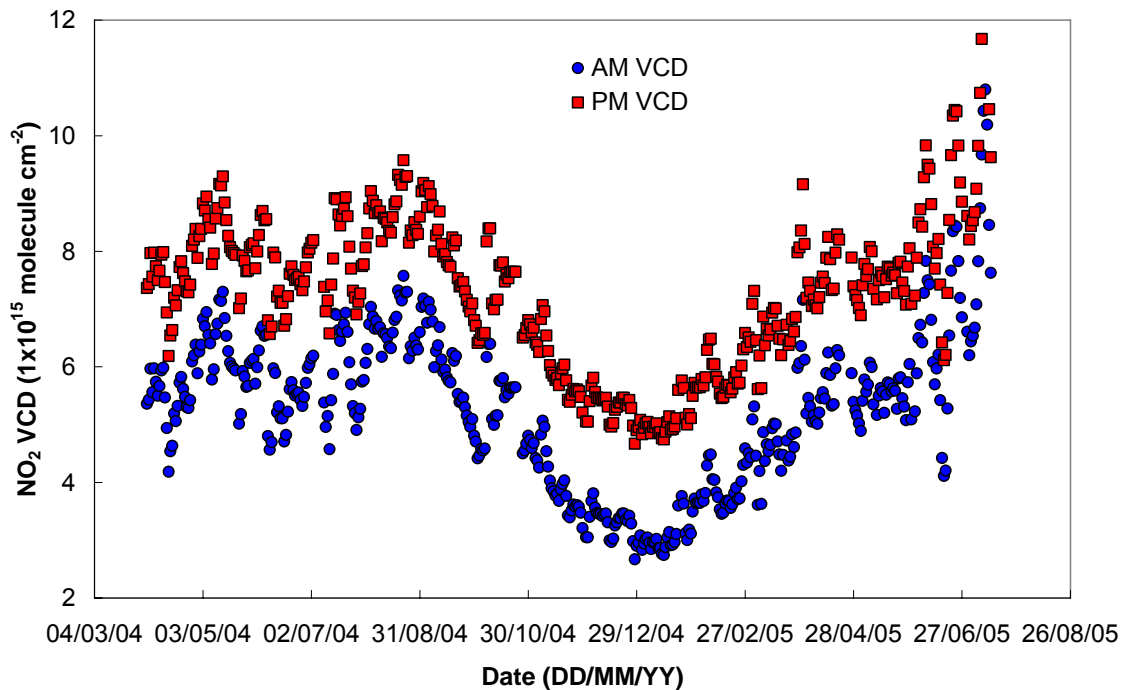
Figure 7.11 – Seasonal variation of NO_2 VCD at 90° of SZA (AM - sunrise and PM - sunset)

Figure 7.12 shows the seasonal variation of the stratospheric O_3, obtained with measurements of the zenith sky radiation performed with the SPATRAM instrument in Evora, and the results of the TOMS equipment for the ozone in the region over Lisbon (140 km eastward of Evora site), from the 1st of April to the 19 November 2004. The result of the comparison is really interesting: the main features of the satellite results are overlapped by the ground based ones. The most exciting aspect of this result is that the TOMS and the SPATRAM values are obtained with different algorithms.
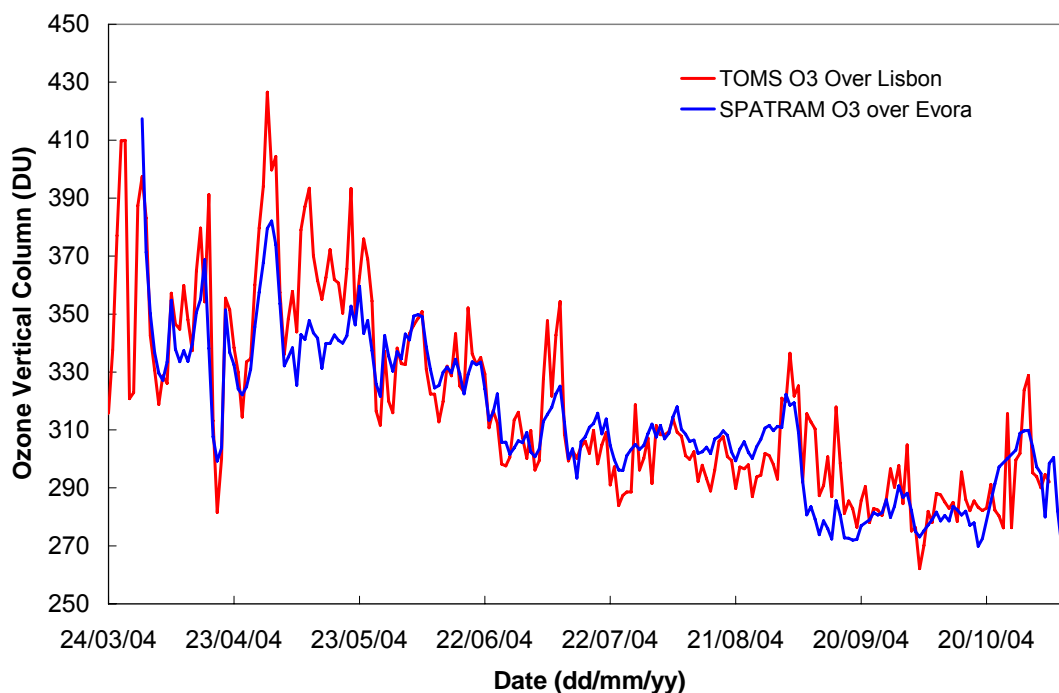
Figure 7.12 – Comparison of the seasonal variation of O_3 VCD at Evora Station with the seasonal variation reported by the TOMS instrument over Lisbon.

Figure 7.13 plots the SCD for O_3 retrieved in Evora with the SPATRAM for 3 days.
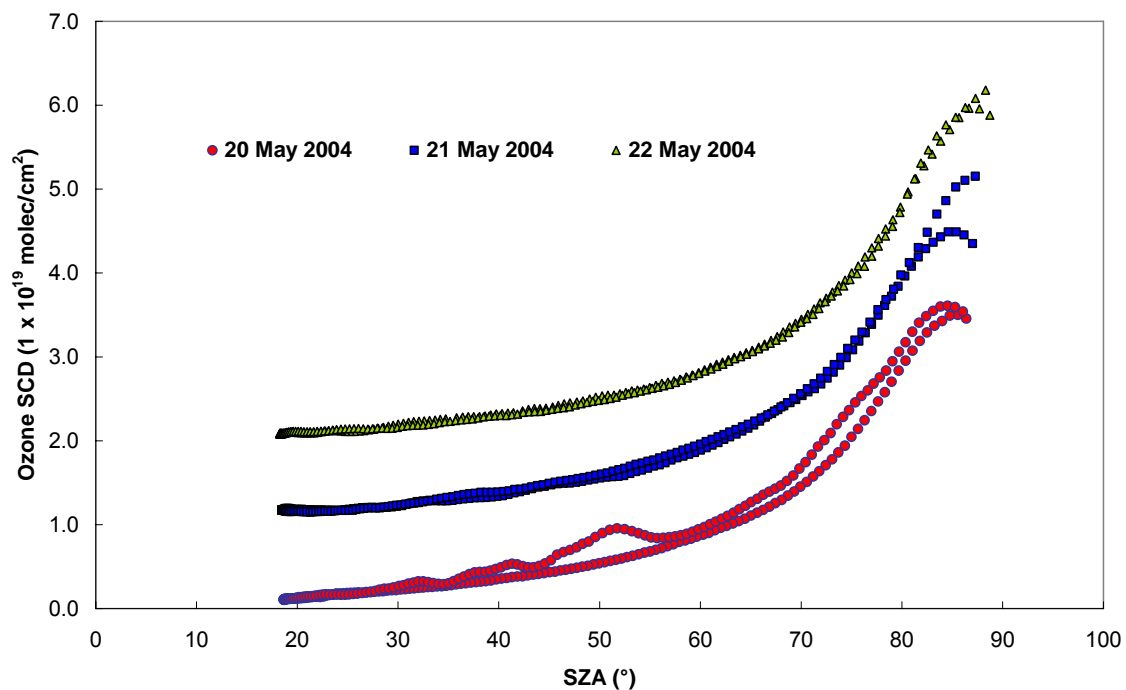
Figure 7.13 – EVORA, O_3 SCD versus the SZA obtained for the 20, 21 and 22 of May 2004. In order to distinguish the different behavior for the 3 days, the

values of the 21 and 22 are vertically shifted of 1 and 2 unit respectively.

In order to highlight the different behaviour of the O_3 diurnal variation during the 3 days an offset of 1 and 2 is introduced along the vertical axis, respectively for the 21 and 22, that is: to have the real slant column density values the 22 data have to be shifted down of 2 and the 21 data of 1, respectively. Analysing the shape of the O_3 SCD for the 20 it is clear that the O_3 SCD values increase in the highest red curve (that are the PM values) in the range 30-60° of SZA. The data for the 21 shows a quite regular behaviour but compared with the results for the 22 some deviations can be identified. Figure 7.14 shows the O_3 vertical column density VCD, plotted as function of Evora local time.
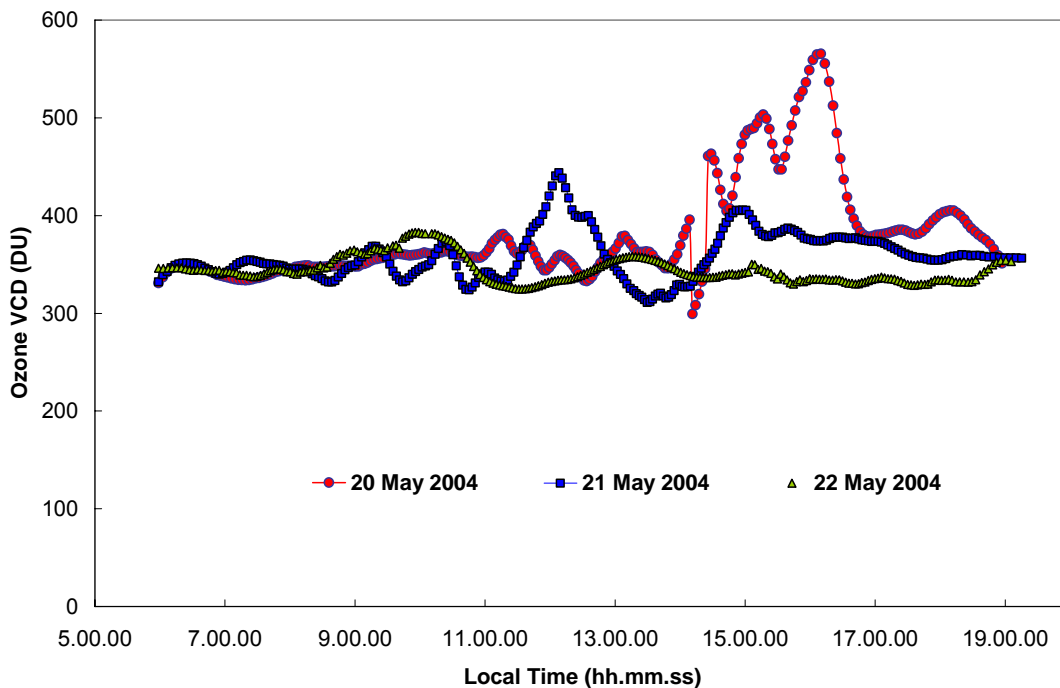
Figure 7.14 – EVORA, Diurnal variation of O_3 VCD for the 20, 21 and 22 of May 2004.

The anomalies shown in Figure 7.13 are amplified due to the application of the AMF to the SCD. The increase in the O_3 VCD for the 20 of May (between 14:00 – 17:00 Evora Local Time the O3 varies from 310 to 570 DU) and the large variations for the 21 (314 – 473 DU) could be explained as strong events of O_3 tropospheric pollution. The results obtained for the 22 of May show that the typical O_3 background content is recovered (320-370 DU) Moreover it can be noted the constancy of the O_3 VCD especially during the afternoon. Considering the geo location and the dimension of the city where the SPATRAM is installed it is very unlikely that an episode of O_3 tropospheric pollution occurred. The reason of this behaviour of the O_3 content had to be found elsewhere. The question was: "Why

the DOAS algorithms gave such high values of O_3 SCD ?" The only answer could be "The SPATRAM measured low amounts of scattered radiation, that means something absorbed the missing radiation". In the considered spectral range of measurement (300 – 360 nm) the ozone is not the only absorber. Also the Saharan dust [82], [83] can reduce the amount of radiation reaching the instrument, deceiving the linear section of the DOAS algorithms and producing an higher value for the DSCD.

In order to confirm the above hypothesis the Aerosol Index retrieved by TOMS for the 20, 21 and 22 of May 2004 was considered (Figure 7.15). On 20 of May a dust intrusion reaches the south of Portugal and the event is still present on the 21. On the 22 Portugal is back to the completely aerosol "free" situation.
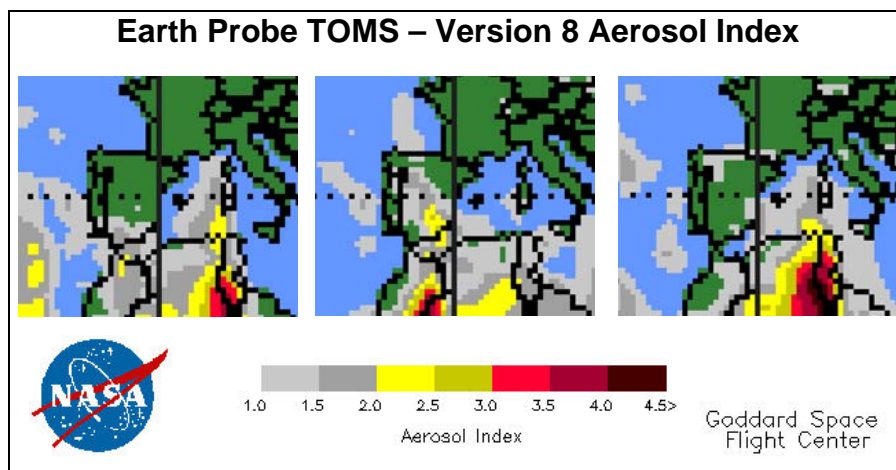
Figure 7.15 – Aerosol Index retrieved by TOMS for the 20, 21 and 22 of May 2004 (from left to right).

Therefore the high values for O_3 VCD measured on the 20 and 21 of May 2004are related not to a real increase of Ozone, but to an increase of absorbed radiation by the aerosol particles. These considerations open another field of application of the DOAS measurement: the possibility to obtain information on desert dust intrusion.

8. Conclusions and future perspectives

8.1. Conclusions

The goal to develop, manufacture and install an automatic DOAS instrument at the Atmospheric Physics Observatory of Évora, Portugal, for the measurements of atmospheric trace gases in unattended and automatic mode was reached. The SPATRAM is fully described both in its components as well as in the operating principles and operating mode. The equipment is a multi-purpose spectrometer with high-tech solutions making it a suitable instrument for the measurements of sky radiance in the zenith direction. The accuracy in the measurements is ensured mainly from the high Signal to Noise Ratio (SNR) that can be obtained thanks to:

- the low torque coefficients of the spectrometer's mechanical parts that are kept at a constant temperature (ensuring the stability over time of the grating's spectral dispersion);
- the low amount of stray-light obtained with the use of a spherical holographic grating, flat and spherical mirror manufactured with great accuracy and precision, and band-pass optical filters;
- the CCD Camera that mounting a thermo-controlled detectors, allows for the minimization of the temperature's related effects such as the dark current;
- the CCD Back illuminated technology allowing for the highest Full Well Capacity.

The sure identification of the Fraunhofer's spectral lines in the solar spectrum confirms the exact capabilities of the SPATRAM measurements.

No problems occur to the SPATRAM equipment during the data acquisition time period.

The algorithms of the Differential Optical Absorption Spectroscopy (DOAS) are presented and explained. Some simple considerations have been introduced improving the "Shift" and "Stretch" procedures. The effects on the output of the DOAS algorithms (the Differential Slant Column Density of the analyzed compounds – DSCD) of the spectrum used as Reference Spectrum ($I_0(\lambda)$) and of the different Cross Section's temperatures have been presented and discussed. The method adopted for the calculation of the "background" content in the Reference spectrum allows for the determination of the Slant Column Density (SCD) and the application of the Air Mass Factor (AMF) to the SCD let the

determination of the actual Vertical Column Density (VCD) of the species under investigation.

Since the DOAS procedures were developed during the feasibility phase of SPATRAM, the software package applying the DOAS algorithms was also applied to the data set obtained with the GASCOD spectrometer (forefather of the SPATRAM equipment) installed at the Italian Antarctic Station of Terra Nova Bay. The results for the determination of stratospheric NO_2 and O_3 vertical column density at high latitude are presented, analyzed and discussed. A clear seasonal variation emerges from the results. During the austral autumn the NO_2 VCD values decrease from a maximum value of about 5.0×10^{15} molecule cm^{-2} to a minimum ($<1.0 \times 10^{14}$ molecule cm^{-2}), at the beginning of the winter season. At the end of the polar night the nitrogen dioxide total column values increase with a different slope. Both features are due to the well-known processes of lower stratospheric denoxification (conversion of NO and NO_2 into HNO_3) in the winter season. The obtained results for stratospheric nitrogen dioxide and ozone vertical columns at high latitude were compared with the retrievals from the Global Ozone Monitoring Experiment (GOME) equipment and from the Total Ozone Mapping Spectrometer (TOMS) instrument respectively showing a very good agreement both in terms of seasonal as well as of diurnal variation. Furthermore, the comparison of the ground based results with the ones achieved with satellite borne equipment is quite satisfactory particularly during the period of low values of vertical column of the analyzed compounds. It is also underlined how the observation of stratospheric NO_2 and O_3 carried out in the Antarctic regions with the GASCOD instruments allowed for the identification of the early disappearing of the polar vortex and of the ozone hole caused by the Sudden Stratospheric Warming occurred in 2002 over Antarctica.

The DOAS technique was applied to the spectral data obtained with SPATRAM installed at the Geophysics Centre of Évora. The expected diurnal variation of NO_2 and O_3 were obtained: the strong photochemical activity of the active nitrogen compounds leads to values of NO_2 Vertical Column at the sunrise (AM values) systematically lower than during the sunset (PM values); instead for O_3, under typical conditions, the AM and PM values are roughly the same. For the seasonal variation of both species the expected variation was observed, presenting the maximum values during summer and the minimum is achieved in the winter months. Once more, the results for NO_2 and O_3 were compared with the GOME and TOMS satellite retrievals. Also this comparison, in terms of seasonal and diurnal variation, revealed a fine agreement, attesting that both the SPATRAM instrument (in zenith sky configuration) as well as the implemented DOAS algorithms are powerful tools for the continuous monitoring of atmospheric

compounds. Regarding the effects of the aerosol contamination on the retrieval of the tracers, a case study that occurred on 20-21 May 2004 was analyzed. The anomalous behaviour observed for the Ozone vertical column during the 20 May, suggested an increase in the Ozone content. Since this raise was considered to be quite improbable mainly for the season and for the location of Évora (faraway from Ozone polluted areas), other aspects have been considered. Analyzing the TOMS Aerosol Index product, a dust intrusion was encountered on 20 May in the south of Portugal. Therefore the high values for O_3 vertical column obtained on 20 May are not related to a real increase of the Ozone, but to an increase of absorbed radiation by the aerosol particles. These considerations open another field of application for the DOAS measurements: the possibility to obtain information on desert dust intrusions.

These activities (monitoring of stratospheric compounds, validation and comparison of the results) could be enlarged as the SPATRAM is similar, in terms of optical design) to other spectrometers installed at the climatic Station of Lampedusa (south of Italy), at the Ottavio Vittori Station over the Mt Cimone (Italy), at the Bulgarian Atmospheric Station in Stara Zagora, at the Italian Antarctic Station and at the Dome/Concordia Antarctic station (Italian French base).

8.2. Future Perspectives

Now that the SPATRAM is installed and working the research is still at the beginning; after this first phase, the objectives of the research could be divided in 2 main fields:

1. the technological one foreseeing the improvement of the measurements capability of the SPATRAM in order to obtain measurements in directions different from the zenith;

2. the scientific one regarding both stratospheric and tropospheric studies. The stratospheric ones concerning the analysis of the diurnal and seasonal variations of stratospheric tracers as ozone, nitrogen dioxide, bromine oxide and sulfur dioxide by the application of the DOAS methodology to the spectral measurements obtained with the SPATRAM instrument operating in zenith sky configuration. The comparison and validation of satellite data with these ground based observations. The use of the obtained results in chemical and climate models for the estimation of the tracer's impact on the Climate Global Change. The tropospheric studies can be summarized as: the possibility to obtain results for the air quality in urban environment, thanks to the new instrumental set-up (Horizontal and OffAxis measurements) for the retrieval of the concentration of some urban pollutants as benzene and toluene; the use of the

spectral measurements for the detection and the characterization of events of aerosol contamination; the comparison of the results with the AERONET data.

A1. The Grating principles

A1.1. History of Grating Development

A *diffraction grating* is a collection of reflecting (or transmitting) elements separated by a distance comparable to the wavelength of light under study. It may be thought of as a collection of diffracting elements, such as a pattern of transparent slits (or apertures) in an opaque screen, or a collection of reflecting grooves on a substrate. A *reflection grating* consists of a grating superimposed on a reflective surface, whereas a *transmission grating* consists of a grating superimposed on a transparent surface. An electromagnetic wave incident on a grating will, upon diffraction, have its electric field amplitude, or phase, or both, modified in a predictable manner.

The first diffraction grating was made by an American astronomer, David Rittenhouse, in 1785, who reported constructing a half-inch wide grating with fifty-three apertures. Apparently he developed this prototype no further, and there is no evidence that he tried to use it for serious scientific experiments.

In 1821, unaware of the earlier American report, Joseph von Fraunhofer began his work on diffraction gratings. His research was given impetus by his insight into the value that grating dispersion could have for the new science of spectroscopy. Fraunhofer's persistence resulted in gratings of sufficient quality to enable him to measure the absorption lines of the solar spectrum. He also derived the equations that govern the dispersive behavior of gratings. Fraunhofer was interested only in making gratings for his own experiments, and upon his death, his equipment disappeared.

By 1850, F.A. Nobert, a Prussian instrument maker, began to supply scientists with gratings superior to Fraunhofer's. About 1870, the scene of grating development returned to America, where L.M. Rutherfurd, a New York lawyer with an avid interest in astronomy, became interested in gratings. In just a few years, Rutherfurd learned to rule reflection gratings in speculum metal that were far superior to any that Nobert had made. Rutherfurd developed gratings that surpassed even the most powerful prisms. He made very few gratings, though, and their uses were limited.

Rutherfurd's part-time dedication, impressive as it was, could not match the tremendous strides made by H.A. Rowland, professor of physics at the Johns

Hopkins University. Rowland's work established the grating as the primary optical element of spectroscopic technology.

Rowland constructed sophisticated ruling engines and invented the concave grating, a device of spectacular value to modern spectroscopists. He continued to rule gratings until his death in 1901.

After Rowland's great success, many people set out to rule diffraction gratings. The few who were successful sharpened the scientific demand for gratings. As the advantages of gratings over prisms and interferometers for spectroscopic work became more apparent, the demand for diffraction gratings far exceeded the supply.

In 1947, Bausch & Lomb decided to make precision gratings available commercially. In 1950, through the encouragement of Prof. George R. Harrison of MIT, David Richardson and Robert Wiley of Bausch & Lomb succeeded in producing their first high quality grating. This was ruled on a rebuilt engine that had its origins in the University of Chicago laboratory of Prof. Albert A. Michelson. A high fidelity replication process was subsequently developed, which was crucial to making *replicas*, duplicates of the tediously generated master gratings. A most useful feature of modern gratings is the availability of an enormous range of sizes and groove spacings (up to 10,800 grooves per millimeter), and their enhanced quality is now almost taken for granted. In particular, the control of groove shape (or blazing) has increased spectral efficiency dramatically. In addition, interferometric and servo control systems have made it possible to break through the accuracy barrier previously set by the mechanical constraints inherent in the ruling engines.

A1.1.1.   The Grating Equation

When monochromatic light is incident on a grating surface, it is diffracted into discrete directions. We can picture each grating groove as being a very small, slit-shaped source of diffracted light. The light diffracted by each groove combines to form a diffracted wavefront. The usefulness of a grating depends on the fact that there exists a unique set of discrete angles along which, for a given spacing d between grooves, the diffracted light from each facet is in phase with the light diffracted from any other facet, so they combine constructively. Diffraction by a grating can be visualized from the geometry in Figure A1.1, which shows a light ray of wavelength λ incident at an angle α and diffracted by a grating (of groove spacing d, also called the pitch) along

angles β_m. These angles are measured from the grating normal, which is the dashed line perpendicular to the grating surface at its center. The sign convention for these angles depends on whether the light is diffracted on the same side or the opposite side of the grating as the incident light. In diagram (a), which shows a reflection grating, the angles $\alpha > 0$ and $\beta_1 > 0$ (since they are measured counter clockwise from the grating normal) while the angles $\beta_0 < 0$ and $\beta_{-1} < 0$ (since they are measured clockwise from the grating normal). Diagram (b) shows the case for a transmission grating. By convention, angles of incidence and diffraction are measured *from* the grating normal *to* the beam. This is shown by arrows in the diagrams. In both diagrams, the sign convention for angles is shown by the plus and minus symbols located on either side of the grating normal. For either reflection or transmission gratings, the algebraic signs of two angles differ if they are measured from opposite sides of the grating normal.
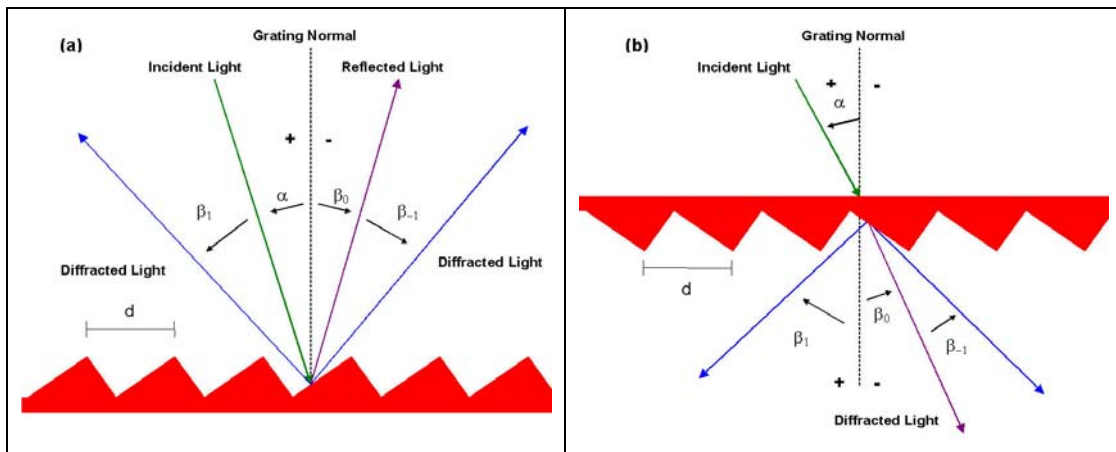
Figure A1.1 - Diffraction by a plane grating. *A beam of monochromatic light of wavelength λ is incident on a grating and diffracted along several discrete paths. The triangular grooves come out of the page; the rays lie in the plane of the page. The sign convention for the angles α and β is shown by the + and – signs on either side of the grating normal. (a) A* reflection grating*: the incident and diffracted rays lie on the same side of the grating. (b) A* transmission grating*: the incident and diffracted rays lies on opposite sides of the grating.*

Other sign conventions exist, so care must be taken in calculations to ensure that results are self-consistent. Another illustration of grating diffraction, using wave fronts (surfaces of constant phase), is shown in Figure A1.2. The geometrical path difference between light from adjacent grooves is seen to be $d \sin\alpha + d \sin\beta$. [Since $\beta < 0$, the latter term is actually negative.] The

principle of interference dictates that only when this difference equals the wavelength λ of the light, or some integral multiple thereof, will the light from adjacent grooves be in phase (leading to constructive interference). At all other angles β, there will be some measure of destructive interference between the wavelets originating from the groove facets. These relationships are expressed by the *grating equation*

$$m\lambda = d\,(\sin\alpha + \sin\beta) \qquad\qquad \text{(A1.1)}$$

which governs the angles of diffraction from a grating of groove spacing *d*. Here *m* is the *diffraction order* (or *spectral order*), which is an integer. For a particular wavelength λ, all values of *m* for which $|m\lambda/d| < 2$ correspond to physically realizable diffraction orders.

It is sometimes convenient to write the grating equation as

$$Gm\lambda = \sin\alpha + \sin\beta \qquad\qquad \text{(A1.2)}$$

where *G = 1/d* is the *groove frequency* or *groove density*, more commonly called "grooves per millimeter".

Equation (A1.1) and its equivalent equation (A1.2) are the common forms of the grating equation, but their validity is restricted to cases in which the incident and diffracted rays are perpendicular to the grooves (at the center of the grating). The vast majority of grating systems fall within this category, which is called *classical* (or *in-plane*) *diffraction*. If the incident light beam is not perpendicular to the grooves, though, the grating equation must be modified:

$$Gm\lambda = \cos\varepsilon(\sin\alpha + \sin\beta) \qquad\qquad \text{(A1.3)}$$

Here ε is the angle between the incident light path and the plane perpendicular to the grooves at the grating center (the plane of the page in Figure A1.2). If the incident light lies in this plane, $\varepsilon = 0$ and Eq. (A1.3) reduces to the more familiar Eq. (A1.2). In geometries for which $\varepsilon = 0$, the diffracted spectra lie on a cone rather than in a plane, so such cases are termed *conical diffraction*.

For a grating of groove spacing *d*, there is a purely mathematical relationship between the wavelength and the angles of incidence and diffraction. In a

given spectral order *m*, the different wavelengths of polychromatic wave fronts incident at angle α are separated in angle:

$$\beta(\lambda) = \arcsin(\frac{m\lambda}{d} - \sin\alpha)$$

(A1.4)

When *m* = 0, the grating acts as a mirror, and the wavelengths are not separated ($\beta = -\alpha$ for all λ); this is called *specular reflection* or simply the *zero order*.
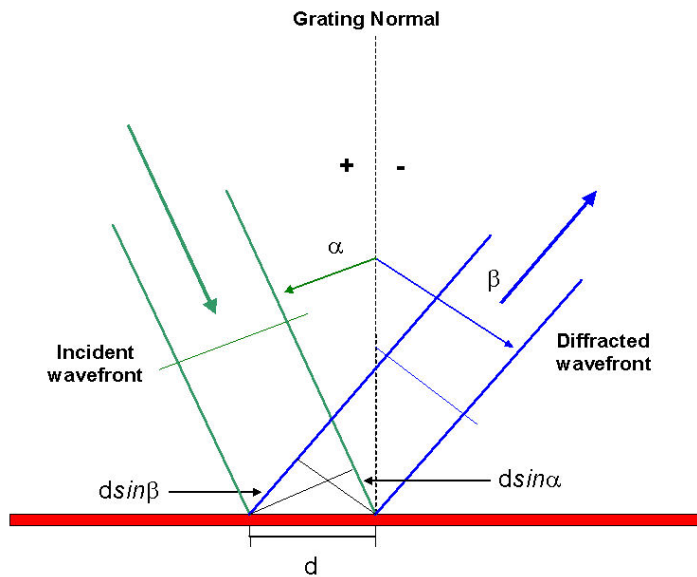
Figure A1.2 - Geometry of diffraction for planar wave front. The terms in the path difference, dsinα and dsinβ, are shown

A special but common case is that in which the light is diffracted back toward the direction from which it came (i.e., α = β); this is called the *Littrow configuration*, for which the grating equation becomes

$$m\lambda = 2d\sin\alpha \text{ , in Littrow}$$

(A1.5)

In many applications (such as constant-deviation monochromators), the wavelength λ is changed by rotating the grating about the axis coincident with its central ruling, with the directions of incident and diffracted light remaining unchanged. The *deviation angle* 2*K* between the incidence and diffraction directions (also called the *angular deviation*) is

$$2K = \alpha - \beta = \text{costant}$$

(A1.6)

while the scan angle ϕ, which is measured from the grating normal to the bisector of the beams, is

$$2\Phi = \alpha + \beta \qquad (A1.7)$$
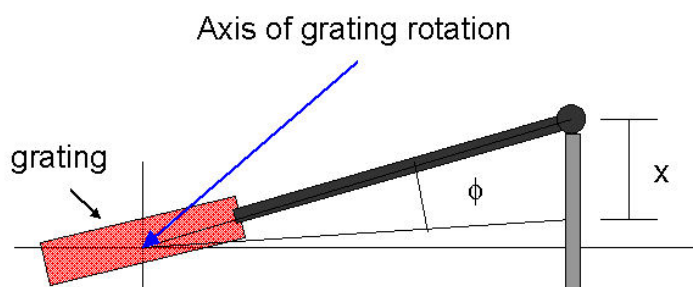
Figure A1.3 - A sine bar mechanism for wavelength scanning. As the screw is extended linearly by the distance x shown, the grating rotates through an angle ϕ in such a way that $\sin\phi$ is proportional to x.

Note that ϕ changes with λ (as do α and β). In this case, the grating equation can be expressed in terms of ϕ and the *half deviation angle K* as

$$m\lambda = 2d \cos K \sin \Phi \qquad (A1.8)$$

This version of the grating equation is useful for monochromator mounts (see § A1.1.15 - A1.1.17). Eq. (A1.8) shows that the wavelength diffracted by a grating in a monochromator mount is directly proportional to the sine of the angle ϕ through which the grating rotates, which is the basis for monochromator drives in which a sine bar rotates the grating to scan wavelengths (Figure A1.3).

A1.1.2. Diffraction Orders

A1.1.2.1. Existence of Diffraction Orders.

 For a particular set of values of the groove spacing d and the angles α and β, the grating equation (A1.1) is satisfied by more than one wavelength. In fact, subject to restrictions discussed below, there may be several discrete

wavelengths which, when multiplied by successive integers *m*, satisfy the condition for constructive interference. The physical significance of this is that the constructive reinforcement of wavelets diffracted by successive grooves merely requires that each ray be retarded (or advanced) in phase with every other; this phase difference must therefore correspond to a real distance (path difference) which equals an integral multiple of the wavelength. This happens, for example, when the path difference is one wavelength, in which case we speak of the positive first diffraction order (*m* = 1) or the negative first diffraction order (*m* = –1), depending on whether the rays are advanced or retarded as we move from groove to groove. Similarly, the second order (*m* = 2) and negative second order (*m* = –2) are those for which the path difference between rays diffracted from adjacent grooves equals two wavelengths.

The grating equation reveals that only those spectral orders for which $|m\lambda/d|$ < 2 can exist; otherwise, $|\sin\alpha + \sin\beta| > 2$, which is physically meaningless. This restriction prevents light of wavelength λ from being diffracted in more than a finite number of orders. Specular reflection (*m* = 0) is always possible; that is, the *zero order* always exists (it simply requires $\beta = -\alpha$). In most cases, the grating equation allows light of wavelength λ to be diffracted into both negative and positive orders as well. Explicitly, spectra of all orders *m* exist for which

$$-2d < m\lambda < 2d, \text{ m an integer.} \tag{A1.9}$$

For l/*d* << 1, a large number of diffracted orders will exist.

As seen from (A1.1), the distinction between negative and positive spectral orders is that

$$\begin{aligned}
\beta &> -\alpha &&\textit{for positive orders } (m > 0) \\
\beta &< -\alpha &&\textit{for negative orders } (m < 0) \\
\beta &= -\alpha &&\textit{for specular reflection } (m = 0)
\end{aligned} \tag{A1.10}$$

This sign convention for m requires that *m* > 0 if the diffracted ray lies to the left (the counter-clockwise side) of the zero order (*m* = 0), and *m* < 0 if the diffracted ray lies to the right (the clockwise side) of the zero order. This convention is shown graphically in Figure A1.4.

A1.1.2.2. Overlapping of Diffracted Spectra.

The most troublesome aspect of multiple order behavior is that successive spectra overlap, as shown in Figure A1.5. It is evident from the grating equation that, for any grating instrument configuration, the light of wavelength λ diffracted in the *m* = 1 order will coincide with the light of wavelength λ/2 diffracted in the *m* = 2 order, *etc.*, for all *m* satisfying inequality (A1.9). In this example, the red light (600 nm) in the first spectral order will overlap the ultraviolet light (300 nm) in the second order. A detector sensitive at both wavelengths would see both simultaneously. This superposition of wavelengths, which would lead to ambiguous spectroscopic data, is inherent in the grating equation itself and must be prevented by suitable filtering (called *order sorting*), since the detector cannot generally distinguish between light of different wavelengths incident on it (within its range of sensitivity). [See also Section A1.1.10 below.]

A1.1.3.   DISPERSION

The primary purpose of a diffraction grating is to disperse light spatially by wavelength. A beam of white light incident on a grating will be separated into its component colors upon diffraction from the grating, with each color diffracted along a different direction. *Dispersion* is a measure of the separation (either angular or spatial) between diffracted light of different wavelengths. Angular dispersion expresses the spectral range per unit angle, and linear resolution expresses the spectral range per unit length.

A1.1.3.1. Angular dispersion

The angular spread dβ of a spectrum of order *m* between the wavelength λ and λ + dλ can be obtained by differentiating the grating equation, assuming the incidence angle α to be constant. The change *D* in diffraction angle per unit wavelength is therefore

$$D = \frac{\partial \beta}{\partial \lambda} = \frac{m}{d \cos \beta} = \frac{m}{d} \cdot \sec \beta = Gm \sec \beta \qquad (A1.11)$$

where β is given by (A1.3). The ratio *D* = dβ /dλ is called the *angular dispersion*. As the groove frequency *G* = 1/*d* increases, the angular dispersion increases (meaning that the angular separation between wavelengths increases for a given order *m*).
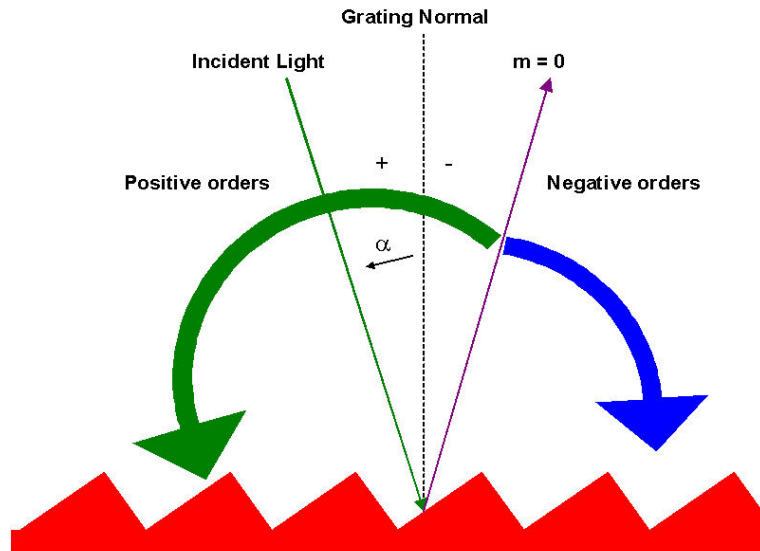
Figure A1.4- Sign convention for the spectral order m. In this example α is positive.
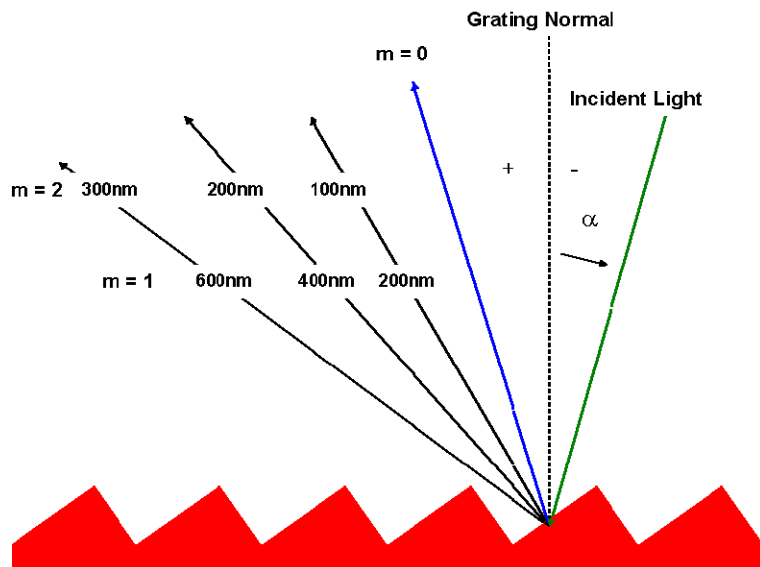
Figure A1.5 - Overlapping of spectral orders*. The light for wavelengths 100, 200 and 300 nm in the second order is diffracted in the same direction as the light for wavelengths 200, 400 and 600 nm in the first order. In this diagram, the light is incident from the right, so α < 0.*

In (A1.11), it is important to realize that the quantity *m/d* is not a ratio which may be chosen independently of other parameters; substitution of the grating equation into (A1.11) yields the following general equation for the angular dispersion:

$$\frac{\partial \beta}{\partial \lambda} = \frac{\sin \alpha + \sin \beta}{\lambda \cos \beta} \qquad (A1.12)$$

For a given wavelength, this shows that the angular dispersion may be considered to be solely a function of the angles of incidence and diffraction. This becomes even more clear when we consider the Littrow configuration ($\alpha = \beta$), in which case (A1.12) reduces to

$$\frac{\partial \beta}{\partial \lambda} = \frac{2}{\lambda} \tan \beta \quad in \ Littrow \qquad (A1.13)$$

When $|\beta|$ increases from 10° to 63° in Littrow use, the angular dispersion increases by a factor of ten, regardless of the spectral order or wavelength under consideration. Once β has been determined, the choice must be made whether a fine-pitch grating (small *d*) should be used in a low order, or a course-pitch grating (large *d*) such as an echelle grating should be used in a high order.

A1.1.3.2. Linear dispersion

For a given diffracted wavelength λ in order *m* (which corresponds to an angle of diffraction β), the *linear dispersion* of a grating system is the product of the angular dispersion *D* and the effective focal length *r'* (β) of the system:

$$\frac{\partial \beta}{\partial \lambda} = \frac{mr'}{d \cos \beta} = \frac{mr'}{d} \sec \beta = Gmr' \sec \beta \qquad (A1.14)$$

The quantity *r'* dβ = d*l* is the change in position along the spectrum (a real distance, rather than a wavelength). We have written *r'* (β) for the focal length to show explicitly that it may depend on the diffraction angle β (which, in turn, depends on λ).

The *reciprocal linear dispersion*, also called the *plate factor P*, is more often considered; it is simply the reciprocal of *r' D*, usually measured in nm/mm:

$$P = \frac{d \cos \beta}{mr'}$$

(A1.15)

P is a measure of the change in wavelength (in nm) corresponding to a change in location along the spectrum (in mm). It should be noted that the terminology *plate factor* is used by some authors to represent the quantity $1/\sin\Phi$, where Φ is the angle the spectrum makes with the line perpendicular to the diffracted rays (Figure A1.6); in order to avoid confusion, we call the quantity $1/\sin\Phi$ the *obliquity factor*. When the image plane for a particular wavelength is not perpendicular to the diffracted rays (i.e., when $\Phi \overline{} 90°$), *P* must be multiplied by the obliquity factor to obtain the correct reciprocal linear dispersion in the image plane.
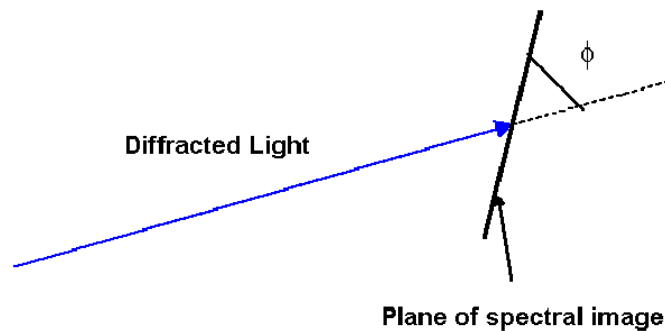
Figure A1.6 - The obliquity angle Φ. The spectral image recorded need not lie in the plane perpendicular to the diffracted ray (i.e., $\Phi \neq 90°$)

A1.1.4. Resolving power

The resolving power *R* of a grating is a measure of its ability to separate adjacent spectral lines of average wavelength λ. It is usually expressed as the dimensionless quantity

$$R = \frac{\lambda}{\Delta\lambda}$$

(A1.*16)*

Here $\Delta\lambda$ is the *limit of resolution*, the difference in wavelength between two lines of equal intensity that can be distinguished (that is, the peaks of two wavelengths λ_1 and λ_2 for which the separation $|\lambda_1 - \lambda_2| < \Delta\lambda$ will be ambiguous). The theoretical resolving power of a planar diffraction grating is given in elementary optics textbooks as

$$R = mN$$

(A1.17)

where *m* is the diffraction order and *N* is the total number of grooves illuminated on the surface of the grating. For negative orders ($m < 0$), the absolute value of *R* is considered.

A more meaningful expression for *R* is derived below. The grating equation can be used to replace *m* in *(A1.17)*:

$$R = \frac{Nd(\sin\alpha + \sin\beta)}{\lambda}$$

(A1.18)

If the groove spacing *d* is uniform over the surface of the grating, and if the grating substrate is planar, the quantity *Nd* is simply the ruled width *W* of the grating, so

$$R = \frac{W(\sin\alpha + \sin\beta)}{\lambda}$$

(A1.19)

As expressed in *(A1.19)*, *R* is not dependent explicitly on the spectral order or the number of grooves; these parameters are contained within the ruled width and the angles of incidence and diffraction. Since

$$|\sin\alpha + \sin\beta| < 2$$

(A1.20)

the maximum attainable resolving power is

$$R_{MAX} = \frac{2W}{\lambda}$$

(A1.21)

regardless of the order *m* or number of grooves *N*. This maximum condition corresponds to the grazing Littrow configuration, i.e., $\alpha \approx \beta$ (Littrow), $|\alpha| \approx 90°$ (grazing).

It is useful to consider the resolving power as being determined by the maximum phase retardation of the extreme rays diffracted from the grating. Measuring the difference in optical path lengths between the rays diffracted from opposite sides of the grating provides the maximum phase retardation; dividing this quantity by the wavelength λ of the diffracted light gives the resolving power R.

The degree to which the theoretical resolving power is attained depends not only on the angles α and β, but also on the optical quality of the grating surface, the uniformity of the groove spacing, the quality of the associated optics, and the width of the slits and/or detector elements. Any departure of the diffracted wavefront greater than $\lambda/10$ from a plane (for a plane grating) or from a sphere (for a spherical grating) will result in a loss of resolving power due to aberrations at the image plane. The grating groove spacing must be kept constant to within about 1% of the wavelength at which theoretical performance is desired. Experimental details, such as slit width, air currents, and vibrations can seriously interfere with obtaining optimal results.

The practical resolving power is limited by the spectral half-width of the lines emitted by the source. This explains why systems with revolving powers greater than 500,000 are usually required only in the study of spectral line shapes, Zeeman effects, and line shifts, and are not needed for separating individual spectral lines.

A convenient test of resolving power is to examine the isotopic structure of the mercury emission line at 546.1 nm. Another test for resolving power is to examine the line profile generated in a spectrograph or scanning spectrometer when a single mode laser is used as the light source. Line width at half intensity (or other fractions as well) can be used as the criterion. Unfortunately, resolving power measurements are the convoluted result of all optical elements in the system, including the locations and dimensions of the entrance and exit slits and the auxiliary lenses and mirrors, as well as the quality of these optics. Their effects are necessarily superimposed on those of the grating.

A1.1.5.   Spectral resolution

While resolving power can be considered a characteristic of the grating and the angles at which it is used, the ability to resolve two wavelengths λ_1 and λ_2 = λ_1 + $\Delta\lambda$ generally depends not only on the grating but on the dimensions and locations of the entrance and exit slits (or detector elements), the aberrations in the images, and the magnification of the images. The minimum wavelength difference $\Delta\lambda$ (also called the *limit of resolution*, or simply *resolution*) between two wavelengths that can be resolved unambiguously can be determined by convoluting the image of the entrance aperture (at the image plane) with the exit aperture (or detector element). This measure of the ability of a grating system to resolve nearby wavelengths is arguably more relevant than is resolving power, since it takes into account the image effects of the system. While resolving power is a dimensionless quantity, resolution has spectral units (usually nanometers).

A1.1.6.   Bandpass

The *bandpass B* of a spectroscopic system is the wavelength interval of the light that passes through the exit slit (or falls onto a detector element). It is often defined as the difference in wavelengths between the points of half-maximum intensity on either side of an intensity maximum. An estimate for bandpass is the product of the exit slit width *w'* and the reciprocal linear dispersion *P*:

$$B \approx w'P \qquad (A1.22)$$

An instrument with smaller bandpass can resolve wavelengths that are closer together than an instrument with a larger bandpass. Bandpass can be reduced by decreasing the width of the exit slit but usually at the expense of decreasing light intensity as well. Bandpass is sometimes called *spectral bandwidth*, though some authors assign distinct meanings to these terms.

A1.1.7.   Resolving power vs. resolution

In the literature, the terms *resolving power* and *resolution* are sometimes interchanged. While the word *power* has a very specific meaning (energy per unit time), the phrase *resolving power* does not involve *power* in this way; as suggested by Hutley, though, we may think of resolving power as 'ability to resolve'.

The comments above regarding resolving power and resolution pertain to planar classical gratings used in collimated light (plane waves). The situation is complicated for gratings on concave substrates or with groove patterns consisting of unequally spaced lines, which restrict the usefulness of the previously defined simple formulae, though they may still yield useful approximations. Even in these cases, though, the concept of maximum retardation is still a useful measure of the resolving power.

A1.1.8. Focal Length and *f*/Number

For gratings (or grating systems) that image as well as diffract light, or disperse light that is not collimated, a *focal length* may be defined. If the beam diffracted from a grating of a given wavelength λ and order *m* converges to a focus, then the distance between this focus and the grating center is the focal length $r'(\lambda)$. [If the diffracted light is collimated, and then focused by a mirror or lens, the focal length is that of the refocusing mirror or lens and not the distance to the grating.] If the diffracted light is diverging, the focal length may still be defined, although by convention we take it to be negative (indicating that there is a virtual image behind the grating). Similarly, the incident light may diverge toward the grating (so we define the incidence or entrance slit distance $r(\lambda) > 0$) or it may converge toward a focus behind the grating (for which $r(\lambda) < 0$). Usually gratings are used in configurations for which *r* does not depend on wavelength (though in such cases *r'* usually depends on λ).

Figure A1.7 shows a typical concave grating configuration; the monochromatic incident light (of wavelength λ) diverges from a point source at A and is diffracted toward B. Points A and B are distances *r* and *r'*, respectively, from the grating center O. In this figure, both *r* and *r'* are positive. Calling the width (or diameter) of the grating (in the dispersion plane) *W* allows the *input* and *output f/numbers* (also called *focal ratios*) to be defined:

$$f/no_{INPUT} = \frac{r}{W}, f/no_{OUTPUT} = \frac{r'(\lambda)}{W}$$

(A1.23)

Usually the input *f*/number is matched to the *f*/number of the light cone leaving the entrance optics (*e.g.*, an entrance slit or fiber) in order to use as much of the grating surface for diffraction as possible. This increases the amount of diffracted energy while not overfilling the grating (which would generally contribute to stray light).

For oblique incidence or diffraction, equations *(A1.23)* are often modified by replacing *W* with the projected width of the grating:

$$f/no_{INPUT} = \frac{r}{W\cos\alpha}, f/no_{OUTPUT} = \frac{r'(\lambda)}{W\cos\beta} \qquad (A1.24)$$

These equations account for the reduced width of the grating as seen by the entrance and exit slits; moving toward oblique angles (*i.e.*, increasing |α| or |β|) decreases the projected width and therefore increases the *f*/number.
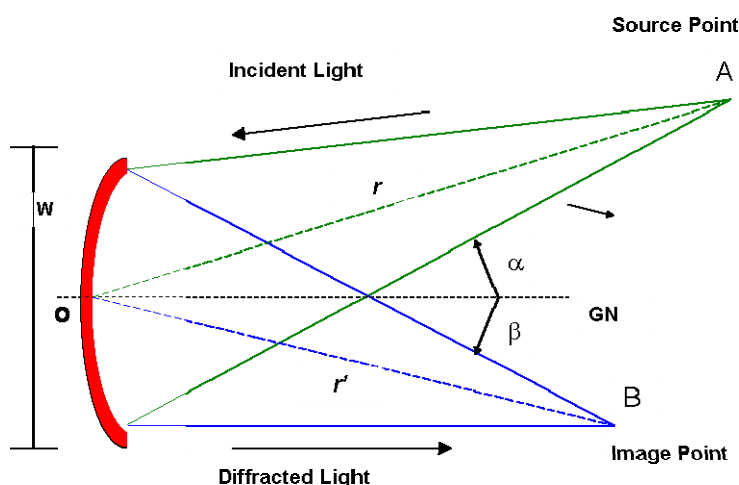
Figure A1.7 - Geometry for focal distances and focal ratios (ƒ/numbers). GN is the grating normal (perpendicular to the grating at its center, O), W is the width of the grating (its dimension perpendicular to the groove direction, which is out of the page), and A and B are the source and image points, respectively.

The focal length is an important parameter in the design and specification of grating spectrometers, since it governs the overall size of the optical system (unless folding mirrors are used). The ratio between the input and output focal lengths determines the projected width of the entrance slit that must be matched to the exit slit width or detector element size. The *f*/number is also important, as it is generally true that spectral aberrations decrease as *f*/number increases. Unfortunately, increasing the input *f*/number results in the grating subtending a smaller solid angle as seen from the entrance slit; this will reduce the amount of light energy the grating collects and consequently reduce the intensity of the diffracted beams. This trade-off prohibits the formulation of a simple rule for choosing the input and output *f*/numbers, so sophisticated design procedures have been developed to minimize aberrations while maximizing collected energy.

A1.1.9. Anamorphic Magnification

For a given wavelength λ, we may consider the ratio of the width of a collimated diffracted beam to that of a collimated incident beam to be a measure of the effective magnification of the grating (Figure A1.8). From this figure we see that this ratio is

$$\frac{b}{a} = \frac{\cos\beta}{\cos\alpha} \tag{A1.25}$$

Since α and β depend on λ through the grating equation (A1.1), this magnification will vary with wavelength. The ratio *b/a* is called the *anamorphic magnification*; for a given wavelength λ, it depends only on the angular configuration in which the grating is used.
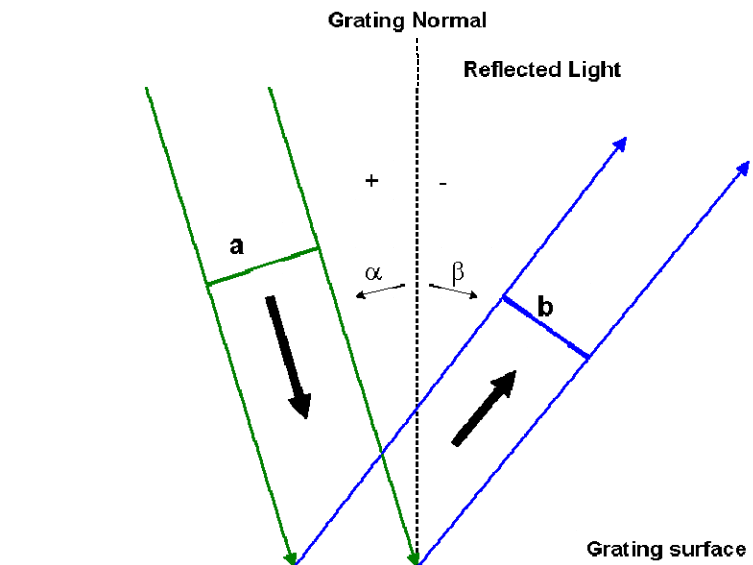
Figure A1.8 - Anamorphic magnification. The ratio b/a of the beam widths equals the anamorphic magnification.

A1.1.10. Free Spectral Range

For a given set of incidence and diffraction angles, the grating equation is satisfied for a different wavelength for each integral diffraction order *m*. Thus light of several wavelengths (each in a different order) will be diffracted along the same direction: light of wavelength λ in order *m* is diffracted along the same direction as light of wavelength $\lambda/2$ in order 2*m, etc.*
The range of wavelengths in a given spectral order for which superposition of light from adjacent orders does not occur is called the *free spectral range Fλ.*

It can be calculated directly from its definition: in order *m*, the wavelength of light that diffracts along the direction of λ_1 in order *m*+1 is $\lambda_1+\Delta\lambda$ where:

$$\lambda_1 + \Delta\lambda = \frac{m+1}{m}\lambda_1$$

(A1.26)

from which

$$F\lambda = \Delta\lambda = \frac{\lambda_1}{m}$$

(A1.27)

The concept of free spectral range applies to all gratings capable of operation in more than one diffraction order, but it is particularly important in the case of echelles, because they operate in high orders with correspondingly short free spectral ranges.

Free spectral range and order sorting are intimately related, since grating systems with greater free spectral ranges may have less need for filters (or cross-dispersers) that absorb or diffract light from overlapping spectral orders. This is one reason why first-order applications are widely popular.

A1.1.11. Energy Distribution (Grating Efficency)

The distribution of incident field power of a given wavelength diffracted by a grating into the various spectral order depends on many parameters, including the power and polarization of the incident light, the angles of incidence and diffraction, the (complex) index of refraction of the metal (or glass or dielectric) of the grating, and the groove spacing. A complete treatment of grating efficiency requires the vector formalism of electromagnetic theory (*i.e.*, Maxwell's equations), which has been studied in detail over the past few decades. While the theory does not yield conclusions easily, certain rules of thumb can be useful in making approximate predictions.

Recently, computer codes have become commercially available that accurately predict grating efficiency for a wide variety of groove profiles over wide spectral ranges.

A1.1.12. Scattered and Stray Light

All light that reaches the image plane from anywhere other than the grating, by any means other than diffraction as governed by (A1.1), is called *stray light*. All components in an optical system contribute stray light, as will any

baffles, apertures, and partially reflecting surfaces. Unwanted light originating from the grating itself is often called *scattered light*.

A1.1.12.1.   Scattered light

Of the radiation incident on the surface of a diffraction grating, some will be diffracted according to (A1.1) and some will be absorbed by the grating itself. The remainder is unwanted energy called *scattered light*. Scattered light may arise from several factors, including imperfections in the shape and spacing of the grooves and roughness on the surface of the grating.

Diffuse scattered light is scattered into the hemisphere in front of the grating surface. It is due mainly to grating surface microroughness. It is the primary cause of scattered light in interference gratings. For monochromatic light incident on a grating, the intensity of diffuse scattered light is higher near the diffraction orders for that wavelength than between the diffracted orders.

M.C. Hutley (National Physical Laboratory) found this intensity to be proportional to slit area, and proportional to $1/\lambda^4$.

In-plane scatter is unwanted energy in the dispersion plane. Due primarily to random variations in the groove spacing or groove depth, its intensity is directly proportional to slit area and probably inversely proportional to the square of the wavelength.

Ghosts are caused by periodic errors in the groove spacing. Characteristic of ruled gratings, interference gratings are free from ghosts when properly made.

A1.1.12.2.   Instrumental stray light

Stray light for which the grating cannot be blamed is called *instrumental stray light*. Most important is the ever-present light reflected into the zero order, which must be trapped so that it does not contribute to stray light. Light diffracted into other orders may also find its way to the detector and therefore constitute stray light. Diffraction from sharp edges and apertures causes light to propagate along directions other than those predicted by the grating equation. Reflection from instrument chamber walls and mounting hardware also contributes to the redirection of unwanted energy toward the image plane; generally, a smaller instrument chamber presents more significant stray light problems. Light incident on detector elements may be reflected back toward the grating and rediffracted; since the angle of incidence may now be different, light rediffracted along a given direction will generally be of

a different wavelength than the light that originally diffracted along the same direction. Baffles, which trap diffracted energy outside the spectrum of interest, are intended to reduce the amount of light in other orders and in other wavelengths, but they may themselves diffract and reflect this light so that it ultimately

reaches the image plane.

A1.1.13. Signal-to-Noise Ratio (SNR)

The *signal-to-noise ratio* (SNR) is the ratio of diffracted energy to unwanted light energy. While we might be tempted to think that increasing diffraction efficiency will increase SNR, stray light usually plays the limiting role in the achievable SNR for a grating system.

Replicated gratings from ruled master gratings generally have quite high SNRs, though holographic gratings sometimes have even higher SNRs, since they have no ghosts due to periodic errors in groove location and lower interorder stray light.

As SNR is an instrument function, not a property of the grating only, there exist no clear rules of thumb regarding what type of grating will provide higher SNR.

A1.1.14. Classical Concave Grating Imaging

A concave reflection grating can be modeled as a concave mirror that disperses; it can be thought to reflect and focus light by virtue of its concavity, and to disperse light by virtue of its groove pattern.

Since their invention by Henry Rowland in 1883, concave diffraction gratings have played an important role in spectrometry. Compared with plane gratings, they offer one important advantage: they provide the focusing (imaging) properties to the grating that otherwise must be supplied by separate optical elements. For spectroscopy below 110 nm, for which the reflectivity of available mirror coatings is low, concave gratings allow for systems free from focusing mirrors that would reduce throughput two or more orders of magnitude.

Many configurations for concave spectrometers have been proposed. Some are variations of the Rowland circle, while some place the spectrum on a flat field, which is more suitable for charge-coupled device (CCD) array instruments.

In Figure A1.9, a classical grating is shown; the Cartesian axes are defined as follows: the *x*-axis is the outward *grating normal* to the grating surface at its center (point O), the *y*-axis is tangent to the grating surface at O and perpendicular to the grooves there, and the *z*-axis completes the right-handed triad of axes (and is therefore parallel to the grooves at O). Light from point source A(ξ , η, 0) is incident on a grating at point O; light of wavelength λ in order *m* is diffracted toward point B(ξ ', η', 0). Since point A was assumed, for simplicity, to lie in the *xy* plane, to which the grooves are perpendicular at point O, the image point B will lie in this plane as well; this plane is called the *principal plane* (also called the *tangential plane* or the *dispersion plane* Figure A1.10). Ideally, any point P(*x*, *y*, *z*) located on the grating surface will also diffract light from A to B. The plane through points O and B perpendicular to the principal plane is called the *sagittal plane*, which is unique for this wavelength. The *grating tangent plane* is the plane tangent to the grating surface at its center point O (*i.e.*, the *yz* plane). The imaging effects of the groove spacing and curvature can be completely separated from those due to the curvature of the substrate if the groove pattern is projected onto this plane.
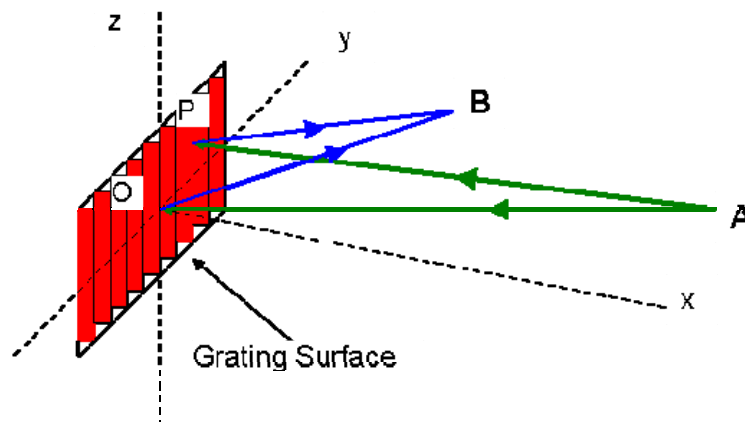
Figure A1.9 - Use geometry. The grating surface centered at O diffracts light from point A to point B. P is a general point on the grating surface. The x-axis points out of the grating from its center, the z-axis points along the central groove, and the y-axis completes the traid.

The imaging of this optical system can be investigated by considering the optical path difference *OPD* between the *pole ray* AOB (where O is the center of the grating) and the *general ray* APB (where P is an arbitrary point on the grating surface). Application of Fermat's principle to this path difference, and the subsequent expansion of the results in power series of

the coordinates of the tangent plane (*y* and *z*), yields expressions for the aberrations of the system.
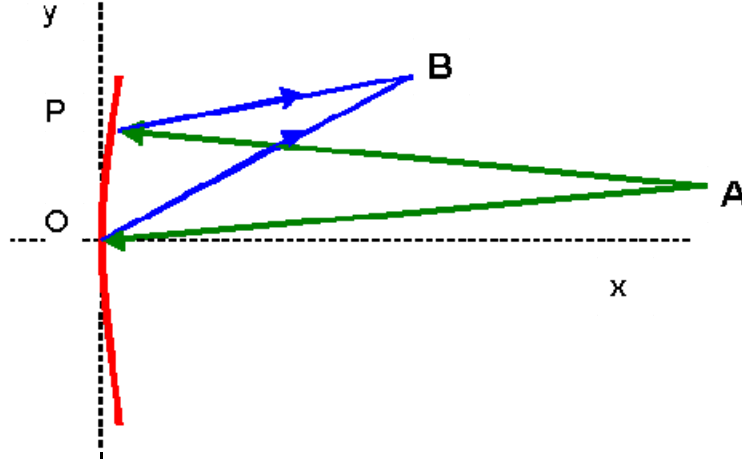
Figure A1.10 - Use geometry – the principal plane. Points A, B and O lie in the xy (principal) plane; the general point P on the grating surface may lie outside this plane. The z-axis comes out of the page at O.

The optical path difference is:

$$OPD =< APB > - < AOB > + Nm\lambda \qquad \text{(A1.28)}$$

where <APB> and <AOB> are the geometric lengths of the general and pole rays, respectively (both multiplied by the index of refraction), *m* is the diffraction order, and *N* is the number of grooves on the grating surface between points O and P. The last term in (A1.28) accounts for the fact that the distances and need not be exactly equal for the light along both rays to be in phase at B: due to the wave nature of light, the light is in phase at B even if there are an integral number of wavelengths between these two distances. If points O and P are one groove apart (*N* = 1), the number of wavelengths in the difference - determines the order of diffraction *m*.

From geometric considerations, we find

$$< APB >=< AP > + < PB >=$$
$$\sqrt{(\xi - x)^2 + (\eta - y)^2 + z^2} + \sqrt{(\xi' - x)^2 + (\eta' - y)^2 + z^2} \qquad \text{(A1.29)}$$

and similarly for <AOB>, if the medium of propagation is air ($n \approx 1$). The optical path difference can be expressed more simply if the coordinates of points A and B are plane polar rather than Cartesian: letting

$$< AO > \ = \ r, \ \ < OB > \ = \ r' \tag{A1.30}$$

It can be written

$$\xi = r\cos\alpha, \ \eta = r\sin\alpha$$
$$\xi' = r'\cos\beta, \ \eta' = r'\sin\beta \tag{A1.31}$$

where the angles of incidence and diffraction (α and β) follow the sign convention described in § A1.1.1.

The power series for *OPD* can be written in terms of the grating surface point coordinates *y* and *z*:

$$OPD = \sum_{i=o}^{\infty}\sum_{j=o}^{\infty} F_{ij}\, y^i z^j \tag{A1.32}$$

where F_{ij}, the expansion coefficient of the (*i*, *j*) term, describes how the rays (or wave fronts) diffracted from point P toward the ideal image point B differ (in direction, or curvature, *etc.*) in proportion to $y^i z$ from those from point O. The *x*-dependence of *OPD* has been suppressed by writing

$$x = x(y,z) = \sum_{i=o}^{\infty}\sum_{j=o}^{\infty} a_{ij}\, y^i z^j \tag{A1.33}$$

This equation makes use of the fact that the grating surface is usually a regular function of position, so *x* is not independent of *y* and *z* (*i.e.*, if it is a spherical surface of radius *R*, then $(x-R)^2 + y^2 + z^2 + = R^2$

By analogy with the terminology of lens and mirror optics, we call each term in series (A1.32) an *aberration*, and F_{ij} its *aberration coefficient*. An aberration is absent from the image of a given wavelength (in a given diffraction order) if its associated coefficient F_{ij} is zero.

Since a plane of symmetry on the system (the principal (*xy*) plane) has been imposed, all terms F_{ij} for which *j* is odd vanish. Moreover, F_{00} = 0, since the expansion (A1.32) is about the origin O. The lowest- (first-) order term F_{10} in the expansion, when set equal to zero, yields the grating equation:

$$m\lambda = d(\sin\alpha + \sin\beta) \tag{A1.1}$$

By Fermat's principle, we may take this equation to be satisfied for all images, which leaves the second-order aberration terms as those of lowest order that

need not vanish. The generally accepted terminology is that a *stigmatic image* has vanishing second-order coefficients even if higher-order aberrations are still present.

$$F_{20} = \cos\alpha\left(\frac{\cos\alpha}{2r} - a_{20}\right) + \cos\beta\left(\frac{\cos\beta}{2r} - a_{20}\right) = T(r,\alpha) + T(r',\beta) \quad \text{(A1.34)}$$

$$F_{02} = \left(\frac{1}{2r} - a_{02}\cos\alpha\right) + \left(\frac{1}{2r} - a_{02}\cos\beta\right) = S(r,\alpha) + S(r',\beta) \quad \text{(A1.35)}$$

F_{20} governs the tangential (or spectral) focusing of the grating system, while F_{02} governs the sagittal focusing. The associated aberrations are called *defocus* and *astigmatism*, respectively. The two aberrations describe the extent of a

monochromatic image: defocus pertains to the blurring of the image - its extent of the image along the dispersion direction (*i.e.*, in the tangential plane). Astigmatism pertains to the extent of the image in the direction perpendicular to the dispersion direction. In more common (but sometimes misleading) terminology, defocus applies to the "width" of the image in the spectral (dispersion) direction, and astigmatism applies to the "height" of the spectral image; these terms imply that the *xy (tangential)* plane be considered as "horizontal" and the *yz (sagittal)* plane as "vertical".

Actually *astigmatism* more correctly defines the condition in which the tangential and sagittal focus are not coincident, which implies a line image at the tangential focus. It is a general result of the off-axis use of a concave mirror (and, by extension, a concave reflection grating as well). A complete three-dimensional treatment of *OPD* shows that the image is actually an arc; image points away from the center of the ideal image are diffracted toward the longer wavelengths. This effect, which technically is not an aberration, is called *(spectral) line curvature*, and is most noticeable in the spectra of Paschen-Runge mounts (see later in this chapter). Figure A1.11 shows astigmatism in the image of a wavelength diffracted off-axis from a concave grating, ignoring line curvature.

Since grating images are generally astigmatic, the focal distances r' in equations (A1.34) and (A1.35) should be distinguished. Calling r'_T and r'_S the

tangential and sagittal focal distances, respectively, we may set these equations equal to zero and solve for the focal curves $r'_T(\lambda)$ and $r'_S(\lambda)$:
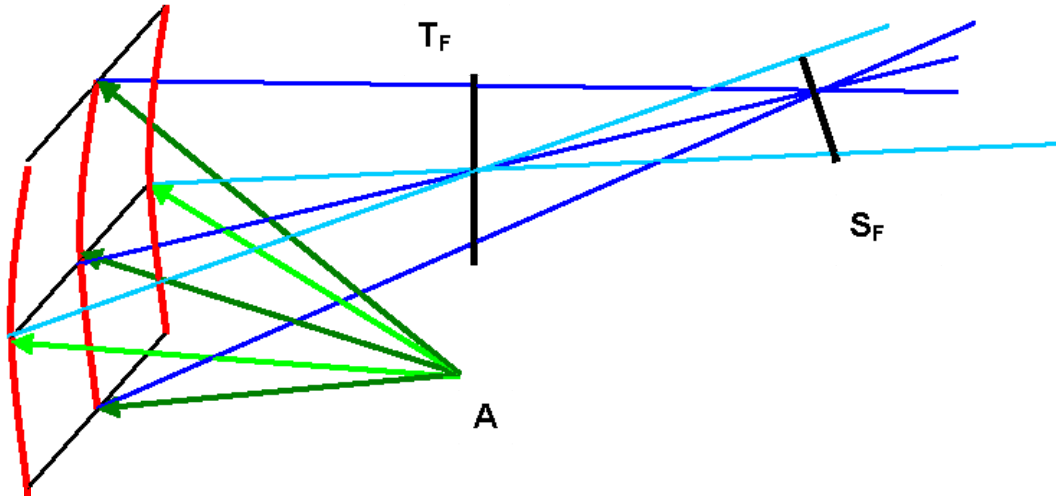
Figure A1.11 - Astigmatic focusing of a concave grating. Light from point A is focused into a line parallel to the grooves at TF (the tangential focus) and perpendicular to the grooves at SF (the sagittal focus). Spectral resolution is maximized at TF.

$$r'_T(\lambda) = \frac{\cos^2 \beta}{A + B\cos\beta} \tag{A1.36}$$

$$r'_S(\lambda) = \frac{1}{D + E\cos\beta} \tag{A1.37}$$

Here we have defined

$$A = B\cos\alpha - \frac{\cos^2\alpha}{r}, \quad B = 2a_{20} \tag{A1.38}$$

$$D = E\cos\alpha - \frac{1}{r}, \quad E = 2a_{02}$$

where a_{20} and a_{02} are the coefficients in (A1.33) (e.g., $a_{20} = a_{02} = 1/(2R)$ for a spherical grating of radius R). These expressions are completely general for classical grating systems; that is, they apply to any type of grating mount or configuration.

Of the two primary (second-order) focal curves, that corresponding to defocus (F_{20}) is of greater importance in spectroscopy, since it is spectral resolution that is most crucial to grating systems. For this reason we do not concern ourselves with locating the image plane at the "circle of least confusion"; rather, we try to place the image plane at or near the tangential focus (where F_{20} = 0). For concave gratings ($a_{20} \neq 0$) there are two well-known solutions to the defocus equation F_{20} = 0.

The *Rowland circle* is a circle whose diameter is equal to the tangential radius of the grating substrate, and which passes through the grating center. If the point source A is placed on this circle, the tangential focal curve also lies on this circle. This solution is the basis for the Rowland circle and Paschen-Runge mounts. For the Rowland circle mount,

$$r = \frac{\cos \alpha}{2 a_{20}} = R \cos \alpha \qquad (A1.39)$$

$$r'_T = \frac{\cos \beta}{2 a_{20}} = R \cos \beta$$

The sagittal focal curve is:

$$r'_S = \left(\frac{\cos \alpha + \cos \beta}{\rho} - \frac{1}{R \cos \alpha} \right)^{-1} \qquad (A1.40)$$

(where ρ is the sagittal radius of the grating), which is always greater than r'_T (even for a spherical substrate, for which ρ = R) unless α = β = 0. Consequently this mount suffers from astigmatism, which in some cases is considerable.

The *Wadsworth mount* is one in which the source light is collimated ($r \rightarrow \infty$), so that the tangential focal curve is given by

$$r'_T = \frac{\cos^2 \beta}{2 a_{20} (\cos \alpha + \cos \beta)} = \frac{R \cos^2 \beta}{\cos \alpha + \cos \beta} \qquad (A1.41)$$

The sagittal focal curve is

$$r'_s = \frac{1}{2a_{02}(\cos\alpha + \cos\beta)} = \frac{\rho}{\cos\alpha + \cos\beta} \qquad \text{(A1.42)}$$

In this mount, the imaging from a classical spherical grating ($\rho = R$) is such that the astigmatism of the image is zero only for $\beta = 0$, though this is true for any incidence angle α.

While higher-order aberrations are usually of less importance than defocus and astigmatism, they can be significant. The third-order aberrations, *primary* or *tangential coma* F_{30} and *secondary* or *sagittal coma* F_{12}, are given by

$$F_{30} = \frac{\sin\alpha}{r}T(r,\alpha) = \frac{\sin\beta}{r'}T(r',\beta) - a_{30}(\cos\alpha + \cos\beta) \qquad \text{(A1.43)}$$

$$F_{12} = \frac{\sin\alpha}{r}S(r,\alpha) = \frac{\sin\beta}{r'}T(r',\beta) - a_{12}(\cos\alpha + \cos\beta) \qquad \text{(A1.44)}$$

where T and S are defined in equations. (A1.34) and (A1.35). Often one or both of these third-order aberrations is significant in a spectral image, and must be minimized with the second-order aberrations.

A1.1.15.   The Rowland Circle Spectrograph

The first concave gratings of spectroscopic quality were ruled by Rowland, who invented them in 1881, also designing their first mounting. Placing the ideal source point on the Rowland circle forms spectra on that circle free from defocus and primary coma at all wavelengths (*i.e.*, $F_{20} = F_{30} = 0$ for all λ); while spherical aberration is residual and small, astigmatism is usually severe. Originally a Rowland circle spectrograph employed a photographic plate bent along a circular arc on the Rowland circle to record the spectrum in its entirety.
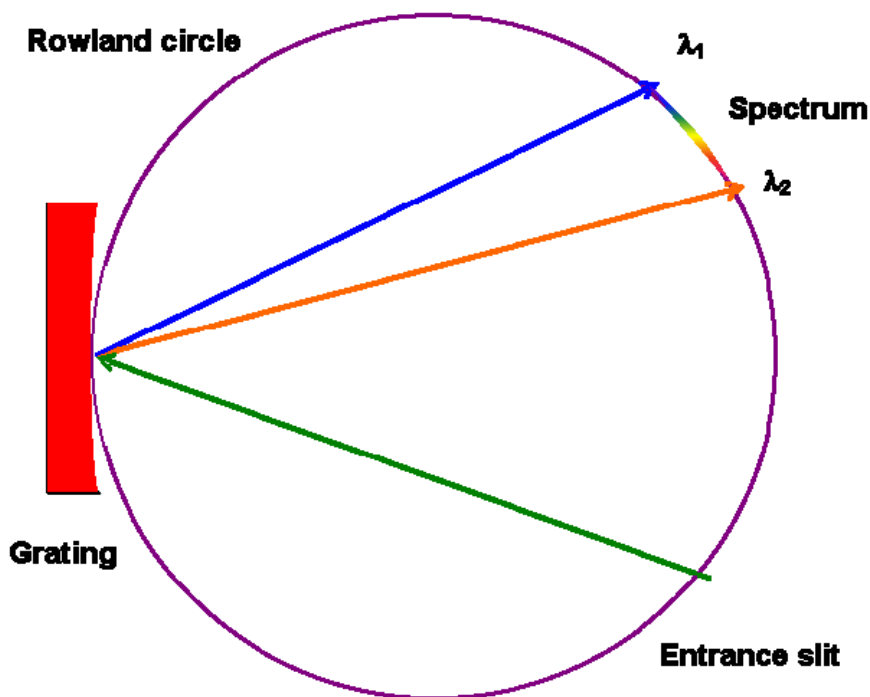
Figure A1.12 - The Rowland Circle spectrograph. Both the entrance slit and the diffracted spectrum lie on the Rowland circle, whose diameter equals the tangential radius of curvature R of the grating and that passes through the grating center. Light of two wavelengths is shown focused at different points on the Rowland circle.

Unless the exit slits (or photographic plates) are considerably taller than the entrance slit, the astigmatism of Rowland circle mounts usually prevents more than a small fraction of the diffracted light from being recorded, which greatly decreases the efficiency of the instrument. Increasing the exit slit heights helps collect more light, but since the images are curved, the exits slits would have to be curved as well to maintain optimal resolution. To complicate matters further, this curvature depends on the diffracted wavelength, so each exit slit would require a unique curvature. Few instruments have gone to such trouble, so most Rowland circle grating mounts collect only a small portion of the light incident on the grating. For this reason these mounts are adequate for strong sources (such as the observation of the solar spectrum) but not for less intense sources (such as stellar spectra).

The imaging properties of instruments based on the Rowland circle spectrograph, such as direct readers and atomic absorption instruments, can

be improved by the use of non classical gratings. Replacing the usual concave classical gratings with concave aberration-reduced gratings, astigmatism can be improved substantially. Rowland circle mounts modified in this manner direct more diffracted light through the exit slits without degrading resolution.

A1.1.16. The Wadsworth Spectrograph

When a classical concave grating is illuminated with collimated light (rather than from a point source on the Rowland circle), spectral astigmatism on and near the grating normal is greatly reduced. Such a grating system is called the *Wadsworth mount* (Figure A1.13). The wavelength-dependent aberrations of the grating are compounded by the aberration of the collimating optics, though use of a paraboloidal mirror illuminated on-axis will eliminate off-axis aberrations and spherical aberrations. The Wadsworth mount suggests itself in situations in which the light incident on the grating is naturally collimated. In other cases, an off-axis parabolic mirror would serve well as the collimating element.

GN
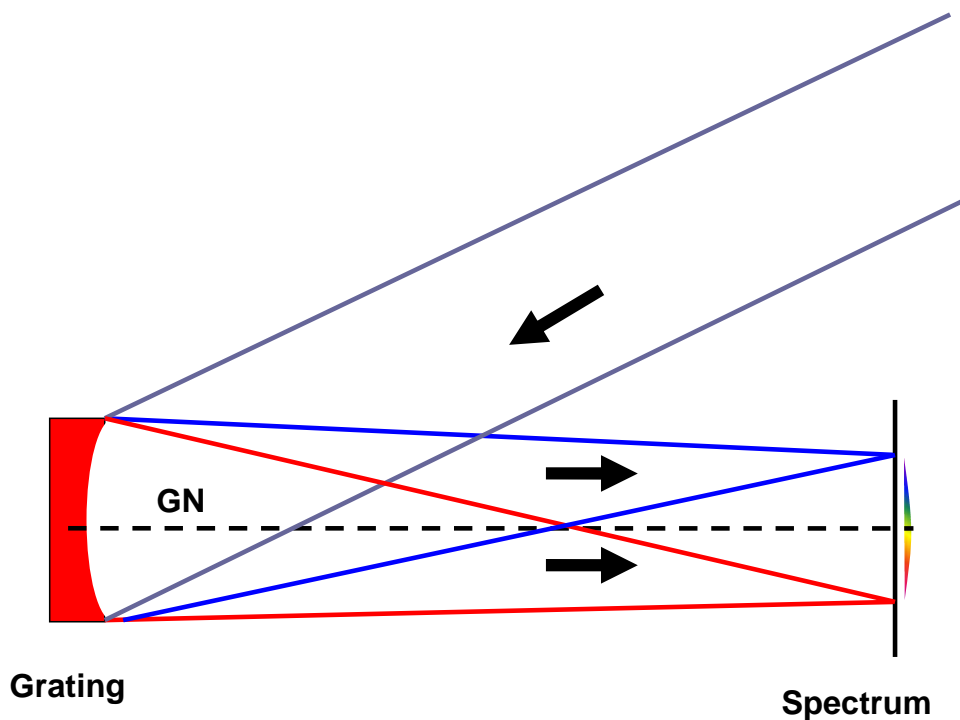
Grating

Spectrum

Figure A1.13 The Wadsworth spectrograph. Collimated light is incident on a concave grating; light of two wavelengths is shown focused ar different points. GN is the grating normal.

A1.1.17. Constant-Deviation Monochromators

In a constant-deviation monochromator, the angle 2*K* between the entrance and exit arms is held constant as the grating is rotated (thus scanning the spectrum; Figure A1.14). This angle is called the *deviation angle* or *angular deviation*. While plane or concave gratings can be used in constant-deviation mounts, only in the latter case can imaging be made acceptable over an entire spectrum without auxiliary focusing optics.
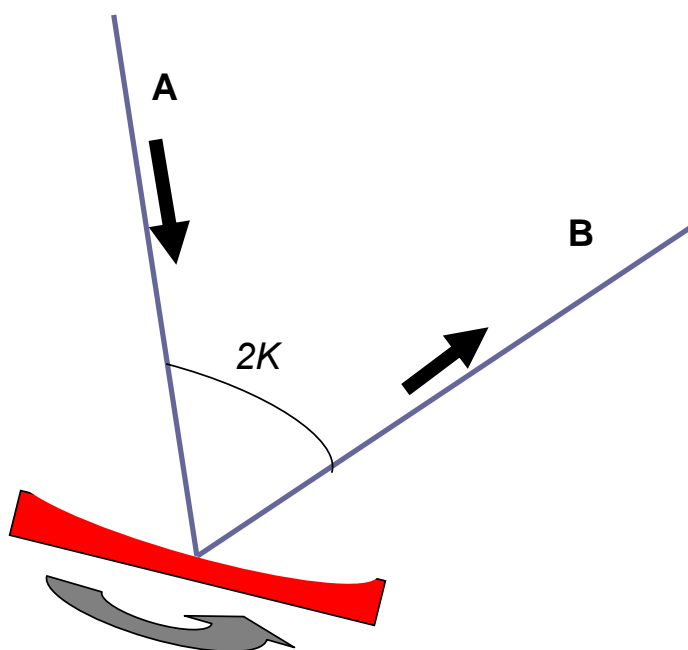
Figure A1.14 - Constant-deviation monochromator geometry. To scan wavelengths, the entrance slit A and exit slit B remain fixed as the grating rotates. The deviation angle 2K is measured from the exit arm to the entrance arm.

The *Seya-Namioka monochromator* is a very special case of constant-deviation mount using a classical spherical grating, in which the deviation angle 2*K* between the beams and the entrance and exit slit distances (*r* and *r'*) are given by

$$2K \;=\; 70°30', \; r \;=\; r' \;=\; R \; \cos(70°30'/2) \tag{A1.45}$$

where R is the radius of the spherical grating substrate. The only moving part in this system is the grating, through whose rotation the spectrum is scanned. Resolution may be quite good in part of the spectrum, though it degrades farther from the optimal wavelength; astigmatism is high, but at an optimum. Replacing the grating with a classical toroidal grating can reduce the astigmatism, if the minor radius of the toroid is chosen judiciously. The reduction of astigmatism by suitably designed interference gratings is also helpful, though the best way to optimize the imaging of a constant-deviation monochromator is to relax the restrictions (A1.45) on the used geometry.

A2. Basic CCD

The CCD sensor (Charged Coupled Device) is a solid state device, by which is possible to acquire images. It is constituted by a matrix of fundamental elements called pixels. In consequence of an exposure, the sensor turns the photons of light which strike him into electrons, and stores them in the matrix. Therefore the charges are associated with a voltage, that can be digitized and sent to the computer disguised as bits.

To better understand how all that happens, the pixels can be considered like a series of glasses which pick up the rainwater (the photons) .The reading process can be represented from a conveyor belt which empties the glasses one at a time (vertical transfer) in a second belt. It is a sequential process by which the content of every single pixel is moved before vertically, then horizontally up to reach the exit node, where it is converted in tension, amplified, digitized and sent to the computer. At the end of the operation, the information's concerning each pixel of the matrix will be available to reconstruct the image on the screen of the PC
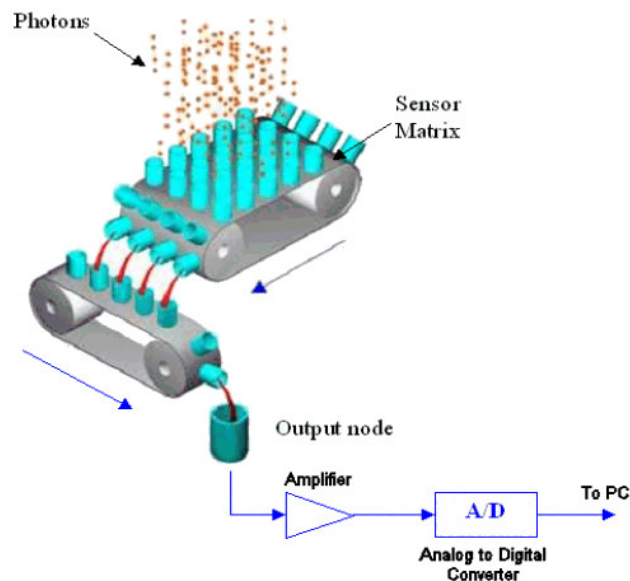
Figure A2.1 – Schematic representation of a CCD Sensor

A2.1. Analog to Digital Conversion

In order that the computer can manage the signals received by the pixels, they must be converted to numbers. In this regard an A/D converter is used. This device turns the entry tension into sequence of bits.

The number of bits, on which the outgoing value is codified, classifies the A/D converters. Typically converters at 8,10,12,14,16 bits can be found. Grater is the number of bits, more refined is the quantization of the signal. In fact, if n is the number of bits, the outgoing signal can assume 2^n different values:

Even if highest number of bits means the widest range, the best choice is not always the highest number of bits. In fact, when a converter has to be chosen, a series of factors has to be considered..

First of all, major it is the number of bits, slower will be the conversion process. This represents a strong limit when it is necessary to read images acquired by sensors of big dimension or to take real-time readings . For instance, an A/D good converter of 16 bits has a time of conversion of 10^{-5} sec: it can read 100.000 pixels per second at the maximum. If the sensor is 1024x1024 pixels, almost 11 second are necessary for reading the full image. Another limit is represented by the space necessary to store the images. With a 16 bit A/D converter, 2 bytes are necessary for the value of each pixel. If the CCD is of 1300x1024 pixels , 2.6 MB of memory, will be necessary while with a 8-bit converter only 1.3 MB.

A further factor which it is necessary to consider to choose the type of converter is the reading noise. It shows itself as a random signal and it is added to the real signal, creating an indetermination amount. Major it is the noise, lower will be the accuracy of the measurement. It is important since it determines the dynamics range of the camera. This parameter shows the capacity to distinguish various levels inside an image.

A2.1.1. Full Well Capacity (FWC)

This parameter shows the capacity of the single pixel that is the number of electrons than they can contain. Also in this case it is very important to consider what purposes the camera will be used for .

Full Well Capacities of 45000/100000 are much common, it is however clear that a FWC of 500000 or more electrons should be preferable since it will be possible inside the same image shoot very intense sources, without causing a blooming (see § A2.2.5) of the pixel, together with weak sources. Furthermore for equal reading noises, a big FWC allows to have superior dynamic ranges. For instance, a sensor with a FWC of 100 Ke- and a reading noise of 10 e- offers a dynamic range of 1:10000 (100000/10) but a sensor with the same reading noise and a FWC of 500000 e-, offers a dynamic range of 1:50000 (500000/10), perfectly compatible with a 16 bits A/D

converter. Unfortunately however the FWC is tight dependent to the dimension of the pixel. Big FWCs have themselves only with pixel of big dimensions (> 20 um), furthermore big FWCs limit the speed of reading of the sensor itself which can exceed 1 Mpix/s.

A2.2. Noise

The random changes are better known with the term noise. It represents a strong limit for the quality of the CCD images and can be caused by various factors.

A2.2.1.1. Dark current or thermal noise

This parameter (expressed in electrons/pixel/second for a fixed temperature) shows the number of electrons which are stored in the pixels when these are not exposed to the light. It represents a type of noise to which the shoot is always subject, and is a strong limit when we must acquire images of low intensity. In fact, if the electrons coming from the image do not exceed the ones due to the noise, we will not be able to distinguish them.
Unfortunately this trouble cannot be physically removed, as it is linked to the nature of the sensor. It can be only attenuated, by cooling the CCD.
Calculation of the dark current for a fixed temperature:

$$Dark = Dk \: / \: 2 \: ((TDk - Top) \: / \: Dd)$$

With:
Dark = Value of the dark current at the requested temperature, expressed in e-pixel per second
Dk = Value of the dark current specified for a certain temperature, expressed in e-pixel per second
TDk = Value of temperature to which Dk refers in Celsius
Top = Value of temperature to which one wants to use the CCD.
Dd = Value in Celsius in which the dark current is halved

A2.2.1.2. Reading noise

It represents the measure of the mistakes executed by the on-chip amplifier during the process of reading of the charges accumulated on the sensor. (Effective value) It is a specification provided by the designer of the CCD,

expressed in electrons. For instance, a value of 10e shows that the average change in the reading of the signal is of 10 electrons.

This kind of noise is only guaranteed if the CDS (Correlated Double Sampling) is used and obviously if electronics of the camera has an equivalent noise much lower.

A2.2.1.3. Quantization noise

The digitalization of the signal coming from the CCD causes this kind of noise. The A/D converter carries out a rounding off, dividing the signal into levels: 256 for 8 bits, 4096 for 12 bits, 65536 for 16 bits. Lower it is the number of levels, major will be the introduced errors.

With a converter of 8 bits the approximation could be greater than the thermal and than the reading noise and therefore limit the accuracy in the acquisition of the images.

The quantization noise is:

$$QN = \frac{FWC}{(2n \times 3.464101515)}$$

Where:
FWC = the Full Well Capacity for every single pixel (number of electrons)
n = bit number of the converter A/D.

A2.2.2. Bias

This word means the signal acquired by the camera with a zero exposure time. The electronics of the camera and the CCD itself cause the Bias that shows itself like a constant value which is added to the ones due to the shoot image, a true offset on the measurement. Because also the CCD sensor produces it, the Bias changes with the temperature of the CCD sensor in accordance with the gain currently in use.

A2.2.3. Gain

As already seen (A/D conversion), the acquisition system converts the outgoing voltage associated to the single pixel in digital and afterwards it treats it as number or ADUs (Analog-to-Digital Units). The voltage necessary

(that is the number of received electrons or photons) to produce one ADU is the gain of the device.

With a typical gain of 10 e/ADU are therefore necessary 10 electrons to give the outgoing value of 1. If a pixel captures 1000 electrons, the outgoing value will be 100 ADUs. With 17.234 electrons we will have 1723 ADUs and not 1723,4 as the exit can only assume integer values. As it is possible to guess, the device resolution is tight connected to the gain, whose value depends in his turn on the type of converter A/D.

Normally for the cameras it is possible to set up various gain values. In a camera that has an only one possible choice, the maximum count of the A/D converter with the maximum FWC of the sensor has to be optimized, in practice if a CCD sensor has a FWC of 200000 e- and a 16 bits converter is used we will have:

3.05 e-/ADU= 200000/65536

In this way it is easy finding the limit operating . For instance, if the binning (different adjacent pixels are joined to form a bigger one – see § A2.2.6) is used, the reduction capacity of exit node which is greater than the single pixel, can be exploit. Therefore a bigger outgoing signals can be obtained, if the gain of the system can be decreased.

A2.2.4.   Quantum Efficiency

This parameter is very important for a CCD sensor, as it expresses his efficiency, the capacity to capture the photons which strike it and use them to produce the outgoing signal, at different wavelengths. It is expressed in percent at a certain wavelength . For instance, a value of 40% means that for 100 photons which strike the sensor 40 are really captured and changed in electrons.

The used manufacture techniques considerably affect the spectrum response of the sensor. As we can see from the image, the various models in fact present different responses.

Going back to the example of the glasses, it is as there were drops of various dimensions. The littlest ones represent the UV wavelengths, while the biggest ones the NIR region. Not all of the drops are received in the same way: the little ones can dissolve before reaching the bottom of the glass, the big ones can not be taken by the glass.

Technically speaking, the CCD loses his sensitivity in the right extreme of the spectrum (infrared), because the photons have not enough energy to

produce electrons inside the cells. From the other side (ultraviolet) the photons are not able to penetrate into the CCD quite deeply to enter into the cells and they are stopped by the superficial layers. Between these two extremes, interference effects can cause various peak and subsidence values in the response.

In general, major it is the Qe value, better is the device. Since the quantum efficiency will be high only for certain values in any case, it is important choose the sensor most suitable for its shooting demands.

A2.2.5. Blooming

The Blooming term means the behaviour of the sensor when the Full Well Capacity of the pixels is exceeded. In the standard CCD, when the pixels exceed the saturation and are filled too much , the charge in excess flows in the adjacent ones, typically above and below the same column, creating some stripes on the image.

Some types of sensors (code with suffix L) are equipped with an Antiblooming protection which prevents this behaviour, but they have a loss of FWC around 50% and the reduction of the fill-in. This allows the over exposition of the sensor avoiding the described effect.

However this option presents some disadvantages. Principally it drastically decreases the sensitive area of the single pixels (fill-in), therefore reducing the sensitivity of the whole sensor.

A2.2.6. Binning

This term means a technique used to increase the sensitivity of the sensor and reduce the download times. It consists in joining various adjacent pixels to form a bigger one.

It is possible to make various types of binning. For instance, if we do a binning 2x2, we join 4 pixels. The resolution of the sensor is halved, but the sensitivity increases of a factor 4 , the time of reading decreases of 2 and the reading noise doubles.

To understand how that happens we go back to the example of the glasses. When for instance we implement a binning 2x2, not one, but two rows of glasses are emptied in a single glass of the horizontal register and then, analogously, two glasses of the register for time are emptied in the final node. .Both the horizontal register, and the exit node must obviously have an appropriate dimension not to be saturated and cause the Blooming effect

A3. The Data Acquisition System (DAS)

A3.1. Introduction

A3.2. The automatic setup

In order to provides a tool for the system configuration for the execution of the DAS program an automatic setup procedure was created . This last creates in the program toolbar the group "Data Acquisition Software x.x.x" (where x.x.x is the release of the program), with some predefined shortcuts.

In addition the setup adds in the windows register the association of DAS with the following type of files:

- **"*.bif"** - binary image format (see A3.4. Data Files Format)
- **"*.dat"** - ASCII image format (see A3.4. Data Files Format)
- **"*.prg"** - ASCII files containing predefined measurements cycles (see A3.6. Measurement chart)
- **"*.log"** - ASCII files generated by DAS during the execution, containing the time series of the working parameters of the instrument (Temperatures of the Optical Mechanical Unit (OMU), of the Electric Control Unit (ECU) and of the CCD Camera)
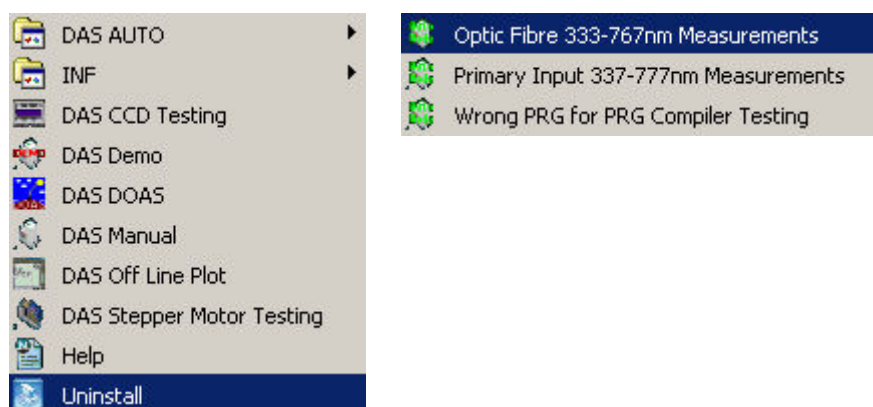
Figure A3.1 – Shortcuts created in the program bar by the Automatic Setup of the DAS for different Execution mode of the main program.

A3.3. Execution modes

The program can be launched using the shortcut created by the automatic setup or clicking on the registered files or the commands can be typed directly at the system prompt.

It is possible to execute the program in different modes:

1. **Manual Use**: the user can manage the instrument.

2. **Automatic Use**: The spectrometer performs a chart of pre-defined measurements cycles.

3. **Automatic timed**: SPATRAM performs different charts of measurements at prefixed period during the day.

4. **Demo**: All the functionality of the Spectrometer without the instrument connected to the PC are simulated - useful during the testing phases of the software.

5. **Off Line Plot**: Allows for the post-visualization of the measured spectral data.

6. **DOAS Mode**: Allows for the off-line processing of the spectral data, for Off Line Plot Visualisation and more (still on going!!!!)

7. **LOG Mode**: Allows for the post-visualization of the log files.

8. **CCD Testing**: In order to test only the CCD sensor.

9. **AD Testing**: In order to test only the AD converter used for the temperature monitoring.

10. **AMS Testing**: In order to test only the adapter devices for the stepper motors.

In the following paragraphs the most important features of the different execution mode will be analyzed.

A3.3.1. Manual Use

For the manual mode is enough a double click on the executable DAS.EXE or the selection of the shortcut "DAS Manual" in the group created by the Automatic Setup. The program starts, the configuration files containing the parameters for a right execution of the program and for the management of the connected devices, are loaded (see A3.5. DAS System Files) and the Graphic User Interface is loaded (Figure A3.2).

The Main Panel of the DAS GUI allows for the monitoring and the management of the equipment.

Figure A3.2 – DAS Main Panel

From Left to Right can be identified:
1. Push Buttons (Left Column)
2. Optical Mechanical Unit (OMU) Parameters
3. OMU Status
4. OMU Status 1
5. Push Buttons (Right Column)

If the initialization of the CCD Camera give a positive result, also the CCD image and the CCD histogram are loaded
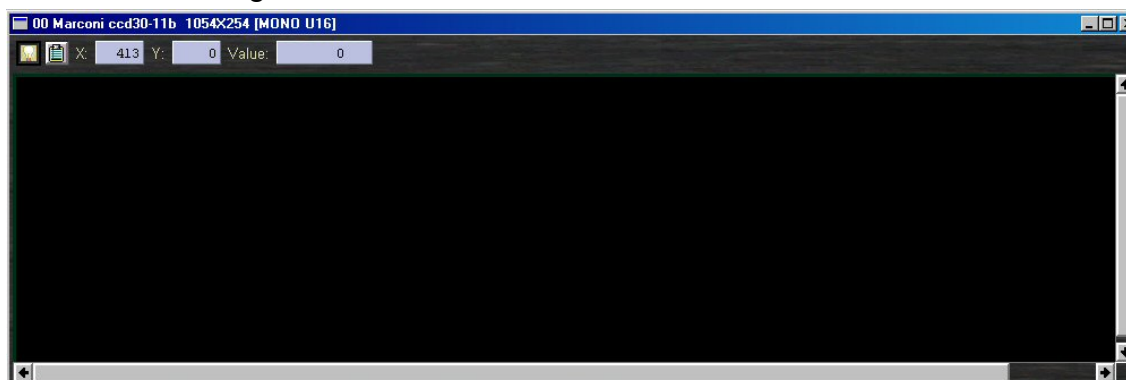
Figure A3.3 – CCD sensor

Figure A3.4 – CCD histogram

otherwise a message error is displayed

Figure A3.5 – CCD Error

Also the AMS devices are initialized and if they are not found a message dialog appears

Figure A3.6 – AMS1 and AMS2 Error Warning

Finally the AD_Converter (the PC104) is initalized and if there are problems a message dialog appears

Figure A3.7 – Ad Error

Now some background tasks as the thermoregulation of the whole equipment, the monitoring of the grating position, the time refresh and the computation of the actual Solar Zenith Angle are activated.

A3.3.2.   Automatic Use

For the automatic use a shortcut to the executable DAS.EXE has to be created with an argument that specify the name of the ASCII file containing the key-words and the parameters for pre-defined measurements cycles (*.PRG), or it can be used one of the shortcuts "DAS AUTO -> xxxxx" in the group created by the Automatic Setup.
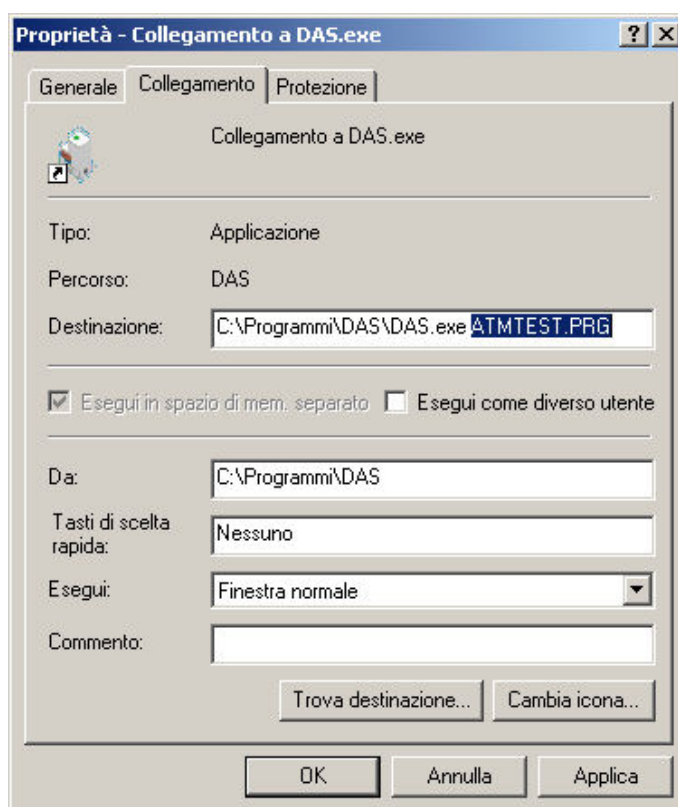
Figure A3.8 – Example of shortcut for the DAS Automatic Use

At the beginning of execution a check on the existence of the PRG file is done.
If the file doesn't exist the user is warned and the program quits
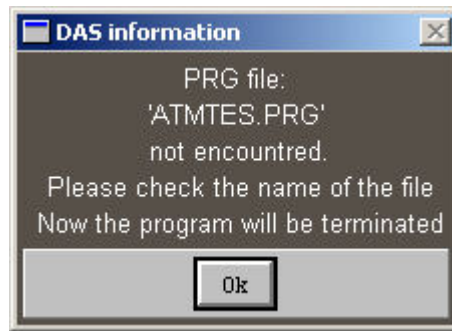
Figure A3.9 – DAS Automatic Use – PRG file not encountered

If the file exists the syntax of the PRG file is checked.

if there are errors on the keywords or the parameters again the DAS ask for action to take.

Figure A3.10 – DAS Automatic Use – Syntax errors encountered in the PRG file

If the button **ViewErr** is pushed, 2 edit windows showing the PRG file and the errors encountered in are created
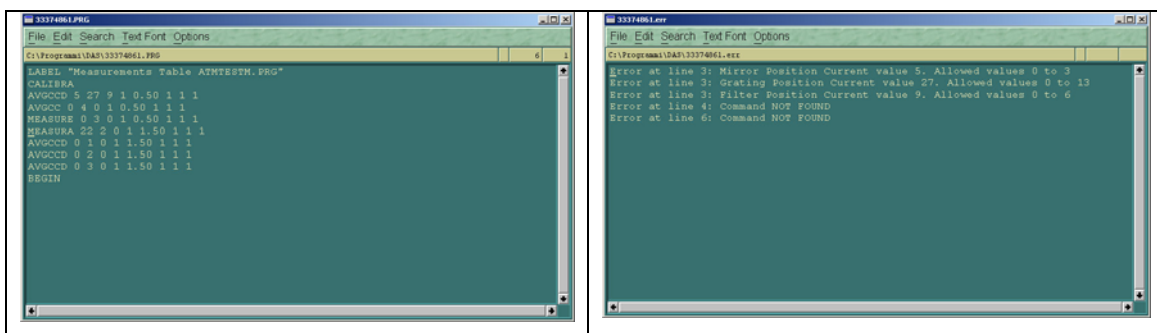
Figure A3.11 – DAS Automatic Use – PRG file and errors in it

After the PRG file is rightly loaded, as for the Manual Use the devices connected to the equipment (CCD Camera, AMSs and ADConverter are initialized DAS waits

until when the working CCD temperature is reached. Only at this moment the cycle of measurements begin.

A3.3.3.   Automatic timed
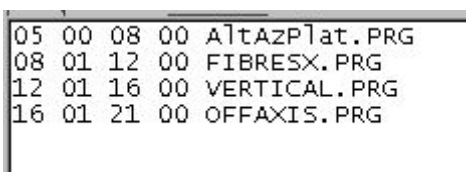
This mode of execution requires the argument "MASTER".MASTER is an ASCII file with so many records as the numbers of PRG files the user wants to execute. A single record has the syntax:

HHi MMi HHe MMe xxxxxxx.PRG

Where:
1) *HHi MMi* - the initial hours and minutes of execution of the tabulated measurement specified in the PRG file given as third argument
2) *HHe MMe* - the finish time of execution of the PRG file
3) The name of a valid PRG file

Figure A3.12 shows an example of MASTER file.

```
05 00 08 00 AltAzPlat.PRG
08 01 12 00 FIBRESX.PRG
12 01 16 00 VERTICAL.PRG
16 01 21 00 OFFAXIS.PRG
```

Figure A3.12 – DAS Automatic timed– Example of a MASTER fil

A3.3.4.   Demo

The argument "Demo" allows for the execution in order to demonstrate the capability of the DAS, without any device connected to the PC. This modality is used mainly in the testing phase of the software package.

A3.3.5.   Off Line Plot

In this case the command to give in the shortcut or at the command prompt is:

DAS.EXE *offlineplot* [filename]

filename is the name of a recognized file of measurements (*.dat -ASCII, or *.bif - Binary). If the program has been installed with tha Automatic Setup a double click on the file of measurements starts also the program.

The program starts and the spectral measurements in the file are plotted.
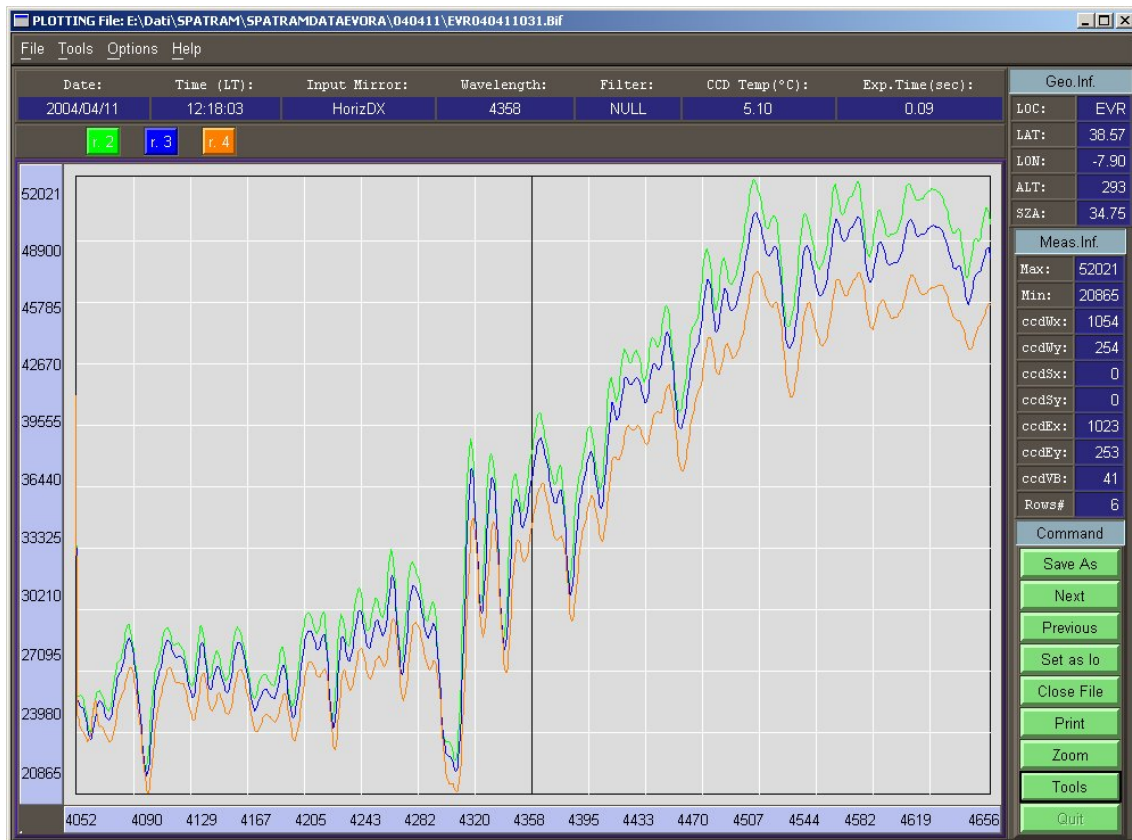
Figure A3.13 – DAS OffLinePlot Use – Plotting of a spectral series obtained with SPATRAM

The push buttons on the right have to be used to browse the file and to operate on the single spectrum (Save, Filter –via the "Tools" button…).

A3.3.6. DOAS Mode

In this case the command to give in the shortcut or at the command prompt is:

DAS.EXE *doas*

The program starts and the DOAS main panel is loaded (Figure A3.14).

Figure A3.14 – DAS DOAS Use – DOAS Main Panel

The implementation of the DOAS module of the DAS program is still on going. The objectives of this execution mode is to provide tools for the real time processing of the collected spectral data. In fact, till now, the DOAS algorithms (described in the chapter 6) can be applied only off line with a software tool also developed by the author.

A3.3.7.   LOG Mode

In this case the command to give in the shortcut or at the command prompt is:

DAS.EXE *[filename].log*

Filename.log is the name of a recognized log file, created by DAS, containing the time series of the working parameters of the instrument (Temperatures of the Optical Mechanical Unit (OMU), of the Electric Control Unit (ECU) and of the CCD Camera). The program starts and the empty plot window is displayed. Then the user has to choose the quantity to plot (Figure A3.15).
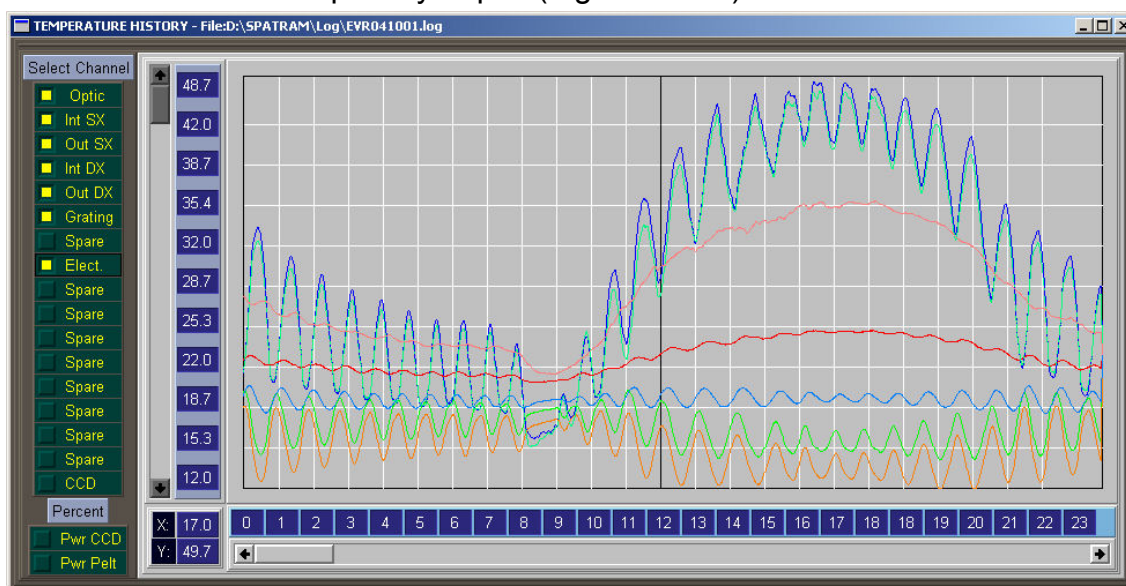
Figure A3.15 – DAS LOG Use – Plotting of a LOG file created by DAS

A3.3.8.   CCD Testing, AD Testing, AMS Testing

These execution modes are used during the testing of the single devices. For the CCD testing the DAS main Panel can be used with the page **Parameters** of the **DAS Config Panel** (see § A3.5.1 and Figure A3.18). This last can be executed, pressing the Config push button in the DAS main Panel or the Config item in the DOAS main Panel Menu.

The AMSs devices, the stepper motors, the opto-insulated output and input ports can be tested with the DAS main Panel and the page **Motors** in the DAS_Config Panel (see § A3.5.1 and Figure A3.19).

In order to test the AD converter for the temperature the page **TEST AD Converter** in the DAS Config Panel has to be used (Figure A3.16).
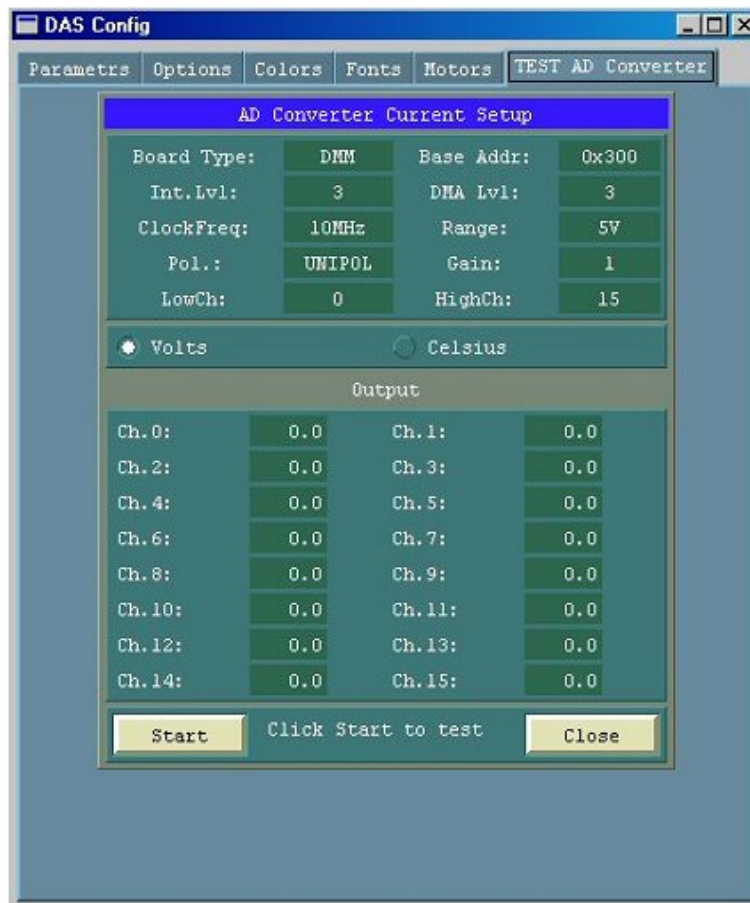
Figure A3.16 – DAS Config Panel – Testing AD Converter page

A3.4. Data Files Format

The data of solar scattered radiation measured by the spectrometer are stored in ASCII or Binary files.

The choice can be done setting the "Saving Mode" in the Options - Page 1.

During the developing and testing phase of the DAS the data were stored mainly in ASCII format, only after the installation of the equipment when the data acquisition became regular, the great amount of data suggested the switch to the binary saving mode.

In fact, each data file has a variable size, mainly due to the parameter that set the vertical binning of the CCD sensor (vb).

For ASCII files that means (256/vb) x 1054 * 2 bytes plus the spaces before and after each value for each spectrum stored).

In addition for each spectrum the ASCII Header with a fixed size of 166 bytes is stored. Fixing the vb to a value of 32, each file (containing 50 measured spectra) has a dimension of (256 / 32 * 1054 * 6 + 172) * 50 = 2478 KB.

In Binary mode the size of the Data file (with the same vertical Binning) is: (256 / 32 * 1054 * 2 + 364) * 50 = 841 KB.

The dimension is quite smaller than the ASCII files even if the Binary Header. is greater than the ASCII one.

A3.4.1. Measurements Header - ASCII

Reading the ASCII header from left to right the following parameters can be identified:

```
LOC: EVR LAT: 38.57 LON: -7.90 ALT[m/asl]: 293 SZA: 78.17
2004/04/01 08:22:31 LT HorizDX 6734 NULL -7.79 6.47 37826      0
0 1054 254 0 0 1023 253 41 6 0 0 0 0
Default Comment
```

Figure A3.17 – Example of ASCII Header

Table A3.1 – DAS Measurements, ASCII Header

1st Record	2nd Record	3rd Record	4th Record
Station (LOC: AAA)	Date (YYYY/MM/DD)	Image type (0 = Mono 1 = RGB),	Character string to insert comments on the measurements (usable when DAS is manual mode)
Latitude (LAT: xx.xx)	Time (HH:MM:SS) - Local time considering also the DST - Daylight Saving Time	CCD Horizontal Pixel	
Longitude (LON: xxx.xx)	Input mirror Position	CCD Vertical Pixels	
Altitude (ALT [M/asl]: xxxxx)	Spectral position	CCD Window X Start	
Solar Zenith Angle (SZA: xx.xx)	Filter wheel position	CCD Window Y Start	
	CCD Temperature (°C)	CCD Window X End	
	Exposure time	CCD Window Y End	
	max value of the measure	Vertical binning	
	Minimum of the measure	Numbers of rows	
		Dummy	
		Dummy	
		Dummy	
		Dummy	

A3.4.2.　　　Measurements Header - Binary

As the ASCII Header the binary one contains all the informations regarding the measures, but the values are stored in consecutives cells of memory, without the spaces necessary in the ASCII format.

Table A3.2 explains the format, the type and the length (in bytes) of each field of the header in binary format.

Table A3.2 – DAS Measurements, Binary Header

Variables	Type	Bytes
Station	Char	4
Latitude	Int	4
Longitude	Int	4
Altitude	Int	4
Solar Zenith Angle	Int	4
Date	Int	4
Time	Int	4
Input Mirror Position	char	8
Grating Position	Int	4
Filter Wheel Position	Char	5
CCD Temperature	Int	4
Image Max.	Int	4
Image Type	Int	4
CCD X Dimension	Int	4
CCD Y Dimension	Int	4
CCD Window, X Start	Int	4
CCD Window, Y Start	Int	4
CCD Window, X End	Int	4
CCD Window, Y End	Int	4
CCD Vertical Binning	Int	4
Number of lines	Int	4
Dummy 1	Int	4
Dummy 2	Int	4
Dummy 3	Int	4
Dummy 4	Int	4
Comment	Char	255

A3.5. DAS System Files

DAS requires the presence in the working directory of several files and sub-folders containing the configuration files and the system files for the execution of the application. In the working directory, besides the executable DAS.EXE, the following files are necessary:

- **DCL.DLL, DTA.DLL** and **WINDRVR.VXD**: the libraries for the Camera management

- **DSCUD51.DLL**: the library for the AD converter management

- **WSC32.DLL**: the library for the Stepper Motor's drivers
- **CAMERA.CFG**: System file for the configuration of the CCD sensor

And also the sub-directory:

- **\CCD**: Definition files for the CCD sensor
- **\CONFIG**: Configuration files for DAS Application
- **\DATA**: Directory where the measured spectral data are stored
- **\DILSYS, \SYS** and **\VIIMG**: System file for the graphics libraries
- **\HP**: Configuration Files for the CCD Driver
- **\LOG**: LOG file for the offline analysis of the spectrometer performance
- **\DOAS**: Configuration files for DOAS module (on Going)
- **\HELP**: Contains the Help for the DAS

The system files containing the settings for the right execution of the program are almost all placed in the \Config directory and they are:

1. PARAM.INI
2. OPTIONS.INI
3. DASSYSCOLORS.INI
4. FTP.INI
5. GEOCOORD.INI
6. CCD_DEFECT.COR

A3.5.1.   PARAM.INI

This files contains: the setting for the CCD Camera and for the OMU thermoregulation and the working parameters for the stepper motors. All these parameters can be changed during the execution of the program using the tool in the page **Parameters** of the "DAS Config" panel (Figure A3.18) that can be accessed pressing the "Config" Button in the DAS Main Panel

Figure A3.18 – DAS Config Panel – Parameters page

The section **CCD & OMU Temp** allows for the modification of the target temperature and power assigned to the Peltiers for the OMU as for the CCD Camera

The section **CCD Window** allows for the choice of the CCD windows used and the setting of the vertical binning

With the **CCDSetup** push Button the type of used CCD can be changed.

The **Apply** push Button applies the changes for the current session, while the **Store** push Button write the new parameters in the file "\Config\PARAM.INI",

At the next DAS execution the new setting will be loaded.

The **Close** button close the DAS_Config Window

The parameters for the stepper motors can be modified with the **Motors** page in the DAS Config (Figure A3.19)

Figure A3.19 – DAS Config Panel – Stepper Motors page

The page **Motors** allows for changing the parameter of the AMS devices (the drivers of the stepper motors).In this panel there are other sub-pages equal to the number of the AMS installed on the equipment. For each motor can be selected: the assigned power, the ratio fixing the Step/Rounds, the slope and the speed of positioning. In addition in the bottom panel the push buttons can be used to test the 8 Opto-Insulated output ports of each AMS (Each port is utilized for activation/deactivation of the related relay).As for the Parameters page, the **Apply** push Button applies the changes for the current session, while the **Store** push Button write the new parameters in the file "\Config\PARAM.INI". At the next DAS execution the new setting will be loaded. The **Close** button close the DAS_Config Window. Figure A3.20 shows an example of file PARAM.INI

```
##################################################
#                 PARAM.INI                      #
#      Main configuration file for SPATRAM       #
#                  equipment                     #
##################################################
# ---------------------------------------------- #
#          by DanBo 17/06/2005 at 10:59:59       #
# ---------------------------------------------- #
# CCD Temp (°C) -------------------------------- #
5.0
# CCD Peltier Init Power × 10 (150 = 15.0)  #
100
# Optical Unit Target Temperature ------------#
16.0
# OMU Peltier Init Power × 10 (500 = 50.0)  #
840
# CCD Window (xstart ys xend ye) -------------#
0 0 1023 253
# Vertical Binning ------------------------#
32
# Input Mirror Stepper Motor - SM1            #
# SM1 Power (0 = 0A - 76 = 1.52A)             #
38
# SM1 Step (0=400s/r, 1=800s/r,2=1000/sr)     #
2
# SM1 Slope (0 - 255)                         #
8
# SM1 Speed Hz (PS = 125*(n+1), n=0,1..255)   #
30
# Grating Stepper Motor - SM2                 #
# SM2 Power (0 = 0A - 76 = 1.52A)             #
38
# SM2 Step (0=400s/r, 1=800s/r,2=1000/sr)     #
5
# SM2 Slope (0 - 255)                         #
8
# SM2 Speed Hz (PS = 125*(n+1), n=0,1..255)   #
95
# Filter wheel Stepper Motor - SM3            #
# SM3 Power (0 = 0A - 76 = 1.52A)             #
38
# SM3 Step (0=400s/r, 1=800s/r,2=1000/sr)     #
3
# SM3 Slope (0 - 255)                         #
8
# SM3 Speed Hz (PS = 125*(n+1), n=0,1..255)   #
5
```

Figure A3.20 – Example of PARAM.INI file

A3.5.2.   OPTIONS.INI

This file contains many parameters optimizing the program performance and trying to obtain the best from the SPATRAM. In order to explain the meaning of all these parameters it is convenient to use the DAS Config as in the previous case. The second page of the DAS Config regards all the options stored in the OPTIONS.INI file:

The Options Panel has 4 sub-pages (Figure A3.21)
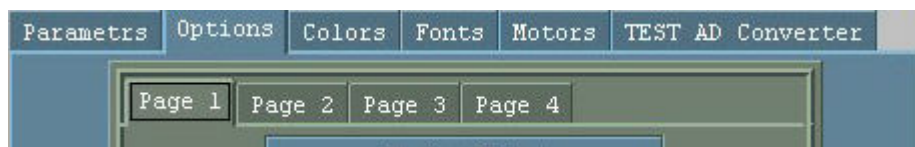
Figure A3.21 – DAS Config Panel – Options page, top

Almost all the options can be changed during the execution of the program in real time, so there is not a button applying the modification (as in the parameters page). The new settings are applied immediately and will be lost at the end of the session. In order to maintain the modified settings also for futures runs of the program the button **Save** has to be used (Figure A3.22).
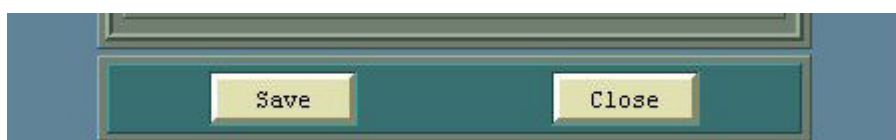
Figure A3.22 – DAS Config Panel – Options page, bottom

A3.5.2.1. Options - Page 1

The first page allows for setting some options regarding mainly spectra and file storage (Figure A3.23)
The saving mode of the spectra can be set to:

- ASCII: Spectra are saved in ASCII mode
- Binary: the binary mode save space on the disk (the best choice!!!)
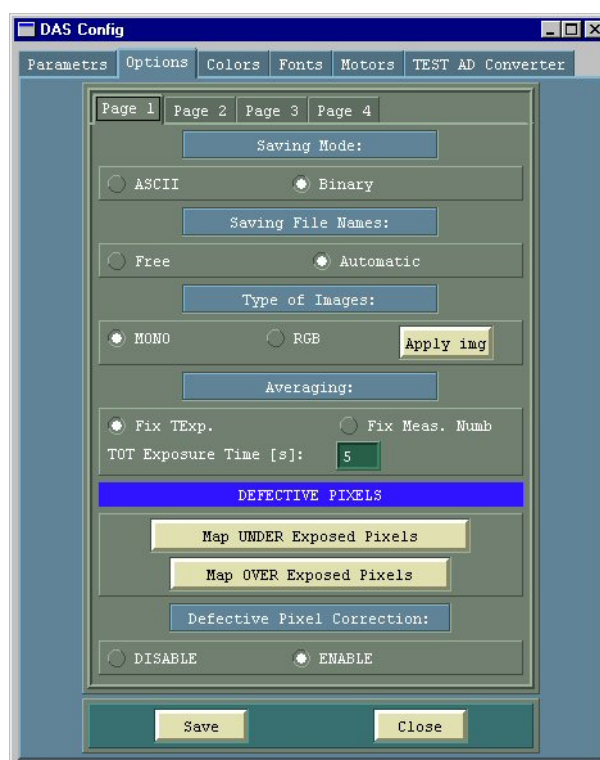
Figure A3.23 – DAS Config; Option Page 1

Also the names of the files where the measured spectra are saved have two option:

- Free: DAS asks for the name of the file where the spectrum will be saved.
- Automatic: DAS assigns to the file names the format ***AAAYYMMDDxxx.ext*** where:

  AAA = Name of the station (in the file " \Config\GeoCoord.ini")

  YY = year

  MM = month

  DD = day

  xxx = progressive number (0,1,....999).

  ext = *bif* or *dat*, according with the Spectra Saving Mode.

Each file will contain 50 spectra

The type of the image is fixed to *Mono* (meaning that the type of the data are Unsigned Integer allowing for a dynamical range of 65535 points. The RGB mode is reserved for future realise.

The Averaging section allows for the choice between:

- Fixed Exposure Time: the text box reports the total time over which the measurements will be performed
- Fixed Number of measurements the text box below report the total number of measurements that will be performed for each scan

The Averaging is a particular type of measurements where the same measurement is repeated or for a Fixed Exposure Time or for a Fixed Number of measurements in order to obtain the highest S/N ratio

The **Defective Pixel** Section take into account that during the life of the instrument the CCD sensor can degrade his performances. In this regard the 2 push buttons Map UNDER Exposed pixels and Map OVER Exposed pixels can build the maps of the defective pixel. The analysis of the maps can produce the file for the correction of the defective pixel.

The Defective pixel correction can be:

- DISABLED - in this case no correction is applied to the CCD Image
- ENABLED - the CCD image is corrected with a cubic spline interpolation over the defective pixels listed in the file map file of the defective pixels.

A3.5.2.2. Options - Page 2

The second page allows for setting some options regarding mainly CCD Dark removal, CCD Target temperature and System files (Figure A3.24)
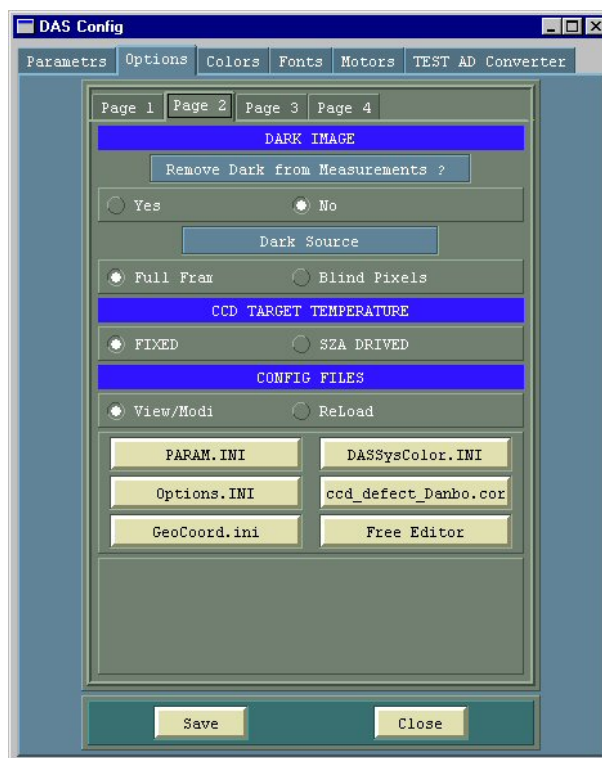
Figure A3.24 – DAS Config; Option Page 2

The **Dark Image** section allows for setting if the dark current has to be removed from the measurements:

- **Yes** - The dark is removed from the measurements
- **No** - The dark is NOT removed from the measurements

And if "Yes" is chosen it is possible to select the Dark source:

- **Full Frame** - the source is the full sensitive area of the CCD sensor (this means that a DARK measurement is carried out before the LIGHT measurement).
- **Blind Pixels** - the source are the 30 Blind Pixels on the right of the CCD sensor (this means that the DARK measurement is not necessary).

The **CCD Target Temperature** section regards the management of the temperature of the CCD that can be:

- **Fixed** - The CCD target temperature remains always that one specified in the Parameters page (or PARAM.INI file)
- **SZA Driven** - The CCD target temperature varies with the Solar Zenith Angle. The temperature starts decreasing when the SZA is grater than 80° in order to obtain an higher S/N ratio for the measurements obtained at sunset and sunrise.

In the **Config Files** section 5 of the 6 buttons can be used for the editing of the configuration files of DAS, the last button is a free editor. The **Reload** radio button allows for the re-loading of the parameters set in each file.

A3.5.2.3. Options - Page 3

The third page allows for setting some options regarding mainly the plot window (Figure A3.25)
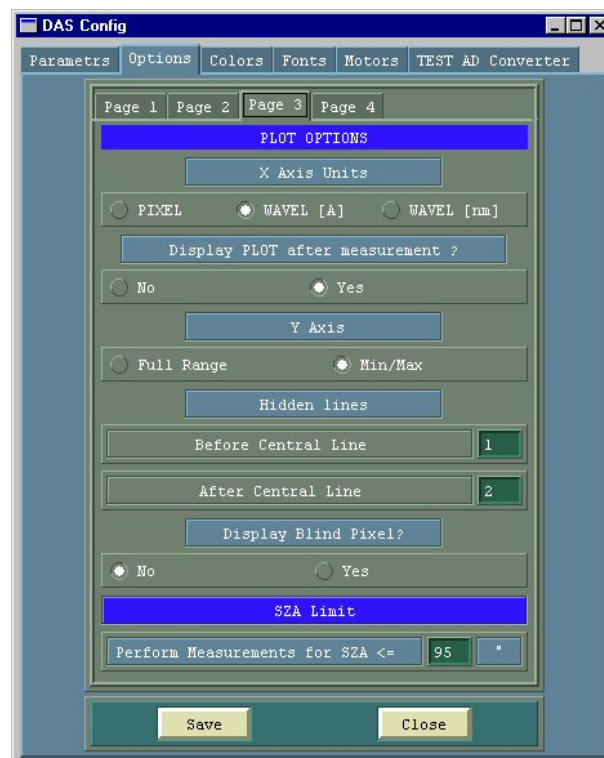
Figure A3.25 – DAS Config; Option Page 3

The **Plot Options** section allows for choosing:
- The Units for the X axes that can be
  - PIXEL
  - WAVEL[A]
  - WAVEL[nm]
- To show the PLOT after the measurement
  - NO
  - Yes
- The range for the Y Axes
  - Full Range (0 - 65535)
  - Min//Max of the measurement

- How many lines will be shown in the plot, in fact the CCD sensor could be not homogeneously illuminated, so some lines could present a mean value too low and if all the line are plotted could not be possible to appreciate the quality of the measurement. Depending on the vertical binning, the numbers of lines to be plotted, after and before the central one, can be selected.
- To show the Blind Pixel. The CCD sensor in use (Marconi CCD3011-Bi) has 1054x256 pixels, but only 1024 are illuminated; the remaining 30 are blind and can be used for the quantification of the read current

The **SZA Limit** section is utilized to set the period of activity of the instrument. Since there are no reasons for the SPATRAM to work during the night, setting the SZA limits at 95° the spectrometer will perform measurements for values of Solar Zenith Angles lower than 95° (only during the day)

A3.5.2.4. Options - Page 4

The fourth page allows for setting some options regarding the daily data back\-up and OMU Thermoregulation (Figure A3.26)
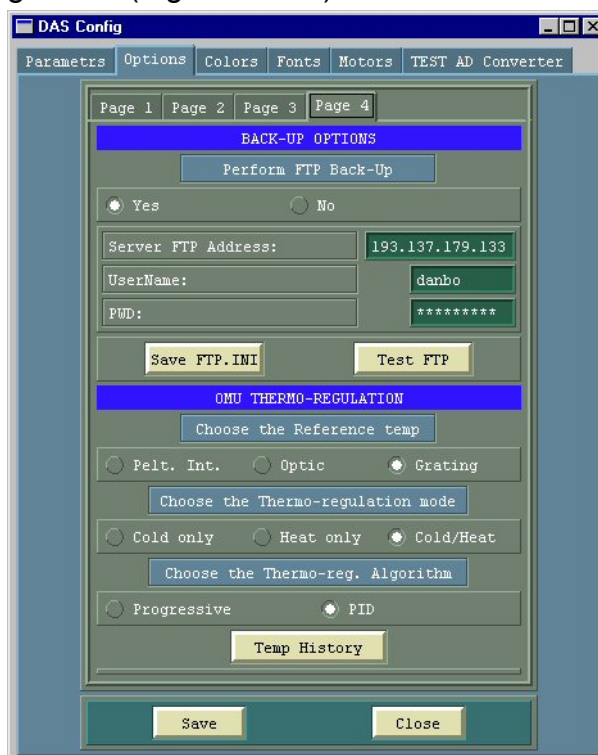
Figure A3.26 – DAS Config; Option Page 4

With the **Back-Up Options** section, it can be selected if the Back-up will be performed during the period of inactivity of the instrument (when the SZA is greater than the fixed values) via FTP in the server specified in the other records The Save FTP Button writes the new settings in the file FTP.INI and the **TestFTP** Button allows for testing the inserted parameters for the FTP connection

The **OMU-Thermo-Regulation** section allows for

- The setting of the OMU target Reference temperature that can be chosen between:
  - o Pelt. Int. (The average of the left and right temperature for the main OMU Peltier)
  - o Optic (temperature of the sensor outside the monochromator but inside the OMU)
  - o Grating (temperature of the sensor inside the monochromator and near the grating)
- The setting of the Thermo-regulation mode that can be choosen.between:
  - o Cold only
  - o Heat only
  - o Cold//Heat
- The setting of the Thermo-regulation Algorithm that can be choosen.between:
  - o Progressive
  - o PID (Proportional, Integer, Derivative

The **Temp History** is employed for the plotting of a log file generated by DAS. This is similar to the DAS LOG mode, even if pressing the button a file browser for the selection of the log file is opened.

Figure A3.27 shows an example of OPTIONS.INI file

```
########################################################
#      Configuration file for OPTIONS Setting.        #
#          by DanBo 25/11/2004 at 12:43:43            #
########################################################
# All these flags can be modified on line             #
# in the CONFIG --> OPTION tabs                        #
#-----------------------------------------------------#
# Please DO NOT change the order of the parameters    #
#-----------------------------------------------------#
# Saving Mode: 0 = ASCII, 1 = Binary                  #
1
# File Names:0 = free, 1 = automatic file names       #
1
# Image Type:0=Mono, 1 = RGB                          #
0
# CCD Pix Correction: 0=NOT Corrected, 1=Corrected    #
1
# Averaging Mode:0 = fixed number, 1 = fixed time     #
1
# Avg Mode fixed Number of measurements               #
25
# Avg Mode fixed Time Exposure [sec]                  #
5
# Remove Dark?: 0 = No, 1 = Yes                       #
0
# Dark source: 0 = Blind Pixels, 1 = Full Frame       #
1
# CCD Temp: 0 = Fixed, 1 = variation vs SZA           #
0
# Plot X Scale: 0 = Pixel #, 1 = wl[A], 2 = wl[nm]    #
1
# Plot display: 0 = NO,  1 = Yes                      #
1
# Plot Y Scale: 0 = FullRange(0-65535), 1 = min/max   #
1
# Measurements performed for SZA <= SZAMax            #
95
# Hidden Lines in Plot-Before and after Cent. line    #
1
2
# Display Blind Pixel: 0 = NO, 1 = Yes                #
0
# Perform FTP Back-UP: 0 = NO, 1 = Yes                #
1
# Reference temperature for OMU Thermo-Regulation:    #
# 0 = AVG Internal Peltier; 1 = Optic; 2 = Grating    #
2
# OMU Thermo-Regulation mode:                         #
# 0 = Cold Only; 1 = Heat only; 2 = Cold/Heat         #
2
########################################################
```

Figure A3.27 – Example of OPTIONS.INI file

A3.5.3.   DASSYSCOLORS.INI

In the file DASSysColors.INI the RGB values of some graphical controls of the DAS are stored. This file can be modified "by hand" trough a text editor (Figure A3.28) or by means of the related button in the page 2 of the Options (see § A3.5.2.2).

```
############################################
#              DAS Default Color           #
#                 by DanBo                  #
############################################
# All these values can be modified, but    #
# DO NOT Exchange the order                 #
############################################
# Selected Buttons   BG                     #
255 255 111
# Unselected Buttons BG                     #
127 220 120
# UnSelected Buttons  FG                    #
0 0 0
# Forms and shell Background                #
87 80 72
# ACTIVE Labels Background                  #
43 40 123
# ACTIVE Labels Foreground                  #
255 255 255
# PASSIVE Labels Background                 #
0 0 33
# PASSIVE Labels Foreground                 #
255 255 255
# Capital Letters Labels Color   UP BG      #
147 158 189
# Capital Letters Labels Color   UP FG      #
0 0 0
# Radio Button BG                           #
0 62 55
# Radio Button FG                           #
255 255 0|
############################################
```

Figure A3.28 – Example of DASSYSCOLOR.INI file

Also for this file one page of the DAS_Config Panel allows for the on-line modification of the displayed colors The page Colors allows for the modification of the DAS Colors(Figure A3.30). Selecting the type of object and modifying the position of the red, green and blue bars the desired colour can be assigne to each of the selected objects. The **Load Palette** Button is employed in order to load and evaluate a RGB colour palette (255 different colors). The Save button store the new setting in the \Config\DASSYSCOLOR.INI file.

A3.5.4.   FTP.INI

As explained in section A3.5.2.4, this file contains the setting for the connection to an FTP server for the daily back-up of the carried out spectral data.

```
##################################################
#     Configuration file for FTP Setting.        #
##################################################
# FTP Server Address                             #
192.167.167.95
# FTP User Name                                  #
danbo
# FTP pwd                                        #
***********
##################################################
```

Figure A3.29 – Example of FTP.INI file
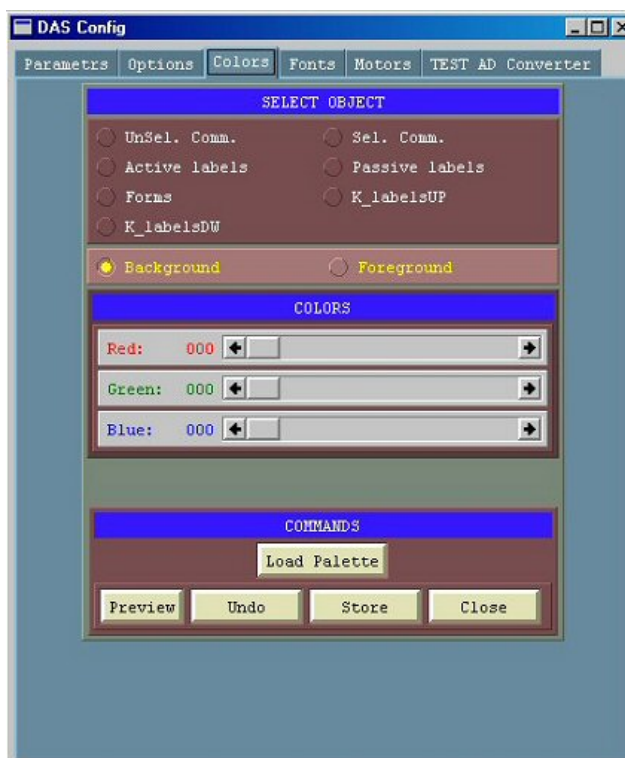
Figure A3.30 – DAS Config; Colors page

A3.5.5.   GEOCOORD.INI

The GEOCOORD.INI file (Figure A3.31) contains the name of the station (3 characters) and the geographical coordinates of the station (Latitude, Longitude and Altitude) Moreover the time zone of the site of measurements has to be provided in order to allow DAS for a right computation of the Solar Zenith Angle.

Figure A3.31 – Example of GEOCOORD.INI file

A3.5.6.   CCD_DEFECT.COR

This is the file taking into account the possibility that the CCD presents some imperfections. The defective pixel can be identified with the procedure described in

section A3.5.2.1 and then, following the instruction reported in the example file (Figure A3.32), the map of the under exposed, over exposed and burn pixels can be build. This procedure was developed in the beginning of the work and it can be greatly improved.

```
DREM By DanBo 21/08/03
DREM List of defective pixels, columns or rows.
DREM Available commands:
DREM
DREM PIX keyword for the beginning of the pixel section
DREM The PIX Keyword is followed by the PITM Keyword, that is
DREM the Number of pixels items
DREM then the coordinate of a defective pixel (x,y),
DREM right, left, up and down pixel for the correction (i.e. 1,1,0,0)
DREM
DREM COL keyword for the beginning of the column section
DREM The COL Keyword is followed by the CITM Keyword, that is
DREM the Number of colons items
DREM then the coordinate of a defective colon (x,start y, end y),
DREM right and left, colon for the correction (i.e. 1,1)
DREM
DREM RAW keyword for the beginning of the raw section
DREM The RAW Keyword is followed by the RITM Keyword, that is
DREM the Number of raws items
DREM then the coordinate of a defective raw (start x, end x, y),
DREM up and down, raws for the correction (i.e. 1,1)
DREM
DREM Start of pixel section
PIX
DREM Number of items of pixel correction
PITM    33
0 0 -2 3 0 0
1 0 -2 3 0 0
101 102 1 1 0 0
107 115 1 1 0 0
136 175 1 1 0 0
234 134 1 1 0 0
```

Figure A3.32 – Example of CCD_DEFECT.COR file

A3.6. Measurement chart

One of the most important features of the DAS program is the capability of carry out measurements in unattended and unmanned mode. With a series of keywords codified in the source code, and given to DAS by means of an ASCII file with default extension *.PRG, the program can perform any kind of measurements that could be obtained in the Manual mode.

Figure A3.33 shows an example of PRG file

```
LABEL "Measurements Table FBRTEST.PRG"
CALIBRA
MEASURE 1 3 0 1 0.50 1 1 1
MEASURE 1 4 0 1 0.50 1 1 1
MEASURE 1 5 0 1 0.50 1 1 1
MEASURE 1 6 0 1 0.50 1 1 1
MEASURE 1 7 0 1 0.50 1 1 1
MEASURE 1 8 0 1 0.50 1 1 1
MEASURE 1 9 0 1 0.50 1 1 1
MEASURE 1 10 0 1 0.50 1 1 1
MEASURE 1 11 0 1 0.50 1 1 1
MEASURE 1 12 0 1 0.50 1 1 1
MEASURE 1 13 0 1 0.50 1 1 1
MEASURE 1 14 0 1 0.50 1 1 1
MEASURE 1 1 0 1 1.50 1 1 1
MEASURE 1 2 0 1 1.50 1 1 1
MEASURE 1 3 0 1 1.50 1 1 1
BEGIN
```

Figure A3.33 – Example of PRG file

Table A3.3 reports the full list of the keywords recognized by DAS and the syntax of the commands. Some of the keywords (as MEASURE and AVGCCD) are followed by some parameters explained in Table A3.4

Table A3.3 – DAS codified Keywords

Keyword	Action	Syntax
AUTORNG	Autoranging for optimal exposure time	AUTORNG
AVGCCD	Averaged measurement setting mirror, filter, grating, TExp	AVGCCD m l f a t d s p
BEGIN	re-start the execution of the PRG file	BEGIN
CALIBRA	Auto calibration with HG Lamp (hg line at 4358A on pix 512)	CALIBRA
DARKC	Perform a DARK Measurement (shutter closed), with the exposure time previously calculated	DARKC
EXPO	Set the exposure time	EXPO t
FILTER	Set the filter position	FILTER f
GETCCD	Performs a LIGHT Measurement (shutter opened)	GETCCD
H_FILTER	Home position for filter wheel	H_FILTER
H_GRAT	Home position for grating	H_GRAT
H_MIRROR	Home position for input mirror	H_MIRROR
HG_OFF	HG lamp OFF	HG_OFF
HG_ON	HG lamp ON	HG_ON
LABEL	text after this command is displayed in the status label	LABEL text
MEASURE	Performs a measurement setting mirror, filter, grating, TExp	MEASURE m l f a t d s p
MIRROR	set mirror position	MIRROR m
PLOT	display plot	PLOT
QJ_OFF	Qj lamp OFF	QJ_OFF
QJ_ON	Qj lamp ON	QJ_ON
REM	text after this is a comment	REM string
SAVE	save the measurement in the predefined file	SAVE
WAIT	Stop the program execution for xx milliseconds	WAIT xx
WAVELEN	set the grating position	WAVELEN l
XEND	stop the execution of the PRG file	XEND

Table A3.4 – DAS: meaning of the keywords parameters

Parameter	Meaning
m	Mirror position [0, 3]
l	Grating position [0, 14]
f	Filter position [0, 5]
a	1 = perform autoranging; 0 = do not perform autoranging
t	Exposure time if the autorange fails (x.xx seconds)
d	1 = Light Measurement 0 = DARK Measurement)
s	1 = save measurement on file, 0 = NOT save
p	1 = Show plot after measurement

0 = NOT Show plot after measurement

Figure A3.34 shows the window created at the pressing of the "Mirror" push button in the DAS Main Panel and from high to low the correspondence between m and the Input Mirror Position is done.

Figure A3.34 – Input Mirror position window

In other words if the desired position for the input Mirror is Calibra, "m" has to have value equal 2.

The same has to be done for the parameter "f" regarding the filter wheel position. Pressing the push button "Filter" in the DAS Main Panel, the window shown in Figure A3.35 is created; the association between "f" and the filter position is made from the top to the bottom (i.e f = 2 → Filter "UG5" is positioned in front the entrance slit).
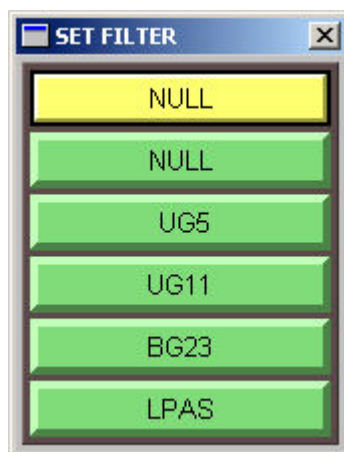
Figure A3.35 – Filter Wheel position window

Figure A3.36 shows the window created pressing the button "Grating" in the DAS Main Panel. This window allows for the association of the parameter "l" for setting

the grating position within the range [0, 14]. The buttons have to be considered from left to right and from the top to the bottom. (i.e. the l = 3 means the grating is positioned at the 4358A spectral position (4358A is the central wavelength of the spectral window).
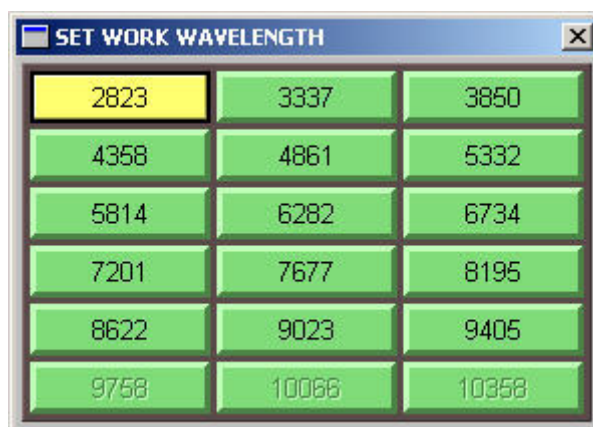
Figure A3.36 – Grating position window

A3.7. Remote control of the SPATRAM

The SPATRAM is equipped of a net card 10/100 Mbps that allows to the spectrometer to be connected to the Internet. Therefore the instrument can be remotely controlled in all its functionality by means of the PCAnyWhere or VNC software tools. Thanks to that facility the instrument can be always monitored by authorized staff. In addition in the DAS is implemented a module providing to the daily back-up of the measured data via FTP on a specified server (see § A3.5.2.4), in order to minimize the risk of loss of data. In fact if the memorization unit (the hard disk of the NOVA 7892) or the monoboard itself became unusable, only the current day of measurement will be lost.

References

[1] Angell, J.K., Global variation in total ozone and layer mean ozone: an update through 1981, *J. Clim. And Appl. Meteorol.*, **22**, 1611-1626, 1983.

[2] Bojkov R., V.E. Fioletov, Estimating the global ozone characteristics during the last 30 years, *J. Geophys. Res*., **100**, 16537-16551, 1995.

[3] Wang, W.C., Climate implication of observed changes in ozone vertical distribution at middle and high latitudes in the northern hemisphere, *Geophys. Res. Lett.*, **20**, 1567-1570, 1993.

[4] Randel, W. J., R.S. Storalski, D.M. Cunnold, J.A.Logan, M.J.Newchurch, J.M. Zawodny, Trends in the vertical distribution of Ozone, *Science*, **285**, 1689-1692, 1999.

[5] Noxon J.F., Stratospheric NO_2, Observational Method and behaviour at mid latitude, *Geophys. Res. Lett.*, **84**, 5047-5065, 1979.

[6] Solomon, S. and R. Garcia, On the distribution of Nitrogen Dioxide in the High latitude stratosphere, *J. Geophys. Res*., **88**, pp. 5229-5239, 1983.

[7] T.Wagner, C.Leue, K. Pfeilsticker and U. Platt: "Monitoring of stratospheric chlorine activation by global Ozone Monitoring Experiment (GOME) OclO measurements in the austral and boreal winters 1995 through 1999" *J. Geophys. Res.,* **106**, 4971-4986, 2001.

[8] Eisinger, M., and J.P. Burrows, Tropospheric sulfur dioxide observed by the ERS-2 GOME instrument, *Geophys. Res. Letters* **25**, 4177-4180, 1998.

[9] Burrows, J.P., M. Weber, M. Buchwitz, V. Rozanov, A Ladstatter-Weissenmayer, A. Richter, R. De Beek, R. Hoogen, K. Bramstedt, K.W. Eichmann, M. Eisinger, and D. Perner, The Global Ozone Monitoring Experiment (GOME): Mission concept and first scientific results, *J. Atmos Sci.*, **56**, 151-175, 1999.

[10] Bovensmann H., J. P. Burrows, M. Buchwitz, J. Frerick, S. Noël, V. V. Rozanov, K. V. Chance, A. P. H. Goede, SCIAMACHY: mission objectives and measurements modes, *J. Atmos. Sci.*, **56**, 127-150, 1999.

[11] Bortoli, D., M.J. Costa, G. Giovanelli, A.M. Silva Vertical Column Of Atmospheric Compounds From Gome Data Analysis, Proc. EUMETSAT-"The 2002 EUMETSAT Meteorological Satellite Data Users' Conference", 669-676, 2003.

[12] Bortoli, D., F. Ravegnani, I. Kostadinov, G. Giovanelli, A. Petritoli and M.J. Costa, NO2, SO2 And Ozone Monitoring By Means Of GOME Data Analysis And Ground-Based Observations In The Mediterranean Area. Proc. EUMETSAT-"The 2001 EUMETSAT Meteorological Satellite Data Users' Conference", 293-300, 2001

[13] Velders G. J. M., C. Grainer, R. W. Portmann, K. Pfeilsticker, M. Weing, T. Wagner, U. Platt, A. Richter, J. P. Burrows, Global tropospheric NO2 column distributions: comparing three-dimensional model calculations with GOME measurements, *J. Geophys. Res.*, **106**, 12643-12660, 2001

[14] Lauer A., M. Dameris, A. Richter, J. P. Burrows, Tropospheric NO2 columns: a comparison between model and retrieved data from GOME measurements, *Atmos. Chem. Phys.*, **2**, 67-78, 2002

[15] Leue C., M. Weing, T. Wagner, O. Klimm, U. Platt, B. Jahne, Quantitative analysis of NOx emissions from Global Ozone Monitoring Experiment satellite image sequences, *J. Geophys. Res.*, **106**, 5493-5505, 2001

[16] Brune, W. H., J. G. Anderson and K. R. Chan, In situ observation of BrO over Antartica: ER-2 aircraft results from 54°S to 72°S latitude. *J. Geophys. Res*, **94**, 16639-16647, 1989.

[17] Giovanelli, G., D. Bortoli, A. Petritoli, E. Castelli, I. Kostadinov, F. Ravegnani, G. Redaelli, C. M. Volk, U. Cortesi, G. Bianchini and B. Carli, Stratospheric minor gas distribution over the Antarctic Peninsula during the APE-GAIA campaign, *Int J. Of Remote Sensing*, in press, 2005

[18] Otten, C., F. Ferlemann, U. Platt, T. Wagner and K. Pfeilsicker. Ground based DOAS UV/Visible measurements at Kiruna (Sweden) during the SESAME winters 1993/94 and 1994/95. *J. of Atmospheric Chemistry* **30**, 141-162, 1998.

[19] Sarkissian, A., G. Vaughan, H. K. Roscoe, L. M. Barlett, F. M. O'Connor, D. G. Drew, P. A. Huges, and D. M.Moore, Accuracy of measurements of total ozone by a SAOZ ground-based zenith sky visible spectrometer, *J. Geophys. Res.* **102**, 1379-1390, 1997.

[20] Noxon J.F., Nitrogen dioxide in the stratosphere and troposphere measured by ground-based absorption spectroscopy. *Science*, **189**, 547-549, 1975.

[21] Giovanelli G., P. Bonasoni, F. Evangelisti, O3 and NO2 Ground-based measurements at Terra Nova Bay, Antarctica. In: Italian research on Antarctic Atmosphere, M. Colacino, G. Giovanelli, L. Stefanutti, Eds, SIF Conference Proceedings, **27**, 255-268, 1990.

[22] Sanders, R. W., S. Solomon, M.A.Carroll AND A. L. Schmeltekopf, Visible and Near-Ultraviolet spectroscopy at McMurdo station, Antarctica. 4. Overview and daily measurements of NO2, O3 and OClO during 1987. *J. Geophys. Res.*, **94**, 11381-11391,1989.

[23] Giovanelli,G. et al., Ozone ground-base measurements by the GASCOD near-UV and visibile DOAS system. in Proceedings of the Quadriennial Ozone Symposium 1992, NASA Confer. Pubblic. 3266, 707-711, Washington D.C., 1994.

[24] Petritoli, G. Giovanelli, P. Bonasoni, T. Colombo, F. Evangelisti, U.Bonafe, D. Bortoli, Iv. Kostadinov and F. Ravegnani. "Ground Based NO_2 and O_3 Analysis at Mt. Cimone Station during 1995-1996: a case study for spring 1995 NO_2 concentration profile", in *Spectroscopic Atmospheric Monitoring Techniques,* K.Schafer, ed., *Proc. EUROPTO* **3867**, 280-289, 1999.

[25] Sussmann R. and M. Buchwitz, Initial validation of ENVISAT/SCIAMACHY columnar CO by FTIR profile retrievals at the Ground-Truthing Station Zugspitze, *Atmos. Chem. Phys.*, **5**, 1497–1503, 2005

[26] Bracher A., M. Weber, K. Bramstedt, M. V. Konig, A. Richter, A. Rozanov, C. Savigny, and J. P. Burrows, 2002:Validation of ENVISAT trace gas data products by comparison with GOME/ERS-2 and other satellite sensors, ENVISAT Validation Workshop, ESA/ESRIN, Frascati,Italy, 9-13 December 2002, to be published by ESA Publications Division as Special Publication SP-531,

[27]   Buchwitz, M., S. Noel, H. Bovensmann, and J. P. Burrows, Verification of SCIAMACHY Level 1 and 2 near-IR nadir data products by WFM-DOAS analysis, ENVISAT Validation Workshop, ESA/ESRIN, Frascati, Italy, 9-13 December 2002, to be published by ESA Publications Division as Special Publication SP-531 (on CD-ROM), 2002.

[28]   Ahmad, S. P., P. F. Levelt, P. K. Bhartia, E. Hilsenrath, G. W. Leppelmeier, and J. E. Johnson, "Atmospheric Products from the Ozone Monitoring Instrument (OMI)", Proceedings of SPIE conference on Earth Observing Systems VIII, San Diego, California, Aug 3-8, 2003.

[29]   Bhartia, P. K., and C. W. Wellemeyer, "OMI TOMS-V8 Total O3 Algorithm", Algorithm Theoretical Baseline Document: OMI Ozone Products, P. K. Bhartia (ed.), vol. II, ATBD-OMI-02, version 2.0, Aug. 2002.

[30]   Boersma, F., E. Bucsela, E. Brinksma, and J. F. Gleason, "NO2", Algorithm Theoretical Baseline Document: OMI Trace Gas Algorithms, K.Chance (ed.), vol. IV, ATBD-OMI-04, version 2.0, Aug. 2002.

[31]   Chance,K., T. P. Kurosu, and L. S. Rothman, "HCHO", "OClO", "BrO", Algorithm Theoretical Baseline Document: OMI Trace Gas Algorithms, K. Chance (ed.), vol. IV, ATBD-OMI-04, version 2.0, Aug. 2002.

[32]   Bortoli, D., F. Ravegnani, Iv. Kostadinov, G. Giovanelli, A. Petritoli, F.Calzolari, MJ. Costa, A.M. Silva, S. Beirle, T. Wagner, M. Wenig and U. Platt, Stratospheric Nitrogen Dioxide In Antarctic Regions From Ground Based And Satellite Observation During 2001, Proc. SPIE, **4882**, 304-313, 2003.

[33]   Bortoli, D., G. Giovanelli, F. Ravegnani, I. Kostadinov, A. Petritoli, T.Catalbiano and J.P. Burrows, GOME Data Analysis And Ground Based In The Mediterranean Area During Etna Volcano Activity, ERS-ENVISAT Symposium "Looking down to Earth in the New Millenium" SP-461, ESA Publication Division, 2000.

[34]   Lambert, J.-C., M. Van Roozendael, P.C. Simon, J.-P. Pommereau, F. Goutail, J.F. Gleason, S.B. Andersen, D.W. Arlander, N.A. Bui Van, H. Claude, J. de La Noë, M. De Mazière, V. Dorokhov, P. Eriksen, A. Green, K. Karlsen Tørnkvist, B.A. Kåstad Høiskar, E. Kyrö, J. Leveau, M.-F. Merienne, G. Milinevsky, H.K. Roscoe, A. Sarkissian, J.D. Shanklin, J. Staehelin, C. Wahlstr¢m Tellefsen, and G. Vaughan, Combined characterisation of GOME and TOMS total ozone measurements from space using ground-based observations from the NDSC, *Adv. Space Res.*, **26**, 1931-1940, 2000.

[35]   Martin, R.V., D.D. Parrish, T.B. Ryerson, D.K. Nicks Jr., K. Chance, T.P. Kurosu, A. Fried, B.P. Wert, D.J. Jacob, and E.D. Sturges, Evaluation of GOME satellite measurements of tropospheric NO2 and HCHO using regional data from aircraft campaigns in the southeastern United States, *J. Geophys. Res.* **109**, D24307, 2004.

[36]   Wallace J. M., P. V. Hobbs, Atmospheric Science, an introductory survey, Academic Press, San Diego, 1977.

[37]   Brasseurs G. P., J. J. Orlando, G. S. Tyndall, eds., *Atmospheric chemistry and global change*, Oxford University Press, New York, 1999

[38]   Finlayson-Pitts B.J. e Pitts J.N.Jr., Atmospheric chemistry: fundamentals and experimentale techniques. J.Wiley & Sons Ed., Wiley Interscience Pub., New York, 1986.

[39] Chapman S., On ozone and atomic oxygen in the upper atmosphere, Phil. Mag., **10**, 369, 1930

[40] Brasseur G. e Solomon S., Aeronomy of the middle atmosphere. D.Reidel Publishing Company, Dordrecht, Holland, 1986.

[41] Rowland, F. S., Nobel Lecture in Chemistry Ed. Bo G Malmström, Chalmers University of Technology; Göteborg University, 273-296, 1997

[42] Platt, U., "Differential Optical Absorption Spectroscopy (DOAS)" in Air Monitoring by spectroscopic Techniques, Ed W. Sigrist, *Chemical Analysis Series*, **127**, 22-85, 1994

[43] SPIE - The International Society of Optical Engineering, Introduction. In Measurement of atmospheric gases, **1433**, 1991.

[44] Edner H., Ragnarson P., Spännare S. e Svanberg S., Differential optical absorption spectroscopy (DOAS) system for urban atmospheric pollution monitoring. *Applied Optics*, **32**, 3, 327-333, 1993.

[45] Solomon, S., A. Schmeltekopf and R. Sanders, , On the interpretation of zenith sky absorption measurements. *J. Geophys. Res*, **92**, 8311-8319, 1987.

[46] Plane J.M.C. e Nien C., Differential optical absorption spectrometer for measuring atmospheric trace gases. *Rev. Sci. Instrum.*, **63(3)**, 1867-1876, 1992.

[47] Platt U., Perner D., Schroeder J., Kessler C. e Toennisen A., The diurnal variation of NO_3. *J. Geophys. Res.*, **86**, 965-970, 1981.

[48] Platt, U., and D. Perner, Direct measurement of atmospheric CH_2O, HNO_2, O_3, and SO_2 by differential absorption in the near UV, *J. Geophys. Res.*, **85**, p. 7453, 1980.

[49] Platt U., Rateije M., Junkermann W., Rudolph J. e Ehhalt D.H., New tropospheric OH measurements. *J. Geophys. Res.*, **93**, 5159-5166, 1988.

[50] Stevens R.K. e Vossler T.L., DOAS urban pollution measurements. In Proc. Measurement of atmospheric gases, H.I.Schiff Ed., SPIE Pub., 1433, 25-35, 1991.

[51] Perliski, L. and S. Solomon, On the evaluation of air mass factor for near-UV and visible absorption spectroscopy. *J. Geophys. Res.*, **98**, 10363-10374, 1993.

[52] Slusser J., K. Hammond, A. Kylling, K. Stamnes, L. Perliski, A. Dahlback, D. Anderson, R. De Majistre, Comparison of air mass computations, *J. Geophys. Res.*, **101**, 9,315-9,321, 1996

[53] Petritoli A., "Distribuzioni verticali di gas in traccia in atmosfera ottenute con metodi di inversione applicati a misure di quantità colonnari", Degree Thesis, 1998.

[54] Sarkissian A., H. K. Roscoe, D. Fish, P. Pommereau, M. Van Roozendael, M. Gil, H. B. Chen, P. Wang, J. Lenoble, Ozone and NO_2 air-mass factor for zenith-sky spectrometres: Intercomparison of calculation with different radiative transfer models. *Geophys. Res. Lett.*, **22**, 1113-1116, 1995.

[55] Sarkissian A., H. K. Roscoe, D. Fish, (a): Ozone measurements by zenith-sky spectrometres: an evaluation of errors in air-mass factors calculated by radiative transfer models, *J. Quant. Spectrosc. Radiat. Transfer*, **54**, 471-480, 1995.

[56] Kondratyev K. Ya., Radiation in the atmosphere. Academic Press, New York and London, 1969.

[57] Junge C. E., Air chemistry and radioactivity, Int. Geophys. Ser., 4, Academic Press, New York and London, 1963.

[58] Goodman, J. W.: Statistical Optics. New York: Wiley, 1985

[59] Kylling A., K. Stamnes, S. C. Tsay, A reliable and efficient two-stream algorithm for radiative transfer; Documentation of accurancy in realistic layered media, *J.Atmos.Chem.*, **21**, 115-150, 1995

[60] Anderson G. P., S. A. Clough, F. X. Kneizys, J. H. Chetwynd, E. P. Shettle, AFGL Atmospheric Constituent Profile (0-120Km). AFGL-TR-86-0110, AFGL (OPI), Hanscom AFB, MA 01736, 1987.

[61] Meinel A. & M., Sunset, twilights, and evening skies. Cambridge University Press, 1983.

[62] Kasten F., A new table and approximation formula for the relative optical air mass, Arch. F. Met. Geophys. Bioklimat., Ser. B, Bd. 14. Heft. 2, 206, 1966.

[63] Evangelisti, F., A. Baroncelli, P. Bonasoni, G. Giovanelli AND F. Ravegnani, Differential optical absorption spectrometer for measurement of tropospheric pollutants. *Applied Optics*, **34**, 2737-2744, 1995.

[64] Giovannelli G., P. Bonasoni, F. Evangelisti, O_3 and NO_2 Ground-based measurements at Terra Nova Bay, Antartica. In: Italian research on Antartic Atmosphere, M. Colacino, G. Giovanelli, L. Stefanutti, Eds, SIF Conference Proceedings, **27**, 255-268, 1990.

[65] Giovannelli G., P. Bonasoni, F. Evangelisti, Determination of gas column amount by solar zenith radiation measurements. In: Italian research on Antartic Atmosphere, M. Colacino, G. Giovanelli, L. Stefanutti, Eds, SIF Conference Proceedings, *35*, 453-467, 1992.

[66] Bortoli, D., F. Ravegnani, G. Giovanelli, Iv Kostadinov, A. Petritoli and G. Trivellone, Continuous Observation Of NO_2 And O_3 Total Columns At Terra Nova Bat Station, Antarctica, Proc. SIF, **69**, 363-374, 2000

[67] Roscoe H. K., P. V. Johnston, M. V. Roozendael, A. Richter, A. Sarkissian, J. Roscoe, K: E. Preston, J.-C. Lambert, C. Hermans, W. Decuyper, S. Dzienus, T. Winterrath, J. Burrows, F. Goutail, J.-P. Pommereau, E. D'Almeida, J. Hottier, C. Courreul, R. Didier, I. Pundt, L. M. Bartlett, C. T. McElroy, J. E. Kerr, A. Elokhov, G. Giovanelli, F. Ravegnani, M. Premuda, I. Kostadinov, F. Erle, T. Wagner, K. Pfeilsticker, M. Kenntner, L. C. Marquard, M. Gil, O. Puentedura, M. Yela, D. W. Arlander, B. A. Kastad Hoiskar, C. W. Tellefsen, K. Karlsen Tornvist, B. Heese, R. L Jones, S. R. Aliwell, R. A. Freshwater, Slant Column measurements of O3 and NO2 During the NDSC intercomparison of Zenith-Sky UV-Visible Spectrometers in June 1996, *J. Atmos. Chem.*, **32**, 281-314, 1999

[68] Fish, D. J., Measurements of stratospheric composition using ultraviolet and visible spectroscopy, Ph. D. Thesis, University of Cambridge, 1994.

[69] Press W.H., Flannery B.P., Teukolsky S.A., Vetterling W. T. Numerical Recipes – The Art of Scientific Computing, Cambridge University Press, Cambridge, 1989.

[70] Harder J. W., Brault J. W., Johnston P.V. and Mount G.H., Temperature dependent NO_2 cross section at high spectral resolution, *J. Geophys. Res.* **102**, 3861, 3879, 1997.

[71] Sanders R. W., Improved analysis of atmospheric absorption spectra by including the temperature dependencies of NO_2, *J. Geophys. Res.* **101**, 20945,20952, 1996.

[72] Bortoli, D., G. Giovanelli, F. Ravegnani, I. Kostadinov and A. Petritoli, Stratospheric Nitrogen Dioxide in the Antarctic, *Int J. Of Remote Sensing*, **26**, 3395–3412, 2005

[73] Burrows,J.P., A. Dehn, B. Deters, S. Himmelmann, A. Richter, S. Voigt, and J. Orphal: Atmospheric Remote-Sensing Reference Data from GOME: 1. Temperature-Dependent Absorption Cross Sections of NO2 in the 231-794 nm Range, *Journal of Quantitative Spectroscopy and Radiative Transfer* **60**, 1025-1031, 1998.

[74] Burrows, J.P. William R.: CART Regression Models for Predicting UV Radiation at the Ground in the Presence of Cloud and Other Environmental Factors. *Journal of Applied Meteorology,* **36**, 5, 531-544, 1997.

[75] Chance, K., P.I. Palmer, R.J.D. Spurr, R.V. Martin, T.P. Kurosu, and D.J. Jacob, Satellite Observations of Formaldehyde over North America from GOME, *Geophys. Res. Lett.*, **27**, 3461-3464, 2000.

[76] Chance, K., Analysis of BrO Measurements from the Global Ozone Monitoring Experiment, *Geophys. Res. Lett.*, **25**, 3335-3338, 1998

[77] Corlett, Gary K., Monks, Paul S., A Comparison of Total Column Ozone Values Derived from the Global Ozone Monitoring Experiment (GOME), the Tiros Operational Vertical Sounder (TOVS), and the Total Ozone Mapping Spectrometer (TOMS), *Journal of the Atmospheric Sciences*: **58**, 9, 1103-1116, 2001.

[78] Weber, M., K.-U. Eichmann, F. Wittrock, K. Bramstedt, L. Hild, A. Richter, J.P. Burrows, and R. Muller, The cold Arctic winter 1995/96 as observed by the Global Ozone Monitoring experiment GOME and HALOE: Tropospheric wave activity and chemical ozone loss, *Q. J. Roy. Meteor. Soc.* **128**, 1293-1319, 2002

[79] Koelemeijer, R. B. A.; de Haan, J. F.; Stammes, P., A database of spectral surface reflectivity in the range 335-772 nm derived from 5.5 years of GOME observations, *J. Geophys. Res.* **108** , 2003

[80] Kondo, Y., W. A. Matthews, S. Solomon, M. Koike, M. Hayashi, K. Yamazaki, H. Nakajima, K. Tsukui, Ground based measurements of column amounts of NO2 over Syowa station, Antarctica. *J. Geophys.. Res.*, **99**, 14535–14548, 1994.

[81] Juckes M.N. and M.E. McIntyre, A high-resolution one-layer model of breaking planetary waves in the stratosphere. *Nature*, **328**, 590-596, 1987.

[82] Herman, J. R., P. K. Bhartia, O. Torres, C. Hsu, C. Seftor, and E. Celarier, Global distributions of UV-absorbing aerosols from Nimbus 7/TOMS data, *J. Geophys. Res*., **102**, 16,911-16,922, 1997.

[83] Immler, F. and O. Schrems, Vertical profiles, optical and microphysical properties of Saharan dust layers determined by a ship-borne lidar, *Atmos. Chem. Phys.*, **3**, 1353–1364, 2003

[84] Rodger C. D., Characterization and error analysis of profiles retrieved from remote sounding measurements, *J. Geophys. Res.*, **95**, 5,587-5,595, 1990.